PSL
UNIVERSITÉ PARIS

THÈSE DE DOCTORAT
DE L'UNIVERSITÉ PSL

Préparée à MINES ParisTech

Seismic imaging: strategies for visco-acoustic full waveform inversion

Imagerie sismique : stratégies d'inversion des formes d'onde visco-acoustique

Soutenue par
Hao JIANG
Le 21 Mai 2019

École doctorale n°398
Géosciences, Ressources Naturelles et Environnement

Spécialité
Géosciences et Géoingénierie

Composition du jury :

M. Jean-Pierre Vilotte Professeur, Inst. de Physique du Globe de Paris	*Président*
Mme Alessandra Ribodetti Chargée de Recherche, Univ. Nice Sophia Antipolis	*Rapporteur*
M. Romain Brossier Maître de Conférences, Univ. Grenoble Alpes	*Rapporteur*
M. Mark Noble Maître de Recherche, MINES ParisTech	*Examinateur*
Mme Fatiha Gamar Chercheur Sénior, CGG	*Examinatrice*
M. Hervé Chauris Professeur, MINES ParisTech	*Directeur de thèse*

MINES ParisTech | PSL

Acknowledgments

I would like to thank all the people who have contributed to this thesis work. The process of research during the PhD is a journey of exciting the curiosity, pursuing the knowledges and answering the unknowns. I always remember all the people's helps during the wonderful journey.

I would like to thank my supervisor Prof. Hervé Chauris with my sincere gratitude. I began my research with him from my internship until the end of my PhD study. He always supported and encouraged me to conduct the research with great patiences. He always had an insight on the problems and gave me good suggestions. It is the most impressive that he always can describe the geophysical problems in a very precise mathematical language. During the time of writing my thesis, he spent much time on correcting my manuscript lines by lines. He guided me to present my works in an easy understanding way with good timing and rhythm for my presentation at EAGE and my final thesis defense. His passion and rigorous attitude on research inspires me a lot, his optimistic philosophy, healthy life style and humor influence me a lot. I appreciate him for all those helps and positive impacts from him.

I would like to thank the juries of my thesis committee. I thank Alessandra Ribodetti and Romain Brossier for reviewing my thesis in details with professional comments and recommendations. I thank Jean-Pierre Vilotte for chairing the thesis defense. I thank Mark Noble and Fatiha Gamar for examining my work.

I would like to thank my school, MINES ParisTech for funding me on the research, and HPC of our Geoscience Center for implementing the computations.

I would like to thank Baotao Qin, Nobuaki Fuji, Patrick Goblet and Laurent De Windt for examining my work during the annual qualification meeting with fruitful advise. I also express my thanks to Feng Yang for his encouragements and helps for preparation of the annual qualification meeting.

Many thanks to the members of the geophysics team at MINES ParisTech. I especially thank Véronique Lachasse for her helps to facilitate the administrative affairs. I thank the permanent researchers Daniela Donno, Alexandrine Gesret and Mark Noble who are also my master teachers, and Pierre Dublanchet, and the scientific visitors Nidhal Belayouni and Pierre-Francois Roux, for their kindness. I also would like to thank all my colleagues Fang Wang, Charles-Antoine Lameloise, Emmanuel Cocher, Sven

Schilke, Yves-Marie Batany, Tiago Barros, Jihane Belhadj, Julien Cotton, Keurfon Luu, Alexandre Kazantsev, Tianyou Zhou, Michelle Almakari, Ahmed Jabrane, Maxime Godano, Zufri Malik Ibrahim, Joshua Lartey, Mohamadhasan Mohomadian Sarvandani, Rita Abou Jaoude and Milad Farshad, for their friendship and helps.

I would like to thank my friends in Fontainebleau, Paris, France, China and other countries, I always remember the friendships and encouragements from: Pranav Audhkhasi, Asma Berrhouma, Fengjuan Chen, Kaiwen Chang, Naixin Chen, Qinglin Deng, Cecilia Dip, Sebatien Drouyer, Minyu Fan, Mario Fernandez, Yuxin Fu, Fang Gao, Xin Gao, Weiguang He, Yanhui He, Hanqin Huang, Shun Huang, Song Jin, Bo Kang, Eleni Kolokyta, Dingan Liao, Zimin Li, Fang Lu, Dac-Thuong Ngo, Dandan Niu, Oleg Ovcharenko, Meng Pang, Zilin Peng, Bin Qiao, Yanfang Qin, Sara Rachdi, Yi Rong, Yang Shen, Xiangdong Song, Yang Song, Adam Sukma Putra, Yuwei Sun, Yuxin Sun, Chaojing Wang, Dandan Wang, Haisheng Wang, Jialan Wang, Shuaitao Wang, Tianyuan Wang, Wei Wang, Zhuangzhuang Wang, Xiaojing Wu, Mingguan Yang, Shuran Yang, Tiantian Yin, Xi Yu, Shihao Yuan, Fan Zhang, Yizhuo Zhang, Zezhong Zhang and other friends. I express my thanks to Yubing for showing me around when I first arrived at Fontainebleau and many research discussions on the trains between Paris and Fontainebleau. I would like to thank Chen Tang for inspiring me to work on seismic imaging when I first began to learn geophysics. I would like to thank my best friend Dezhi Wang for keeping encouraging me to pass through the hard time. I can not write down all the helps from my friends in every details, but I will keep them always in my heart.

Finally, I would like to express my deepest gratitude to my family. Without their supports and encouragements, I could never accomplish the PhD degree. My grandfather was the headmaster of my primary school and my grandmother was my mathematical teacher for the two first years during my primary school. Their loves and educations will always accompany my whole life.

Abstract

Seismic imaging is an important way to reconstruct the subsurface structures. Conventional seismic imaging is based on acoustic assumption. The interpretation only relies on mono-parameter acoustic wave velocity. With the demand of high-resolution imaging, more physical parameters have been put forward to characterize the subsurface geological bodies. Seismic attenuation is a useful physical parameter to describe the properties of specific geological bodies, e.g., saturated rocks and gas clouds. The introduction of attenuation can improve the seismic migration image and remove the blurring of images under the gas clouds. Seismic attenuation is also more sensitive than velocity changes for fluid detection. Attenuation combined with velocity analysis provide extra information on the subsurface.

Seismic attenuation is represented by the quality factor Q. The reciprocal of Q is defined as the proportion of energy loss per wave propagation cycle. Frequency-independent constant Q model is consistent with observations. Classical approaches for estimating Q models, consist of analyzing seismic spectrum amplitudes or spectrum distortions based on ray methods. Full waveform inversion considered here is an alternative approach that takes into account the finite frequency aspect of seismic waves. In practice, both seismic velocities and attenuation have to be determined. It is known that the multi-parameter inversion suffers from cross-talks.

To mitigate cross-talks and balance the different gradient sensitivities, conventional inversion strategies include sequential inversion and simultaneous inversion. Sequential inversion usually first retrieves velocity and then Q, but it may over-estimate the parameter. Simultaneous inversion reconstructs velocity and Q at the same time. It has to overcome the different sensitivities between parameters without the estimation of the Hessian matrix. There is not yet a clear statement about the optimal recommendation. Therefore, this thesis focuses on retrieving velocity and attenuation and mitigating cross-talks between parameters. I propose a two-step hybrid inversion scheme without the need for the estimation of Hessian matrix, and compare it with conventional inversion strategies.

Attenuation effects lead to phase velocity dispersion. Phase velocity increases as frequency and attenuation increase. It indicates that different combinations of velocity and attenuation result in the same *kinematic velocity* for band-limited seismic data. We

call this relation the *kinematic relationship*. The kinematic velocity model controls the kinematic of wave propagation. It means the traveltime of recorded data is same, but the amplitudes are different. The model is different from the P-velocity model because of attenuation. The hybrid inversion strategy first updates the kinematic velocity model, then subsequently inverts the P-velocity and attenuation models for a fixed kinematic velocity model. Those two steps are alternated with each other to further update the kinematic velocity, then decouple the two parameters based on updated kinematic velocity.

The hybrid inversion strategy is developed and first applied to transmitted-wave-dominated models, in particular a synthetic model with a Gaussian attenuation anomaly and the 2D synthetic Middle-East model. Then the hybrid strategy is applied for the reflected-wave-dominated Marmousi model to investigate the feasibilities on more complex models. We also compare all the results of the hybrid strategy with conventional strategies. The main contributions of the thesis are: (1) a hybrid visco-acoustic FWI strategy to guide the inversion by explicitly incorporating the kinematic relationship between velocity and attenuation; (2) comparisons between different inversion strategies to better understand the visco-acoustic Full Waveform Inversion for transmitted and reflected waves.

Résumé

L'imagerie sismique est un moyen important pour reconstruire les structures de la subsurface. L'imagerie sismique conventionnelle se base sur l'approximation acoustique. L'interprétation se fait uniquement sur un seul paramètre qui est la vitesse de propagation des ondes P. Avec la demande de résolution plus grande, il est nécessaire de pouvoir caractériser la Terre avec plus de paramètres. L'atténuation sismique est l'un de ces paramètres qui peut servir d'indicateur de la présence de fluides et de gaz. L'introduction de l'atténuation dans le processus d'imagerie peut améliorer la qualité des images migrées.

L'atténuation sismique est représentée par le facteur de qualité Q. L'inverse de Q définit la proportion de la perte d'énergie par cycle de propagation des ondes. Les observations montrent des valeurs de Q indépendantes de la fréquence. Les approches classiques pour estimer Q analysent le spectre d'amplitudes ou la distorsion de ce spectre avec des méthodes d'optique géométrique. L'inversion des formes d'onde (Full Waveform Inversion en anglais) est une approche alternative qui prend en compte la fréquence finie des ondes sismiques. En pratique, à la fois les vitesses sismiques et l'atténuation doivent être estimées. Il est connu que l'inversion multi-paramètre ne permet pas de retrouver une décomposition unique.

Pour mitiger cet aspect et pour relativiser les différentes sensibilités des paramètres, les approches conventionnelles ont proposé l'inversion séquentielle et l'inversion conjointe. L'inversion séquentielle retrouve d'abord la vitesse, puis le facteur Q qui peut-être surestimé. L'inversion conjointe reconstruit en même temps la vitesse et l'atténuation. Sans le recours au Hessien (dérivées secondes), il n'est pas simple de contrecarrer les sensibilités différentes. Actuellement, il n'y a pas de recommandation optimale pour l'une ou l'autre approche. Ce travail a pour objectif de retrouver la vitesse et l'atténuation et de mitiger les interférences entre les deux paramètres. Je propose une inversion hybride en deux étapes, sans estimation du Hessien, et je compare cette approche aux stratégies conventionnelles.

L'atténuation conduit à la dispersion de la vitesse de phase. La vitesse de phase augmente lorsque la fréquence et l'atténuation augmentent. Ceci indique que différentes combinaisons de vitesse et d'atténuation conduisent à la même *vitesse cinématique* pour des données à fréquences limitées. Nous appelons cette relation la *relation cinématique*.

Le modèle de vitesse cinématique contrôle la cinématique de propagation des ondes. Ceci signifie que le temps de trajet est le même, mais que les amplitudes sont différentes. L'inversion hybride met d'abord à jour le modèle cinématique, puis inverse pour les modèle de vitesse P et pour l'atténuation, avec la contrainte d'un modèle cinématique fixe. Ces deux étapes sont répétées.

L'inversion hybride est développée ici puis appliquée sur des modèles avec principalement des ondes transmises, en particulier un modèle synthétique avec une atténuation de forme gaussienne et le modèle synthétique 2D du Moyen-Orient. Ensuite, la stratégie hybride est appliquée sur le modèle Marmousi (ondes réfléchies) pour évaluer la faisabilité sur des modèles plus complexes. Nous comparons aussi la stratégie hybride avec les autres approches conventionnelles. Les principales contributions de ces travaux sont (1) une stratégie d'inversion des formes d'onde visco-acoustique pour guider l'inversion avec l'incorporation explicite de la relation cinématique entre vitesse et atténuation; (2) la comparaison entre différentes stratégies d'inversion pour mieux comprendre l'impact de la méthode sur les ondes transmises et réfléchies.

Contents

List of Figures

List of Tables

Chapter 1

Introduction

Contents

Résumé du chapitre 1

L'atténuation sismique est un paramètre physique utile pour détecter la présence de fluides et de gaz en profondeur. L'introduction de l'atténuation peut améliorer la qualité des images migrées et résoudre des problèmes d'amplitudes faibles sous le gaz. Avec l'information de la vitesse, c'est un facteur important pour caractériser la sub-surface.

Dans ce chapitre, j'introduis d'abord l'atténuation sismique et discute des effets de dissipation et de dispersion intrinsèque et liée au "scattering". Je donne aussi des valeurs pour des roches communes. J'introduis plusieurs modèles de Q. Dans la deuxième partie de ce chapitre, je donne un état de l'art sur l'imagerie des structures avec de l'atténuation. Enfin, je conclus avec les motivations pour cette recherche et avec l'organisation de ce travail. Les détails techniques sont introduits dans le chapitre 2.

Seismic attenuation is a useful physical parameter to describe the properties of specific geological bodies, e.g., saturated rocks and gas clouds. The introduction of attenuation can improve the seismic migration image and remove the blurring of images under the gas clouds. Seismic attenuation is also more sensitive than velocity changes for fluid detection. Thus, attenuation combined with velocity analysis provide extra information on the subsurface.

In this chapter, I first introduce seismic attenuation including dissipation and dispersion phenomenon, intrinsic and scattering attenuation. I also give attenuation values for common rocks. Based on rock experiments on attenuation, I introduce different Q models. The second part of this chapter is an overview of the methods on attenuation imaging. Finally, I conclude with the motivation for my research and with the organization of the thesis. In this chapter, I only introduce a few notations and equations. More technical details are presented in Chapter 2.

1.1 Seismic attenuation

1.1.1 Attenuation phenomenon and impacts

Seismic attenuation is the term to characterize the seismic energy loss through the subsurface media, including the intrinsic and scattering attenuation (Section 1.1.2). It is a useful property to characterize geological bodies as lithology discriminator. Due to attenuation, absorption impacts waves, resulting in change in the shape of waveform after passing through attenuation media. The energy absorption can be expressed by the quality factor Q. The reciprocal of Q is defined as the proportion of energy loss per wave propagation cycle (Aki and Richards, 1980; Sheriff and Geldart, 1995; Wang, 2008).

$$\frac{1}{Q} = \frac{\Delta E}{2\pi E}. \tag{1.1}$$

On the one hand, seismic attenuation information can supply extra information on the subsurface media solely or combined with velocity information. Attenuation is more sensitive to pore pressure, saturation, and fracture compared to velocity changes (Gardner et al., 1964; Winkler and Nur, 1982; Klimentos, 1995; Muller et al., 2010).

For reservoir detection and characterization, the information of attenuation is crucial. For example, the large attenuation or small Q values on seismic image indicate gas clouds in Figure 1.1. Further more, different ratios of Q_p and Q_s associated to P and S waves, can determine the reservoir contents (Winkler and Nur, 1979, 1982; Cadoret et al., 1998). Lab experiment of sandstone samples are resonated at frequency mainly from 500 Hz to 1700 Hz, to study the attenuation related to fractional sliding and fluid flow mechanism (Winkler and Nur, 1982). Compared to dry rock, the P and S wave attenuation of partial water saturation rock increases significantly, which leads to a larger

P wave attenuation than S wave attenuation (i.e., $Q_p^{-1} > Q_s^{-1}$). As the water saturation increases, the S wave attenuation reaches the peak value until the full saturation, meanwhile the P wave attenuation increases to maximum value as water saturation is between 60–90 percent. Those phenomenons of lab experiment further extend to the frequency range of exploration seismology (Murphy, 1982; Walls et al., 2002) and well logging (Klimentos, 1995; Qi et al., 2017). Partly under the exploration seismology frequency range from 25 Hz to 400 Hz, Murphy (1982) demonstrates the same conclusion that P and S wave attenuation are sensitive to partial water saturation, leading to $Q_p^{-1} > Q_s^{-1}$. The sonic well logging (i.e., 10–20 kHz) results indicate that Q_p^{-1} is larger than Q_s^{-1} when the gas or condensate is inside the sandstone (Klimentos, 1995). Similar values of P wave attenuation and S wave attenuation indicate the full saturation of water or water + oil.

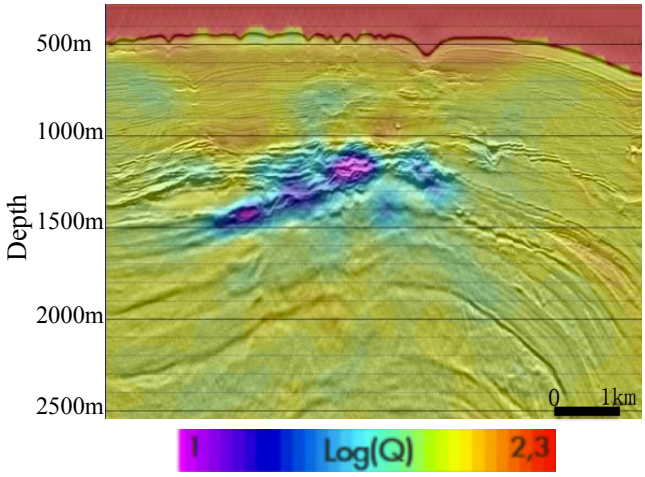

Figure 1.1: Q image of subsurface superimposed to velocity model in an offshore Malaysia reservoir; the purple area indicates the gas clouds (adapted from Plessix et al. (2016))

In global seismology, the attenuation model retrieved from Rayleigh wave provides extra information on the temperature, composition, melt content, and volatile content of the rocks of Earth (Dalton and Ekstrom, 2006; Bao et al., 2016). Attenuation is more sensitive than velocity to temperature increasing for fixed subsurface pressure (Anderson, 1967; Sato et al., 1989; Karato, 1993; Goes et al., 2000; Jackson et al., 2002). Besides, increased attenuation and lower velocity can be caused by partial melting of mantle materials (Hammond and Humphreys, 2000b,a; Faul et al., 2004). Combined with velocity information, attenuation helps to reduce the ambiguity for the interpretation of media state of Earth interiors.

On the other hand, seismic attenuation information can be used to improve the resolution of seismic images. For the scope of exploration seismology, it supplies the

extra information to improve the resolution of seismic migration image. For linearized inversion, Q model can be applied for Q-compensated migration to remove the image blurring under the gas clouds (Figure 1.2) (Zhang et al., 2010; Zhou et al., 2011; Fletcher et al., 2012; Zhu et al., 2014; Gamar et al., 2015, 2016). Q model also can be used as a passive parameter for visco-elastic least-squares migration to improve the resolution of migration images (Dutta and Schuster, 2014). For non-linear visco-elastic full waveform inversion, the Q-compensated inversion can accelerate the convergence speed (Xue et al., 2017).

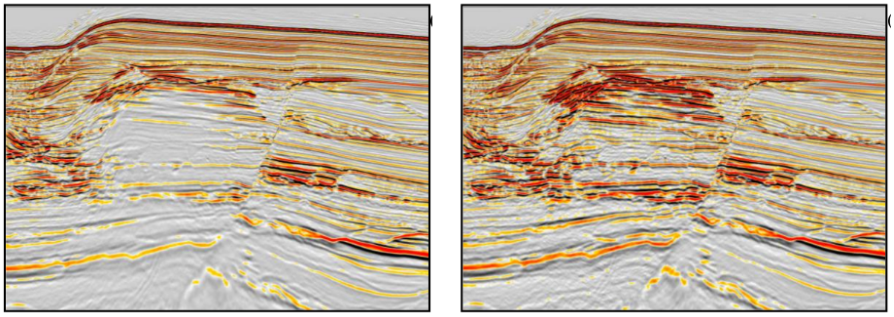

Figure 1.2: Migrated image without (left) and with compensation for attenuation (right) (adapted from Zhou et al. (2011))

1.1.2 Intrinsic and scattering attenuation

Seismic wave attenuation includes *intrinsic attenuation* (Voigt, 1892; Ricker, 1953; Kolsky, 1956; Jackson and Anderson, 1970; Aki and Richards, 1980) and *scattering attenuation* (Aki, 1980a,b; Shapiro and Kneib, 1993; Shapiro and Hubra, 1999; Hong, 2004; Bongajum, 2011; Sato et al., 2012), which cause wave dissipation and dispersion. The total quality factor (Aki, 1982; Mukhopadhyay and Tyagi, 2008; Fielitz and Wegler, 2015; Shen, 2016) is given as

$$\frac{1}{Q} = \frac{1}{Q_{int}} + \frac{1}{Q_{sct}}, \tag{1.2}$$

where Q is the total quality factor, Q_{int} is the intrinsic quality factor and Q_{sct} is the scattering quality factor.

Scattering is a common wave phenomenon and can happen in any kind of media with scatters or highly heterogeneous media. Wave energy is transferred to later arrivals or to waves from other directions caused by scattering attenuation (Figure 1.3). Meanwhile, intrinsic attenuation is the property of anelastic material due to the internal friction. The internal friction transfers wave energy to heat, which results in energy loss and lack of high frequency waves (Figure 1.4). The dissipation affects the amplitude of the waves

and dispersion leads to kinematic phase shift compared to purely acoustic wave. The total attenuation effects are the combination of intrinsic and scattering attenuation. The two kinds of attenuation are caused by distinct factors. In this thesis, I only focus on the **intrinsic attenuation**. For the models with few scatters, the attenuation is almost composed of intrinsic attenuation. All the Q in the thesis denotes the intrinsic quality factor Q_{int},

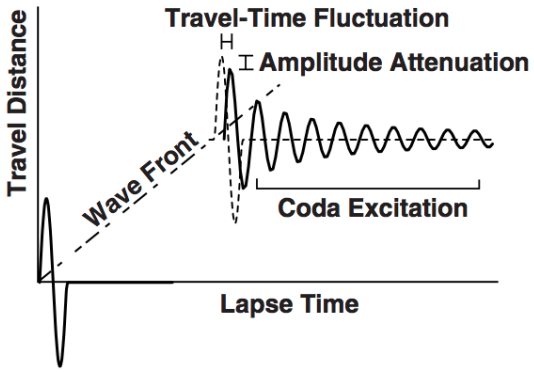

Figure 1.3: Scattering attenuation effects in highly heterogeneous media: the amplitude decays and traveltime fluctuates (Adapted from Sato et al. (2012)); the coda waves are made up of incoherent scattered waves.

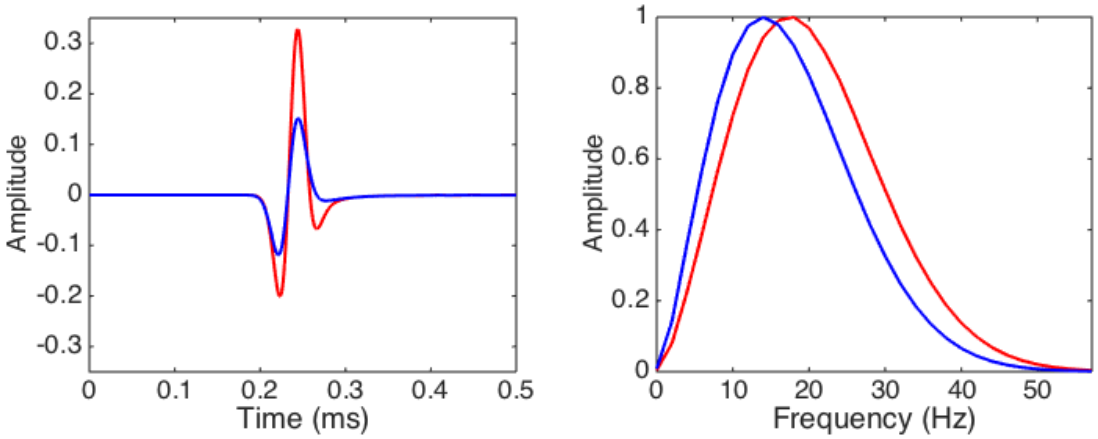

Figure 1.4: Intrinsic attenuation effects for one seismic trace in time domain (left) and normalized spectrum in frequency domain (right), the solid red line is the acoustic wave, and the solid blue line is the visco-acoustic wave with Q = 15.

The typical Q values of rocks are shown in Table 1.1. Q_p is the quality factor of P waves and Q_s is the quality factor of S waves.

Table 1.1: Typical Q values of common rocks from Thorne and Wallace (1995).

Rock types	Shale	Sandstone	Granite	Peridotite	Midmantle	Lowermantle
Q_p	30	58	250	650	360	1200
Q_s	10	31	70-250	280	200	520

1.1.3 Different Q models

Seismic data lack the high frequency parts and have lower wave energy after traveling through the Earth. To explain the phenomenon, people consider the Earth as a frequency filter or a visco-elastic media (Ricker, 1953). Visco-elastic media is related to intrinsic attenuation. Different from elastic and acoustic media, the ratio between stress and strain is variable with time in visco-elastic media. To simulate the effects of intrinsic attenuation, there are mainly three Q model, including: Voigt-Ricker model (Voigt, 1892; Ricker, 1953), the nearly constant Q model (Kolsky, 1956; Futterman, 1962; Liu et al., 1976; Day and Minister, 1984) and the constant Q theory (Strick, 1967; Kjartansson, 1979).

For **Voigt-Ricker model**, the attenuation effect is regarded as an energy absorption term, which is described by adding a single damping term to the acoustic wave equation in the model (Ricker, 1953). Because of this simplicity, the theory of wave propagation with absorption has been widely adopted to compute the synthetic seismograms in early researches (Boore et al., 1971; Munasinghe and Farnell, 1973; Deng and McMechan, 2007). However, the Q varies with frequency. The observations contradict the frequency-dependence of Q: other models have thus been developed.

In exploration seismology, within the specific frequency bandwidth, the nearly constant Q or constant Q theory means that the effect of attenuation of seismic waves for various frequencies are different (Knopoff, 1964; Toksoz et al., 1979; Toksoz and Johnston, 1981; Barton, 2007). The attenuation of seismic waves can be defined by the attenuation factor or attenuation coefficient or absorption factor (Aki and Richards, 1980; Sheriff and Geldart, 1995; Wang, 2008), given as

$$\alpha = \frac{\omega}{2cQ}, \tag{1.3}$$

where c is the speed of waves. With constant Q assumption, the high frequency part attenuates faster than lower frequency one, which is consistent with many laboratory experiments (Peselnick and Zietz, 1959; Peselnick and Outerbridge, 1961; Toksoz et al., 1979) and field measurements (McDonal et al., 1958; Tullos and Reid, 1969; Hamilton, 1972). One example of field measurement of Q was conducted by McDonal et al. (1958) in Pierre shale (Figure 1.5). The attenuation factor α is linear within the 100–500 Hz frequency range, the equivalent Q is around 32.5. A constant or nearly constant Q model is widely used in exploration seismology.

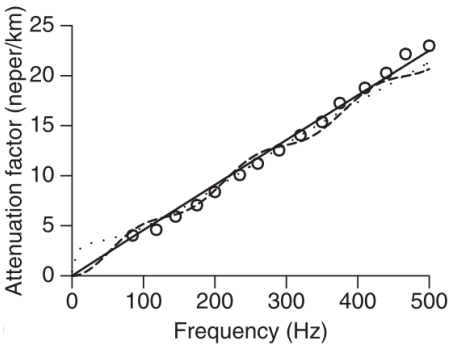

Figure 1.5: Q measurements in Pierre shale. The open circles are field experiments measured by McDonal et al. (1958), the solid line is the fitting curve between α and frequency, the dotted and dashed lines are computed by numerical modeling method from Carcione et al. (2002) (Adapted from Carcione (2011).

For **nearly constant Q model**, attenuation coefficients are determined such that Q is constant within the desired frequency bandwidth. Liu et al. (1976) firstly connected the nearly constant Q model with a physically rheological model. The nearly constant Q is obtained by superimposing L pairs of Zener model. A classical Zener body is called standard linear solid (SLS). Day and Minister (1984) first incorporated realistic attenuation into the time-domain computation using the Padé approximation. Many authors developed the nearly constant Q models and visco-elastic or visco-acoustic wave equations based on different rheological models, mainly including generalized Maxwell body (GMB) (Emmerich and Korn, 1987; Carcione et al., 1988a,b; Emmerich, 1992; Fah, 1992; Moczo et al., 1997; Kay and Krebes, 1999) and generalized Zener body (GZB) (Robertsson et al., 1994; Blanch et al., 1995; Xu and McMechan, 1995; Robertsson, 1996; Hestholm, 2002). Moczo and Kristek (2005) prove both GMB and GZB are equivalent to implement realistic attenuation in the time-domain. The rheological models will be further discussed in Section 2.3.

The **constant Q model** corresponds to the description of wave propagation and attenuation with Q exactly independent of frequency (Kjartansson, 1979). However, the purely constant Q model leads to a infinite phase velocity, as the frequency increases to infinity (Carcione, 2011). This contradicts the physical reality. Therefore, the application of this model should be used within a limited frequency bandwidth, e.g, under the frequency range of exploration seismology. Some authors incorporated the constant Q theory in the visco-elastic or visco-acoustic wave equations (Carcione et al., 2002; Carcione, 2010; Zhang et al., 2010; Zhu and Harris, 2014). Kjartansson (1979) constant Q model involves fractional derivative wave equation in the time-domain. The fractional derivatives can be implemented in the wavenumber domain using extra space Fourier transform (Zhu and Harris, 2014).

Compared with constant Q, nearly constant Q needs several pairs of rheological models to obtain the Q being constant over a specific frequency range. The nearly constant Q model is widely applied in visco-acoustic / visco-elastic modeling due to a simple implementation in the time domain.

1.2 Estimation of attenuation

In exploration seismology, there are different kinds of methods to estimate Q. Mainly, they can be divided into ray-based methods under the high frequency approximation and wave equation methods. Ray-based methods can either use spectral amplitude loss or spectrum distortion to estimate the attenuation along the wave travel path. Wave equation methods rely on the full waveform inversion to update the Q. Independently of this classification, the estimation of attenuation can be applied in the time and frequency domains. Ray-based methods can both measure the wavelet broadening time in the time domain or estimate the spectrum changes in the frequency domain. Wave equation methods can also be implemented in the time and frequency domains. Furthermore, Q estimation also can be derived in data domain or image domain. The data domain methods update the Q model by fitting the calculated data and observed data. The image domain methods retrieve the Q model by focusing the image panels, with the construction in subsurface image domain. We review those three approaches in this section.

1.2.1 Ray-based methods

Seismic dissipation caused by attenuation, leads to spectrum amplitude loss and spectrum distortion of seismic data. Apart from the scattering, geometric spreading, source and receiver coupling, radiation patterns, and transmission/reflection effects, the recorded amplitude loss and spectrum distortion are proportional to the integration of attenuation over the distance between source and receiver positions. With a known velocity, this information links the attenuation and traveltime. Thus, the Q model can be estimated by the ray-based method. The ray theory is based on the high frequency asymptotic approximation. Traveltime and amplitude are solutions of the Eikonal and transport equations, respectively. In this context, the Q estimation by the usage of traveltime is mainly into two main categories, the amplitude method and spectrum distortion method.

Spectrum amplitude loss method (Brzostowski and McMechan, 1992; Leggett et al., 1992; Cavalca and Fletcher, 2009; Cavalca et al., 2011) is first needed to estimate a velocity model, commonly by the standard traveltime tomography. Then the spectrum amplitude loss is estimated along the rays to obtain Q values. The relation between source and observed received amplitude along ray path (Futterman, 1962; Aki and Richards,

1980; Bregman et al., 1989; Tonn, 1991) is

$$A_k(f) = A_s(f)\exp[-\pi f \int_{ray^k} \frac{ds}{Q(x,y,z)v(x,y,z)}], \tag{1.4}$$

where $A_s(f)$ is the source amplitude, and $A_k(f)$ is the observed amplitude along the ray k. The velocity model is obtained by a prior velocity tomography, then the Q model is determined by equation 1.4. However, the spectrum amplitude of seismic data is easily contaminated by many factors such as scattering, geometric spreading, source and receiver coupling, radiation patterns, and transmission/reflection effects. The assumption of this method is that geometrical spreading and scattering effects are first well removed.

The other way is to use the spectrum distortion method. Because of attenuation, the high frequency waves attenuate faster than low frequency waves, which leads to the downshift of centroid frequency. Quan and Harris (1997) first estimated Q based on centroid shift method. The advantage of the method is that only the attenuation is responsible for centroid frequency shift, compared with amplitude loss method contaminated by many other factors. However, this method is based on the assumption that the spectrum of incident waves is known. Based on centroid frequency method, Plessix (2006a) applied the method to estimate Q using limited frequency band data in cross-well case. Zhang and Ulrych (2002) applied the method to obtain quality factors from common midpoint records using a layer-stripping approach.

Additionally, another way for estimating perturbed Q is to combine the ray theory and Born approximation (Ribodetti and Virieux, 2000; Ribodetti et al., 2000). The Geen's function has an asymptotic expression. The perturbed wavefields caused by the perturbed Q are obtained according to the Born approximation. The perturbed Q is reconstructed by minimizing the data misfit between perturbed wavefields and recorded data. This linearized inversion is fast compared with full waveform inversion, and is devoted to the situation of the short wavelength components of the attenuation model.

1.2.2 Wave equation methods

Full waveform inversion (FWI) exploits all the waveform information by minimizing the data difference (Lailly, 1983; Tarantola, 1984a). It is a powerful method to retrieve physical models of the subsurface, including pressure and shear velocity as well as models. Tarantola (1988) extended the FWI algorithm to retrieve the elastic parameters and attenuation parameter. As the computation ability increases, the theory and applications of FWI have been widely developed, mainly after the 2000's with a better understanding of the role of low frequency in the inversion (Pratt, 1999). At the same time, visco-elastic or visco-acoustic FWI also has been developed for more realistic physical models, with applications on both synthetic and real data cases. Visco-elastic or visco-acoustic FWI can be implemented in the time domain (Liao and McMechan, 1995; Charara et al.,

1996, 2000; Barnes et al., 2004; Charara et al., 2004; Barnes and Charara, 2009, 2010; Bai et al., 2012; Kurzmann et al., 2013; Bai et al., 2014; Barnes et al., 2014; Kurzmann et al., 2015; Belahi et al., 2015; Cheng et al., 2015; Li et al., 2015; Plessix et al., 2016; Fabien-Quellet et al., 2017; Jiang and Chauris, 2018; Wang et al., 2018; Yang et al., 2018) and frequency domain (Song et al., 1995; Causse and Mittet, 1996; Liao and McMechan, 1996; Causse et al., 1999; Hicks and Pratt, 2001; Pratt et al., 2005; Kamei and Pratt, 2008; Malinowski et al., 2011; Kamei and Pratt, 2013; Prieux et al., 2013; Operto et al., 2014, 2015; Gao and Wang, 2016; Operto and Miniussi, 2018) (more details in Chapter 2).

The advantage of FWI is that it applies for all the kinds of wave and exploits all the waveform information, with higher resolution compared with ray-based methods. However, it is a highly nonlinear problem, and it is hard to retrieve the velocity and Q due to different parameter sensitivities. Because of the low sensitivity to Q, some researches focus on the data representation to study when it is acceptable to neglect the Q model (Kurzmann et al., 2013; Barnes et al., 2014; Belahi et al., 2015). Their results show it is worth to implement the visco-acoutic or visco-elastic FWI. Visco-elastic FWI leads to better results of elastic parameters than purely elastic FWI (Barnes et al., 2014). Furthermore, researches investigate the sensitivities of parameters and inversion strategies (Kamei and Pratt, 2013; Prieux et al., 2013; Operto et al., 2014, 2015; Plessix et al., 2016; Jiang and Chauris, 2018) to better retrieve the velocity and Q models. The different inversion strategies recommended by different authors mainly include the sequential inversion (Fabien-Quellet et al., 2017), the simultaneous inversion (Plessix et al., 2016) and the hierarchical inversion (Prieux et al., 2013; Operto et al., 2014, 2015). Sequential inversion first updates the velocity model, then continues to update the Q model. It can handle the different parameter sensitivities; however it may over-estimate the parameters (Plessix et al., 2016). Simultaneous inversion updates the velocity and Q at same time, but suffers from the differences between parameter sensitivities without the estimation of the Hessian matrix (Métivier et al., 2013, 2014; Yang et al., 2018). Hierarchical inversion first retrieves a good velocity model, then follows a subsequent simultaneous inversion. Fabien-Quellet et al. (2017) applied the sequential inversion to estimate the Q factor, which is used to monitor the CO_2 injection in Cambrian-Ordovician sedimentary basin of the St. Lawrence Platform in southern Quebec, Canada. Plessix et al. (2016) used the simultaneous inversion to obtain the high resolution velocity and Q models. They precisely detected the gas cloud in offshore Malaysia. Prieux et al. (2013); Operto et al. (2014, 2015) conducted synthetic study for imaging density, velocity and Q and recommended the hierarchical inversion strategy. They applied this strategy to a real data from Valhall field in North sea. The seismic images and Q model reveal the precise location of gas clouds. All those successful real data examples show FWI is a powerful tool to obtain high resolution images of velocity and Q. Therefore, this thesis continues the research on velocity and Q inversion under the framework of FWI, to investigate a new inversion strategy to guide the inversion and mitigate cross-talks be-

tween parameters without relying on the Hessian matrix (see motivations in Section 1.3 and methodology and results in Chapter 4 and 5).

1.2.3 Data domain and image domain methods

As mentioned in the introduction, the methods of estimating Q also can be divided into data (Brzostowski and McMechan, 1992; Quan and Harris, 1997; Tarantola, 1988) and image domains (Symes, 2008; Shen and Zhu, 2015; Shen, 2016). Data domain methods are based on the data fitting to update the Q model. Image domain methods retrieves the Q model by focusing the image panel (Chauris, 2000; Shen, 2016; Cocher et al., 2017; Chauris and Cocher, 2017; Chauris et al., 2017; Li, 2018). Image domain can be implemented in common-shot and subsurface gathers (Symes, 2008, 2017). This is not a common approach for estimating Q (Shen and Zhu, 2015; Shen, 2016).

In data domain, ray-based methods (section 1.2.1) and wave-equation methods (section 1.2.2) measure the misfit of observed and calculate data to update Q model. For the ray-based methods, the observed data is exactly the spectrum amplitude or central frequency. For wave-equation methods, the observed data are the wavefields recorded at specific positions. The data can be all kinds or specific kinds of waves with whole or limited time window, e.g., direct waves, transmission waves, reflections.

The image domain methods back-project the image residuals to update the macro models (Sava and Biondi, 2004; Symes, 2008; Sava and Vasconcelos, 2011; Shen et al., 2012). Inaccurate velocity or Q leads to a defocused energy of image panel (Figure 1.6). Based on this criteria, the macro Q model can be updated with a known fixed velocity (Shen and Zhu, 2015; Shen, 2016).

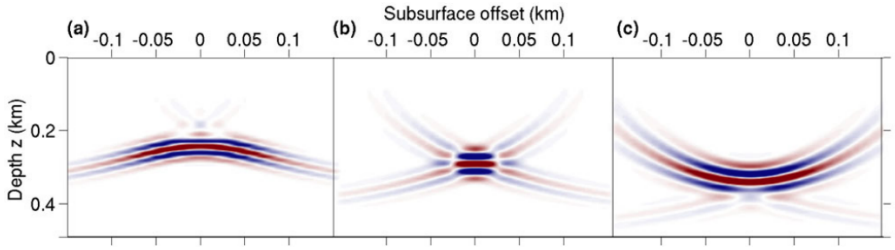

Figure 1.6: Image panel (i.e, common image gather) in subsurface domain, a lower background velocity (a), a correct background velocity (b) and a higher background velocity (c) (Adapted from Lameloise et al. (2015).

Data domain methods are straightforward. However, it is sensitive to the data quality, e.g., signal-to-noise ratio. Data domain methods, e.g., FWI can produce high resolution image. Image domain methods are based on Born approximation, dividing the model into a macro and perturbed model. Image domain method focusing on reconstructing

the macro model. Methods in both domains suffer from the leakage between velocity and Q. In image domain, the image panel is focused when the background kinematic model is correct. For example, attenuation leads to dispersion phase velocity. Different velocity and Q can have same kinematic information. In this situation, the inversion of correct Q relies on prior known correct velocity model.

1.3 Motivation, strategy and thesis organization

In the previous sections, I introduce the attenuation effects. On the one side, attenuation information can solely be used as the lithology discriminator, e.g., detection of the gas clouds and saturated layers. On the other side, attenuation model can be applied to improve the velocity images. Attenuation can be represented as quality factor Q. Different Q models can be used to explain the attenuation effects. In the exploration seismology, the constant or nearly constant Q model is widely applied and consistent with field observations. Based on this Q model, ray-based and wave-equation methods are applied to retrieve velocity and Q models. Wave equation methods have the advantages of high resolution. The thesis focuses on the reconstruction of velocity and Q models under the frame of visco-acoustic FWI, without the estimation of the Hessian matrix. We encounter the well-known difficulties related to cross-talks between velocity and Q and different parameter sensitivities. Our objectives of the thesis are: (1) investigating the inversion strategies to handle different sensitivities of parameters, and (2) introducing extra information to guide the inversion and mitigate cross-talks between parameters.

1.3.1 Motivation: Inversion strategies to reconstruct velocity and attenuation

Visco-acoustic FWI like many other multi-parameter inversion suffers from cross-talks between the parameters (Plessix et al., 2016). Additionally, due to the limited observed information on the surface, similar radiation patterns for velocity and Q (Malinowski et al., 2011), and different sensitivities of parameters, those difficulties lead to the insufficient resolution of velocity and Q of visco-acoustic FWI, referring to cross-talks. The cross-talks can be observed in the pattern of the gradient of objective function with respect to parameters (Figure 1.7). The lack of resolution of data disparity can also lead to cross-talks (Figure 1.8).

Velocity and Q have the different sensitivities due to physical properties. The changes of v_p and Q can both generate a kinematic phase shift and amplitude changes. However, v_p changes greatly impact the kinematic phase, leading to a large data difference. A scaling factor is needed to balance the magnitude. The incorporation of inverse of the Hessian matrix (Métivier et al., 2013, 2014; Yang et al., 2018) in the minimization

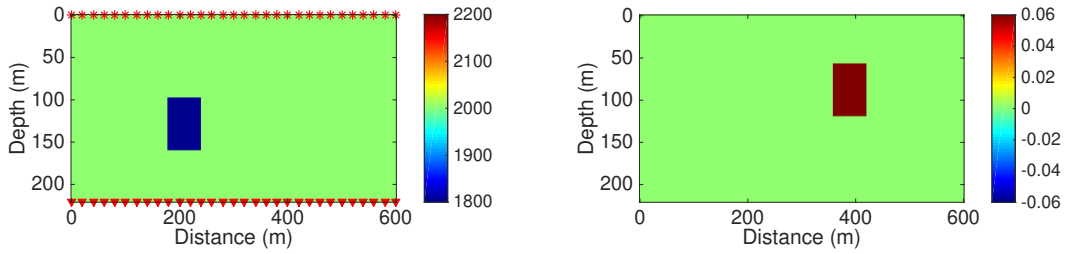

(a) True v_p (b) True τ

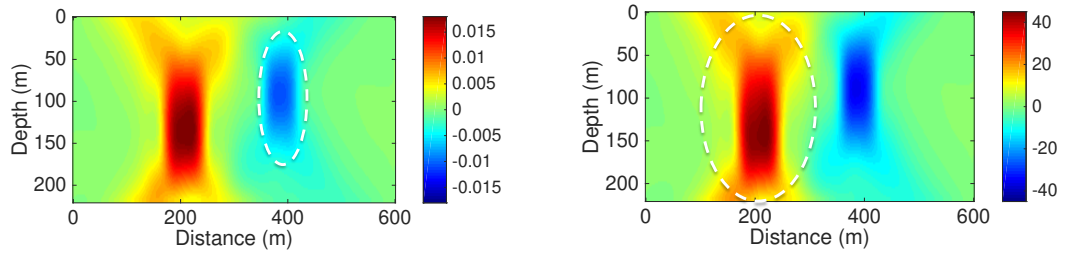

(c) $\partial\mathcal{J}/\partial v_p$ (d) $\partial\mathcal{J}/\partial\tau$

Figure 1.7: Effects of cross-talks between P-wave velocity v_p and τ (approximates to the inverse of Q), $\mathcal{J}$ is the FWI objective function. The true v_p model is homogenous v_p = 2000 m/s with an low value anomaly 1800 m/s (a), and the true τ model is homogeneous τ = 0.001 with a high τ anomaly 0.07 (b). Both gradients with respect to v_p (c) and τ (d) contain information on τ and v_p, respectively (circles).

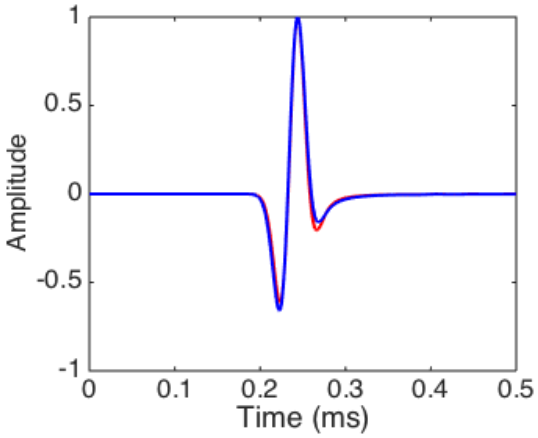

Figure 1.8: Two normalized recorded seismic traces with velocity and attenuation being (v_p = 2234 m/s, Q = infinity) (red) and (v_p = 2168 m/s, Q = 50) (blue). The associated data are almost identical.

process is one solution, but computation costs are very heavy, even with the truncated Newton approaches.

To mitigate cross-talks and balance the different gradient sensitivities, conventional inversion strategies include sequential inversion (Fabien-Quellet et al., 2017), simultaneous inversion (Plessix et al., 2016) and hierarchical inversion (Prieux et al., 2013; Operto et al., 2014, 2015). Sequential inversion (Figure 1.9, left) usually first retrieves the velocity and then Q, but it may over-estimate the parameter (Plessix et al., 2016). Simultaneous inversion (Figure 1.9, middle) reconstructs velocity and Q at the same time. It has to overcome the different sensitivities between parameters without the estimation of the Hessian matrix. Hierarchical inversion first retrieves velocity model then continues with a simultaneous inversion. There is not yet a clear statement about the optimal recommendation. Therefore, we investigate different inversion strategies and propose a hybrid inversion scheme without the estimation of Hessian matrix.

1.3.2 Strategy: Kinematic relationship to guide the inversion

As indicated above, one difficulty of visco-acoustic FWI is cross-talks between two parameters. In this sense, the inversion process of fitting the same observed data can lead to different inversion results. To improve the inversion, more information is needed to guide the inversion and reduce the searching model parameter space, without necessarily relying on the information of the Hessian matrix.

Attenuation effects lead to phase velocity dispersion (Futterman, 1962; Aki and Richards, 1980). Phase velocity increases as frequency and attenuation increase. It means that different combinations of velocity and attenuation result in the same *kinematic velocity* v_k for band-limited seismic data. We call this relation the *kinematic relationship*. The v_k model controls the kinematic of wave propagation. It means the traveltime of recorded data is same, but the amplitudes are different. It is different from the P-velocity model v_p because of attenuation.

We propose a two-step process (hybrid strategy) by incorporating the kinematic relationship (Figure 1.9 right): (1) For a fixed Q, we iteratively update v_k. (more details in Chapter 4). (2) In a second-step, we update v_p, but here for a fixed v_k model. The gradient of the objective function is modified accordingly. During the second phase, Q is the passive parameter, i.e. is automatically updated when v_p is modified. Unlike conventional inversion strategies with more flexibilities to search the parameters in whole model space, the model searching space of the hybrid inversion strategy in the second-step is only limited to be along kinematic curve (Figure 1.10). Therefore, the key factor is to obtain the kinematic velocity for the inversion. We will discuss if it is easier to obtain the kinematic velocity for transmitted waves compared to reflection waves. We first apply this inversion strategy on models with mainly transmitted waves to obtain kinematic velocity. With this information, we then apply our hybrid inversion strategy to retrieve the velocity and Q. Those two steps are alternated with each other to further

update the kinematic velocity, then decouple the two parameter based on updated kinematic velocity. We will discuss how this extra information can guide the inversion and mitigate cross-talks between parameters, especially on the model of Gaussian anomaly case in Chapter 4. Then we further extend this hybrid strategy to reflections dominated model, i.e., Marmousi model (Chapter 5).

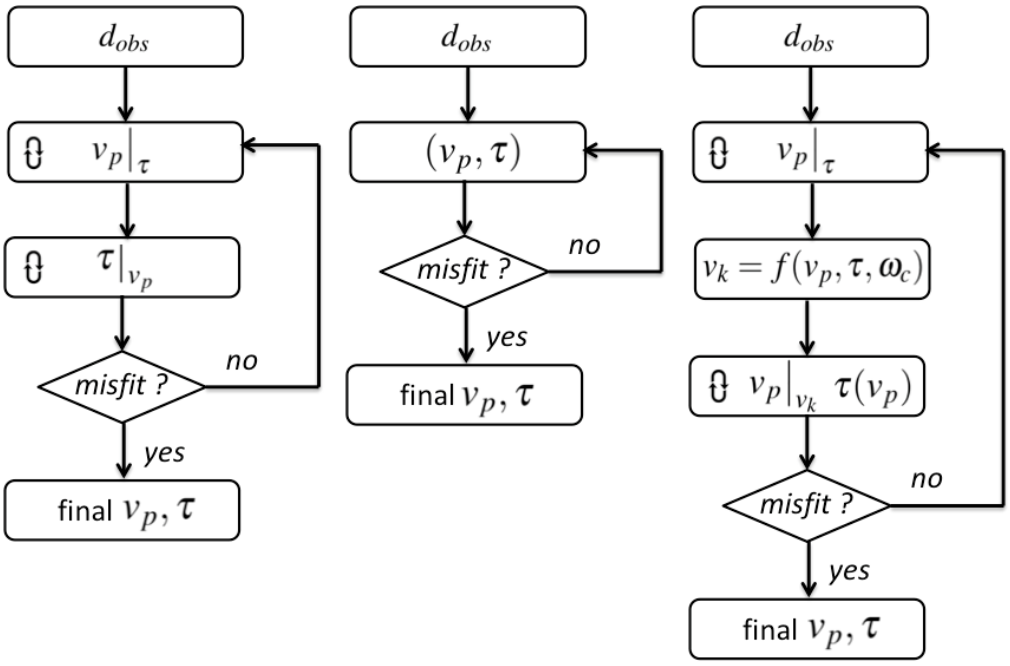

Figure 1.9: Workflow of the sequential (left) simultaneous (middle) and hybrid (right) strategies. τ approximates to the inverse of Q. $v_k = f(v_p, \tau, \omega_c)$ is the kinematic relationship, ω_c is the central frequency of the source (more details in Section 2.6.3 and Chapter 4).

1.3.3 Thesis organization

The thesis is organized as followed:

- In Chapter 2, I introduce the visco-elasticity based on different rheological models, constant Q optimizations, and visco-acoustic / visco-elastic wave equations. I propose a modified optimization for nearly constant Q model. Based on this Q model, I obtain the visco-acoustic wave equation. Further, I introduce the finite-difference method in the time domain to solve the visco-acoustic wave equation and analyze the stability conditions and numerical dispersion. I apply Convolutional Perfectly Matched Layer (CPML) to absorb the boundary reflections (Komatitsch and Martin, 2007; Martin and Komatitsch, 2009). Then I compare the

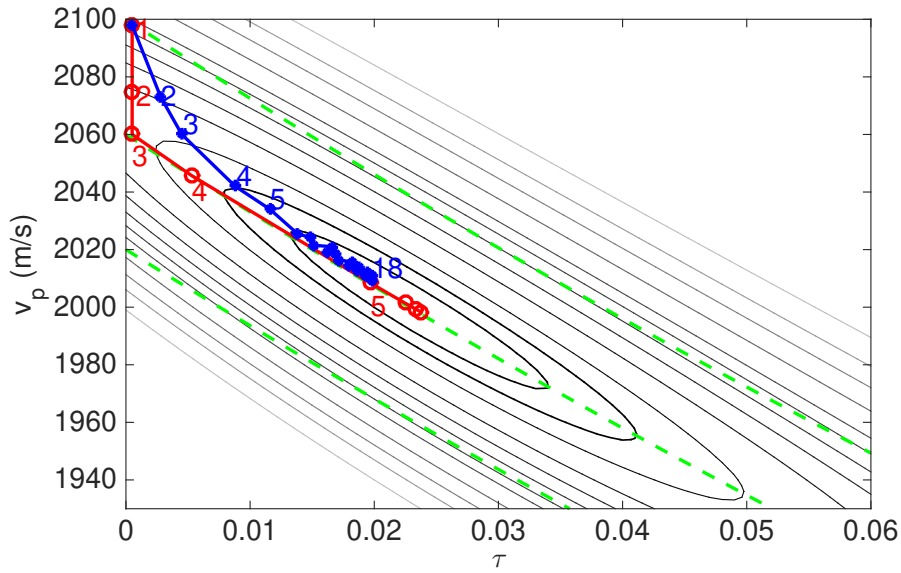

Figure 1.10: The sketch of searching direction of strategies: the kinematic curves (dashed green line) superimposed to the contour lines of the misfit distribution (gray solid) with the true values being v_p = 2000 m/s and τ = 0.023 (Q = 50). The blue dots and red hollow circles are the searching direction of the simultaneous and hybrid strategies, respectively. For the hybrid strategy: v_k updates (1 to 3) and the v_p updates for fixed v_k (3 to 5), more details in Chapter 4.

numerical seismogram with analytical results to evaluate the accuracy of the numerical solution. Finally, I analyze the visco-elastic effects. The visco-elastic waves have dissipation and dispersion. The dispersion effect lead to an equivalent kinematic velocity. The kinematic velocity will be used as an extra information to guide the inversion.

- In Chapter 3, the objective of this chapter is to better relate the different forms of visco-elastic wave equations mainly based on nearly constant, constant Q models and power law. Those models can be rewritten as a general relation between stress and strain with either ordinary or fractional derivatives. The general relationship between stress and strain can turn into different rheological models. Those rheological models include Generalized Maxwell body, Generalized Zener body and Scott-Blair model. Starting from the unification form, we can obtain the commonly used visco-acoustic wave equations in exploration geophysics. This unification form also can be used as a way to derive other forms of visco-elastic wave equation. Those equations are not limited to constant Q and can have complex relationship between Q and frequency.

- In Chapter 4, I develop a hybrid inversion strategy for visco-acoustic FWI to re-

trieve velocity v_p and Q. This chapter first starts with the review of current research status on visco-acoustic or visco-elastic FWI. Main issues include cross-talks between parameters and different gradient sensitivities. To deal with these problems, people investigate different inversion strategies, the role of Hessian matrix and pre-conditioning operators. In this chapter, I incorporate the kinematic relationship into the inversion to obtain a hybrid inversion strategy (indicated in Section 1.3.2) based on conjugate gradient method, without the estimation of inverse of Hessian matrix and pre-conditioning operators. I test this strategy on 4 different models and compare with mono-velocity inversion and simultaneous inversion strategies. The key factor of this hybrid strategy is to obtain the kinematic velocity. First, I apply this strategy in a homogeneous model and in another blocky anomaly model with known kinematic velocity. Then I test this strategy on a Gaussian anomaly model. Finally, I test this strategy on 2D synthetic Middle-East model, mainly dominated by transmitted waves. I develop the way to retrieve kinematic velocity v_k, through updating v_k for fixed v_p. We update the kinematic velocity and continue to retrieve v_p and Q, alternately. Finally, we compare the results with conventional inversion strategies.

- In Chapter 5, I apply the hybrid inversion strategy to Marmousi model. The Marmousi model is different from the models in Chapter 4. The dominated waves in Marmousi model are reflections. We demonstrate the feasibility of the modified inversion strategy. We also apply the frequency continuation inversion when higher frequencies are progressively included in the inversion scheme.

- In Chapter 6, I conclude the thesis and propose some directions for further study: Q-compensated reverse-time migration (RTM), Q least-squares RTM (LS-RTM), and migration velocity analysis (MVA) with Q. The three cases incorporate Q as a passive parameter to obtain macro velocity model or velocity perturbation based on linearized inversion.

1.3.4 Contributions

I reviewed visco-acoustic theories, forward modeling and inversion. I implemented the codes of 2D visco-acoustic wave simulation and inversion using MPI, a modified τ method to optimize nearly constant Q, forward modeling based on staggered grid finite difference (Virieux, 1986) with CPML (Komatitsch and Martin, 2007; Martin and Komatitsch, 2009), validation with analytical solution (Chapter 2), investigating a self-joint back-propagation formula to obtain the gradient (Plessix, 2006b), stabilization for back-propagation, validation the gradient with comparison with FD method, conjugate gradient optimization and MPI implementation (part of Chapter 4). I investigated a unification formalism of visco-elastic wave equations, including fractional-order, stan-

dard linear solids based and power-law based visco-elastic wave equations (Chapter 3). Based on those modeling and inversion code packages, I propose a hybrid visco-acoustic FWI scheme, including kinematic velocity analysis, a total gradient by introducing the relation between Q and velocity, compare with different inversion strategies, and test on simple models, the synthetic Middle-East model (part of Chapter 4) and Marmousi model (Chapter 5). I draw some perspectives on Q migration velocity analysis and Q-compensated reverse-time migration (Chapter 6). Main contributions are:

- A modified τ method to optimize nearly constant Q in Chapter 2;
- A unification formalism to link different forms of the visco-elastic wave equations in Chapter 3;
- A hybrid visco-acoustic FWI strategy to guide the inversion by incorporating the kinematic relationship between velocity and Q in Chapter 4;
- A new term $\partial\tau(v_p)/\partial v_p$ acting as a scaling factor to balance the gradient sensitivities in Chapter 4;
- Comparisons of different inversion strategies to better understand the visco-acoustic FWI for transmitted and reflected waves in Chapter 4 and Chapter 5.

Part of the results has been presented / accepted in

- JIANG, H. and Chauris, H. [2018] A modified 2D visco-acoustic waveform inversion scheme. 80th EAGE Conference & Exhibition, Copenhagen, Denmark;
- JIANG, H. and Chauris, H. [2019] A hybrid inversion strategy for visco-acoustic full waveform inversion: application to the Marmousi model. 81st EAGE Conference & Exhibition, London, United Kingdom.

and / or submitted to publication,

- JIANG, H. and Chauris, H. [2019] Alternative strategy in visco-acoustic full waveform inversion. Prepare to submit;
- JIANG, H. and Chauris, H. [2019] Reviews and unification formalism of visco-elastic wave equation formulations and the associated specific examples based on rheological models. In preparation;
- JIANG, H. and Chauris, H. [2019] The coupling of macro velocity and Q for linearized inversion. In preparation.

Chapter 2

Visco-elasticity and visco-acoustic wave equation

Contents

Résumé du chapitre 2

Ce chapitre est dédié à l'introduction des simulations numériques de l'atténuation et aux équations des ondes visco-élastiques pour un modèle de Q constant ou presque constant. Les modèles de Q constant sont conformes aux observations : le coefficient d'absorption est proportionnel à la fréquence, ce qui veut dire que Q est indépendant de la fréquence. La partie haute fréquence des ondes s'atténue plus vite que la partie basse fréquence, ce qui conduit à un décalage fréquentiel. Ce chapitre introduit d'abord les modèles physiques pour représenter la visco-élasticité en fonction des modèles qui servent à représenter Q. Ici, nous utilisons l'équation d'onde visco-acoustique de GZS (Generalized Zener Solids), avec une implémentation dans le *domaine temporel*. Ensuite, le chapitre introduit les solutions numériques pour simuler les ondes visco-élastiques (solveur différences finies, dispersion numérique, bords absorbants). Enfin, les effets visco-élastiques sont analysés dans les domaines temps et fréquence. Une attention particulière est portée sur la *vitesse cinématique* et la *relation cinématique*.

2.1 Introduction

This chapter is dedicated to introducing the numerical simulation of attenuation and visco-elastic wave equations based on constant or nearly constant Q model. Constant Q models are consistent with the field observations. In other word, the absorption coefficient is proportional to frequency, which means the Q is independent of frequency. High frequency waves attenuate faster than low frequency ones, leading to central frequency downshifts. This chapter first introduces the physical models to represent visco-elasticity, then extends to different constant Q models. Based on those Q models, different forms of visco-elastic or visco-acoustic wave equations are obtained. In the thesis, we use the visco-acoustic wave equation based on Generalized Zener Solids, implemented in **time domain**. Then this chapter introduces the numerical solution to simulate visco-acoustic waves, including finite-difference solver, numerical dispersion and stability criteria, and absorbing boundary condition. Finally, this chapter analyzes the visco-elastic effects in time and frequency domain, the dispersion curve, **kinematic velocity** and **kinematic relationship**.

2.2 Visco-elasticity

The linear visco-elasticity represents the phenomenon that the stress at any moment depends on the whole strain history. The stress-strain relationship or constitutive relationship can be built by a time-dependent function (Boltzmann, 1876; Christensen, 1982). In contrast to visco-elastic media, the ratio of stress and strain in elastic media is invariable with time (Fung, 1965). This ratio is called the elastic modulus. The simplest elastic media can be represented with a spring (Hooke element), with the relation $\sigma(t) = M\ \epsilon(t)$. $t$is the time, $\sigma(t)$ means stress, $\epsilon(t)$ is strain, and M is the elastic modulus. A dashpot is an damper, combined with a spring to exhibit visco-elastic behavior. The stress-strain relationship of a dashpot is $\sigma(t) = \eta\ \frac{d\epsilon(t)}{dt}$. η is the coefficient of viscosity. It is a linear relationship between the stress and the time derivative of the strain. One simple visco-elastic media is a Maxwell body; it consists of a spring and a dashpot in parallel. Different combinations of springs and dashpots compose Generalized Maxwell Body (GMB) and Generalized Zener Body (GZB). They are commonly used for visco-elastic media in exploration geophysics (Liu et al., 1976; Emmerich and Korn, 1987; Carcione et al., 1988a,b; Robertsson et al., 1994; Blanch et al., 1995; Moczo and Kristek, 2005). n pairs of Maxwell bodies and one spring in parallel make up the GMB. A spring in parallel with a Maxwell body form the one kind of Zener bodies, also called Stand Linear Solid (SLS). n pairs of Zener/SLS bodies in parallel are called Generalized Zener Body (GZB) or Generalized SLS (Figure 2.1).

To obtain the stress-stain relation for visco-elastic media, we start from the elastic

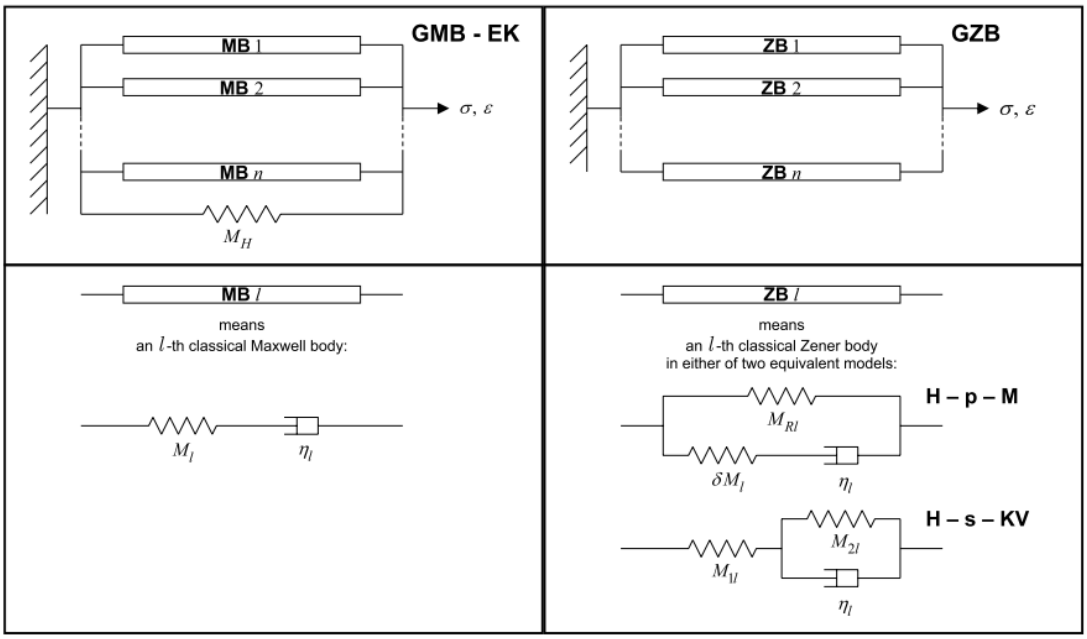

Figure 2.1: (Left) Generalized Maxwell Body: MB denotes Maxwell body, formed by a spring with elastic modulus M_l and a dashpot with viscosity coefficient η_l. n pairs of Maxwell bodies and one spring with elastic modulus M_H in parallel make up the GMB, here denoted as GMB-EK to refer to the model from paper of Emmerich and Korn (1987). (Right) Generalized Zener Body: ZB denotes the Zener body. n pairs of Zener bodies form the GZB. There are two kinds of Zener bodies. M_{Rl}, δM_l, M_{1l} and M_{2l} are elastic modulus, and η_l is the viscosity coefficient (adapted from Moczo and Kristek, 2005).

media for comparison. The *elastic* stress-strain relationship is given as

$$\sigma(t) = M\epsilon(t). \tag{2.1}$$

$\sigma(t)$ is the stress and $\epsilon(t)$ is the strain. M is the elastic modulus. It is constant and invariant with time.

For a linear isotropic *visco-elastic* media, the stress depends on the previous history of strain. The stress-strain relationship is obtained in a time convolutional form (Boltzmann, 1876) given as

$$\begin{aligned} \sigma(t) &= \int_{-\infty}^{t} \psi(t-\tau)\frac{d\epsilon(\tau)}{d\tau}, \\ &= \psi(t) * \dot{\epsilon}(t), \\ &= \dot{\psi}(t) * \epsilon(t), \end{aligned} \tag{2.2}$$

where $\sigma(t)$ and $\epsilon(t)$ are same as before, representing the stress and strain. $\dot{\epsilon}(t)$ is the first order time derivative of strain. A time integration can be written into a convolution form, where $*$ is the time convolutional operator. $\psi(t)$ is the stress relaxation function, which is the stress response to a Heaviside step function of strain. It can be measured by laboratory experiments (Zener, 1948; Christensen, 1982; Sasso et al., 2011).

To compare with the elastic stress-strain relation, we write the third formula of equation 2.2 in frequency domain. The convolution in time turns into a product in frequency,

$$\sigma(\omega) = M(\omega)\epsilon(\omega), \tag{2.3}$$

where $M(\omega)$ is denoted as the complex modulus of visco-elastic media. It is equal to $\mathcal{F}[\dot{\psi}(t)]$, where $\mathcal{F}$ is the Fourier transform operator. The transform pair of modulus and stress relaxation function is

$$M(\omega) = \mathcal{F}\left[\dot{\psi}(t)\right], \tag{2.4}$$

$$\psi(t) = \mathcal{F}^{-1}\left[\frac{M(\omega)}{i\omega}\right], \tag{2.5}$$

where $\mathcal{F}^{-1}$ is the inverse Fourier transform operator. Frequency domain $M(\omega)$ is easy to be obtained by the analyzing the stress-strain relation based on rheological models, e.g. SLS. $\psi(t)$ is therefore deduced by the inverse Fourier transform of $M(\omega)/i\omega$.

Taking the SLS as example in Figure 2.1, SLS is composed of a spring and a dashpot in parallel, then with another spring in series. Complex modulus in the frequency domain and stress relaxation function in time domain respectively, are given by

$$M(\omega) = M_R\frac{1+i\omega\tau_\epsilon}{1+i\omega\tau_\sigma}, \tag{2.6}$$

$$\psi(t) = M_R\left[1-\left(1-\frac{\tau_\epsilon}{\tau_\sigma}\right)\exp\left(-t/\tau_\sigma\right)\right]H(t). \tag{2.7}$$

$H(t)$ is the Heaviside step function. $\tau_\sigma = \eta/(M_1+M_2)$ is called stress relaxation time, where M_1 and M_2 are the elastic modulus of the springs inside the SLS in series (Figure 2.1). It depends on the stress relaxation rate. $\tau_\epsilon = \eta/(M_2)$ is called strain relaxation time, which is related to strain creep rate. M_R is called relaxed modulus obtained when $\omega = 0$ or $t = \infty$, defined as $M_1M_2/(M_1+M_2)$. It means the visco-elastic media reaches the relaxed status after long time continuous stress imposing. When $\omega = \infty$ or $t = 0$, the visco-elastic media is imposed by an instantaneous stress M_U, which is called unrelaxed modulus equal to $M_R\,\tau_\epsilon/\tau_\sigma$. During the stress imposing history, the strain is unchanged (Figure 2.2). The complex modulus of visco-elasticity media varies with time. The complex modulus can be used for further discussion on Q models.

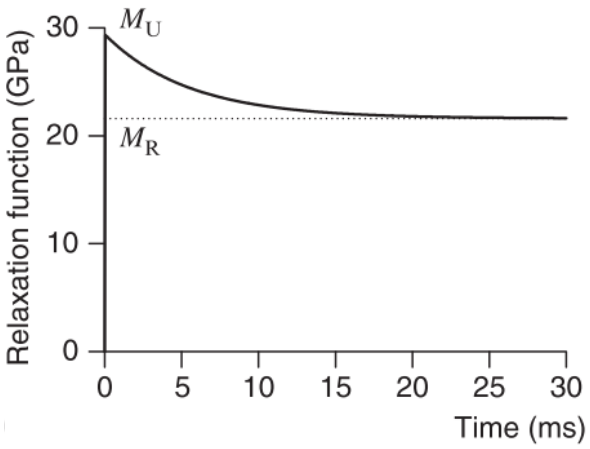

Figure 2.2: The stress relaxation function of a SLS. The strain is unchanged, the imposed stress gradually decreases from unrelaxed M_U to relaxed M_R (adapted from Carcione (2011).

2.3 Constant Q approximation

The reciprocal of Q is defined as the proportion of energy loss per wave propagation cycle. It is obtained by ratio of imaginary part and real part of the visco-elastic modulus (Boit, 1954; Knopoff, 1956; Fung, 1965; O'Connell and Budiansky, 1978; Ben-Menahem and Singh, 1981), yielded by

$$\frac{1}{Q(\omega)} = \Im[M(\omega)]/\Re[M(\omega)]. \tag{2.8}$$

$\Re[M(\omega)]$ and $\Im[M(\omega)]$ are related to the time-averaged strain-energy and dissipated energy, respectively. The constant Q models are consistent with the field observations. It is widely applied in exploration seismology. There are two kinds of constant Q models. The first one is based on the model proposed by Kjartansson (1979). The visco-elastic wave equation is deduced with fractional derivative. The other one is called nearly constant Q model. It mainly is based on rheological models (Liu et al., 1976; Emmerich and Korn, 1987; Carcione et al., 1988a,b; Robertsson et al., 1994; Blanch et al., 1995), e.g, GZB and GMB. The nearly constant Q model has to be approximated over a frequency range. The fractional derivative is hard to solve by a finite-difference method in the time domain. Thus, the latter nearly constant Q model is widely applied. We first introduce the constant Q model, and continue to discuss nearly constant Q model.

2.3.1 Kjartansson constant Q

Kjartansson (1979) Q model is independent with frequency. Based on laboratory experiments, it is reasonable to have relaxation function in a power law, similar to the shape displayed in Figure 2.2. Constant Q model is obtained by giving a specific stress relaxation function

$$\psi(t) = \frac{M_0}{\Gamma(1-2\gamma)}(\frac{t}{t_0})^{-2\gamma}, \qquad 0 < 2\gamma < 1, \tag{2.9}$$

where M_0 is the modulus, and Γ is the gamma function. For $t < 0$, relaxation function is zero. According to equation 2.5, the complex modulus $M(\omega)$ is the Fourier transform of the time derivative of $\dot{\psi}(t)$.

$$M(\omega) = M_0(\frac{i\omega}{\omega_0})^{2\gamma} = M_0|\frac{\omega}{\omega_0}|^{2\gamma}e^{i\pi\gamma\,\mathrm{sgn}(\omega)}, \tag{2.10}$$

where ω_0 is the reference frequency. At reference frequency, all waves have same velocity. γ is a constant, with $0 < 2\gamma < 1$. When $\omega > 0$, $\mathrm{sgn}(\omega) = 1$. For $\omega < 0$, $\mathrm{sgn}(\omega) = -1$.

Substituting the complex modulus into equation 2.8, the constant quality factor is

$$\frac{1}{Q(\omega)} = \tan(\pi\gamma). \tag{2.11}$$

Q is independent of frequency and represented by the parameter γ. When γ trends 0, the visco-elasticity turns into elasticity. Oppositely, the viscoelastic media is highly attenuated when γ trends 0.5.

Based on Kjartansson (1979) Q model, the scalar visco-acoustic wave equation is obtained as

$$\frac{\partial^{2-2\gamma}p}{\partial^{2-2\gamma}t} - \frac{M_0}{\rho}\omega_0^{-2\gamma}\nabla^2 p = 0, \qquad 0 < 2\gamma < 1, \tag{2.12}$$

where p is the pressure wavefields. The wave equation involves a fractional derivative. It is hard to solve by finite-difference in the time domain. $\gamma \to 0$ turns the time derivative of pressure wavefields into $\partial^2 p/\partial^2 t$, the equation becomes an elastic propagation function. Meanwhile, $\gamma \to 0.5$, the time derivative of pressure wavefields is a diffusion term $\partial p/\partial t$. It indicates the fractional visco-acoustic wave-equation is between the propagation and diffusion equations.

Constant Q is easily achieved by using a single γ over all the frequency band. However, it not a realistic due to the infinitely large modulus when frequency increases to infinity (Equation 2.10). The application should be limited to a finite frequency range. Nearly constant Q models is optimized to find best value to have Q constant within a frequency bandwidth.

2.3.2 Nearly Constant Q model

Due to the difficulty to solve fractional derivatives, alternative nearly Q models are widely used. The nearly constant Q can be estimated based on rheological models (Liu et al., 1976; Emmerich and Korn, 1987; Carcione et al., 1988a,b; Robertsson et al., 1994; Blanch et al., 1995), e.g., GMB and GZM. Analyzing the stress-strain relation of GMB or GZB, the complex modulus $M(\omega)$ is obtained (Equation 2.6). As before, Q is equal to the ratio of real and imaginary term of $M(\omega)$. **The nearly constant Q is approximated within a frequency bandwidth**. We first introduce the Q models based on GZB and GMB, then show the equivalence between the two approaches.

The modulus of a Zener body / SLS is given in equation 2.6. The total modulus of a GZM is the sum of modulus of L pairs of Zener body / SLS in parallel (Moczo and Kristek, 2005; Carcione, 2011), given by

$$M(\omega) = \sum_{l=1}^{L} M_{Rl} \frac{1 + i\omega\tau_{\epsilon l}}{1 + i\omega\tau_{\sigma l}}, \tag{2.13}$$

$$= M_R \sum_{l=1}^{L} \frac{1}{L} \frac{1 + i\omega\tau_{\epsilon l}}{1 + i\omega\tau_{\sigma l}}, \tag{2.14}$$

where M_{Rl} is the elastic modulus of spring inside each Zener body. To be modified in accordance to GMB, M_{Rl} is defined as $\frac{1}{L}M_R$, where M_R is the total relaxed modulus of a GZB (Moczo and Kristek, 2005). $\tau_{\sigma l}$ and $\tau_{\epsilon l}$ are the stress and strain relaxation time inside each Zener body (Pipkin, 1986). According to the relation between $M(\omega)$ and relaxation time function $\psi(t)$ in equation 2.5, $\psi(t)$ is obtained as

$$\psi(t) = M_R(1 - \frac{1}{L}\sum_{l=1}^{L}(1 - \frac{\tau_{\epsilon l}}{\tau_{\sigma l}})e^{-t/\tau_{\sigma l}})H(t), \tag{2.15}$$

The relaxation function is used for constructing the wave equations in next section 2.4.

The ratio between the real and imaginary part of complex modulus is defined as Q (equation 2.8). The Q based on a GZB model is given as

$$\frac{1}{Q(\omega)} = \Im[M(\omega)]/\Re[M(\omega)],$$

$$= \frac{\sum_{l=1}^{L} \frac{\omega(\tau_{\epsilon l} - \tau_{\sigma l})}{1+\omega^2\tau_{\sigma l}^2}}{\sum_{l=1}^{L} \frac{1+\omega^2\tau_{\epsilon l}\tau_{\sigma l}}{1+\omega^2\tau_{\sigma l}^2}} \tag{2.16}$$

The nearly constant Q model can also be based on GMB (Emmerich and Korn, 1987). A Maxwell body is composed of a spring and a dashpot in parallel. The GMB is

obtained by L pairs of Maxwell bodies and a spring in parallel. The complex modulus is given by

$$M(\omega) = M_R + \sum_{l=1}^{L} \frac{M_l i\omega\tau_{\sigma_l}}{1 + i\omega\tau_{\sigma_l}}, \tag{2.17}$$

M_R is the relaxed modulus, is related to single parallel spring inside the GMB. $\tau_{\sigma_l} = \eta_l/M_l = 1/\omega_l$ is called stress relaxation time of Maxwell body. M_l is the elastic modulus of each spring and η_l is the viscosity inside the same Maxwell body.

Therefore, the qualify factor is achieved as

$$\frac{1}{Q(\omega)} = \frac{\sum_{l=1}^{L} \frac{M_l}{M_R} \frac{\omega\tau_{\sigma l}}{1+\omega^2\tau_{\sigma l}^2}}{1 + \sum_{l=1}^{L} \frac{M_l}{M_R} \frac{\omega^2\tau_{\sigma l}^2}{1+\omega^2\tau_{\sigma l}^2}} \tag{2.18}$$

Q formulas based on GZB (Equation 2.16) and GMB (Equation 2.18) may appear to be different. By defining

$$\alpha_l = \frac{1}{L}\left(\frac{\tau_{\epsilon l}}{\tau_{\sigma l}} - 1\right) \tag{2.19}$$

for Equation 2.16, and

$$\alpha_l = M_l/M_R \tag{2.20}$$

for Equation 2.18, an equivalent Q formula is derived as

$$\frac{1}{Q(\omega)} = \frac{\sum_{l=1}^{L} \frac{\alpha_l\omega\tau_{\sigma l}}{1+\omega^2\tau_{\sigma l}^2}}{1 + \sum_{l=1}^{L} \frac{\alpha_l\omega^2\tau_{\sigma l}^2}{1+\omega^2\tau_{\sigma l}^2}}. \tag{2.21}$$

α_l is a positive parameter to determine the constant Q value within a frequency bandwidth $[\omega_{min}, \omega_{max}]$. $\tau_{\sigma l}$ is determined in advance, empirically given by $1/\omega_l$, where ω_l is chosen evenly over the frequency bandwidth in a logarithm scale to optimize the nearly constant Q.

The same Q format based on GZB and GMB turns into a rheology-independent Q model (Moczo and Kristek, 2005). However, rheology models are still useful to understand and analyze the stress-strain relationship and visco-elastic behaviors. The term α_l in total number L is optimized to have nearly constant Q values. Generally, when L is larger, the constant Q trends to be more flat within the frequency bandwidth. However, L number of α_l leads to computationally expensive numerical schemes. Taking L equal to 1 is not enough to approximate constant Q. We will introduce the τ method (Blanch et al., 1995) with a single value (Section 2.3.3).

2.3.3 Modified optimization of nearly constant Q

The nearly constant Q is approximated within a frequency bandwidth. The τ method (Blanch et al., 1995) with a single term is convenient for inversion, first assuming all α_l in Equation 2.21 are replaced by a single τ, turning into

$$\frac{1}{Q(\omega)} = \frac{\sum_{l=1}^{L} \frac{\tau\omega\tau_{\sigma l}}{1+\omega^2\tau_{\sigma l}^2}}{1+\sum_{l=1}^{L} \frac{\tau\omega^2\tau_{\sigma l}^2}{1+\omega^2\tau_{\sigma l}^2}}, \tag{2.22}$$

where τ is the parameter for representing Q. To achieve the nearly constant Q, the least-squares objective function of determining optimal τ, given by

$$J[\tau] = \int_{\omega_{min}}^{\omega_{max}} (Q^{-1}(\omega,\tau) - Q_0^{-1})^2 d\omega, \tag{2.23}$$

where ω_{min} and ω_{max} are upper and bottom bounds of the frequency range. Q_0 is the desired value. To minimize the misfit function, the τ method finds the optimal τ by setting the derivative of $J[\tau]$ with respect to τ as zero. To obtain a fast analytical solution, the second assumption of the τ method is $\tau \ll 1$, leading to $1+\tau \approx 1$. Under this approximation, the Equation 2.21 turns into

$$\frac{1}{Q(\omega)} \approx \sum_{l=1}^{L} \frac{\tau\omega\tau_{\sigma l}}{1+\omega^2\tau_{\sigma l}^2}. \tag{2.24}$$

Finally, the τ is determined by a analytical solution,

$$\tau = \frac{1}{Q_0} \frac{\int_{\omega_{min}}^{\omega_{max}} F(\omega) d\omega}{\int_{\omega_{min}}^{\omega_{max}} F(\omega)^2 d\omega}, \tag{2.25}$$

where $F(\omega)$ is defined as $\sum_{l=1}^{L} \frac{\omega\tau_{\sigma l}}{1+\omega^2\tau_{\sigma l}^2}$.

However, the τ method over-estimates the Q value. Because the approximation of $1+\tau \approx 1$, for same τ value, the Q defined in Equation 2.24 is smaller than the Q defined in Equation 2.22. Equation 2.22 is **the actual Q formula and connected to visco-elastic wave equation**. To solve the over-estimation, the way is to give a lower pre-determined value Q_{pre}, other than the desired Q_0 to approximate the constant Q. For example, the desired quality factor is 15, the Q_{pre} may be around 13 or 12 (Figure 2.3).

Therefore, we propose a modified τ method based on grid search for Equation 2.23, to find more precise τ to simulate constant Q within the desired frequency bandwidth. In practice, we search the τ values from 0 to 1 with a fine interval 0.00005. Each constant Q value corresponds to a best τ value. Here, we present some results for comparison between the τ method and the modified method (Figure 2.4 and 2.5). The modified

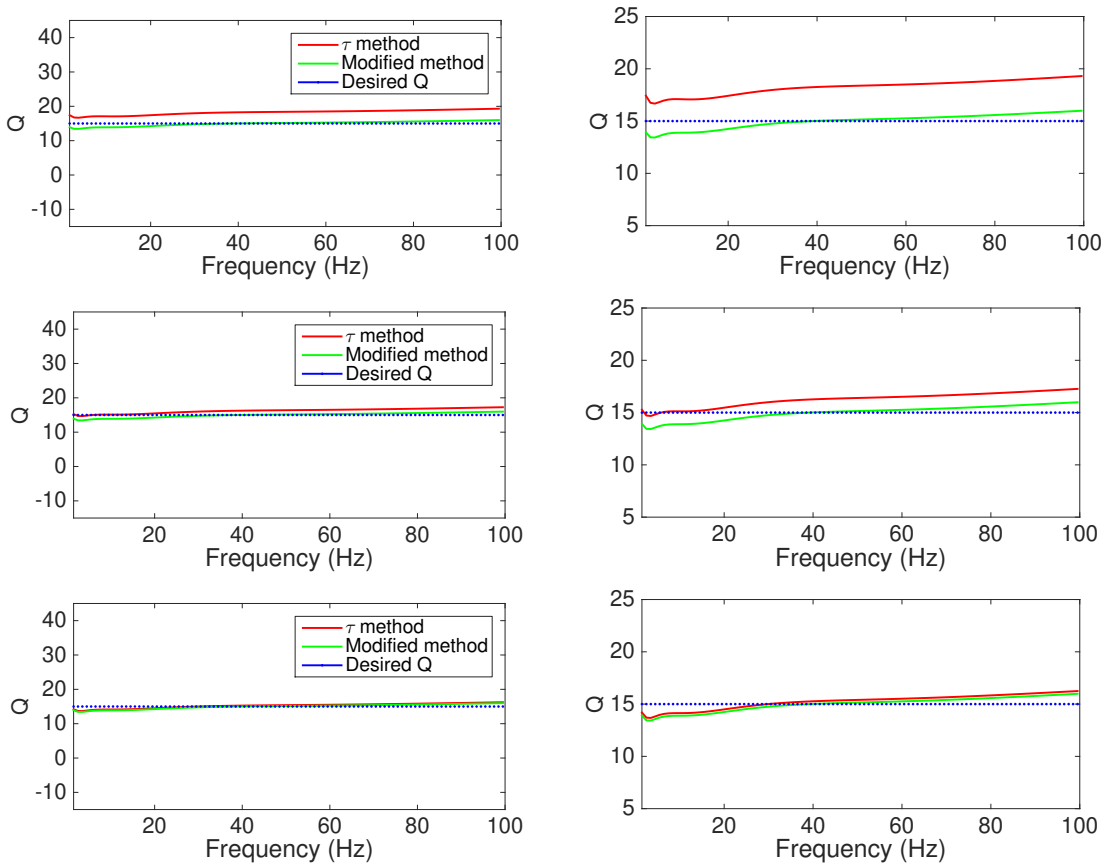

Figure 2.3: The optimization frequency range is from 1.5 Hz to 100 Hz for desired Q = 15, with empirically given Q_{pre} with 15 (top), 13 (middle) and 12 (bottom). The τ method is the analytical solution with different pre-defined Q_{pre}, the modified method is the global searching method.

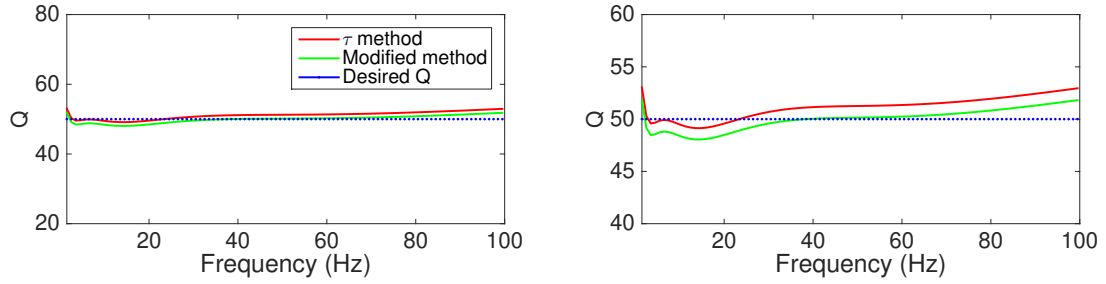

Figure 2.4: The optimization frequency range is from 1.5 Hz to 100 Hz for Q_0 = 50 with empirically given Q_{pre} with 48.

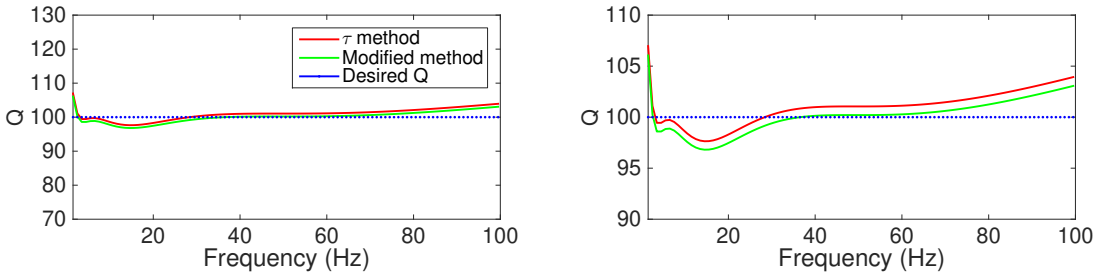

Figure 2.5: Same as Figure 2.4, but for Q = 100 with empirically given Q with 98.

method is more accurate and without estimating a empirical initial Q_{pre}. 5 SLS can simulate a constant Q over 1.5 Hz to 100 Hz, and we use $L = 5$ for our later visco-acoustic wave equation.

The τ method (Blanch et al., 1995) is widely applied due to its simplicity with analytical solution. However, this method over-estimates the desired Q value. Our modified τ method is more precise without estimating a lower Q_{pre} to approach the desired Q_0. Based on this modified method, we obtain nearly Q model and the associated visco-acoustic wave equation. This is a fast procedure compared with the computation of the wave equations.

2.4 Visco-acoustic wave equations

Visco-elastic / visco-acoustic wave equations have various formats. We split the wave equations into three categories corresponding to Q models in Section 1.1.3, including Voigt-Ricker model, constant Q model and nearly constant Q model.

First, based on the second-order acoustic wave equation, a first-order time derivative of pressure wavefields describes the energy dissipation (Ricker, 1953). Because of this simplicity, this wave equation theory with absorption has been widely adopted to compute the synthetic seismograms in early researches (Boore et al., 1971; Munasinghe and Farnell, 1973; Deng and McMechan, 2007). However, the Q varies with frequency, which contradicts observations. Under the seismic frequency bandwidth, a constant Q is realistic. Based on constant Q (Kjartansson, 1979), the wave equation has to solve a fractional derivative in time domain, leading to few applications (Section 2.3.1).

Based on the nearly constant Q model (Section 2.3.2), visco-elastic / visco-acoustic wave equations are obtained by incorporating the complex modulus or complex velocity in frequency domain (Aki and Richards, 1980; Song et al., 1995; Liao and McMechan, 1996; Stekl and Pratt, 1998; Hicks and Pratt, 2001; Pratt et al., 2005; Operto et al., 2007b; Brossier et al., 2010; Prieux et al., 2013; Gosselin-Cliche and Giroux, 2014; Operto et al., 2014, 2015) or time convolution in time domain (Emmerich and Korn, 1987;

Carcione et al., 1988a,b; Emmerich, 1992; Fah, 1992; Robertsson et al., 1994; Blanch et al., 1995; Xu and McMechan, 1995; Robertsson, 1996; Moczo et al., 1997; Kay and Krebes, 1999; Hestholm, 2002). Frequency domain methods are easy to implement by incorporating complex modulus or complex velocity. However, modeling of one frequency wave with a finite-difference method requires solving a large, sparse system of linear equations (Operto et al., 2007b; Brossier et al., 2009), especially for 3D applications. The time domain methods incorporate the time convolution into equations. The stress is presented by visco-elastic or visco-acoustic modulus convoluting with strain. Based on nearly constant Q model and the methods of optimizing constant Q, the visco-elastic modulus is written as nth-order rational function, turning time convolution into nth-order differential equation.

In this thesis, we apply the visco-elastic / visco-acoustic wave equation based on nearly constant Q model. The nearly Q is approximated by modified τ method, representing the attenuation parameter (Section 2.3.3).

First, we start from the stress relaxation function based on GZB (Equation 2.15), replaced with parameter τ, the stress relaxation functions related to P and S waves in a isotropic visco-elastic media (Carcione et al., 1988a,b; Robertsson et al., 1994) are given by

$$\psi^P(t) = (\lambda + 2\mu)(1 + \sum_{l=1}^{L} \tau^P e^{-t/\tau_{\sigma l}})H(t), \tag{2.26}$$

$$\psi^S(t) = \mu(1 + \sum_{l=1}^{L} (1 + \tau^S e^{-t/\tau_{\sigma l}})H(t), \tag{2.27}$$

where $\psi^P(t)$ and $\psi^S(t)$ are the stress relaxation functions related to P and S waves, respectively. As before, $H(t)$ is the Heaviside function. τ^P and τ^S are attenuation parameters for P and S waves. λ and μ are the Lamé parameters. $\lambda + 2\mu$ is the relaxed modulus of P waves and μ is the relaxed modulus of S waves. l means the lth SLS, and total number is L to simulate constant Q.

For an isotropic elastic media, the constitutive relation is $\sigma_{ij} = \lambda\delta_{ij}\epsilon_{kk} + 2\mu\epsilon_{ij}$. The index i, j, k denote x, y in 2D media and x, y, z in 3D media. According the convolution relation between stress and strain in a linear visco-elastic media in Equation 2.2, the stress-strain in isotropic visco-elastic media is

$$\sigma_{ij} = \dot{\psi^\lambda} * \delta_{ij}\epsilon_{kk} + 2\dot{\psi^\mu} * \epsilon_{ij}, \tag{2.28}$$

where $\dot{\psi}$ denotes the time derivative of ψ, $*$ denotes the time convolution, σ is stress and ϵ is strain. The term ψ^λ and ψ^μ are defined as

$$\psi^\mu = \psi^S, \tag{2.29}$$

$$\psi^\lambda = \psi^P - 2\psi^S. \tag{2.30}$$

The strain-displacement relationship is

$$\epsilon_{ij} = \frac{1}{2}(\partial_i u_j + \partial_j u_i), \tag{2.31}$$

where u is displacement. Replacing the displacement u with velocity of particles, the time derivative of strain is

$$\dot{\epsilon_{ij}} = \frac{1}{2}(\partial_i v_j + \partial_j v_i), \tag{2.32}$$

v is velocity of particle, equal to $\dot{u}$. Substituting Equation 2.32 into time derivative of Equation 2.28, the relation between stress and velocity of particles is

$$\dot{\sigma_{ij}} = (\dot{\psi^P} - 2\dot{\psi^S}) * \partial_k v_k + 2\dot{\psi^S} * \partial_i v_j, \qquad i = j, \tag{2.33}$$

$$\dot{\sigma_{ij}} = \dot{\psi^S} * (\partial_i v_j + \partial_j v_i), \qquad i \neq j, \tag{2.34}$$

Introducing the relaxation function (Equation 2.27) into the convolution of Equation 2.33 and 2.34, the convolution equation turns into a ordinary differential form

$$\dot{\sigma_{ij}} = \left[(\lambda + 2\mu)\left(1 + L\tau^P\right) - 2\mu\left(1 + L\tau^S\right)\right]\partial_k v_k + 2\mu\left(1 + L\tau^S\right)\partial_i v_j + \sum_{l=1}^{L} r_{ij}^l, \qquad i = j, \tag{2.35}$$

$$\dot{\sigma_{ij}} = \mu(1 + L\tau^S)(\partial_i v_j + \partial_j v_i) + \sum_{l=1}^{L} r_{ij}^l, \qquad i \neq j, \tag{2.36}$$

with memory variables r_{ij}^l, denoted as

$$\dot{r_{ij}^l} = -\frac{1}{\tau_{\sigma l}}(r_{ij}^l + \left[(\lambda + 2\mu)\tau^P - 2\mu\tau^S\right]\partial_k v_k + 2\mu\tau^S\partial_i v_j, \quad i = j, \tag{2.37}$$

$$\dot{r_{ij}^l} = -\frac{1}{\tau_{\sigma l}}(r_{ij}^l + \mu\tau^S(\partial_i v_j + \partial_j v_i)), \qquad i \neq j, \tag{2.38}$$

According to the Newton's second law, the relation between velocity of particles and stress is

$$\dot{v_i} = \frac{1}{\rho}\partial_j \sigma_{ij}. \tag{2.39}$$

Finally, the visco-elastic wave-equation in stress-velocity format is composed by Equations 2.36, 2.36, 2.37, 2.38 and 2.39. If $\tau^P = \tau^S = 0$, the visco-elastic wave equation becomes the elastic one. Setting μ and τ^S as zero, the *visco-acoustic* wave-equation is

$$\frac{\partial p}{\partial t} + \kappa(L\tau + 1)(\nabla \cdot \boldsymbol{v}) + \sum_{l=1}^{L} r_p^l = f(x_s, t), \tag{2.40}$$

$$\frac{\partial \boldsymbol{v}}{\partial t} + \frac{1}{\rho}\nabla p = 0, \tag{2.41}$$

$$\frac{\partial r_p^l}{\partial t} + \frac{1}{\tau_\sigma^l}(r_p^l + \tau\kappa(\nabla \cdot \boldsymbol{v})) = 0. \qquad l =\in [1, L] \tag{2.42}$$

p is the pressure wavefield, $\boldsymbol{v}$ is the particle velocity. $\kappa = \rho v_p^2$ denotes for relaxed bulk modulus. This modulus is obtained as the limit of the visco-acoustic complex modulus when t $\rightarrow \infty$ or $\omega \rightarrow 0$ (Section 2.2 and Figure 2.2). τ is the term to represent Q model. The visco-acoustic wave equation has two parameters v_p for P wave velocity and τ for attenuation. Based on the visco-acoustic wave equation, we introduce the numerical solution.

2.5 Numerical soltuion

Wave equations can be solved numerically in many schemes, including the finite difference method (FDM) (Alterman and Karal-Jr., 1968; Kelly et al., 1976; Virieux, 1986) and the finite element method (FEM) (Smith, 1975; Marfurt, 1984). FEM is more flexible to deal with complex geological body interfaces, as well as with the topography. Among the FEM family, spectral element method (SEM) (Komatitsch, 1997; Komatitsch and Vilotte, 1998) combines the flexibility of FEM with the accuracy of the analytical / semi-analytical spectral method, which is gaining the popularities in global seismology and strong motion seismology (Komatitsch and Tromp, 1999, 2002; Chaljub et al., 2007). However, FEM is expensive in terms of computational costs. FDM provides a relatively more efficient and cheaper implementation, as a compromise between the accuracy and computational costs. It is widely adopted in exploration seismology, can be implemented in the time (Virieux, 1986; Levander, 1988; Graves, 1996) or in the frequency (Pratt, 1990; Jo et al., 1996; Pratt, 1999) domains. The efficiency and complexity of the different numerical modeling methods are reviewed by Virieux et al. (2011). In this thesis, I use FDM to simulate the visco-acoustic in the time domain.

2.5.1 Finite difference solver

FDM is a natural way to solve partial differential equations. The method directly estimates each differential term using the Taylor expansion on a regular grid. The numerical solutions by FDM for visco-elastic wave eqution is more straightforward to solve in frequency domain by incorporating a complex and frequency-dependent visco-elastic modulus in the constitutive relation (Stekl and Pratt, 1998; Operto et al., 2007a,b; Brossier et al., 2010; Operto et al., 2014). However, modeling of one frequency wave with a finite-difference method requires solving a large, sparse system of linear equations (Operto et al., 2007b; Brossier et al., 2009). A sparse direct solver needs large

memories to store the matrix during LU decomposition, especially for 3D appliations. Therefore, visco-elastic wave equation can be solved in time domain by efficiently discretizing the convolution integral constitutive equations (Liu et al., 1976; Emmerich and Korn, 1987; Robertsson et al., 1994; Blanch et al., 1995; Carcione et al., 2002; Saenger and Bohlen, 2002, 2004).

The 2D spatial samplings are Δx and Δz and the time step is Δt, the first-order derivatives in temporal coordinates and in the spatial coordinates (lateral position x and depth position z) and are both approximated by second-order approximation (Figure 2.6), given as

$$\begin{aligned}
\frac{\partial v_x}{\partial t}|^k_{i,j} &= \frac{v^{k+\frac{1}{2}}_{x_{i,j}} - v^{k-\frac{1}{2}}_{x_{i,j}}}{\Delta t}, \\
\frac{\partial v_z}{\partial t}|^k_{i+\frac{1}{2},j+\frac{1}{2}} &= \frac{v^{k+\frac{1}{2}}_{z_{i+\frac{1}{2},j+\frac{1}{2}}} - v^{k-\frac{1}{2}}_{z_{i+\frac{1}{2},j+\frac{1}{2}}}}{\Delta t}, \\
\frac{\partial p}{\partial t}|^{k+\frac{1}{2}}_{i+\frac{1}{2},j} &= \frac{p^{k+1}_{i+\frac{1}{2},j} - p^{k}_{i+\frac{1}{2},j}}{\Delta t},
\end{aligned} \tag{2.43}$$

and

$$\begin{aligned}
\frac{\partial v_x}{\partial x}|^{k+\frac{1}{2}}_{i+\frac{1}{2},j} &= \frac{v^{k+\frac{1}{2}}_{x_{i+1,j}} - v^{k+\frac{1}{2}}_{x_{i,j}}}{\Delta x}, \\
\frac{\partial v_z}{\partial z}|^{k+\frac{1}{2}}_{i+\frac{1}{2},j} &= \frac{v^{k+\frac{1}{2}}_{z_{i+\frac{1}{2},j+\frac{1}{2}}} - v^{k+\frac{1}{2}}_{z_{i+\frac{1}{2},j-\frac{1}{2}}}}{\Delta z}, \\
\frac{\partial p}{\partial x}|^{k}_{i,j} &= \frac{p^{k}_{i+\frac{1}{2},j} - p^{k}_{i-\frac{1}{2},j}}{\Delta x}, \\
\frac{\partial p}{\partial z}|^{k}_{i+\frac{1}{2},j+\frac{1}{2}} &= \frac{p^{k}_{i+\frac{1}{2},j+1} - p^{k}_{i+\frac{1}{2},j}}{\Delta z},
\end{aligned} \tag{2.44}$$

where i, j are the 2D spatial coordinates and k is the temporal coordinate. $\pm\frac{1}{2}$ means that the position of the grid is shifted by half a grid point, corresponding to staggered grids (Virieux, 1986). The first-order velocity-pressure wave equation is solved under the staggered grid scheme. v_x ,v_z and p are at the grids, shifted by half a grid point with each other (Figure 2.6). The memory variables r^l_p are related to p, and have the same positions as p.

Substituting the Taylor expansion in the visco-acoustic wave equation, the components v_x, v_z, p and r_{pl} are updated as

$$v^{k+\frac{1}{2}}_{x_{i,j}} = v^{k-\frac{1}{2}}_{x_{i,j}} - \frac{1}{\rho}\frac{\Delta t}{\Delta x}(p^{k}_{i+\frac{1}{2},j} - p^{k}_{i-\frac{1}{2},j}),$$

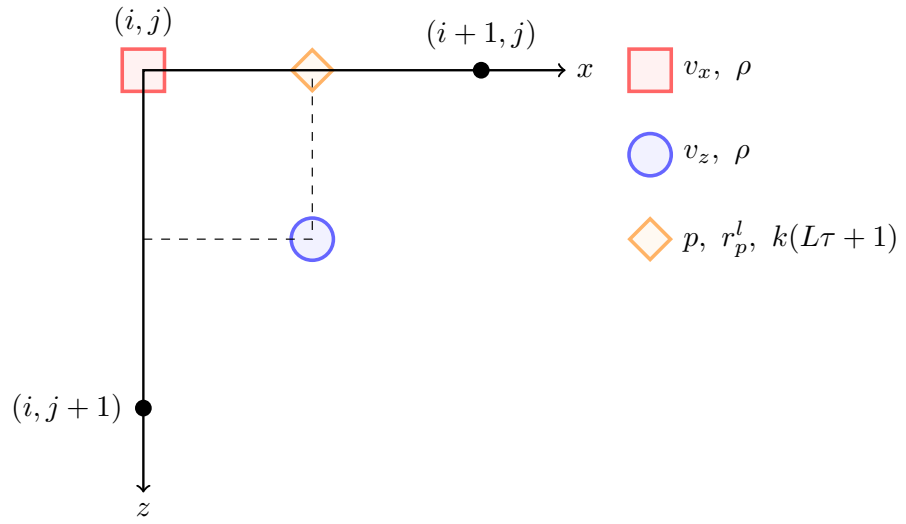

Figure 2.6: Discretization of the media on a staggered grid, p is the pressure wavefields, v_x and v_z are particle velocity components.

$$
\begin{aligned}
v^{k+\frac{1}{2}}_{z_{i+\frac{1}{2},j+\frac{1}{2}}} &= v^{k-\frac{1}{2}}_{z_{i+\frac{1}{2},j+\frac{1}{2}}} - \frac{1}{\rho}\frac{\Delta t}{\Delta z}(p^{k}_{i+\frac{1}{2},j+1} - p^{k}_{i+\frac{1}{2},j}),\\
p^{k+1}_{i+\frac{1}{2},j} &= p^{k}_{i+\frac{1}{2},j} - \kappa(L\tau+1)\left[\frac{\Delta t}{\Delta x}(v^{k+\frac{1}{2}}_{x_{i+1,j}} - v^{k+\frac{1}{2}}_{x_{i,j}}) + \right.\\
&\quad \left.\frac{\Delta t}{\Delta z}(v^{k+\frac{1}{2}}_{z_{i+\frac{1}{2},j+\frac{1}{2}}} - v^{k+\frac{1}{2}}_{z_{i+\frac{1}{2},j-\frac{1}{2}}})\right] - \Delta t\sum_{l=1}^{L} r^{k}_{pl_{i+\frac{1}{2},j}},\\
r^{k+1}_{pl_{i+\frac{1}{2},j}} &= r^{k}_{pl_{i+\frac{1}{2},j}} - \frac{\Delta t}{\tau_{\sigma l}} r^{k}_{pl_{i+\frac{1}{2},j}} - \frac{\kappa\tau}{\tau_{\sigma l}}\frac{\Delta t}{\Delta x}(v^{k+\frac{1}{2}}_{x_{i+1,j}} - v^{k+\frac{1}{2}}_{x_{i,j}})\\
&\quad -\frac{\kappa\tau}{\tau_{\sigma l}}\frac{\Delta t}{\Delta z}(v^{k+\frac{1}{2}}_{z_{i+\frac{1}{2},j+\frac{1}{2}}} - v^{k+\frac{1}{2}}_{z_{i+\frac{1}{2},j-\frac{1}{2}}}), \qquad l =\in [1, L]
\end{aligned}
\tag{2.45}
$$

where the physical parameters κ, τ and ρ have the same space positions as the updating component.

The last equation for updating r_{pl} has an explicit form. The implicit form is obtained by replacing $r^{k}_{pl_{i+\frac{1}{2},j}}$, leading to

$$
\begin{aligned}
r^{k+1}_{pl_{i+\frac{1}{2},j}} &= \left[(1 - \frac{1}{2}\frac{\Delta t}{\tau_{\sigma l}}) r^{k}_{pl_{i+\frac{1}{2},j}} - \frac{\kappa\tau}{\tau_{\sigma l}}\frac{\Delta t}{\Delta x}(v^{k+\frac{1}{2}}_{x_{i+1,j}} - v^{k+\frac{1}{2}}_{x_{i,j}})\right.\\
&\quad \left. -\frac{\kappa\tau}{\tau_{\sigma l}}\frac{\Delta t}{\Delta z}(v^{k+\frac{1}{2}}_{z_{i+\frac{1}{2},j+\frac{1}{2}}} - v^{k+\frac{1}{2}}_{z_{i+\frac{1}{2},j-\frac{1}{2}}})\right] / (1 + \frac{1}{2}\frac{\Delta t}{\tau_{\sigma l}}).
\end{aligned}
\tag{2.46}
$$

With the staggered grid discretization, all the components of visco-acoustic wave equa-

tion are updated inside the time loop.The spatial discretization of FDM is usually implemented with a regular rectangle grid. Irregular boundaries and shapes limit the application and resolution of modeling by FDM, especially dealing with topography. Finite element methods (Marfurt, 1984) is more flexible to solve irregular boundaries. Due to the computation efficiency reason and for regular boundary, I apply FDM for forward modeling.

2.5.2 Stability and dispersion

FDM is discretized by finite steps. The spatial steps and temporal step should satisfy the Courant-Friedrichs-Lewy (CFL) condition to meet the numerical stability (Courtant et al., 1928). The theoretical analysis assuming a homogeneous media (Virieux, 1986; Levander, 1988; Saenger and Bohlen, 2004; Martin et al., 2008) gives the following condition for a second-order approximation both in spatial and temporal space

$$\max(v_p)\Delta t\sqrt{\frac{1}{\Delta x^2}+\frac{1}{\Delta y^2}+\frac{1}{\Delta z^2}} \leq 1. \tag{2.47}$$

Similar to the analog elastic schemes to satisfy the stability criteria, maximum v_p has to be adjusted to the highest phase velocity along the frequency bandwidth in visco-acoustic media (Robertsson et al., 1994; Igel et al., 1995; Saenger and Bohlen, 2004). In practice, the maximum values of frequency of source and attenuation leads to highest phase velocity. For 2D simulation with $\Delta x = \Delta z = \Delta h$, stability condition becomes

$$\max(v_p)\frac{\Delta t}{\Delta h} \leq \frac{1}{\sqrt{2}}. \tag{2.48}$$

If the criteria is not satisfied, numerical simulation is unstable generating results as shown in Figure 2.7b. For purely elastic media, body waves are not dispersive waves. However, finite difference discretization generates numerical dispersion during the simulation of wave propagation. The spatial sampling Δh should be defined such that

$$\Delta h \leq \frac{\lambda_{min}}{n_\lambda} = \frac{v_{min}}{f_{max}}\frac{1}{n_\lambda}, \tag{2.49}$$

where λ_{min} is shortest wavelength depending on the maximum frequency f_{max} and the minimum velocity v_{min}. n_λ is grid point number per wavelength, it is related to spatial and temporal orders in the Taylor expansion. $n_\lambda = 10$ or more is adequate for second-order approximation in space and time, versus $n_\lambda = 5$ or more for fourth-order in space and second-order in time (Alford et al., 1974), within a propagation up to 100 wavelengths through the media (Sei and Symes, 1995). It the criterion is not satisfied, the simulation generates numerical dispersion (Figure 2.7c). One important point mentioned is that numerical dispersion is different with the physical dispersion of visco-acoustic or visco-elastic waves.

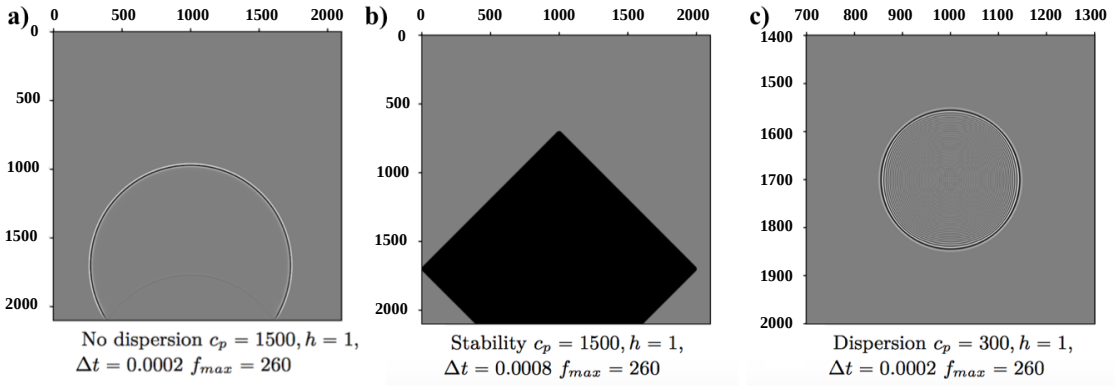

Figure 2.7: One snapshot of wavefields: stable wave propagation without numerical dispersion (a), unstable wave propagation (b), stable condition with numerical dispersion (c) (adapted from Thorbecke, 2015).

2.5.3 Boundary condition

Different from the real seismic propagation, the numerical simulation encounters with a finite space due to the limited computation capacities. When waves reach the boundaries of the model, the waves will reflect back from the rigid boundaries, which generates the non-physical waves. To solve the problem, absorbing boundaries should be adopted to eliminate the artificial reflected waves. The intuitive way is adding extra layers around the computational space as sponges to absorb incident waves. It is effective with normal incident waves. Non-physical spurious reflections appear from other incident angles (Brossier et al., 2009).

A new kind of absorbing boundary called perfectly matched layer (PML) was firstly applied to electromagnetic wave-equation to absorb the boundary reflections (Bérenger, 1994). PML is widely used in the seismic wave equation (Chew and Liu, 1996; Collino and Tsogka, 2001; Komatitsch and Tromp, 2003). Furthermore, the behavior of PML at grazing incidence can be improved using an unsplit convolutional approach called Convolutional PML (CPML) proposed by Komatitsch and Martin (2007). Martin and Komatitsch (2009) introduced CPML to visco-elastic wave equation. The principal is to damp the wave energy until it is weak enough, by introducing the complex spatial derivatives inside the CMPL.

We implemented CMPL for numerical simulation with limited model extension. For example, a homogeneous model has 941 grid points in length and 941 grid points in depth, with the grid size Δh = 5 m. The simulation time is 2 seconds with Δt = 0.001 s. The CPML has 30 grid points with Δh = 5 m around four each side. The central frequency for the Ricker source is 10 Hz. Spurious reflections appear when the wave arrives at the boundary without CPML (Figure 2.8). With CMPL boundary for visco-acoustic wave equation modeling, boundary reflections are absorbed (Figure 2.9).

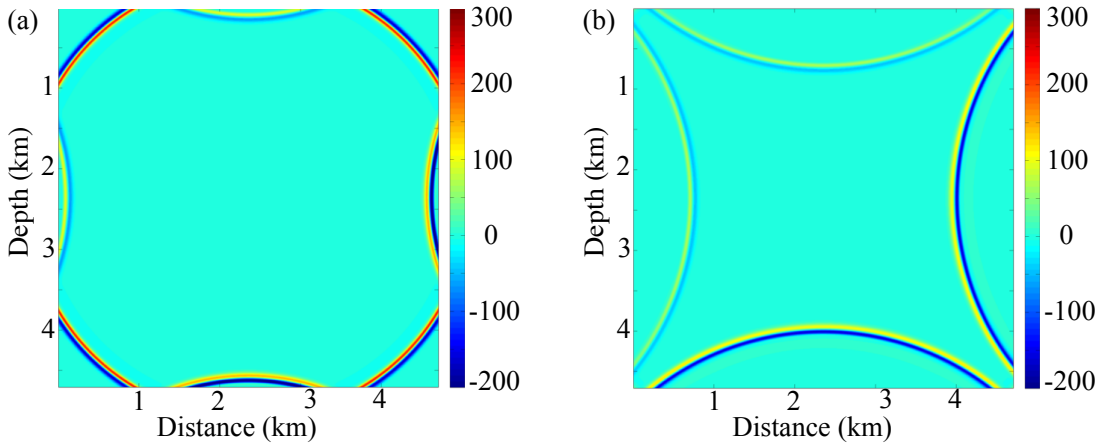

Figure 2.8: Snapshot without CPML at 1.4 s (a) and 1.7 s (b).

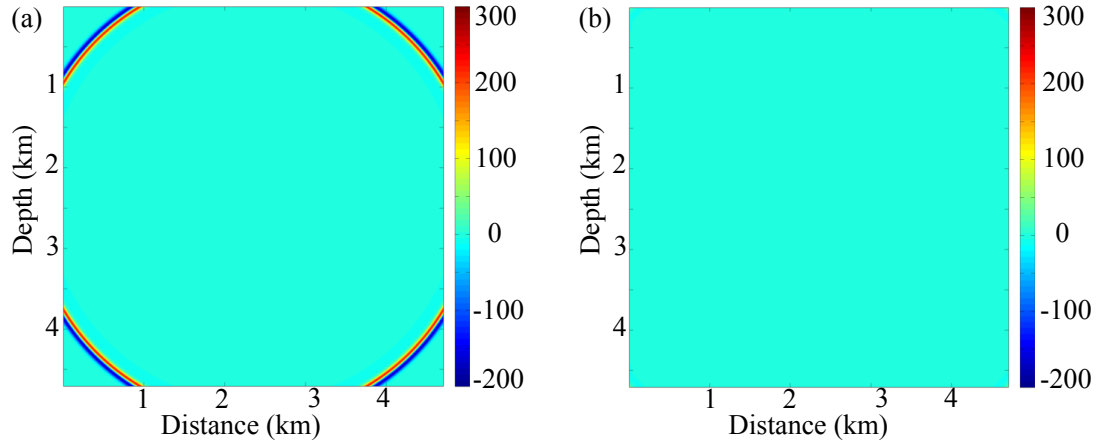

Figure 2.9: Same as Figure 2.8, but snapshot with CPML at 1.4 s (a) and 1.7 s (b).

The CMPL works well and absorbs the boundary reflections. In this thesis, we put CMPL around each side of the model for simulation. We now compare the numerical solution with analytical solution to validate accuracy our FDM program.

2.5.4 Analytical and numerical comparison

To validate the accuracy of the finite difference solution, we compare the analytical solution with the staggered grid finite difference method in the pure acoustic media, by setting visco-acoustic parameter $\tau = 0$. The 2D homogeneous acoustic analytical

solution (Aki and Richards, 1980) is

$$G_{2D}(\boldsymbol{x},t) = \frac{1}{2\pi}\frac{H(t-\frac{r}{c})}{\sqrt{t^2-\frac{r^2}{c^2}}}, \tag{2.50}$$

where $\boldsymbol{x}$ is spatial coordinate, r is the distance between source and recorded location, c is the velocity. In frequency domain, it becomes

$$G_{2D}(\boldsymbol{x},\omega) = \frac{i}{4}H_0^1(\omega\frac{r}{c}), \tag{2.51}$$

where H is the Heaviside function and H_0^1 is the Hankel's function of order 1. According to the representation theorem (Aki and Richards, 1980), the seismic trace is obtained as the convolution of source term with the Green's function. We use a Ricker wavelet as source term with central frequency 20 Hz. To compare the analytical solution with the numerical solution, the source term for first order velocity-pressure wave equation is the time integration of Ricker wavelet. The acoustic velocity is 2000 m/s. The spatial grid size is 5 m in both horizontal and vertical directions. Two solutions are compared at distance 200 m and 800 m (Figure 2.10), corresponding to 5 and 20 wavelengths for the maximum frequency waves, respectively. The maximum relative difference is 2%. It validates the accuracy of the finite difference method for solving the wave equation in the acoustic case. As for the visco-elastic case, the analytical solution is obtained by introducing the complex modulus.

2.6 Visco-acoustic effects

The seismic attenuation effects include the dissipation and dispersion, leading to the wave energy loss, central frequency downshifting and kinematic changes. We first illustrate the spectrum distortion of 2D propagation of acoustic waves. After clarifying the spectrum distortion caused by 2D propagation, then we analyze the visco-elastic effects. Finally, we rewrite the visco-acoustic wave equation in the frequency domain, with a complex velocity. The real term of the complex velocity is related to the kinematic information, defined as *kinematic velocity*.

2.6.1 Distortion of 2D propagation

Seismic attenuation causes the spectrum distortion of the visco-elastic waves. The recorded data has lower central frequency than the source wavelet. However, the spectrum distortion also occurs for the acoustic waves in 2D propagation. It is necessary to check the acoustic propagation distortion in 2D media by both numerical and analytical solutions. We use a central 20 Hz Ricker wavelet as the source time function

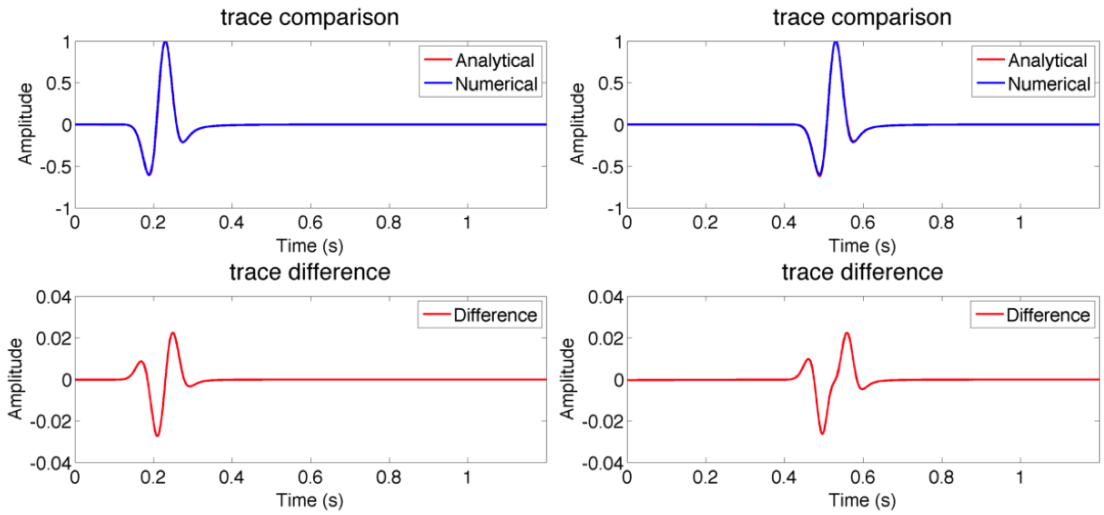

Figure 2.10: Numerical solution compares with analytical solution and at distance 200 m (left) and 800 m (right) with the spatial grid space being 5 m. Top: trace comparisons, bottom: trace difference.

(Figure 2.11), given by

$$S(t) = (1 - 2\pi^2 f_c^2 (t - t_0)^2) \exp\left(-\pi^2 f_c^2 (t - t_0)^2\right), \tag{2.52}$$

where t is the time, t_0 is the time shift, and f_c is the central frequency, equal to 20 Hz.

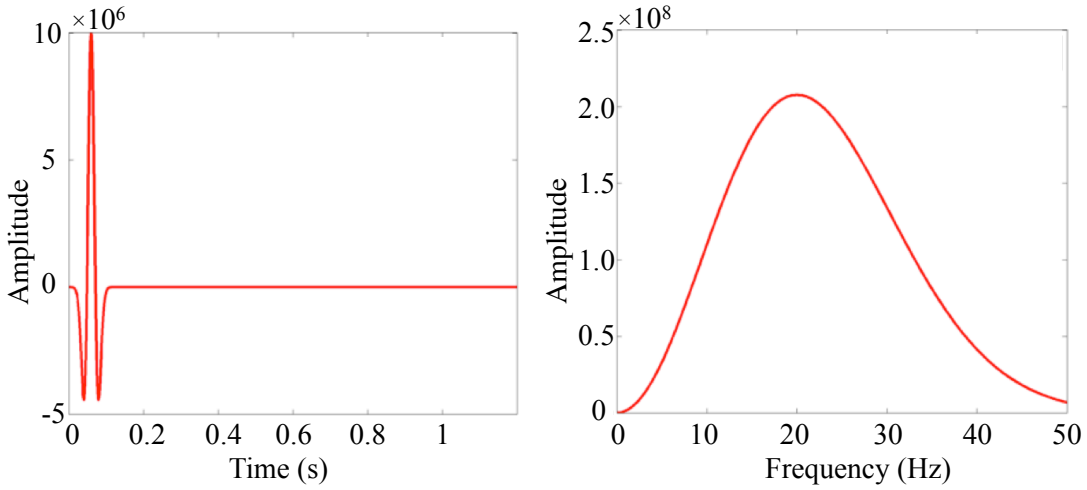

Figure 2.11: 20 Hz central Ricker wavelet in the time (left) and frequency (right) domain.

The analytical solution is obtained by the source term convoluting with 2D Green's function (Equation 2.50). In 2D media, because of Hankel's transform, the central frequency is not preserved. The central frequency of a recorded trace is 17.5 Hz computed by analytical, and also by numerical solutions, lower than the central frequency of the source wavelet (Figure 2.12). The central frequency is invariant for 3D acoustic propagation. Therefore, one should pay attention to the central frequency downshifting of visco-acoustic waves. The phenomenon is caused by the effects of both attenuation and 2D geometric spreading. This kind of frequency downshifting should be compensated in 2D media for central frequency shift method for estimating attenuation.

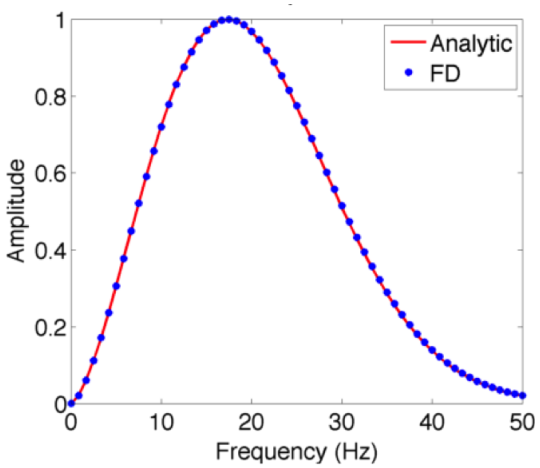

Figure 2.12: Spectrum of the recorded trance by analytical and numerical solutions, the central frequency of trace is 17.5 Hz computed by analytical solution (solid red) and finite difference method (dashed blue), lower than the source central frequency with 20 Hz.

2.6.2 Visco-acoustic effects in the time and frequency domains

To analyze the visco-elastic effects, we simulate one trace of acoustic and visco-acoustic waves at a distance of 400 m from the source (Figure 2.13). The visco-acoustic model has $Q = 15$ and same velocity as the last subsection. The central frequency of the source is 20 Hz. Because of 2D propagation distortion, the central of the acoustic wave at receiver position is 17.5 Hz. The central frequency of the visco-acoustic is 15 Hz due to attenuation. For the snapshots (Figure 2.14), the left half snapshots are acoustic waves, the right half ones are visco-acoutic waves. We notice the visco-acoustic waves have lower amplitude and faster velocity because the phase dispersion. We now introduce the kinematic changes and the kinematic velocity.

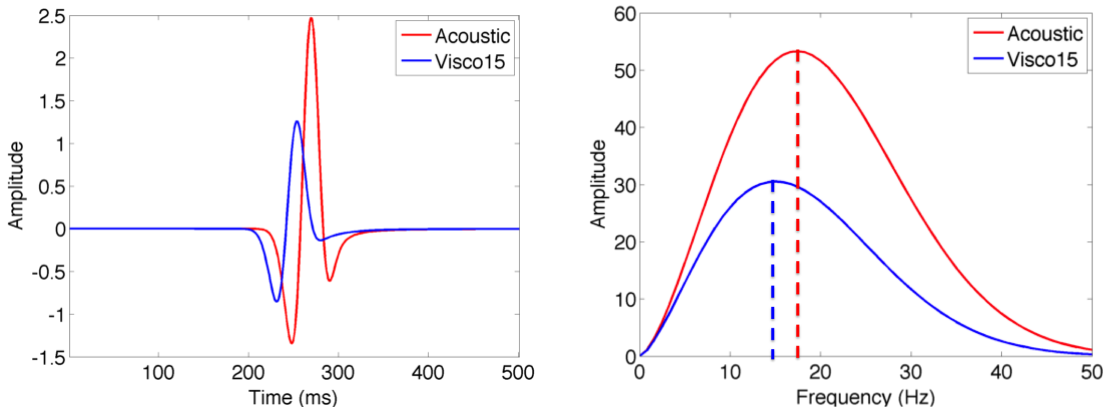

Figure 2.13: Trace comparison between acoustic (red) and visco-acoustic (blue) waves in time domain (left panel) and frequency domain (right panel).

2.6.3 Kinematic velocity

Seismic attenuation leads to dispersion, leading to phase velocity changes. The kinematic information of visco-acoustic waves changes. We call the actual traveling speed of visco-acoustic waves the *kinematic velocity*. Here, we use the visco-acoustic wave equation to analyze the kinematic changes and introduce the kinematic velocity. First, the visco-acoustic wave equation (Equations 2.42) in frequency domain reads

$$i\omega p + \kappa(L\tau + 1)(\nabla \cdot \boldsymbol{v}) + \sum_{l=1}^{L} r_p^l = f(x_s, \omega), \tag{2.53}$$

$$i\omega \cdot \boldsymbol{v} + \frac{1}{\rho}\frac{\partial p}{\partial x} = 0, \tag{2.54}$$

$$(i\omega + \frac{1}{\tau_\sigma^l})r_p^l + \frac{1}{\tau_\sigma^l}\tau\kappa(\nabla \cdot \boldsymbol{v}) = 0, \qquad l =\in [1, L], \tag{2.55}$$

where $\kappa = \rho v_p^2$ is called relaxed modulus, and v_p is the P wave velocity. We substitute the term r_p^l from the third equation into the first equation, then taking divergence on the both sides of the second equation to replace the term $\nabla \cdot \boldsymbol{v}$. The second-order wave equation with constant density gives as

$$(i\omega)^2 p - \frac{1}{\rho}\left[\kappa(L\tau + 1) - \sum_{l=1}^{L} \frac{\kappa\tau}{1 + i\omega\tau_\sigma^l}\right]\nabla^2 p = F(x_s, \omega), \qquad l =\in [1, L]. \tag{2.56}$$

The new equation is equal to a second-order wave equation

$$(i\omega)^2 p - v_c^2 \nabla^2 p = F(x_s, \omega), \tag{2.57}$$

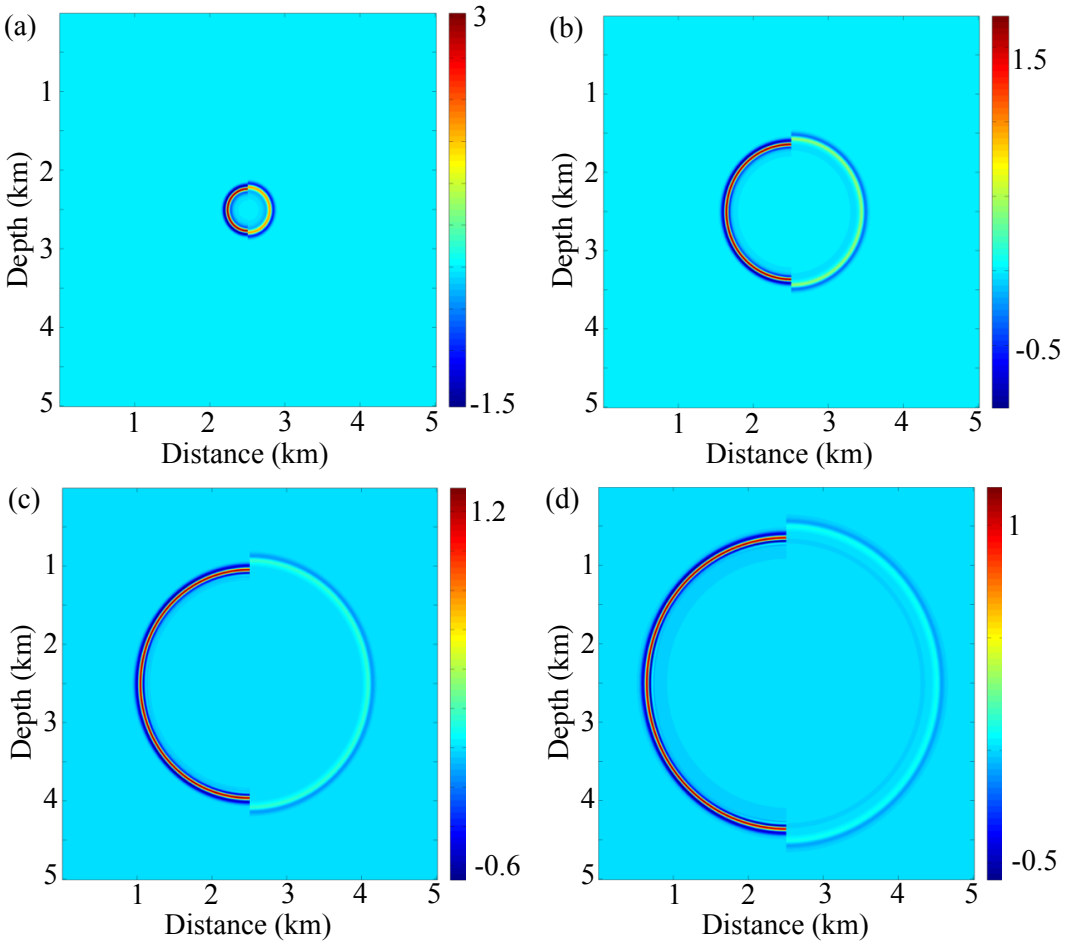

Figure 2.14: Snapshot comparison for acoustic (left parts of the images) and visco-acoustic (right parts) waves at 200 ms (a), 500 ms (b), 800 ms (c) and 1000 ms (d).

with a complex velocity

$$\begin{aligned} v_c^2(v_p,\tau,\omega) &= v_p^2\left[(L\tau+1)-\sum_{l=1}^{L}\frac{\tau}{1+i\omega\tau_\sigma^l}\right], \\ &= v_p^2\left[(L\tau+1)-\sum_{l=1}^{L}\frac{\tau}{1+\omega^2\tau_{\sigma l}^2}\right]+i\cdot v_p^2\left[\sum_{l=1}^{L}\frac{\tau\omega\tau_{\sigma l}}{1+\omega^2\tau_{\sigma l}^2}\right]. \end{aligned} \quad (2.58)$$

The complex velocity can be spitted into a real term plus a imaginary part

$$v_c(v_p,\tau,\omega) = v_k(v_p,\tau,\omega)+i\cdot v_l(v_p,\tau,\omega), \quad (2.59)$$

with

$$v_k = \sqrt{\frac{\sqrt{\Re[v_c^2]^2 + \Im[v_c^2]^2} + \Re[v_c^2]}{2}}, \tag{2.60}$$

$$v_l = \sqrt{\frac{\sqrt{\Re[v_c^2]^2 + \Im[v_c^2]^2} - \Re[v_c^2]}{2}}. \tag{2.61}$$

where v_k is corresponding to kinematic effects, controlling the travel time. We call it the equivalent *kinematic velocity*. v_l is related to the energy loss (Appendix 2.8). The v_k is the function of ω, v_p and τ, whose explicit form is

$$v_k = v_p \sqrt{\frac{\sqrt{\left[L\tau + 1 - \sum_{l=1}^{L} \frac{\tau}{1+\omega^2\tau_{\sigma l}^2}\right]^2 + \left[\sum_{l=1}^{L} \frac{\tau\omega\tau_{\sigma l}}{1+\omega^2\tau_{\sigma l}^2}\right]^2} + \left[L\tau + 1 - \sum_{l=1}^{L} \frac{\tau}{1+\omega^2\tau_{\sigma l}^2}\right]}{2}}. \tag{2.62}$$

For example, three kinds of waves have the same v_p = 2000 m/s with Q being infinite (acoustic), 50 and 15. The corresponding τ values are 0, 0.023 and 0.0923, respectively. Due to the dispersion, the kinematic velocity of three kinds of waves is different. Accordingly, v_k of three waves at 28 Hz is 2000 m/s, 2065 m/s and 2250 m/s. Attenuation is stronger, the kinematic velocity is higher (Figure 2.15 left). On the other side, waves with different combinations of velocity and attenuation can have same kinematic velocity. For example, with the same kinematic velocity v_k = 2250 m/s at 28 Hz, we have three kinds of waves with v_p = 2250 m/s and infinite Q (acoustic), v_p = 2180 m/s and Q = 50 and v_p = 2000 m/s and Q = 15 (Figure 2.15 right).

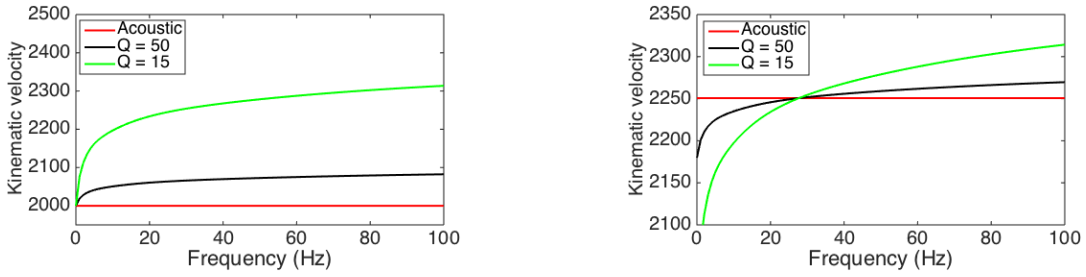

Figure 2.15: Left: different kinematic velocity v_k at 28 Hz for three kinds of waves: (infinite Q, v_p = 2000 m/s) in red, (Q = 50, v_p = 2000 m/s) in black and (Q = 15, v_p = 2000 m/s) in green. Right: same kinematic velocity v_k = 2250 m/s at 28 Hz for three kinds of waves: (infinite Q, v_p = 2250 m/s) in red, (Q = 50, v_p = 2180 m/s) in black and (Q = 15, v_p = 2000 m/s) in green.

For the band-limited seismic waves, we choose one single reference frequency to determine the kinematic velocity for the propagation of seismic waves. Generally, v_k **is**

determined for the central frequency of the source. For example, we simulate three kinds of waves with a 28 Hz central frequency Ricker wavelet (Figure 2.16). We set the kinematic velocity at 28 Hz, which is 2250 m/s. The three waves at the near and far offset have different amplitudes in the time domain and spectrum in the frequency domain in Figure 2.16. The correct traveltime is obtained at the maximum amplitude.

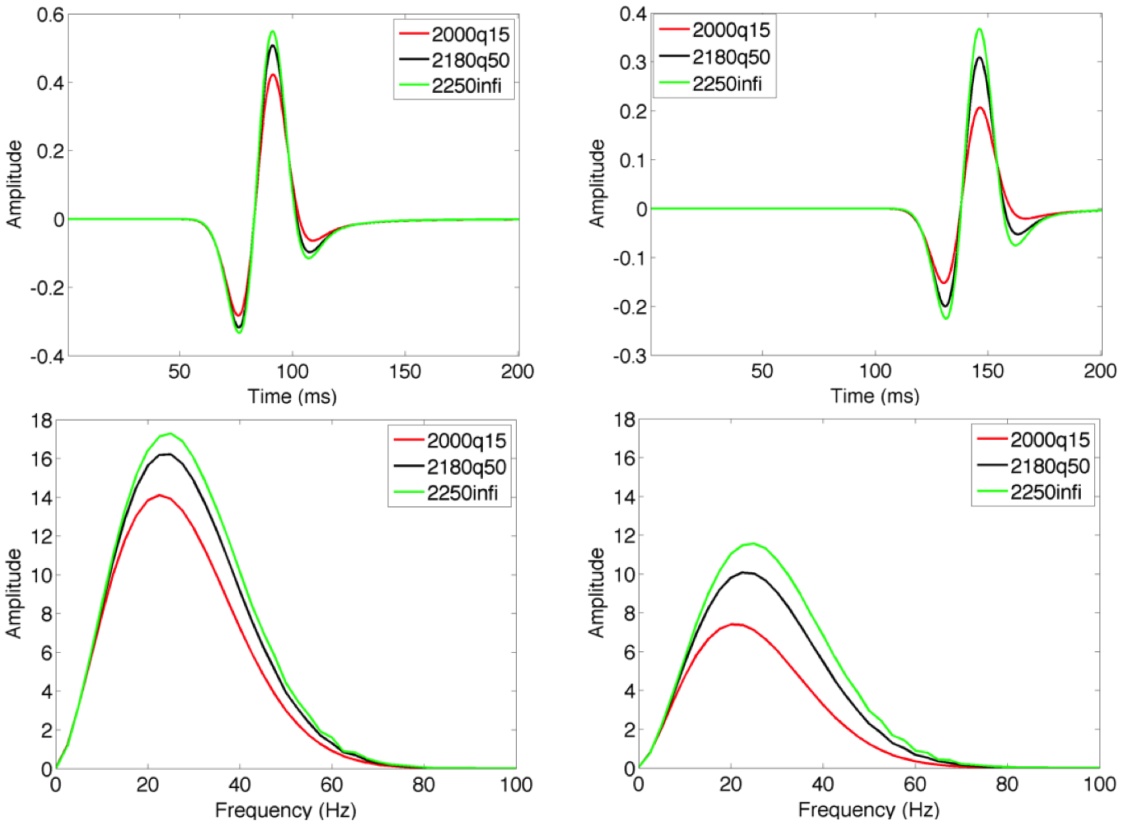

Figure 2.16: Traces for three different Q and velocity combinations (the same configurations as Figure 2.15 right): (infinite Q, v_p = 2250 m/s) in green, (Q = 50, v_p = 2180 m/s) in black and (Q = 15, v_p = 2000 m/s) in red at the near offset (left) and far offset (right), in the time (top) and frequency domains (bottom).

The different combinations of velocity and attenuation lead to the same kinematic velocity. This relation is called *kinematic relationship*, it will be applied to guide the inversion to retrieve the velocity and Q models (Chapter 4).

2.7 Summary

This chapter first reviews visco-elasticity represented by rheological models and introduces the concept of complex modulus and stress relaxation function of visco-elastic media. To be consistent with field observations, different kinds of Q models including constant Q and nearly constant Q models are introduced. Constant Q is deduced by assuming a relaxation function in the shape of power function. Nearly constant Q models represented by rheological models are intuitive, e.g., GMB and GZB. *A unification formalism of Q models represented by rheological description will be introduced in the next chapter*. Nearly constant Q is widely applied in exploration seismology due to the simplicity of the implementation. The visco-elastic / visco-acoustic wave equation in the time domain is obtained based on the method of nearly constant Q optimization. The τ method reduces the number of attenuation parameters to a single term τ. We propose a modified τ method to avoid an empirical initial guess for nearly constant Q optimization. Based on 2D visco-acoustic wave equation, we have implemented the forward simulation based FDM and analyzed the accuracy by comparing with an analytical solution. Finally, we have analyzed the visco-elastic effects including dispersion and dissipation. The former leads to phase shift, and the latter causes the amplitude loss. In frequency domain, the visco-acoustic wave equation can be represented by a complex velocity. The real and imaginary term of complex velocity corresponding to kinematic effect and amplitude loss respectively. For a fixed frequency, visco-acoutic waves with various combinations of v_p and Q (or τ) have the same kinematic velocity except that the amplitudes are different. The information is important for building a relation between v_p and Q (or τ) to guide the inversion. This aspect will be introduced in Chapter 4.

2.8 Appendix: Analysis of the wave propagation

We analyze the plane wave propagation in a homogeneous visco-acoustic media. A plan wave at distance x and time t is represented by

$$u(x,t) = u_0 \exp\left[i\omega\left(t - \frac{x}{v}\right)\right], \tag{2.63}$$

where $u(x,t)$ denotes the plane wave propagation. u_0 is the initial amplitude. ω is the angular frequency. v is the velocity of the waves. This is a constant real value for a homogenous elastic media.

For a homogenous attenuated media, the amplitude of visco-acoustic waves decays along with the propagation distance and velocity disperses with frequency, caused by attenuation. The wave propagation is written as

$$u(x,t) = u_0 \exp\left[-\alpha(\omega)x\right] \exp\left[i\omega\left(t - \frac{x}{v(\omega)}\right)\right], \tag{2.64}$$

where $v(\omega)$ is real and changes with frequency. The phase of waves is determined by $i\omega(t - x/v(\omega))$. $\alpha(\omega)$ is the attenuation coefficient, equal to $\omega/2v(\omega)Q$. The wavefield with attenuation is

$$u(x,t) = u_0 \exp\left\{i\omega\left[t - \frac{x}{v(\omega)}\left(1 - \frac{i}{2Q}\right)\right]\right\}, \tag{2.65}$$

with a complex velocity (Aki and Richards, 1980)

$$\frac{1}{v_c(\omega)} = \frac{1}{v(\omega)}\left[1 - \frac{i}{2Q}\right]. \tag{2.66}$$

With the first order approximation (Aki and Richards, 1980; Toksoz and Johnston, 1981; Tarantola, 1988; Malinowski et al., 2011; Prieux et al., 2013) with $Q \gg 1$, it is equivalent to

$$v_c(\omega) = v(\omega)\left[1 + \frac{i}{2Q}\right]. \tag{2.67}$$

The complex velocity has a real and imaginary term, related to kinematic effects and energy loss. Recall the complex velocity (Equation 2.59)

$$v_c(v_p, \tau, \omega) = v_k(v_p, \tau, \omega) + i \cdot v_l(v_p, \tau, \omega),$$

and the definition of Q (Equation 2.8)

$$\frac{1}{Q(\omega)} = \frac{\Im[M(\omega)]}{\Re[M(\omega)]},$$

Q is rewritten as

$$\begin{aligned} Q(\omega) &= \frac{\Re[v_c^2]}{\Im[v_c^2]}, && (2.68)\\ &= \frac{v_k^2 - v_l^2}{2v_k v_l}, && (2.69)\\ &= \frac{1}{2}\left(\frac{v_k}{v_l} - \frac{v_l}{v_k}\right). && (2.70) \end{aligned}$$

Reorganize the third term, the ratio of v_k and v_l is

$$\frac{v_k}{v_l} = 2Q + \frac{v_l}{v_k} \;>\; 2Q. \tag{2.71}$$

We can neglect the small value term v_l/v_k due to

$$\frac{v_l}{v_k} < \frac{1}{2Q} \;\ll\; 1. \tag{2.72}$$

leading to the Q defined as (Song et al., 1995; Kamei and Pratt, 2013)

$$Q = \frac{v_k}{2v_l}. \tag{2.73}$$

Finally, we have

$$v_l = \frac{v_k}{2Q}, \tag{2.74}$$

which means that Equation 2.59 is consistent with Equation 2.67. v_k is related to the kinematic effects, controls the phase of waves, and v_l is related to the energy loss.

Chapter 3

Unification of visco-elastic wave equations

Contents

Résumé du chapitre 3

La visco-élasticité est un élément essentiel pour l'imagerie quantitative. Les équations reposent principalement sur un modèle de Q constant. Avec les modèles rhéologiques, Emmerich and Korn (1987) a proposé les "Generalized Maxwell Bodies" (GMB) avec une implémentation dans le domaine temporel. Carcione et al. (1988a) a utilisé les GZB également dans le domaine temps. Moczo and Kristek (2005) a montré que le module complexe visco-élastique était équivalent dans les deux approches. Cependant, du point de vue rhéologique, ce formalisme ne peut pas prendre en compte les équations d'onde visco-élastiques fractionnelles avec un Q constant (Kjartansson, 1979). Mainardi (2010) le premier indiqua que le modèle de Q constant est basé sur un modèle de Scott-Blair. La relation entre la contrainte et la déformation est à mi-chemin entre un ressort et un patin. Ainsi, nous proposons ici un regard différent et plus large sur le lien entre équations d'onde et modèles rhéologiques.

Ce chapitre rassemble des approches existantes dans différents papiers et différents champs d'applications que sont le calcul fractionnel, la rhéologie, la mécanique et la sismologie. Avec cette approche d'unification, des liens plus clairs sont mis en avant.

Abstract

Visco-elasticity is the essential ingredient for quantitative seismic imaging and geological interpretation in a number of contexts, such as in the presence of gas clouds. Decades of developments of numerical simulation of visco-elastic wave equations in seismology are mainly based on constant Q model, leading to numerous different forms of time-domain visco-elastic wave equations. Based on rheological models, Emmerich and Korn (1987) adopted the Generalized Maxwell body (GMB) to implement visco-elastic wave equations in time domain. Carcione et al. (1988a) incorporated the Generalized Zener body (GZB) into the time-domain visco-elastic wave equation. Moczo and Kristek (2005) proved that visco-elastic complex modulus based on GMB and GZB are equivalent. However, from the rheological point of view, this formalism can not incorporate the fractional visco-elastic wave equations based on the constant Q model (Kjartansson, 1979). Mainardi (2010) first mentioned that the constant Q model is based on a fractional Scott-Blair model. The stress-strain relationship of the Scott-Blair model is between a spring and a dashpot. Therefore, we review the various visco-elastic wave equations in the text of seismology. Based on the stress-strain constitutive law of rheological models, we propose a unification way to describe the existed visco-elastic wave equations. The unification formalism indicates that each kind of visco-elastic wave equation is composed by the combination of basic rheological elements, e.g., GMB, GZB.

In this chapter, we gather knowledge usually available in separated papers in the fields of fractional calculus, rheology, mechanics, and seismology. By unification formalism, we can establish more clearly links between different approaches used in seismology.

3.1 Introduction

Linear visco-elasticity means that the stress is represented by a time relaxation function convoluted with strain. There are mainly 3 ways to describe the visco-elasticity. First, from the rheological point of view, the stress-strain relationship for a linear viscoelastic system can be represented by a spring-dashpot mechanical model (Figure 3.0a, b). Different combinations of springs and dashpots compose the family of visco-elasticity models. The general form of constitutive relation is expressed by an ordinary differential equation (Fung, 1965)

$$\sum_{n=0}^{N} a_n \frac{d^n \sigma(t)}{dt^n} = \sum_{m=0}^{M} b_m \frac{d^m \epsilon(t)}{dt^m}, \tag{3.1}$$

where n and m are integer coefficients. Taking different orders of derivative and coefficients of a_n and b_m can obtain the constitutive relation between stress and strain,

which represent different rheological models, such as: Maxwell body (MB), Kelvin body (KB), Zener body (ZB), Burgers body, Generalized Maxwell body (GMB) or Generalized Zener Body (GZB) (Figure 3.0d, e, f, g, h, i).

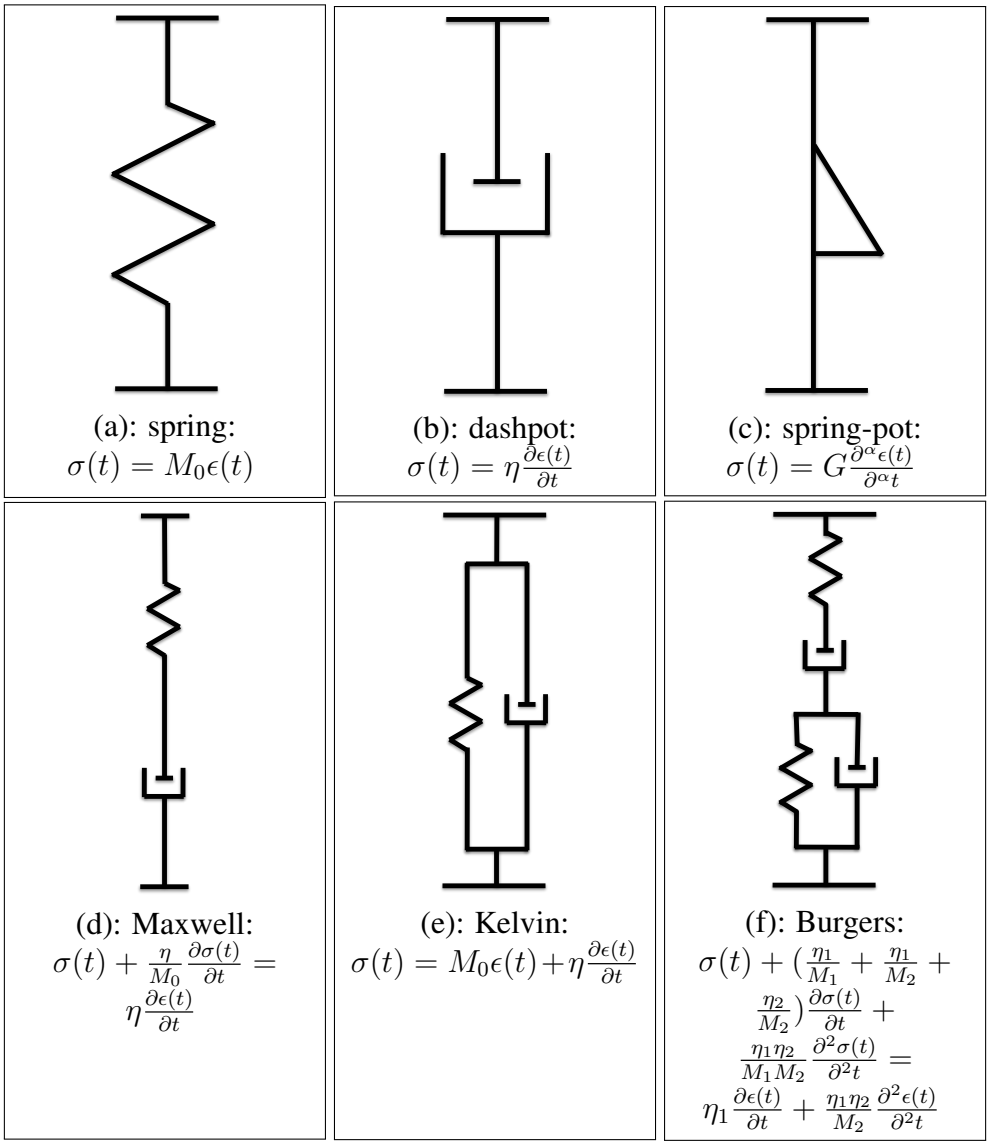

(a): spring: $\sigma(t) = M_0\epsilon(t)$

(b): dashpot: $\sigma(t) = \eta\frac{\partial\epsilon(t)}{\partial t}$

(c): spring-pot: $\sigma(t) = G\frac{\partial^\alpha\epsilon(t)}{\partial^\alpha t}$

(d): Maxwell: $\sigma(t) + \frac{\eta}{M_0}\frac{\partial\sigma(t)}{\partial t} = \eta\frac{\partial\epsilon(t)}{\partial t}$

(e): Kelvin: $\sigma(t) = M_0\epsilon(t) + \eta\frac{\partial\epsilon(t)}{\partial t}$

(f): Burgers: $\sigma(t) + (\frac{\eta_1}{M_1} + \frac{\eta_1}{M_2} + \frac{\eta_2}{M_2})\frac{\partial\sigma(t)}{\partial t} + \frac{\eta_1\eta_2}{M_1M_2}\frac{\partial^2\sigma(t)}{\partial^2 t} = \eta_1\frac{\partial\epsilon(t)}{\partial t} + \frac{\eta_1\eta_2}{M_2}\frac{\partial^2\epsilon(t)}{\partial^2 t}$

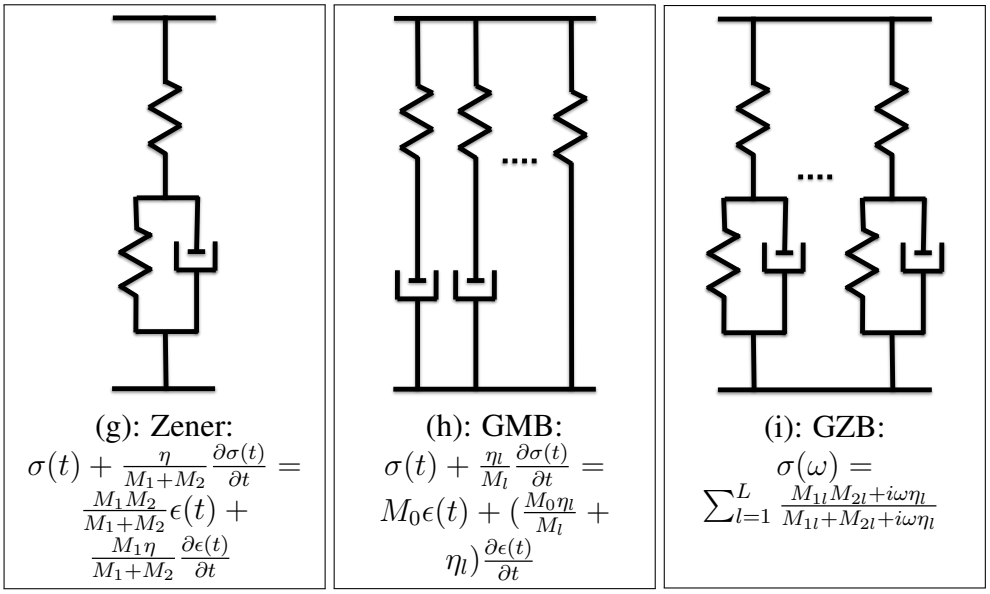

(g): Zener: $\sigma(t) + \frac{\eta}{M_1+M_2}\frac{\partial\sigma(t)}{\partial t} = \frac{M_1M_2}{M_1+M_2}\epsilon(t) + \frac{M_1\eta}{M_1+M_2}\frac{\partial\epsilon(t)}{\partial t}$

(h): GMB: $\sigma(t) + \frac{\eta_l}{M_l}\frac{\partial\sigma(t)}{\partial t} = M_0\epsilon(t) + (\frac{M_0\eta_l}{M_l} + \eta_l)\frac{\partial\epsilon(t)}{\partial t}$

(i): GZB: $\sigma(\omega) = \sum_{l=1}^{L}\frac{M_{1l}M_{2l}+i\omega\eta_l}{M_{1l}+M_{2l}+i\omega\eta_l}$

Figure 3.0: Elastic / rheological models and constitutive relations in the time domain, except GZB in the frequency domain due to the complexity in the time domain, M_l is the elastic modulus of spring, η_l is the viscosity coefficient and G is the coefficient of spring-pot.

However, there is another kind of equation describing the relation between stress and strain. The idea behind is that the material properties are determined by various states between an elastic solid and a viscous fluid characterized as spring-pot (Figure: 3.0c), rather than a combination of an elastic and a viscous element represented by previous ordinary differential formula (Gemant, 1938; Blair et al., 1947). It can be represented by a fractional-order differential form (Park, 2001)

$$\sum_{n=0}^{N} a_n \frac{d^{p_n}\sigma(t)}{dt^{p_n}} = \sum_{m=0}^{M} b_m \frac{d^{q_m}\epsilon(t)}{dt^{q_m}}, \qquad 0 \leq p_n, q_m \leq 1 \tag{3.2}$$

where p_n and q_m are fractional derivative. In analogy with ordinary differential models, Mainardi (2010) and Mainardi and Spada (2011) displayed the fractional rheological models by replacing integer differential coefficients with fractional ones, e.g., fractional Maxwell model and fractional Zener body. Fractional differential models are widely applied in fields of materials and microstructure.

Finally, another widely used theory to explain the visco-elasticity behaviors is called power law based on phenomenological models. The relaxation or creep time function has the shape of power function, which can well fit the observations of relaxation or creep behaviors of visco-elastic media (Nutting, 1921). The classic stress relaxation function gives as

$$\psi(t) = M_0 t^{-\alpha}, \qquad 0 \leq \alpha \leq 1, \tag{3.3}$$

where, $\psi(t)$ is the stress relaxation function, M_0 is the elastic modulus, and α is the power of the function. The stress is the time convolution between the relaxation function with the time derivative of strain in the time domain (Equations 2.2, 2.5), leading to

$$\sigma(t) = M_0\Gamma(1-\alpha)\frac{d^\alpha \epsilon(t)}{dt^\alpha}, \tag{3.4}$$

where $\Gamma(1-\alpha)$ is the gamma function, α is the time differential coefficient. The first introduction in seismology of constant Q model by Kjartansson (1979) is based on the phenomenological power law. The power law with fractional coefficient actually belongs to fractional derivative models (Bagley, 1989; Park, 2001), which is also applied for the visco-elastic simulation and inversion in seismology (Hanyga and Seredynska, 2003; Ribodetti and Hanyga, 2004).

After analyzing the three formulas, we can write Equations 3.1, 3.2 and 3.4 as a general form

$$\sum_{n=0}^{N} a_n^l \frac{d^{p_n}\sigma(t)}{dt^{p_n}} = \sum_{m=0}^{M} b_m^l \frac{d^{q_m}\epsilon(t)}{dt^{q_m}}, \qquad 1 \le l \le L \tag{3.5}$$

where l is associated to a rheological model among total number L, $p_n = n$ and $q_m = m$ correspond to ordinary order representing, e.g., GZB, $0 \le p_n, q_m \le 1$ corresponds to fractional order representing fractional derivative models, and models with $N = 0, M = 0$ can be explained by the classic power law.

To clarify the relations of different theories and the connections between different visco-elastic wave equations, we review different rheological models and applications in seismology. Most commonly used vicso-elastic wave equations obtained by the combinations of springs and dashpots, e.g. GZB and GMB models, are based on nearly constant Q model. Kjartansson (1979) constant Q model and associated visco-elastic wave equation are based on power law. Other applications in seismology are based on power law (Hanyga and Seredynska, 2003; Ribodetti and Hanyga, 2004; Wang, 2016). The power law belongs to the family of fractional derivative models.

Two prominent papers should be mentioned. The first one is written by Carcione (2011), who gave different mechanical visco-elastic models and relevant wave equations. Those mechanical models can be obtained from ordinary differential equation (Equation 3.1). The second is written by Mainardi (2010), who mentioned that Kjartansson (1979) constant Q is a specific example of fractional differential models called Scott-Blair model. Those different visco-elastic wave equations and their rheological models need a unification formalism to be represented in exploration seismology. Thus we combine the three equations (Equation 3.1, 3.2 3.4) into a unification formula (Equation 3.5). This unification formula is a easy way to identify each specific form of visco-elastic wave equations and the related rheological models (Table 3.1). Furthermore, it is a way to obtain other visco-elastic wave equation to describe more complicated attenuation behaviors, which is not limited to seismology. We begin from the unified stress-

Table 3.1: A review of visco-elasticity, $\Downarrow$ &$\Leftarrow$ lead to the contents in the arrow direction.

In seismology	Viscoelasticiy		
Existing equations	ZB, MB, GZB, GMB ... (Nearly constant Q) Emmerich and Korn (1987) Carcione et al. (1988a) $\Downarrow$	Constant Q Kjartansson (1979) $\Downarrow$	$\Leftarrow$ Power law Bagley (1989) $\Downarrow$
Differential equation	Ordinary order Moczo and Kristek (2005) Carcione (2011) $\Downarrow$	Fractional order Mainardi (2010) $\Downarrow$	
Stress-strain relationship	Unification formalism (**Here**) $\Downarrow$		
Specific example	One spring with L pairs of M = N = 1, $p_0 = 0$, $q_0 = 0$ and $p_1 = 1$, $q_1 = 1$	M = N = 0, $p_0 = 0$, $q_0 = \alpha$ and $L = 1$	Others, e.g., fractional Zener M = N = 1, $p_0 = 0$, $q_0 = 0$ and $p_1 = \alpha$, $q_1 = \beta$ $L = 1$ Mainardi (2010)
Q model	Nearly constant Q	Constant Q	Others
Rheological elements	Spring, dashpot	Spring-pot (Scott-Blair model)	Combinations of Spring, dashpot and spring-pot

strain relationship to obtain the general visco-elastic wave equation, and give specific examples with their associated rheological models and visco-ealstic wave equations.

3.2 Complex modulus and visco-elastic wave equations

For L pairs of rheological models in parallel, the stress and strain relation in frequency domain is given by

$$\sum_{n=0}^{N} a_n^l (i\omega)^{p_n} \sigma(\omega) = \sum_{m=0}^{M} b_m^l \, (i\omega)^{q_m} \epsilon(\omega), \qquad 1 \le l \le L. \tag{3.6}$$

Then the complex modulus (Bland, 1960; White, 1965) reads

$$M(\omega) = \sum_{l=1}^{L} \frac{\sum_{m=0}^{M} b_m^l \, (i\omega)^{q_m}}{\sum_{n=0}^{N} a_n^l (i\omega)^{p_n}}. \tag{3.7}$$

The imaginary part corresponds to energy loss. The Q factor (Boit, 1954; Knopoff, 1956; Fung, 1965; O'Connell and Budiansky, 1978; Ben-Menahem and Singh, 1981) is defined as

$$\frac{1}{Q} = \frac{\Im[M(\omega)]}{\Re[M(\omega)]}. \tag{3.8}$$

From the constant Q or nearly constant Q model based on the observations of seismic waves and rock experiments (McDonal et al., 1958), one first needs to have the proper number for M, N, p_n and q_m to dertermine the basic rheological element. Then the objective is to determine the a_n and b_m corresponding to elastic modulus and viscosity coefficients and L to obtain constant Q within the frequency range (Liu et al., 1976). With the constant Q optimization, then the general form of visco-ealstic wave equation is obtained with the complex modulus in the frequency domain. The general form of visco-acoustic wave equation with constant density is

$$(i\omega)^2 p - \frac{1}{\rho} M(\omega) \nabla^2 p = 0, \tag{3.9}$$

where p is the pressure and ρ is the density. The complex modulus $M(\omega)$ leads to visco-elastic effects including dispersion and dissipation. Different forms of $M(\omega)$ are obtained from different ways, e.g., phenomenological observation of relaxation or creep function, leading to the existed various forms of visco-elastic wave equations. From a rheological point of view, $M(\omega)$ can be derived from various rheological models. Thus we will derive visco-acoustic wave equations from the unification formalism including nearly constant Q based on GMB and Kjartansson (1979) constant Q. Compared with the visco-acoustic wave equation, visco-elastic wave equation only requires to introduce Q_p for P wave and Q_s for S wave separately. Both Q_p and Q_s are determined by the same way. Thus we only illustrate the visco-acoustic wave equations from the unification formalism based on different rheological models, instead of visco-elastic wave equations.

3.3 Example I: Nearly constant Q and associated wave equations

Nearly constant Q model is approximated by several rheological models like GZB and GMB. Emmerich and Korn (1987) first introduced the GMB rheological model to obtain nearly constant Q. Carcione et al. (1988a,b) incorporated the GZB into the time-domain visco-elastic wave equation. Moczo and Kristek (2005) proved the equivalence between GZB and GMB and put forward a material-independent formula. However, this material-independent formula is still based on the ordinary differential constitutive relation (Equation 3.1). We choose the integer values to obtain nearly constant Q from equation (Equation 3.5) and visco-acoustic wave equations.

The GMB is composed by a spring and L pairs of Maxwell body in parallel. A spring is represented as $M = N = 0$, $p_0 = 0$, $q_0 = 0$: the constitutive relation is

$$\sigma(\omega) = M_0 \epsilon(\omega). \tag{3.10}$$

A Maxwell body is represented by $M = N = 1$, $p_0 = 0$, $q_0 = 0$ and $p_1 = 1$, $q_1 = 1$: the constitutive relation leads to

$$\sigma(t) + \frac{\eta_l}{M_l}\sigma^{(1)}(t) = M_l \frac{\eta_l}{M_l}\epsilon^{(1)}(t). \tag{3.11}$$

In frequency domain is expressed as

$$\sigma(\omega) + \frac{i\omega}{\omega_l}\sigma(\omega) = M_l \frac{i\omega}{\omega_l}\epsilon(\omega). \tag{3.12}$$

ω_l is equal to $1/t_l$, in which t_l is referred to the relaxation time from the stress relaxation function of Maxwell body $\psi(t) = M_l \exp(-t/t_l)H(t)$. t_l is defined as η_l/M_l. Complex modulus for l Maxwell body is

$$M^l(\omega) = \frac{M_l i\omega}{\omega_l + i\omega}. \tag{3.13}$$

Therefore the total complex modulus of GMB is

$$\begin{aligned} M(\omega) &= M_0 + \sum_{l=1}^{L} \frac{M_l i\omega}{\omega_l + i\omega}, \\ &= M_0 + \delta M \sum_{l=1}^{L} \frac{\alpha_l i\omega}{\omega_l + i\omega}, \end{aligned} \tag{3.14}$$

with $\alpha_l \delta M = M_l$. M_l is the elastic modulus of each Maxwell body and M_0 is the elastic modulus of the spring. Based on rheological models, one needs to optimize a_n and b_m corresponding to elastic modulus and viscosity coefficients and L to obtain constant Q within the frequency range (Equation 3.7, 3.8). Here a_n and b_m have been parameterized as ω_l and α_l. ω_l is usually determined logarithmically over the frequency range (Blanch et al., 1995). Different α_l optimizes different Q values.

The wave-equation reads

$$(i\omega)^2 p - \frac{1}{\rho}(M_0 + \delta M \sum_{l=1}^{L} \frac{\alpha_l i\omega}{\omega_l + i\omega})\nabla^2 p = 0 \tag{3.15}$$

Therefore the form in time domain is

$$\frac{\partial p}{\partial t} + \frac{1}{\rho}(M_0 + \delta M \sum_{l=1}^{L} \alpha_l)(\nabla \cdot \boldsymbol{v}) + \sum_{l=1}^{L} r_p^l = f(x_s, t),$$

$$\begin{aligned} \frac{\partial \boldsymbol{v}}{\partial t} + \frac{1}{\rho}\nabla p &= 0, \\ \frac{\partial r_p^l}{\partial t} + \omega_l (r_p^l + \delta M \alpha_l \nabla \cdot \boldsymbol{v}) &= 0, \qquad l =\in [1, L]. \end{aligned} \tag{3.16}$$

$\boldsymbol{v}$ is the particle velocity vector. r_p^l is the memory variables.

From the general formula of stress-strain relationship, we get the visco-acoustic wave-equation based on GMB rheological model. The visco-equation can be obtained by GZB rheological model. Next section, we introduce the Kjartansson (1979) constant Q visco-acoustic wave equation the under frame of the unification formalism.

3.4 Example II: Kjartansson constant Q and associated wave equations

Kjartansson (1979) gives a relaxation function and complex modulus defined as

$$M(\omega) = M_0 (\frac{i\omega}{\omega_0})^{2\gamma}, \quad 0 < 2\gamma < 1 \tag{3.17}$$

where ω_0 is the reference frequency. The complex modulus is derived from a power creep function. Mainardi (2010) pointed out this form can be obtained from the rheological model called Scott-Blair model. In fact, the Scott-Blair model called by Mainardi (2010) is a spring-pot model (Figure 3.0). The stress of a spring-pot is linear, with the fractional derivative of strain. Taking $M = N = 0$, $p_0 = 0$, $q_0 = \alpha$ and $L = 1$ in Equation 3.5, the constitutive relation turns into

$$\sigma(t) = M_0 (\frac{\eta_0}{M_0})^{\alpha} \epsilon^{(\alpha)}(t) \tag{3.18}$$

by choosing the b_0/a_0 as $M_0(\eta_0/M_0)^{\alpha}$. M_0 stands for the elastic modulus, η is the viscous coefficient of a dashpot. Defining $t_0 = 1/\omega_0$ as η_0/M_0, t_0 is referred as the relaxation time. The stress-strain relation in the frequency domain is

$$\sigma(\omega) = M_0 (\frac{1}{\omega_0})^{\alpha} (i\omega)^{\alpha} \epsilon(\omega). \tag{3.19}$$

Thus the complex modulus is defined as

$$M(\omega) = M_0 (\frac{i\omega}{\omega_0})^{\alpha} = M_0 (\frac{i\omega}{\omega_0})^{2\gamma}, \tag{3.20}$$

with $\alpha = 2\gamma$, we have the complex modulus equivalent to Equation 3.17 which is obtained through the power law. The parameter α depends the Q value. The wave equation is derived by introducing the complex modulus as

$$(i\omega)^2 p - \frac{1}{\rho} M_0 (\frac{i\omega}{\omega_0})^{2\gamma} \nabla^2 p = 0. \tag{3.21}$$

Combing the $(i\omega)^{2\gamma}$ with $(i\omega)^2$ and transferring into time domain, the visco-acoustic wave equation reads

$$\frac{\partial^{2-2\gamma} p}{\partial t^{2-2\gamma}} - \frac{M_0}{\rho}\omega_0^{-2\gamma}\nabla^2 p = 0. \tag{3.22}$$

This function is consistent with the result of Carcione et al. (2002). This form of visco-acoustic wave equation is obtained with a spring-pot rheological model. The constant Q visco-acoustic wave equation in time domain involves with time-domain fractional derivatives. It is hard to be solved by finite difference method. Thus the commonly applied visco-acoustic wave equation is based on GMB / GZB rheological models by introducing memory variables instead of solving fractional time derivative (Emmerich and Korn, 1987; Carcione et al., 1988a).

3.5 Conclusions

The general constitutive relation of stress and strain combines ordinary differential system, fractional order differential system and power law together. From the constitutive relation, the unification formalism is a way to describe and summarize visco-elastic wave equations in seismology. Depending on the different strategies of optimizing constant Q, the rheological models of visco-elastic wave equations contain different combinations of basic rheological elements with springs, dashpots and spring-pots. The widely applied visco-elastic wave equations in seismology can be characterized as different specific cases. Furthermore, it is a way to obtain other kinds of visco-elastic wave equations, e.g. based on fractional Zener model. Those visco-elastic wave equations can be summarized under the unification formalism.

Chapter 4

Visco-acoustic Full Waveform Inversion strategies

Contents

(Adapted from the article submitted to *Geophysical Journal International*.)

Résumé du chapitre 4

L'inversion des formes d'ondes (FWI) est une méthode avancée et potentiellement plus puissante que les approches qui utilisent des rais. FWI exploite le champ d'onde complet pour estimer la vitesse et l'atténuation. Cependant, il est difficile de retrouver indépendamment les deux paramètres. Beaucoup de pistes ont été proposées, en particulier l'inversion séquentielle, l'inversion conjointe et l'inversion hiérarchique. À cause de la dispersion, plusieurs combinaisons de paramètres conduisent à la même vitesse cinématique. Nous proposons une inversion hybride. Dans un premier temps, l'inversion classique est appliquée pour un facteur de qualité fixe. Ensuite, une version modifiée de la FWI est menée. Dans ce cas, la vitesse cinématique est maintenue fixe. Ceci conduit à un gradient différent. Si la vitesse cinématique doit être remise à jour, plusieurs cycles sont répétés. La FWI hybride est plus rapide que les stratégies conventionnelles. Les validations sont réalisées sur exemples synthétiques (exemple gaussien et du Moyen-Orient) avec chacun ses caractéristiques. L'inversion hybride mitige les interférences entre vitesse et atténuation.

Abstract

Seismic attenuation is a very useful property to detect fluid and gas clouds combined with the conventional velocity-based seismic imaging in exploration geophysics. To obtain attenuation and velocity models, visco-acoustic full waveform inversion (FWI) is an advanced and accurate method compared to traditional ray-based methods. Visco-acoustic FWI has more realistic rheology characterizing the Earth media and exploits all the wave information to retrieve attenuation and velocity. However, attenuation and velocity inversion suffers cross-talks between parameters and different parameter sensitivities. Many researches focus on different inversion strategies to mitigate cross-talks. Those strategies mainly include sequential inversion, simultaneous inversion and hierarchical inversion. Because of dispersion, different combinations of attenuation and velocity may have the same kinematic information for band-limited data, called kinematic relationship. The real travel speed of visco-acoustic waves is called kinematic velocity. We propose a hybrid strategy to explicitly use the kinematic relationship during full waveform inversion to retrieve the parameters. In a first step, a classical visco-acoustic inversion is applied for a fixed quality factor to obtain kinematic velocity. Then a subsequent FWI with a modified gradient of the objective function is put forward by introducing the relation between attenuation and velocity based on the kinematic velocity. In case of inaccurate kinematic velocity derived in the first step, we perform alternate steps between the determination of kinematic model and visco-acoustic models. The hybrid FWI leads to a faster convergence compared to the conventional inversion strategies. This is first validated on simple 2D synthetic data sets mainly dominated by transmitted waves. Finally, the hybrid strategy is applied to a synthetic Middle-East model with surface acquisition geometry; the inversion has a fast convergence and lower final misfit. The retrieved attenuation has closer exact average values compared with conventional inversion strategies. Both simple and complex models validate that the hybrid inversion strategy can mitigate cross-talks between two parameters and retrieve attenuation and velocity more effectively.

4.1 Introduction

Conventional seismic inversion relies on an acoustic Earth model only depending on velocity. As the demands of high-resolution inversion, more accurate rheology models have been taken into consideration, such as elasticity, anisotropy, and attenuation. For fluid and gas clouds detection, attenuation is more sensitive than velocity of pure acoustic assumption (Toksoz and Johnston, 1981; Best et al., 1994; Wang, 2008). The property of attenuation is very useful to compensate for energy loss and subsequently to obtain accurate seismic images, such as removing seismic image blurring beneath the gas clouds (Zhou et al., 2011). Seismic attenuation is divided into two categories, one is

the scattering attenuation (Marion and Coudin, 1992) and the other one is the intrinsic attenuation (Aki and Richards, 1980; Klimentos and MaCann, 1990; Thomsen et al., 1997). The scattering attenuation can happen in any kind of media with multi scatters. The intrinsic attenuation is related to the property of media. Waves transfers the energy to heat due to the internal friction. The seismic attenuation usually refers to intrinsic attenuation, which can be represented by quality factor Q (Knopoff, 1956). The reciprocal of Q stands for the wave energy loss per traveling cycle.

Traditional methods for estimating Q include ray-based methods, based on the spectral amplitude loss or spectrum distortion due to attenuation. Spectral amplitude loss method (Brzostowski and McMechan, 1992; Leggett et al., 1992; Cavalca and Fletcher, 2009; Cavalca et al., 2011) retrieves the velocity and Q model using traveltime tomography. Q is estimated by integrating the amplitude loss along the ray path (Futterman, 1962; Aki and Richards, 1980; Bregman et al., 1989; Tonn, 1991). However, amplitude of seismic waves is easily contaminated by many factors such as scattering, geometric spreading, source and receiver coupling, radiation patterns, and transmission/reflection effects. It is hard to eliminate those effects. To overcome this problem, spectrum distortion methods include pulse broadening method (Zucca et al., 1994) and centroid frequency shift method (Quan and Harris, 1997; Plessix, 2006a). Those methods compare the spectrum difference between incident and recorded data to estimate the Q model. This kind of methods is based on the assumption that the spectrum of incident waves is known, and the observed spectrum also has the similar shape.

Beyond the traditional methods using ray information, full waveform inversion (FWI) (Lailly, 1983; Tarantola, 1984a) is a powerful method to retrieve physical models of subsurface, including velocity, density, attenuation and anisotropy. FWI is effectively applied to non-linear multi-parameter inversion by exploiting full wave information (Virieux and Operto, 2009). Tarantola (1988) first derived the full waveform inversion algorithm to retrieve the elastic and attenuation parameters. Visco-elastic or visco-acoustic FWI can be implemented in frequency domain (Song et al., 1995; Causse and Mittet, 1996; Liao and McMechan, 1996; Causse et al., 1999; Hicks and Pratt, 2001; Pratt et al., 2005; Kamei and Pratt, 2008; Malinowski et al., 2011; Kamei and Pratt, 2013; Prieux et al., 2013; Operto et al., 2014, 2015; Gao and Wang, 2016; Operto and Miniussi, 2018) and time domain (Liao and McMechan, 1995; Charara et al., 1996, 2000; Barnes et al., 2004; Charara et al., 2004; Barnes and Charara, 2009, 2010; Bai et al., 2012; Kurzmann et al., 2013; Bai et al., 2014; Barnes et al., 2014; Kurzmann et al., 2015; Belahi et al., 2015; Cheng et al., 2015; Li et al., 2015; Plessix et al., 2016; Fabien-Quellet et al., 2017; Jiang and Chauris, 2018; Wang et al., 2018; Yang et al., 2018). Frequency-domain FWI is implemented by incorporating a complex modulus or complex velocity into elastic wave equation. Time-domain FWI needs to introduce extra memory variables instead of solving the time convolution. For large-scale 3D inversion, the preferred choice is applied in the time-domain (Plessix et al., 2016; Yang et al., 2018). For computational reasons, the applications rely on the visco-acoustic

assumption and not on the visco-elasticity (Plessix et al., 2016; Wang et al., 2018).

Visco-acoustic FWI with two parameters still encounters many difficulties. First, due to attenuation, energy of waves in visco-elastic media is weaker than pure elastic waves. With a simple but fairly correct Q model, mono-parameter velocity FWI regards Q as a passive parameter. Dissipation happens twice during source propagation and back-propagation of adjoint source. The weak energy leads to the difficulty of retrieving velocity. Kurzmann et al. (2013) applied a smooth Q as a passive parameter to retrieve v_p using visco-acoustic FWI. The shallow part is well retrieved, however resolution of the deep part decreases as the attenuation increases with traveling distance of wave.

Second, the limited observation leads to the problem of non-uniqueness (Barnes et al., 2014; Kurzmann et al., 2015). Different solutions can represent the data well. As the two parameters v_p and Q are characterized as a complex velocity in the frequency domain, v_p and Q have the same radiation patterns (Plessix et al., 2016; Yang et al., 2018). The gradients of the objective function with respect to v_p and Q are hard to distinguish, especially with limited acquisition (Fabien-Quellet et al., 2017; Yang et al., 2018). It leads to the low resolution of parameters, which can be explained as cross-talks (Kamei and Pratt, 2013).

Third, parameter gradients have different sensitivities Malinowski et al. (2011). Different inversion strategies have to be considered, which include sequential inversion, simultaneous inversion and hierarchical inversion. *Sequential inversion* consists of first determining the velocity parameter for a fixed Q factor, and in a second phase of inverting the Q parameter as the velocity model is better reconstructed. Fabien-Quellet et al. (2017) suggested this inversion strategy for a cross-hole model to decrease the footprints of simultaneous inversion. However, this sequential approach may lead to data over-fitting (Kurzmann et al., 2013; Plessix et al., 2016). To avoid this, *simultaneous inversion* updates v_p and Q at the same time with gradient optimizations. The gradients of v_p and Q have different magnitudes without the introduction of the Hessian matrix (second-order derivative of the objective function). However, the inverse of Hessian to normalize the gradients of different parameters is hard due to the ill-posed Hessian (Prieux et al., 2013). Therefore, proper magnitude of damping factors have to be added to the Hessian matrix to scale the parameter gradients and reconstruct the models. The *hierarchical inversion* (Prieux et al., 2013) combines a mono-parameter velocity inversion with simultaneous inversion to focus on the dominant information v_p. A good estimation of v_p contributes to the prior information for latter simultaneous inversion (Fabien-Quellet et al., 2017).

Besides those, prior information, smoothing operator and regularization have to be considered (Kamei and Pratt, 2013; Prieux et al., 2013; Yang et al., 2018). Pratt et al. (2005) and Kamei and Pratt (2013) suggested a stronger Q smoothing factor than velocity smoothing factor to retrieve a better results in a highly heterogeneous attenuated media. A strong soothing can effectively overcome the oscillatory artefacts on the attenuation model. Regularization is applied to handle the ill-posed problem, but the

choice of damping factor is still challenging (Kamei and Pratt, 2013; Prieux et al., 2013; Fabien-Quellet et al., 2017).

Despite recent progresses, visco-acoustic FWI still needs to find a way to decouple the two parameters. The previous inversion strategies have more flexible degrees of freedom to update each parameter. On the one side, the inversion could reach to a global minimum with the correct updating direction. On the other side, the inversion may be stuck into a local minimum due to cross-talks between parameters. We propose to introduce a constrained relation to guide the inversion.

The dispersion of visco-acoustic waves leads to phase velocity modifications. Because of the band-limited aspect of seismic waves, different combinations of velocity and Q parameters can have the same equivalent kinematic velocity. v_p is the dominant information compared with Q, FWI preferentially retrieves the velocity information due to the impacts on kinematics (Kamei and Pratt, 2013; Prieux et al., 2013; Fabien-Quellet et al., 2017). The mono-parameter velocity inversion for visco-acoustic data tends to update the kinematic velocity. In this work, we propose a hybrid FWI algorithm to take into account the kinematic information to retrieve the two parameters. The objective is to handle cross-talks between velocity and attenuation, without relying on the information of the Hessian matrix. The paper is organized as follows: we first indicate how we model attenuation, then we present the modified FWI approach. It mainly leads to a modified gradient of the objective function. We compare the behaviors of the classical and new hybrid strategies on 2D inversions on simple synthetic data sets, and draw some first conclusions on the recommended strategy for inverting velocity and attenuation. Finally, we apply the modified algorithm to a more complex 2D synthetic Middle-East model.

4.2 Visco-acoustic FWI

Attenuation effects lead to phase velocity dispersion (Futterman, 1962; Aki and Richards, 1980). It means that different combinations of velocity and attenuation result in the same kinematic velocity v_k for band-limited seismic data. The v_k model controls the kinematic of wave propagation. The v_k model, precisely defined in the next section, is different from the P-velocity model v_p because of attenuation. Based on v_k, we put forward a hybrid inversion strategy for visco-acoustic FWI.

4.2.1 Visco-acoustic wave equation and kinematic velocity

The time-domain visco-acoustic wave-equation based on nearly constant Q theory (Liu et al., 1976; Emmerich and Korn, 1987; Carcione et al., 1988a,b; Robertsson et al., 1994; Blanch et al., 1995) involves a time convolution in the stress-strain relation. The constant Q theory can be obtained by L pairs of Standard Linear Solid (SLS) within

desired frequency range, which is given as

$$\frac{1}{Q(\omega)} = \frac{\Im[M(\omega)]}{\Re[M(\omega)]} = \frac{\sum_{l=1}^{L} \frac{\omega(\tau_{\epsilon l} - \tau_{\sigma l})}{1+\omega^2\tau_{\sigma l}^2}}{\sum_{l=1}^{L} \frac{1+\omega^2\tau_{\epsilon l}\tau_{\sigma l}}{1+\omega^2\tau_{\sigma l}^2}}. \tag{4.1}$$

The reciprocal of quality factor Q is defined as the ratio of imaginary and real part of complex modulus $M(\omega)$. $\tau_{\sigma l}$ and $\tau_{\epsilon l}$ are the stress and strain relaxation times for the lth SLS within total number L. To obtain constant Q within a frequency range, $\tau_{\sigma l}$ are given in advance and distributed logarithmically over the frequency range of interest, which yields good approximations to a constant Q with $\tau_{\sigma l}$= 1 /ω_l. $\tau_{\epsilon l}$ in total number L are optimized to have constant Q. To simplify the implementation, the τ method (Blanch et al., 1995) is applied to reduce the L parameters into one parameter $\tau = \tau_{\epsilon l}/\tau_{\sigma l} - 1$. With the single τ parameter, the visco-acoustic wave-equation reads

$$\frac{\partial p}{\partial t} + \kappa(L\tau + 1)(\nabla \cdot \boldsymbol{v}) + \sum_{l=1}^{L} r_p^l = f(x_s, t), \tag{4.2}$$

$$\frac{\partial \boldsymbol{v}}{\partial t} + \frac{1}{\rho}\nabla p = 0, \tag{4.3}$$

$$\frac{\partial r_p^l}{\partial t} + \frac{1}{\tau_\sigma^l}(r_p^l + \tau\kappa(\nabla \cdot \boldsymbol{v})) = 0, \qquad l =\in [1, L] \tag{4.4}$$

where $\boldsymbol{v}$ is the velocity vector, p is acoustic pressure field, and $\kappa = \rho v_p^2$ is the relaxed modulus. The wavefields depend on the source position $\boldsymbol{s}$, the space coordinate $\boldsymbol{x}$ and the time t, written as $p(\boldsymbol{s}, \boldsymbol{x}, t)$ and $\boldsymbol{v}(\boldsymbol{s}, \boldsymbol{x}, t)$. Model parameters are related to model space $\boldsymbol{x}$, wring as $v_p(\boldsymbol{x})$ and $\tau(\boldsymbol{x})$. To analyse the visco-acoustic kinematic velocity in details, we rewrite the constant density wave equation in the frequency domain as a second-order differential equation

$$(i\omega)^2 p - v_c^2 \Delta p = F(x_s, \omega), \tag{4.5}$$

with a complex velocity

$$v_c^2 = v_p^2 \left[(L\tau + 1) - \sum_{l=1}^{L} \frac{\tau}{1 + i\omega\tau_\sigma^l} \right]. \tag{4.6}$$

The complex velocity can be split into a real term and an imaginary part

$$v_c = v_k(v_p, \tau, \omega) + i v_l(v_p, \tau, \omega), \tag{4.7}$$

where v_k and v_l are the real and imaginary parts of the complex velocity, associated to the kinematic part and the energy loss, respectively. We call v_k the equivalent *kinematic*

velocity. It stands for real travel speed of visco-acoustic waves. v_k is the function of v_p, τ and frequency ω. We call it the *kinematic relationship*, written as

$$v_k = f(v_p, \tau, \omega) = v_p \sqrt{\frac{\sqrt{\left[L\tau + 1 - \sum_{l=1}^{L} \frac{\tau}{1+\omega^2\tau_{\sigma l}^2}\right]^2 + \left[\sum_{l=1}^{L} \frac{\tau\omega\tau_{\sigma l}}{1+\omega^2\tau_{\sigma l}^2}\right]^2} + \left[L\tau + 1 - \sum_{l=1}^{L} \frac{\tau}{1+\omega^2\tau_{\sigma l}^2}\right]}{2}}. \tag{4.8}$$

For a given frequency, different combinations of v_p and τ can have same v_k. For example, v_k is 2250 m/s at 20 Hz. Combinations of v_p and τ for a given v_k are linked according to the curve in Figure 4.1. It indicates that, waves with different v_p and τ have the same traveling time but different amplitude. For a given same kinematic velocity, v_p and τ is related.

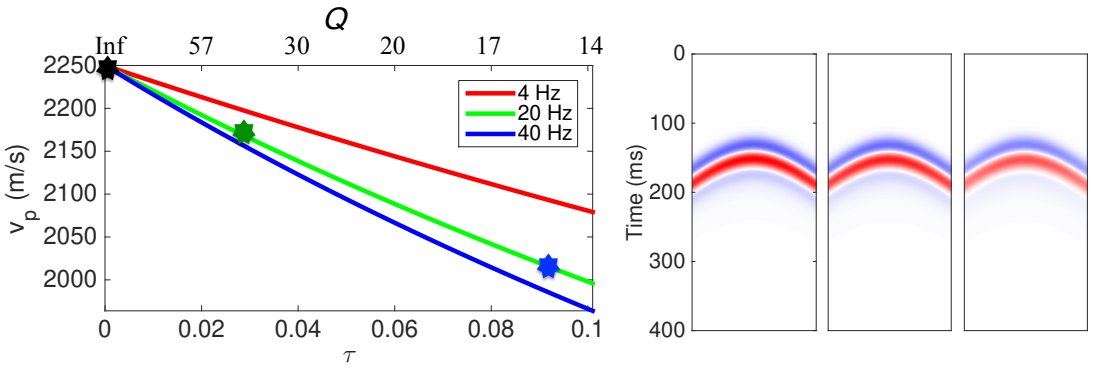

Figure 4.1: Different combinations of v_p and τ, leading to the same v_k = 2250 m/s at reference frequency 4, 20 and 40 Hz (left) and comparison of three shot gathers for different combinations of v_p and τ at 20 Hz (right), the traveltime is same and amplitude becomes weaker as attenuation increases.

4.2.2 FWI Strategies

FWI exploits all the wave information to retrieve the model parameters. The basic principle is matching the waveform to reduce the data misfit between the calculated and observed data (Tarantola, 1984a; Virieux and Operto, 2009). The objective function is given as

$$\mathcal{J}(\boldsymbol{m}) = \frac{1}{2}\|d_{cal}(\boldsymbol{s}, \boldsymbol{r}, t) - d_{obs}(\boldsymbol{s}, \boldsymbol{r}, t)\|^2. \tag{4.9}$$

$d_{cal}(\boldsymbol{s}, \boldsymbol{r}, t)$ is the selected from the whole wavefields at the source $\boldsymbol{s}$ and receiver $\boldsymbol{r}$. $\boldsymbol{m}$ is the model parameter. $\boldsymbol{m}$ is composed of $v_p(\boldsymbol{x})$ and $\tau(\boldsymbol{x})$ for visco-acoustic FWI.

Theoretically, $\boldsymbol{m}$ can be retrieved from a global optimization method through the whole model space, e.g. Monte-Carlo method (Sambridge and Mosegaard, 2002). However, it is almost impossible due to the large model space and computation limitations. The practical solution is to apply FWI based on gradient updating method, e.g. conjugate gradient method (details of FWI is in Appendix 4.6).

Conventional visco-asouctic full waveform inversion suffers from cross-talks between velocity and τ (or Q) parameters. To overcome cross-talks, the inversions strategies (Kamei and Pratt, 2013; Plessix et al., 2016) include: sequential inversion, simultaneous inversion and hierarchical inversion. The key point of the different inversion strategies based on the conjugate gradient method is to compute the gradients of the objective function in equation 4.25. The derivatives of $\mathcal{J}$ with respect to v_p and τ can be obtained with the adjoint state method (details in Appendix 4.7). We review different inversion strategies (Strategies A and B) and introduce the new approach (Strategy C and the hybrid strategy).

4.2.2.1 Strategy A

Visco-acoustic FWI preferentially retrieves the velocity information due to the kinematic effects (Kamei and Pratt, 2013; Prieux et al., 2013; Fabien-Quellet et al., 2017). If τ is a passive parameter, the mono-parameter velocity inversion tends to retrieve the kinematics. The kinematics are the combinations of the retrieved v_p and fixed τ (Equation 4.8). The gradient of the objective function is

$$\frac{\partial \mathcal{J}(v_p,\tau)}{\partial v_p}\Big|_{\tau}, \tag{4.10}$$

where $|_\tau$ means the derivative is obtained for fixed τ. This strategy is called **Strategy A** to retrieve v_p. If τ is zero, Strategy A is a purely acoustic FWI. In this case, the acoustic FWI is also used to examine the Q impacts on the data. For a fixed τ, the iteratively updating of v_p leads to a modified v_k according to Equation 4.8.

4.2.2.2 Strategy B

Simultaneous inversion updates the velocity and attenuation at the same time. It is applied to avoid parameter over-estimating (Plessix et al., 2016). We call this simultaneous inversion as **Strategy B**. The gradients of the objective function are

$$\frac{\partial \mathcal{J}(v_p,\tau)}{\partial v_p}\Big|_{\tau} \tag{4.11}$$

and

$$\frac{\partial \mathcal{J}(v_p,\tau)}{\partial \tau}\Big|_{v_p}, \tag{4.12}$$

where $|_\tau$ and $|_{v_p}$ mean the derivatives are obtained for fixed τ and v_p, respectively. v_p and τ are considered as independent parameters.

4.2.2.3 Strategy C – new approach

Different combinations of v_p and τ, visco-acoustic waves have same the kinematic velocity at a given frequency in equation 4.8. When the kinematic velocity v_k is fixed, v_p and τ are linked by the kinematic relationship. A modified inversion strategy is applied to decouple the v_k as the combinations of updated v_p and τ to match the amplitudes. For fixed v_k, τ is the function of v_p. The gradient of v_p turns into a full differential formula

$$\frac{d\mathcal{J}(v_p,\tau(v_p))}{dv_p}\Big|_{v_k} = \frac{\partial\mathcal{J}(v_p,\tau(v_p))}{\partial v_p}\Big|_{v_k} + \frac{\partial\tau(v_p)}{\partial v_p}\Big|_{v_k}\frac{\partial\mathcal{J}(v_p,\tau(v_p))}{\partial\tau}\Big|_{v_k}, \tag{4.13}$$

where

$$\frac{\partial\tau(v_p)}{\partial v_p}\Big|_{v_k} = -\frac{\partial f(v_p,\tau)}{\partial v_p}\Big/\frac{\partial f(v_p,\tau)}{\partial\tau}\Big|_{v_k}. \tag{4.14}$$

$|_{v_k}$ means the derivative is obtained for fixed v_k. $f(v_p,\tau)$ is the function of kinematic velocity (Equation 4.8). The derivative of $\tau(v_p)$ with respect to v_p for a fixed v_k (Equation 4.14) can be obtained analytically (details in Appendix 4.8). The first step is to update v_p based on Equation 4.13. Then τ is updated form the kinematic relationship (Equation 4.8). This strategy is called Strategy C, which guides the non-linear visco-acoustic FWI. **Strategy C needs a kinematic velocity model. The first step consists of updating the kinematic velocity v_k and then further decouple the v_p and τ parameters.**

4.2.2.4 Hybrid strategy

When the kinematic velocity is not correct enough, v_k can be updated for fixed τ. The objection function is function of v_p. Then the updated v_k can be used for the kinematic velocity for Strategy C. The gradient is

$$\frac{d\mathcal{J}(v_p(v_k))}{dv_k}\Big|_{\tau} = \frac{\partial v_p(v_k)}{\partial v_k}\Big|_{\tau}\frac{\partial\mathcal{J}(v_p(v_k))}{\partial v_p}\Big|_{\tau}, \tag{4.15}$$

where

$$\frac{\partial v_p(v_k)}{\partial v_k}\Big|_{\tau} = 1\Big/\frac{\partial f(v_p,\tau)}{\partial v_p}\Big|_{\tau}. \tag{4.16}$$

$|_\tau$ means the derivative is obtained for fixed τ. The derivative of $v_p(v_k)$ with respect to v_k is explained in Appendix 4.9.

This hybrid strategy includes a first step for retrieving v_k, and a subsequent step of Strategy C to update v_p and τ for a fixed v_k. Actually, the first step is equivalent to the Strategy A (details in Appendix 4.9). In practice, we propose the two-step hybrid strategy: (1) For a fixed τ, we iteratively update v_p (Strategy A). This leads to a modified v_k model according to kinematic relationship (Equation 4.8). (2) In a second-step, we still update v_p, but here for a fixed v_k model. The gradient of the objective function is modified accordingly. During the second phase, τ is the passive parameter, i.e. is automatically updated when v_p is modified (Strategy C).

In this paper we have 2 schemes of the hybrid inversion strategies include A $\rightarrow$ C, and A $\rightarrow$ C $\rightleftharpoons$ A ($\rightarrow$: followed by, $\rightleftharpoons$: alternate scheme). For the simple models, the A $\rightarrow$ C scheme is enough. For the complex models, the scheme of A $\rightarrow$ C $\rightleftharpoons$ A is preferred. The first several iterations of A is to obtain an initial v_p model and v_k model for Strategy C, then alternate C $\rightleftharpoons$ A is applied to retrieve v_p and τ and continuously improve the kinematic velocity. Additionally, without updating the kinematic velocity v_k by Strategy A, the hybrid strategy turns into pure Strategy C. We also test the Strategy C with known v_k for simple models. Among the schemes of the hybrid inversion strategies, Strategy C is the key algorithm to guide the visco-acoustic FWI.

In summary (Table 4.1):

- Strategy A is visco-acoustic inversion, where only v_p is updated, while τ (or Q) remains fixed (Equation 4.10);
- Strategy B is the classical visco-acoustic FWI where v_p and τ (or Q) are simultaneously inverted with conjugate gradient (Equation 4.11 and 4.12);
- Strategy C is the modified viso-acoustic FWI based on fixed v_k, v_p is updated by Equation 4.13, then τ (or Q) is derived from Equation 4.8.
- Hybrid Strategy is composed of Strategies A and C alternately; Strategy A is used for updating v_k, and Strategy C is applied to guide the inversion to retrieve v_p and τ.

4.3 Numerical examples

We apply Strategy C and the hybrid strategy to investigate the feasibilities on different models, and compare with Strategy A and Strategy B (Table 4.2). Those numerical examples are divided into 3 categories. The first category (example 4.3.1 and 4.3.2) is to investigate the advantage of Strategy C based on **known correct kinematic velocity**. This category includes a homogeneous model and a blocky model test. In this test, we investigate the features and advantages of Strategy C. The second category (example 4.3.3) is applied to uncorrelated structure between velocity and attenuation models to

Table 4.1: Comparison of different strategies.

	Inversion sequence	Initial v_p	Initial τ	Additional information
Strategy A	v_p	A given initial v_p^0	A given initial τ^0 (e.g., a homogeneous model) – no updating	no updating of τ and v_k
Strategy B	(v_p,τ) simultaneously	A given initial v_p^0	A given initial τ^0 (e.g., a homogeneous model)	no updating of v_k
Strategy C	$(v_p, \tau(v_p))\big\|_{v_k}$	nth iteration of Strategy A: v_p^n	nth iteration of Strategy A (no updating): $\tau^n = \tau^0$	fixed v_k, $v_k = f(v_p^n, \tau^n)$
Hybrid strategy	A $\rightarrow$ C, or A $\rightarrow$ C $\rightleftharpoons$ A	A given initial v_p^0	A given initial τ^0	v_k is updated by Strategy A, $v_k = f(v_p^A, \tau^A)$

retrieve the parameters. The velocity model is homogeneous, but the attenuation model has a Gaussian anomaly. The last category (example 4.3.4) is applied to 2D synthetic Middle-East model. The objective is to show the feasibility of Strategy C and the hybrid strategy on complex models. The key factors are: (1) how to obtain an accurate kinematic velocity for complex models, and (2) how to guide the inversion based on fixed v_k. Finally, we discuss if the method is a way of decoupling the parameters by explicitly introducing the kinematic relationship.

Table 4.2: Inversion strategies for 4 different models.

Tests	Models	Strategies			
Test1: 4.3.1	Homogeneous	A	B	C	
Test2: 4.3.2	Blocky	A	B	C	
Test3: 4.3.3	Gaussian	A	B	C	A $\rightarrow$ C $\rightleftharpoons$ A
Test4: 4.3.4	Middle-East	A	B		A $\rightarrow$ C $\rightleftharpoons$ A

4.3.1 Homogeneous model – transmission acquisition

We consider sources on the surface and receivers on the bottom of the model at 200 m depth. 61 sources are located between 200 and 440 m laterally, every 4 m, while receivers are deployed between 0 and 640 m. The exact model is homogeneous with v_p = 2000 m/s and τ = 0.023 (or Q = 50) (Figures 4.2a, b). The equivalent kinematic

velocity for a central frequency at 20 Hz is 2060 m/s. The initial model is also homogeneous, with v_p = 2150 m/s and τ = 0 (Q is infinite) (Figures 4.2c, d).

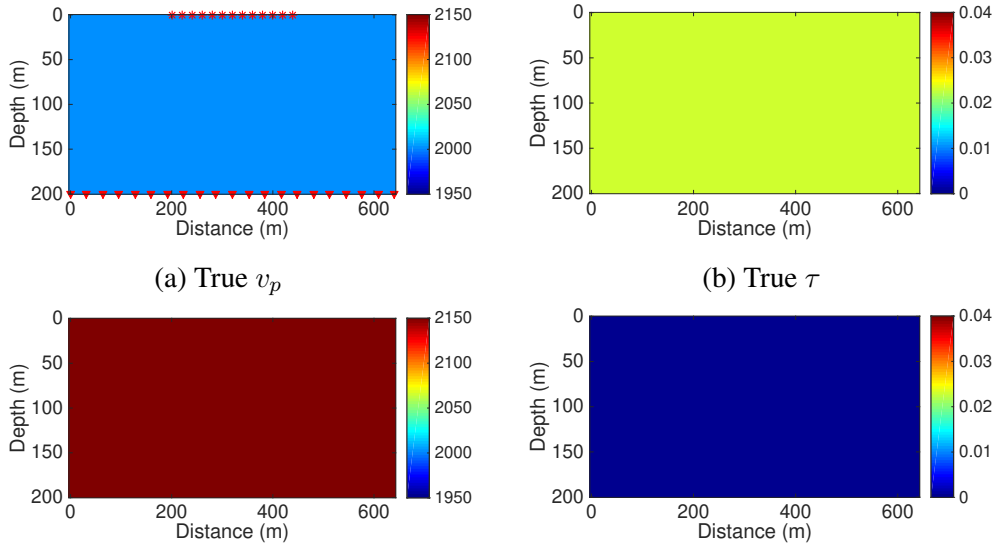

(a) True v_p (b) True τ

(c) Initial v_p (d) Initial τ

Figure 4.2: True velocity (a) and τ (b) models, initial velocity (c) and τ (d) models.

In a first phase, we perform visco-acoustic FWI setting τ = 0 as a passive parameter and only update v_p (Strategy A). The objective function decreases from 1.00 to 0.08 (Figure 4.4, red curve) and cannot go below as the quality factor is not updated. The mean value of final v_p is around 2060 m/s and fails in a local minimum (Figure 4.3 c). After 3 iterations, the mean value of velocity is already around the kinematic velocity 2060 m/s (Figure 4.3 a). With the visco-acoustic inversion, more than 20 iterations are needed with the standard Strategy B (Figure 4.3, green curve). After 30 iterations, the velocity is around the correct v_p = 2000 m/s and τ = 0.023 (or Q = 50) (Figures 4.3g, h).

Starting from the same initial models, we first apply three iterations with Strategy A, followed by 3 other iterations with the new Strategy C. **The kinematic velocity is given by the mean value of the 3rd iteration of Strategy A**. The convergence rate for Strategy C (Figure 4.4, blue line) is faster than the classical FWI approach (Figure 4.4, green line). The final results show that the inverted velocity is around the correct v_p = 2000 m/s and τ = 0.023 (or Q = 50) (Figures 4.3i, j). It is comparable to the conventional result after 30 iterations. Comparing strategy B with C, our new FWI converges faster than conventional visco-acoustic FWI for the same final quality.

To analyze the features of different strategies, we project the mean values of results of each iterations to the kinematic curve, to obtain the the searching direction for the three strategies (Figure 4.5).

First, for the results of mono-parameter velocity inversion (Strategy A) and simultaneous inversion (Strategy B) after first several iterations, results are located on the kinematic curve. v_p is close to the correct v_k 2060 m/s, τ is close to zero. Thus the first several inversions focus on correcting the kinematic information. It indicates that the visco-acoustic FWI preferentially retrieves the v_p to match the phase of the observed and calculated data.

Second, after several iterations of Strategy B, the inversion results show that v_p and τ are on the kinematic curve (e.g., 2rd iteration). The next searching direction (e.g., 3rd iteration) do not follow the kinematic curve to decouple the v_p and τ. Once the result is located on kinematic curve, it means that the phase is matched well (Figure 4.6a). The updating space for velocity is very limited, due to good match of phase, leading to small values of v_p gradient under the area of acquisition coverage (Figure 4.8a). The τ gradient (Figure 4.8b) is obviously positive. In this iteration, the kinematic information is accurate enough, the velocity updating depends on τ updating. Then the updated velocity will distort the phase match (Figure 4.6b), that is the reason why the searching direction is off the kinematic curve. The next followed iteration (e.g., 4th iteration) updates v_p to correct the kinematic information (Figure 4.6c). The v_p gradient in Figure 4.8b is large, leading to large decreases to approach the true value. v_p is the dominant information to update.

Third, the searching direction of Strategy B indicates velocity updating is not always enough. The searching direction of Strategy C strictly follows the kinematic curve to decrease the amplitude difference and keep the phase matching (Figure 4.7). Thus, the modified inversion scheme by building the relation between velocity and τ compensates and corrects the velocity updating, with obvious positive full derivative $d\mathcal{J}/dv_p$ (Figure 4.9). The positive $d\mathcal{J}/dv_p$ denotes the large decreases for velocity updating.

Fourth, without the estimation of the inverse of Hessian matrix, the scaling between the $\partial\mathcal{J}/\partial v_p$ and $\partial\mathcal{J}/\partial\tau$ has to be estimated and given in advance, under conjugate gradient scheme. During the inversion, the fixed scaling factor may constrain the parameter updating. For example, the retrieved results which are on the kinematic curve of Strategy B, the increase scaling factor on $\partial\mathcal{J}/\partial v_p$ will improve the velocity updating. Thus, the velocity derivative with respect to τ acts as a scaling factor between velocity and τ gradients.

In summary, we apply Strategy C for a homogeneous model, and compare with the mono-parameter inversion (Strategy A) and simultaneous inversion (Strategy B). With a given kinematic velocity, Strategy C is a guided inversion and keeps phase matching. In the end, it converges faster than simultaneous inversion. In next section, we still apply the three strategies, but for a model with blocky anomalies to further investigate the inversion strategies.

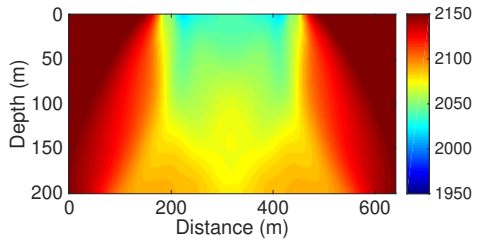

(a) 3rd iteration over v_p with Strategy A

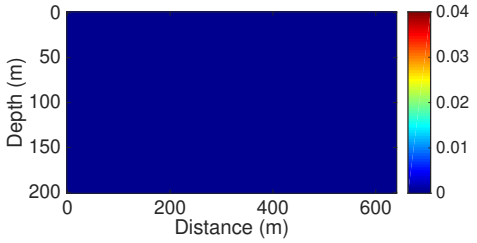

(b) 3rd iteration over τ with Strategy A

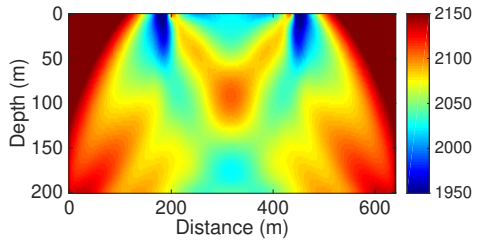

(c) 30th iteration over v_p with Strategy A

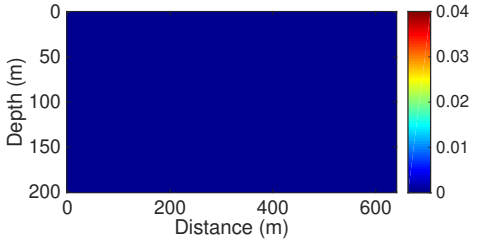

(d) 30th iteration over τ with Strategy A

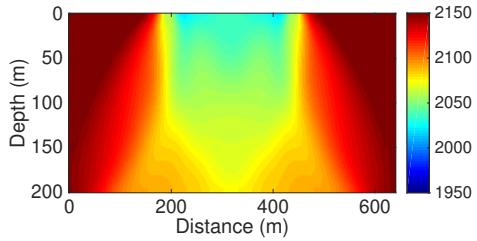

(e) 3rd iteration over v_p with Strategy B

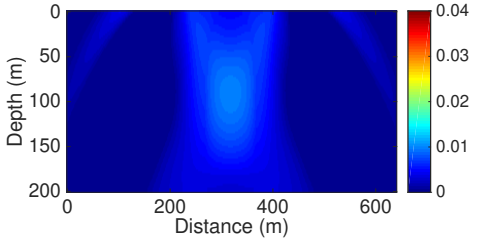

(f) 3rd iteration over τ with Strategy B

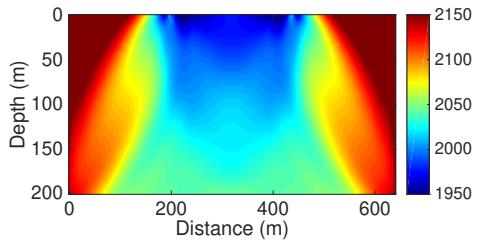

(g) 30th iteration over v_p with Strategy B

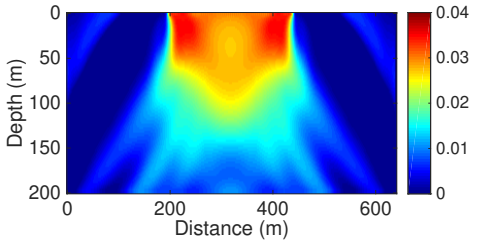

(h) 30th iteration over τ with Strategy B

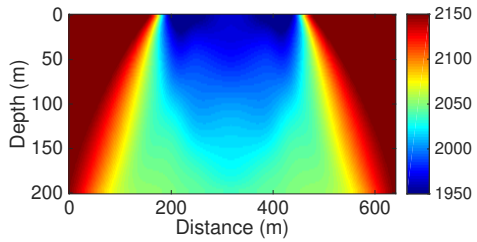

(i) 3rd iteration over v_p with Strategy C

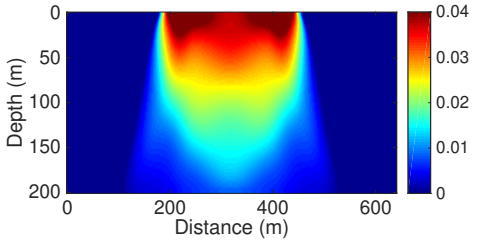

(j) 3rd iteration over τ with Strategy C

Figure 4.3: Updated velocity (a) and τ (b) models after 3 iterations (Strategy A), updated velocity (c) and τ (d) models after 30 iterations (Strategy A), updated velocity (e) and τ (f) models after 3 iterations (Strategy B), updated velocity (g) and τ (h) models after 3 iterations (Strategy B), updated velocity (i) and τ (j) models after 3 iterations (Strategy C).

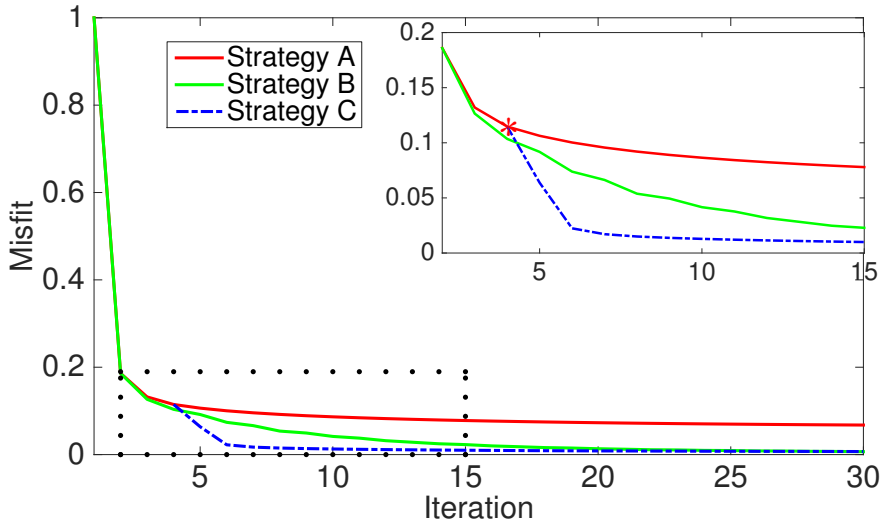

Figure 4.4: Misfit comparison for three different strategies: Strategy A (red), Strategy B (green), and Strategy C (blue).

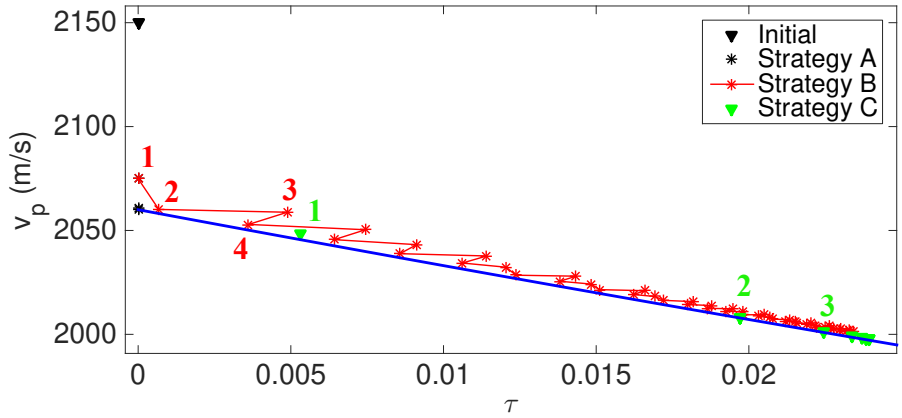

Figure 4.5: Search direction for Strategies A, B and C, the blue line is the kinematic curve for all combinations of v_p and τ equal to v_k 2060 m/s, red solid line is the searching direction of Strategy B. The dots are the mean values of each iteration results.

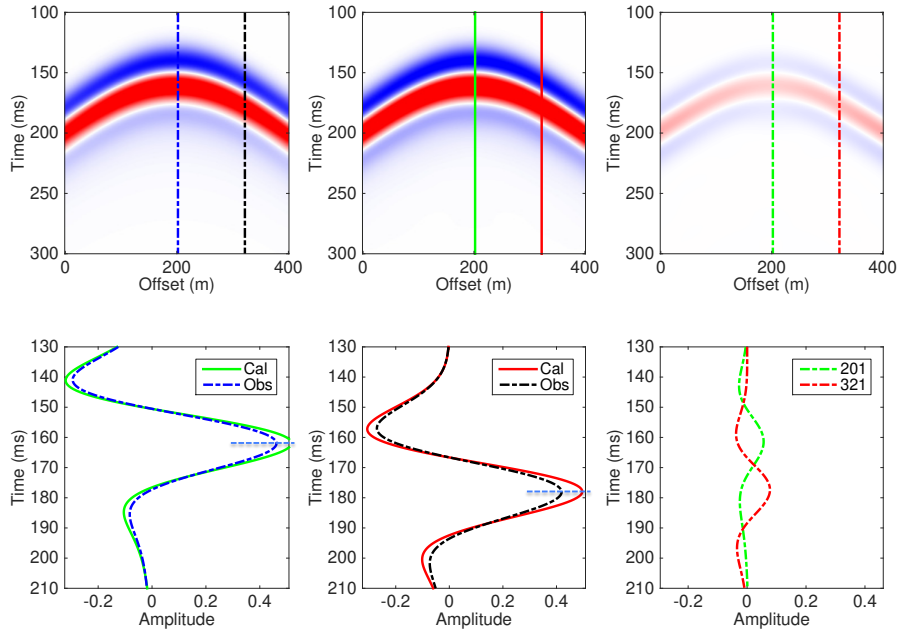

(a) Data comparison after 2 iterations

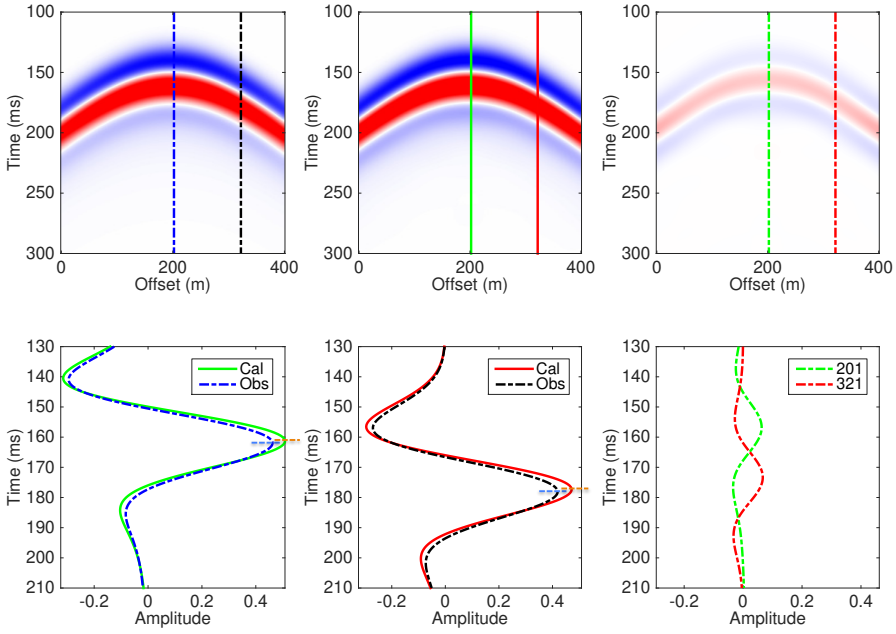

(b) Data comparison after 3 iterations

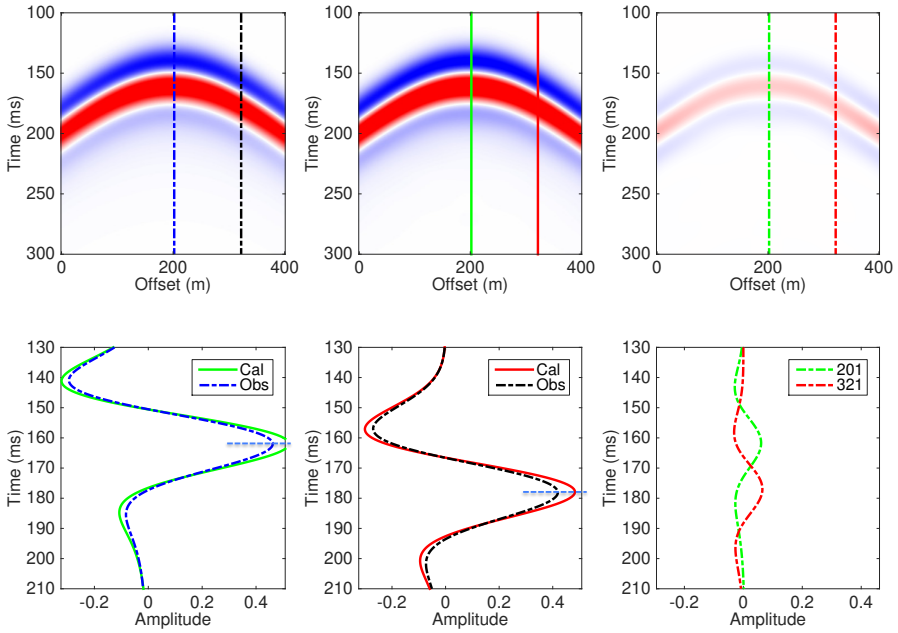

(c) Data comparison after 4 iterations

Figure 4.6: Data comparison of Strategy B after 2 (a), 3 (b), 4 (c) iterations, in each subfigure, the upper left is the real data, upper middle is the calculated data, upper right is the data difference, the bottom left is one trace comparison at 201 m, the bottom middle is one trace comparison at 321 m, the bottom right the one trace difference at 201 m and 321 m respectively. The phase of data after 2 (a) and 4 iterations (c) are matched, meanwhile the phase of data after 3 iterations (b) has a shift.

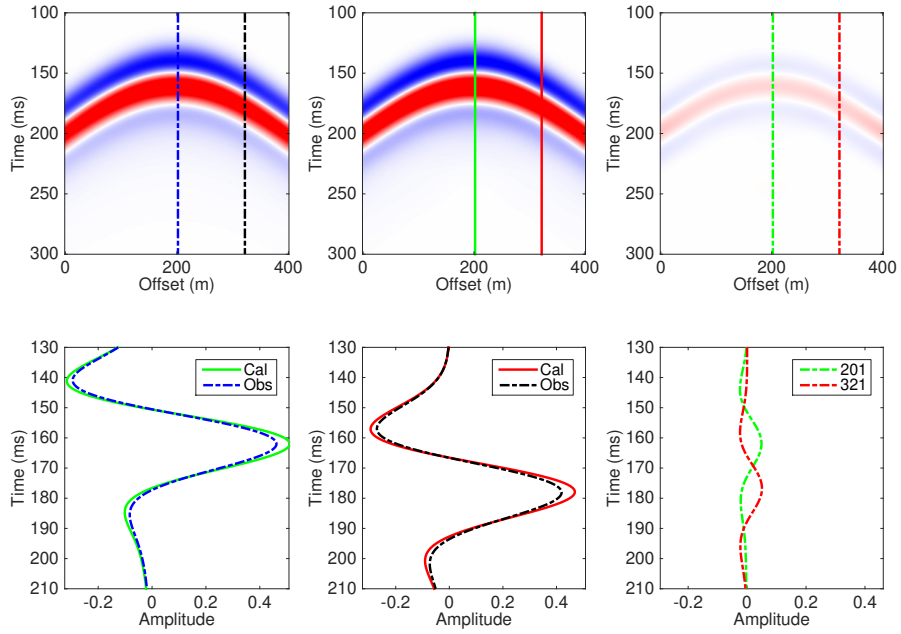

(a) Data comparison after 1 iteration

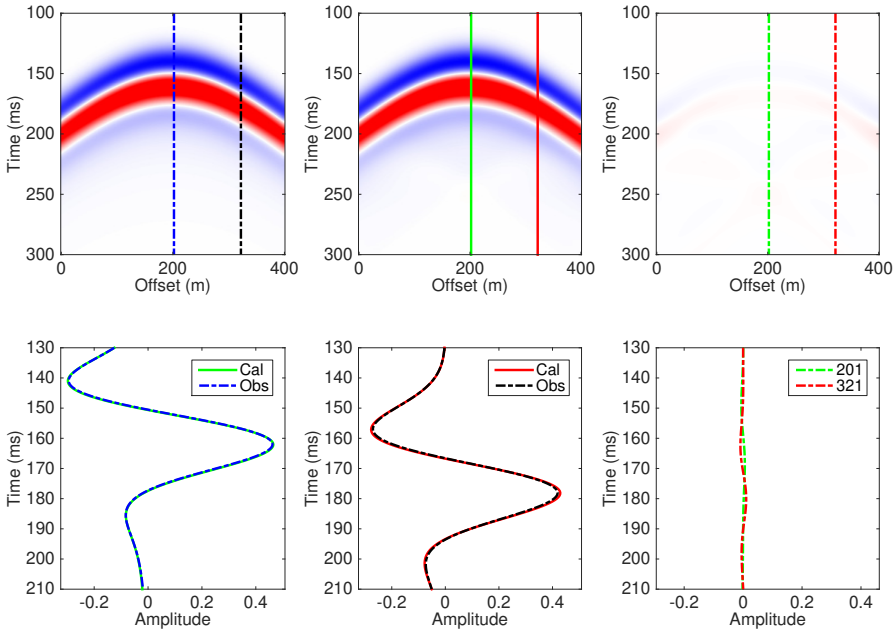

(b) Data comparison after 2 iterations

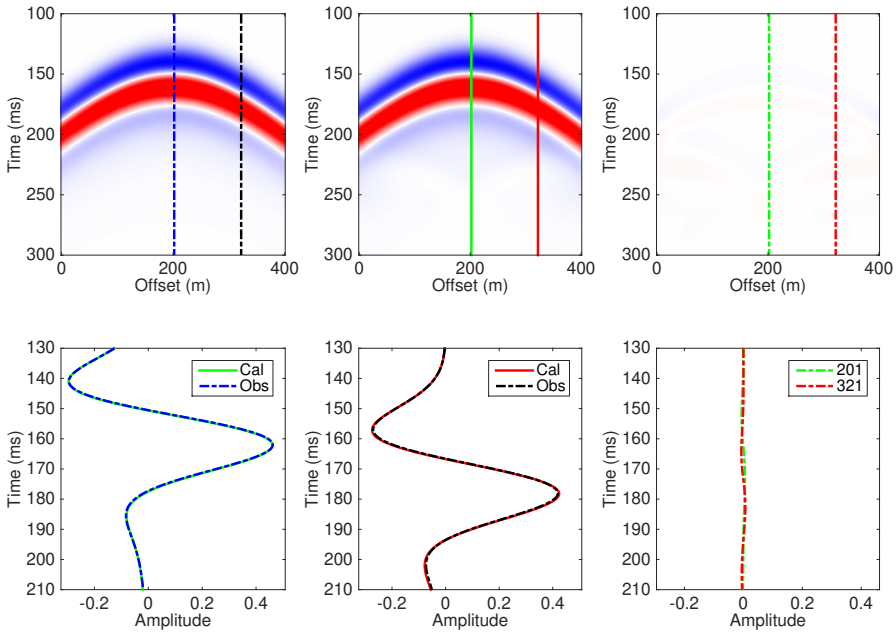

(c) Data comparison after 3 iterations

Figure 4.7: Same as Figure 4.6, except for data comparison of Strategy C after 1 (a), 2 (b), 3(c), the phase of data is kept during the inversion.

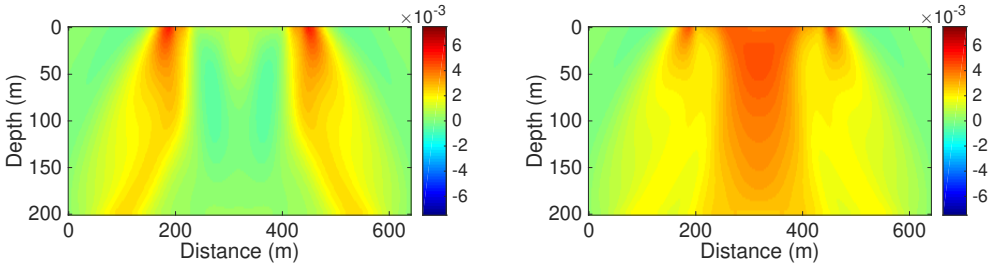

(a) $\partial\mathcal{J}/\partial v_p$ after 2 iterations

(b) $\partial\mathcal{J}/\partial v_p$ after 3 iterations

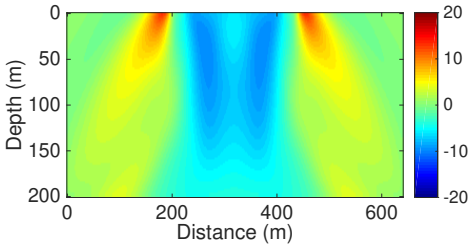

(c) $\partial\mathcal{J}/\partial\tau$ after 2 iterations

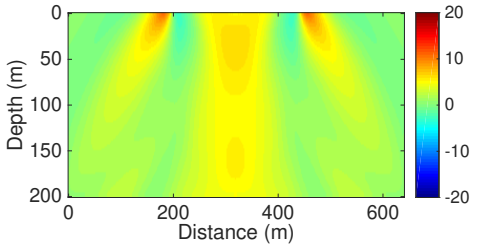

(d) $\partial\mathcal{J}/\partial\tau$ after 3 iterations

Figure 4.8: Gradients of v_p and τ for Strategy B, the left panels (a) and (c) are gradients after 2 iterations, and the bottom two panels (b) and (d) are gradient after 3 iterations.

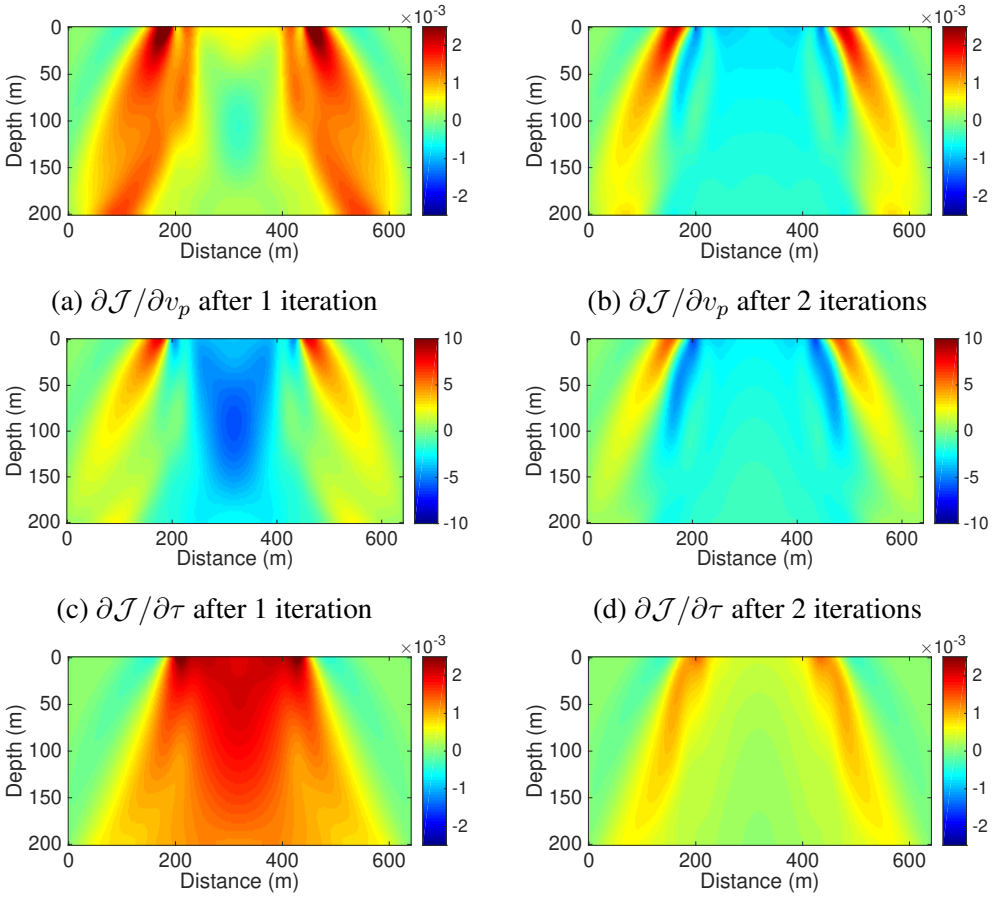

(a) $\partial\mathcal{J}/\partial v_p$ after 1 iteration

(b) $\partial\mathcal{J}/\partial v_p$ after 2 iterations

(c) $\partial\mathcal{J}/\partial\tau$ after 1 iteration

(d) $\partial\mathcal{J}/\partial\tau$ after 2 iterations

(e) $d\mathcal{J}/dv_p$ after 1 iteration

(f) $d\mathcal{J}/dv_p$ after 2iterations

Figure 4.9: Same as Figure 4.8, but for gradients of v_p and τ of Strategy C. The left panels (a) (c) and (e) are gradients after 1 iteration, and the right panels (b) (d) and (f) are gradient after 2 iterations. The full derivative $d\mathcal{J}/dv_p$ (e, f) are positive for the area under the acquisition coverage.

4.3.2 Blocky model – transmission acquisition

In this section, we further test the Strategy C for a slightly more complex model with blocky v_p and τ anomalies, and compare with the other two strategies.

The model size is 200 m in depth and 640 m laterally. 61 sources are located on the top from 200 m to 420 m. Each source has 201 receivers on the bottom. The true velocity model is 2000 m/s embedded with a blocky v_p anomaly being 2060 m/s (Figure 4.10a). The true τ model is 0.023 (Q = 50) embedded by a non-attenuated block (Q is infinite) (Figure 4.10b). The initial models are homogenous, with initial v_p = 2150 m/s (Figure 4.10c) and initial τ = 0 (Figure 4.10d). The source is a Ricker wavelet with central frequency being 20 Hz. The kinematic velocity is 2060 m/s at 20 Hz for the combination of v_p = 2000 m/s and τ = 0.023, which means that the kinematic velocity is homogeneous 2060 m/s.

Following the same inversion sequence as previous test 4.3.1, we first apply the Strategy A for mono-parameter inversion. A few iterations (3 iterations in Figure 4.11a, b) leads to close value between mean velocity of v_p and true v_k. This is consistent with the previous discussion that the first a few iterations of visco-acoustic FWI preferentially update the kinematic information. More iterations (30 iterations in Figure 4.11c, d) generate more artifacts, leading to the over-estimation of v_p without introducing τ. It is necessary to update τ, as well as v_p.

Strategy B updates the two parameters simultaneously. 3 iterations over v_p with Strategy B (Figure 4.11e) has the similar result of Strategy A, meanwhile, the retrieved τ after 3 iterations (Figure 4.11f) is not obvious. This indicates that the first several iterations focus on the kinematic information. After more iterations with Strategy B (Figure 4.11g, h), the anomaly is gradually retrieved, but not very clear.

The Strategy C is also applied to reconstruct the v_p and τ models. The initial model of Strategy C is from the v_p result of Strategy A after 3 iterations (Figure 4.11a). The initial τ is zero, also same as Strategy A. **The kinematic velocity** (Figure 4.12) **is obtained by smoothing** v_p **result of Strategy A after 3 iterations.** Results of Strategy C after 3 iterations (Figure 4.11i, j) are comparable with the results of Strategy B after 30 iterations. After more iterations with Strategy C, the v_p and τ anomalies are more obvious (30 iterations in Figure 4.11k, l).

From the misfit curve (Figure 4.13), the misfits of Strategy A and Strategy B have similar values for the first several iterations, focusing on the match of the kinematic information. The misfit of Strategy A could not decrease further without including the attenuation. Strategy B has a lower misfit with more iterations. Compared with Strategy B, Strategy C decreases faster during the first several iterations and has lower misfit up to 30 iterations.

We analyze the inversion results under the area of effective acquisition coverage, noticing the strong edge effects (Figure 4.11). The inverted values of v_p and τ change gradually from the sources to the receivers, relying on the information derived from

transmitted waves. According to the test and analysis of the previous section, Strategy B converges slowly because the inversion is always off the kinematic curve, but Strategy C is guided and follows the kinematic curve. It leads to that Strategy C has better and more obvious inversion results on v_p and τ anomalies compared with Strategy B.

In this section, as well as the previous section, the kinematic velocity v_k of the two tests is homogeneous and obtained by the results of Strategy A after 3 iterations. In the next section, we extend the different inversion strategies to a more complex models, with the updating of v_k model.

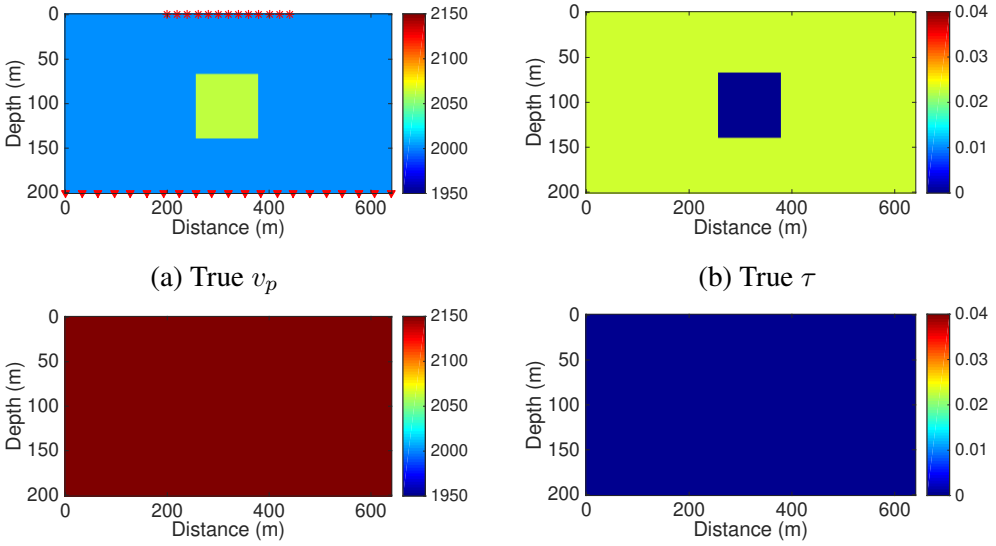

(a) True v_p

(b) True τ

(c) Initial v_p

(d) Initial τ

Figure 4.10: True v_p (a) and τ (b) models, initial v_p (c) and τ (d) models.

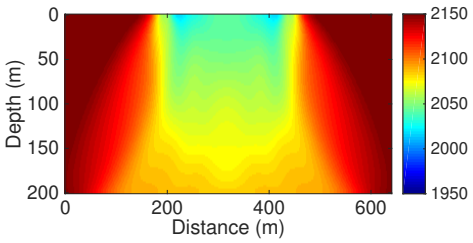

(a) 3rd iteration over v_p with Strategy A

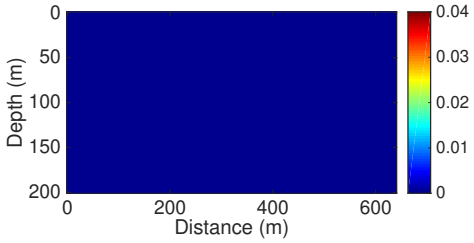

(b) 3rd iteration over τ with Strategy A

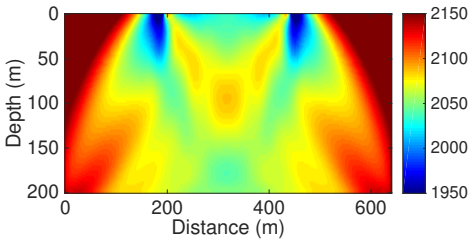

(c) 30th iteration over v_p with Strategy A

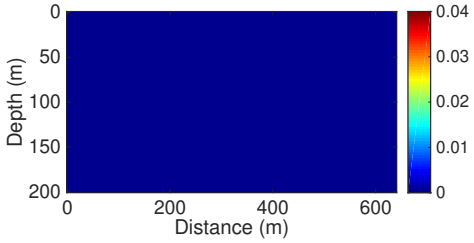

(d) 30th iteration over τ with Strategy A

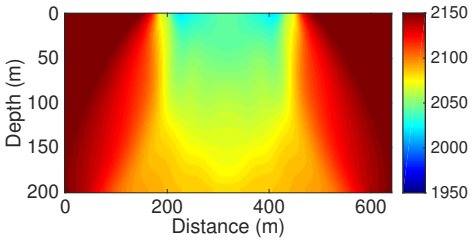

(e) 3rd iteration over v_p with Strategy B

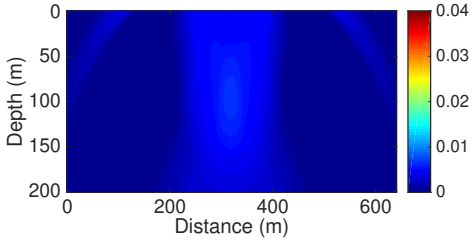

(f) 3rd iteration over τ with Strategy B

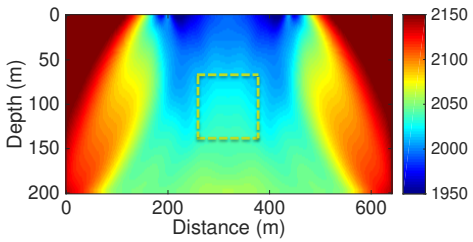

(g) 30th iteration over v_p with Strategy B

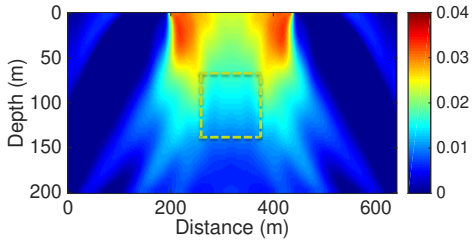

(h) 30th iteration over τ with Strategy B

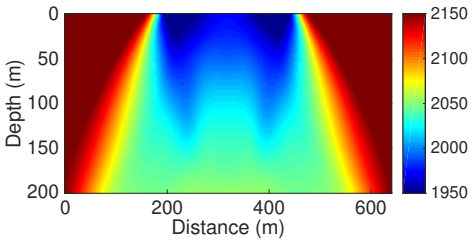

(i) 3 iterations over v_p with Strategy C

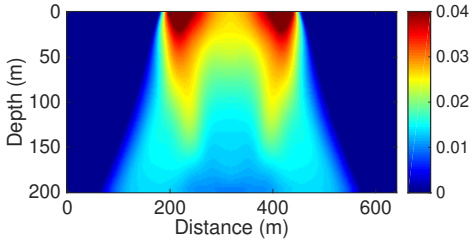

(j) 3 iterations over τ with Strategy C

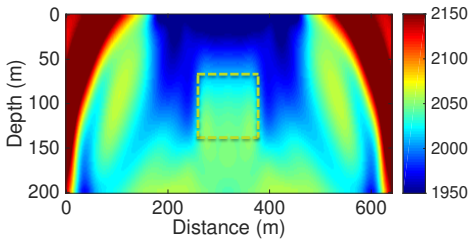

(k) 30 iterations over v_p with Strategy C

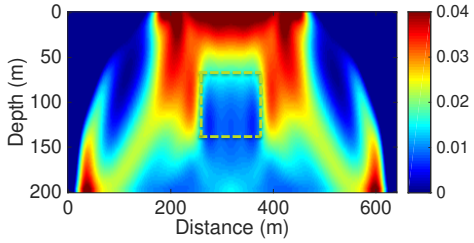

(l) 30 iterations over τ with Strategy C

Figure 4.11: Inversion results: updated v_p (a) and τ (b) models after 3 iterations (Strategy A), updated v_p (c) and τ (d) models after 30 iterations (Strategy A), updated v_p (e) and τ (f) models after 3 iterations (Strategy B), updated v_p (g) and τ (h) models after 3 iterations (Strategy B), updated v_p (i) and τ (j) models after 3 iterations (Strategy C), updated v_p (k) and τ (l) models after 30 iterations (Strategy C). The dashed lines in (i), (j), (k) and (l) denote the position of the v_p and τ anomalies.

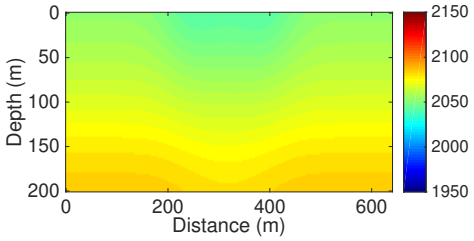

Figure 4.12: Kinematic velocity v_k model for Strategy C, it is obtained by smoothing v_p (Figure 4.11a).

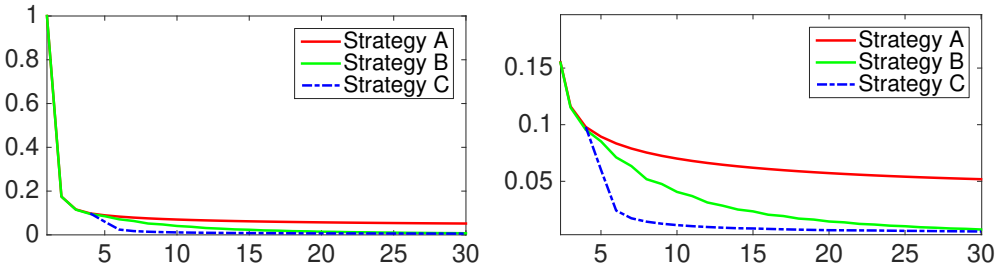

Figure 4.13: Misfit curve of 3 strategies (left), and enlarge in details (right).

4.3.3 Gaussian model – transmission acquisition

In the previous sections (Section 4.3.1, 4.3.2), we tested two simple models. In this section, we test Strategy C and the hybrid strategy on the model containing a τ Gaussian anomaly. The v_p and τ models have uncorrelated structures.

The model size is 220 m in depth and 600 m laterally. The geometry is same as previous test 4.3.2. 76 sources are located on the top from the left to the right edge. 301 receivers are distributed on the bottom. The source is a Ricker wavelet with central frequency being 20 Hz. The true v_p is homogeneous 2000 m/s (Figure 4.14a). The true τ is 0.001 (Q is around 1000) with a Gaussian anomaly, the maximum value of τ is 0.0702 (Q is around 18) (Figure 4.14b). The initial v_p is homogeneous 2000 m/s (Figure 4.14c), same as the true model. The initial τ is homogeneous 0.001 (Figure 4.14d).

Same as in the previous sections, we perform 3 iterations with Strategy A (Figure 4.15a, b). The inverted v_p has artifacts at the same position as the τ anomaly inside the true τ model. The τ anomaly turns into the v_p artifacts due to cross-talks. More iterations with Strategy A (30 iterations in Figure 4.15c, d) lead to the more localized v_p artifacts with higher values. It appears that the v_p inversion tends to mach the kinematic information without updating τ. The misfit curve of Strategy A stops to decrease with 10% final data difference left (Figure 4.16 red).

Strategy B updates both v_p and τ models. The inverted τ is only slightly updated after 3 iterations, but with a strong v_p artifacts (Figure 4.15e, f). With more iterations, the inverted v_p has stronger artifacts. The inverted τ anomaly (Figure 4.15h) increases, but is much lower than the true value. The misfit curve of Strategy B can not decrease any more (Figure 4.16 green).

To mitigate the v_p artifacts, we apply the hybrid strategy for this model, defining as A3 $\rightarrow$ C $\rightleftharpoons$ A (A3 denotes the 3 iterations of Strategy A). After 3 iterations of Strategy A, we start with Strategy C for 2 iterations, then continue another 2 iterations with Strategy A. To improve the kinematic velocity v_k, we perform each 2 iterations of Strategy A and Strategy C in an alternate way until the end. Following this sequence with 3 iterations, the τ anomaly (Figure 4.15i) is slightly updated. The v_p model (Figure 4.15j) still has artifacts. With more iterations, the final inverted τ anomaly (30 iterations in Figure 4.15k) is more obvious than the one obtained with Strategy B, and the v_p artifacts are much lower. The final misfit of the hybrid strategy is also lower than Strategy B (Figure 4.16 blue).

Due to cross-talks between parameters, the final results of simultaneous inversion (Strategy B) leave strong v_p artifacts. The hybrid strategy guides the inversion and mitigates cross-talks. Although, the final results still have v_p artifacts, but those artifacts are much lower than the one obtained with Strategy B. The τ anomaly is better retrieved. Without the introduction of the Hessian matrix, the parameter gradients of the objective function need a scaling factor to balance the sensitivities. The extreme situation is that the scaling factor of v_p gradient is fixed at zero, leading to no contributions on v_p up-

dating. The inversion only focuses on retrieving τ anomaly. The term $\partial\tau(v_p)/\partial v_p|_{v_k}$ of the hybrid strategy acts as the scaling factor to balance the sensitivities. The $\tau(v_p)$ derivative with respect to v_p is based on the fixed v_k. Accurate v_k is important for Strategy C to mitigate cross-talks. We apply the Strategy C **with known aproximated** v_k (Figure 4.17). The final inversion results have much less v_p artifacts and more obvious τ anomaly (Figure 4.18a, b) with lower misfit, compared with the results associated to Strategy B (Figure 4.19).

In the next section, we apply the hybrid strategy for the 2D synthetic Middle-East model, to test the feasibility on more complex models.

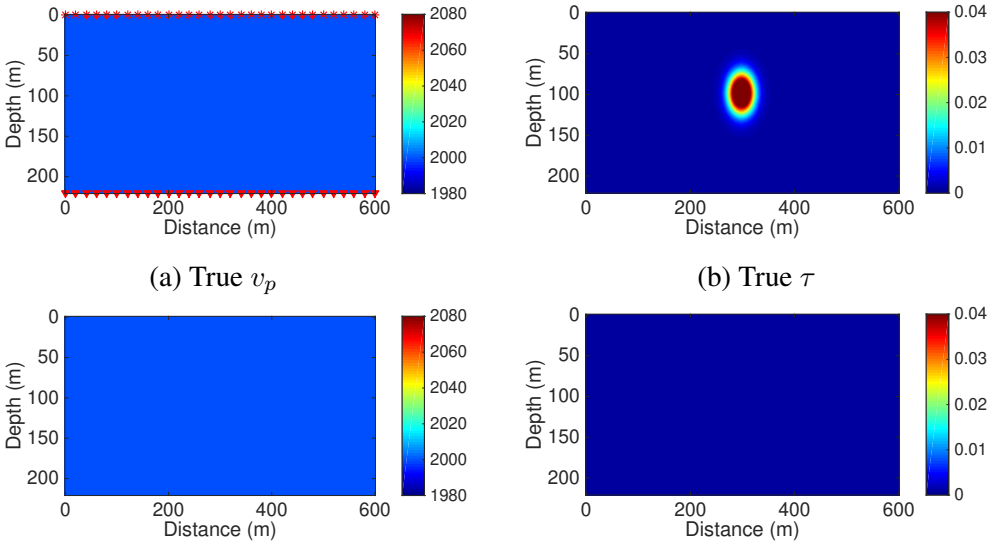

(a) True v_p

(b) True τ

(c) Initial v_p

(d) Initial τ

Figure 4.14: True v_p (a) and τ (b) models, initial v_p (c) and τ (d) models.

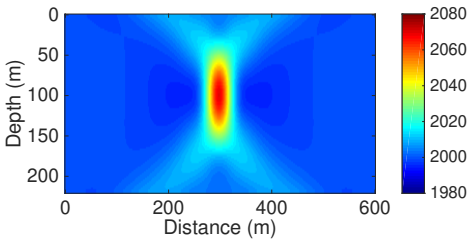

(a) 3rd iteration over v_p with Strategy A

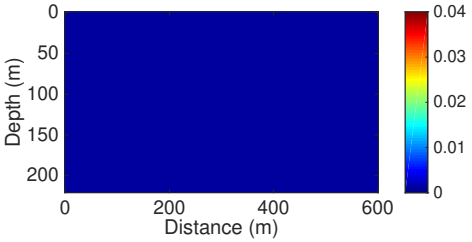

(b) 3rd iteration over τ with Strategy A

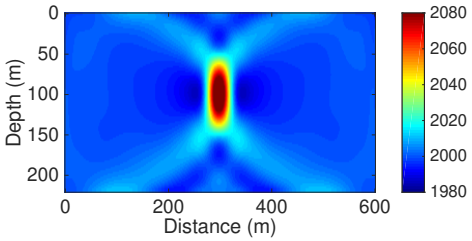

(c) 30th iteration over v_p with Strategy A

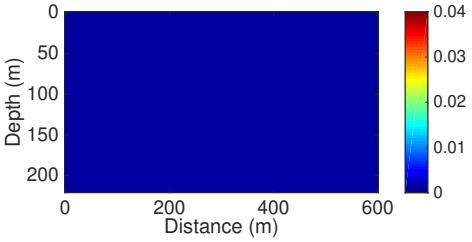

(d) 30th iteration over τ with Strategy A

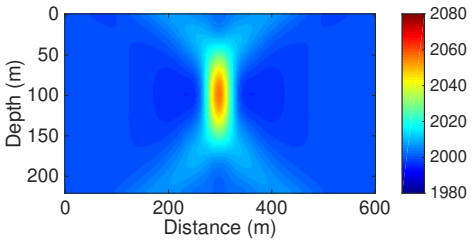

(e) 3rd iteration over v_p with Strategy B

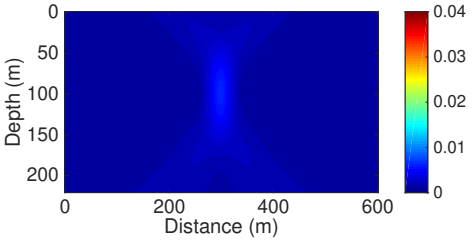

(f) 3rd iteration over τ with Strategy B

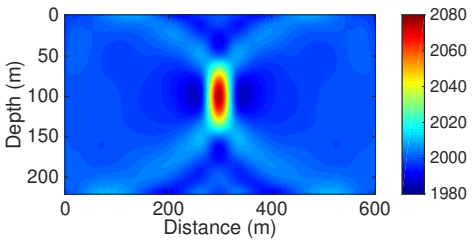

(g) 30th iteration over v_p of Strategy B

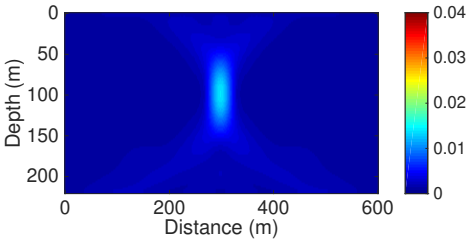

(h) 30th iteration over τ of Strategy B

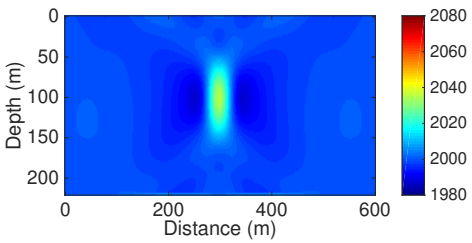

(i) 3 iterations over v_p with the hybrid strategy

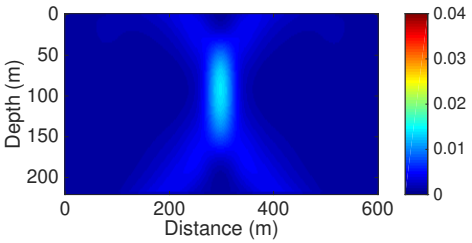

(j) 3 iterations over τ with the hybrid strategy

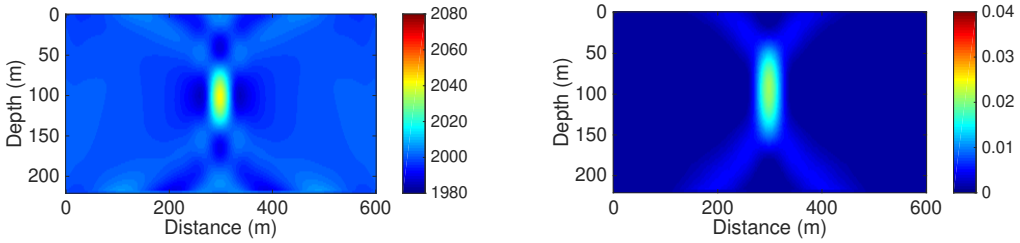

(k) 30 iterations over v_p with the hybrid strategy

(l) 30 iterations over τ with the hybrid strategy

Figure 4.15: Inversion results: updated v_p (a) and τ (b) models after 3 iterations (Strategy A), updated v_p (c) and τ (d) models after 30 iterations (Strategy A), updated v_p (e) and τ (f) models after 3 iterations (Strategy B), updated v_p (g) and τ (h) models after 3 iterations (Strategy B), updated v_p (i) and τ (j) models after 3 iterations (the hybrid strategy), updated v_p (k) and τ (l) models after 30 iterations (the hybrid strategy).

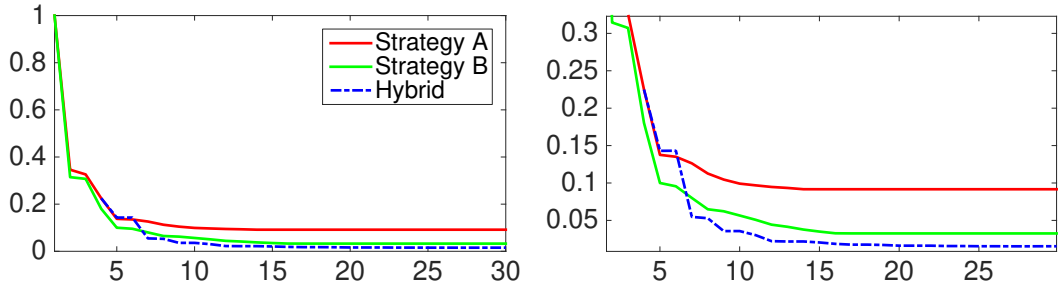

Figure 4.16: Misfit curves for Strategy A (solid red), Strategy B (solid green), the hybrid strategy (dashed blue).

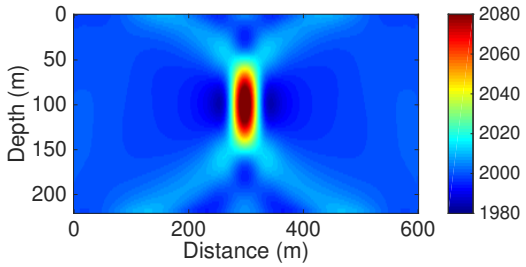

Figure 4.17: The kinematic velocity v_k model, obtained by mono-parameter v_p inversion.

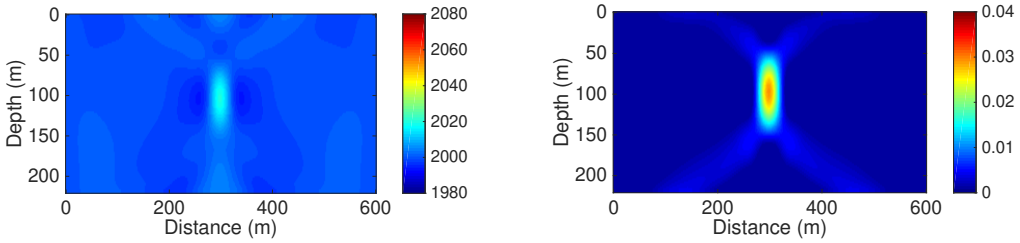

(a) 30th iteration over v_p with Strategy C (b) 30th iteration over τ with Strategy C

Figure 4.18: Inversion results of Strategy C, updated v_p (a) and τ (b) models after 30 iterations.

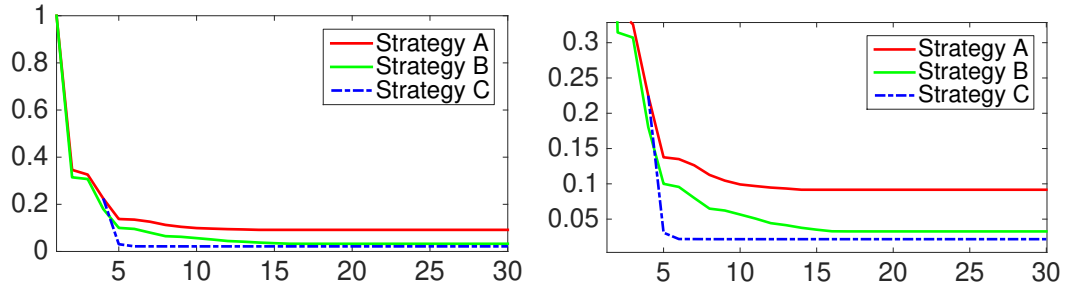

Figure 4.19: Misfit curves for Strategy A (solid red), Strategy B (solid green), Strategy C (dashed blue).

4.3.4 Middle-East model – surface acquisition

The previous tests are based on simple models to investigate the features and feasibility of the hybrid strategy and Strategy C. The first several iterations with a mono-parameter inversion could basically retrieve the kinematic velocity. Based on a good approximate kinematic velocity, this modified strategy decouples the parameters and mitigates cross-talks, with faster convergence than the classical simultaneous inversion. However, the question is how to retrieve the kinematic model in complicated models. In this section, we apply the hybrid strategy to iteratively update v_k and decouple v_p and τ in a 2D synthetic Middle-East model. As for the previous sections, we also compare the hybrid strategy with Strategy A, Strategy B and an additional sequential inversion (Figure 1.9).

The model is 800 m laterally and 212 m in depth. 20 m water layer is on the top of the model. 81 sources are located on the surface from 80 m to 720 m, with 361 receivers evenly distributed on the surface from 40 m to 760 m. The source is a Ricker wavelet with central frequency being 40 Hz. The true velocity is from 1500 m/s to 4500 m/s (Figure 4.20a). τ is set to 0 in the water layer (Q is infinite). The the true τ except in water layer is from 0.015 to 0.033 (Q is from 75 to 35) (Figure 4.20b). We start the inversion, with an initial velocity model obtained by smoothing the true model (Figure 4.20c) and an initial $\tau = 0$ (Figure 4.20d).

As for the previous sections, we have inversion results of Strategy A, Strategy B and the hybrid strategy. 3 iterations with Strategy A briefly reconstruct the shallow part of v_p model (Figure 4.21a, b). With 30 iterations, inverted v_p contains more detailed structures, especially on the shallow part (Figure 4.21c, d). At the same time, 3 (Figure 4.22a) and 30 (Figure 4.22c) iterations over v_p with Strategy B leads similar inversion results as Strategy A, but in some parts, the v_p values in the layer in the depth of 50 m between 500 m–700 m laterally are lower than v_p values obtained with Strategy A. The inverted τ has very lower values after 3 iterations (Figure 4.22b). With more iterations, the inverted τ has increased values (30 iterations in Figure 4.22 d), but the retrieved τ values are still much lower than the true ones. The misfit of Strategy B keeps lower than the misfit of Strategy A during the inversion (Figure 4.24).

The hybrid strategy starts with the results of Strategy A after 3 A-iterations, and continues with each 4 C-iterations and 4 A-iterations in an alternate way until the end. We count iteration times as the sum of times of A-iterations and C-iterations in sequence. v_p and τ models (Figure 4.23a, b) are slightly updated after 3 iterations. The inverted τ has slightly obvious result than the result of Strategy B. With more iterations, the inverted v_p has more detailed structures, and the inverted τ is significantly improved. The hybrid strategy has higher misfit for the first 18 iterations compared with the misfit of Strategy B (Figure 4.24), because the kinematic velocity v_k needs to be iteratively updated. With good v_k, the final misfit of the hybrid strategy is lower than the misfit of Strategy B.

We perform more iterations for the three strategies. The misfit curve of Strategy A

stops to decrease after 50 iterations (Figure 4.26 red). We compare the results of Strategy B and the hybrid strategy after 80 iterations. The v_p result of Strategy B (Figure 4.25a) is close to the inverted v_p of the hybrid strategy C (Figure 4.25c). The inverted τ of Strategy B (Figure 4.25b) is still lower than the true model, but the retrieved area is almost on the shallow part and the deeper part is less reconstructed. Meanwhile, the inverted τ of the hybrid strategy (Figure 4.25b) has more close average values to the true τ. With more iterations, the hybrid strategy (Figure 4.26 black) has smaller misfit than the misfit of Strategy B (Figure 4.26 green). The two strategies both have small final misfit values. The final data residuals of the hybrid strategy (Figures 4.27 and 4.29) are smaller than Strategy B final data residuals (Figure 4.30).

Additionally, we also apply the sequential inversion. This strategy includes a first step for updating v_p with fixed τ, and a subsequent step for updating τ with fixed v_p. The hybrid strategy is composed of a first step for updating v_p with fixed τ (v_k updating) and the alternate step of Strategy C. We perform the sequential inversion same as the hybrid strategy, except that we replace the alternate each 4 C-iteration with 4 mono-parameter τ inversion with fixed v_p. The misfit curves (Figure 4.31) shows that the hybrid strategy has faster convergence and a lower final misfit, compared with the sequential inversion. It indicates that Strategy C guiding the inversion with fixed v_k, leads to faster convergence.

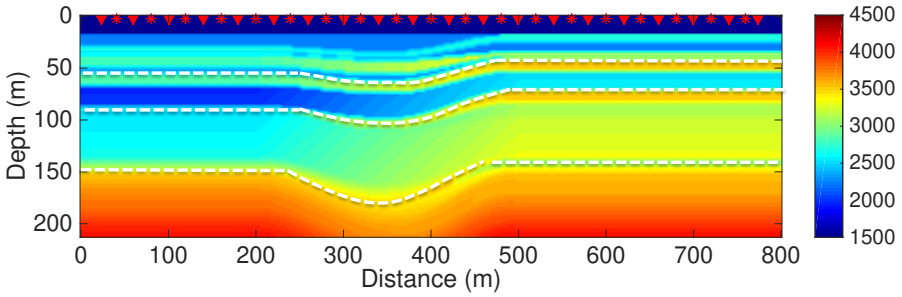

(a) True v_p model

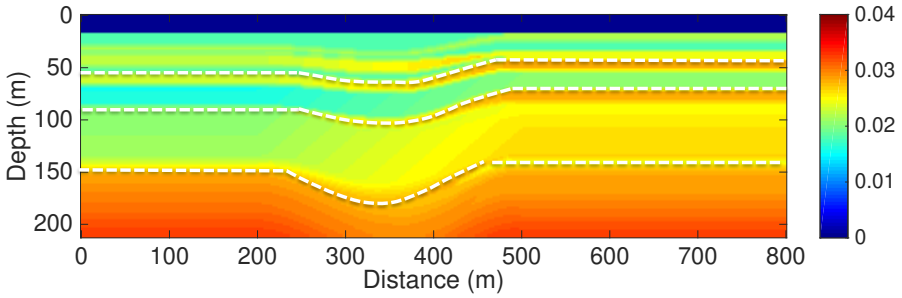

(b) True τ model

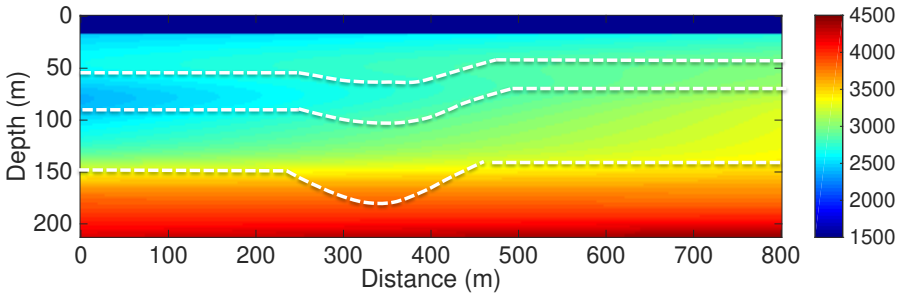

(c) Initial v_p model

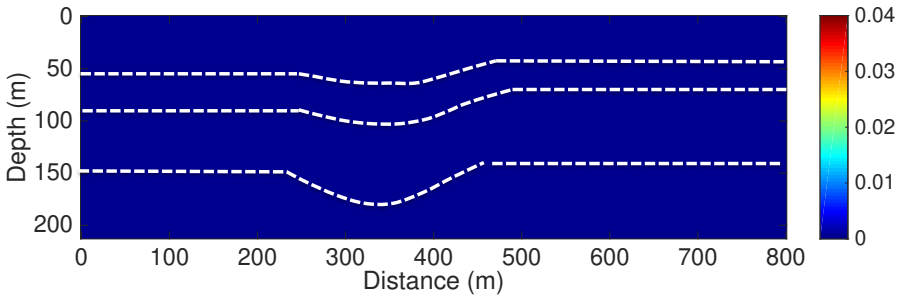

(d) Initial τ model

Figure 4.20: True and initial models: true v_p (a), true τ (b), initial v_p (c) and initial τ (d). In (a), the stars denote the source positions and the reversed triangles represent the receiver positions; the dashed white lines denote the interfaces where the true v_p rapidly changes.

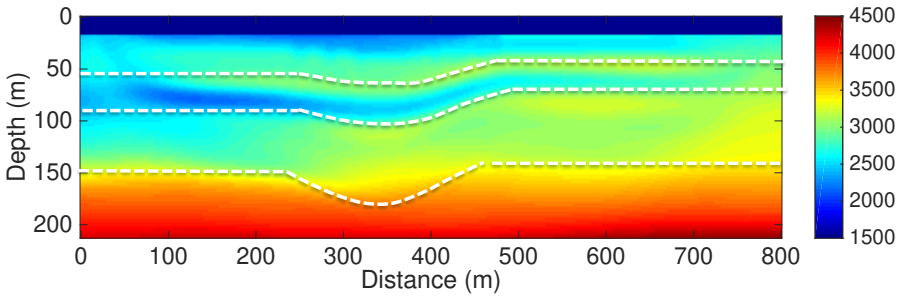

(a) 3 iterations over v_p with Strategy A

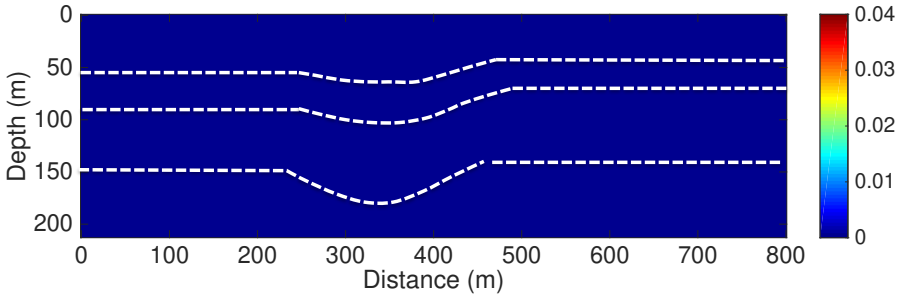

(b) 3 iterations over τ with Strategy A

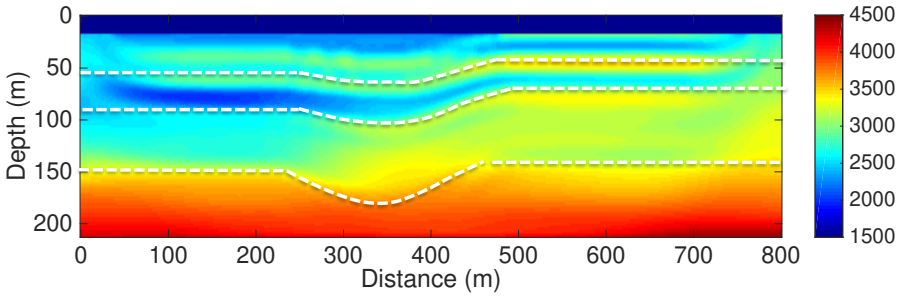

(c) 30 iterations over v_p with Strategy A

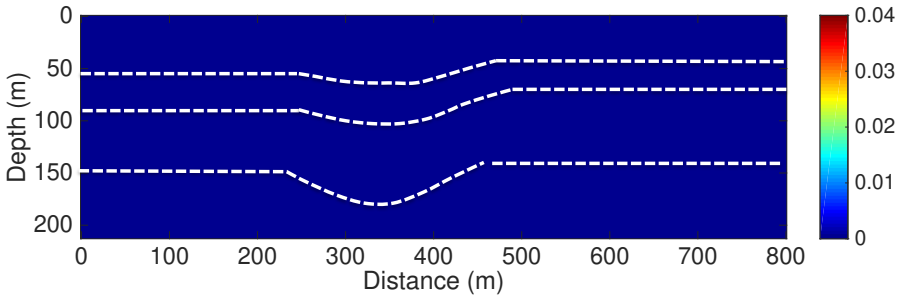

(d) 30 iterations over τ with Strategy A

Figure 4.21: Inversion results of Strategy A.

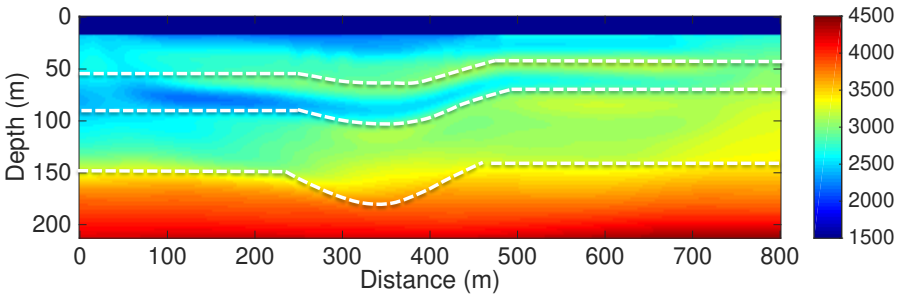

(a) 3 iterations over v_p with Strategy B

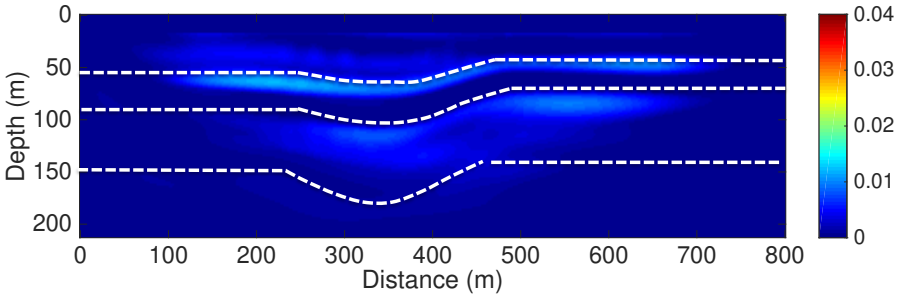

(b) 3 iterations over τ with Strategy B

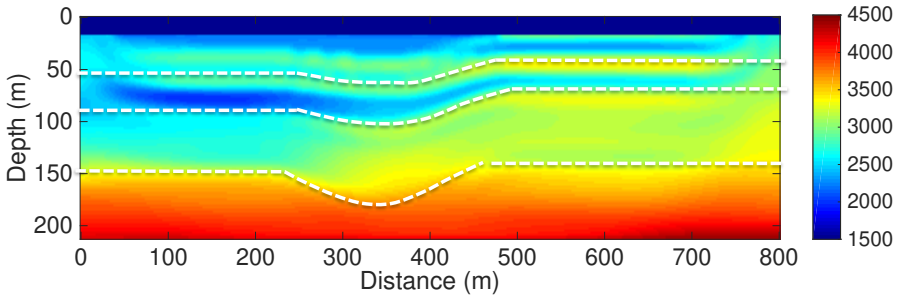

(c) 30 iterations over v_p with Strategy B

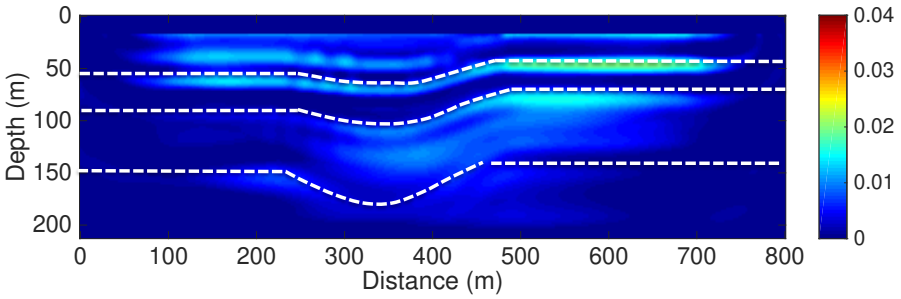

(d) 30 iterations over τ with Strategy B

Figure 4.22: Inversion results of Strategy B.

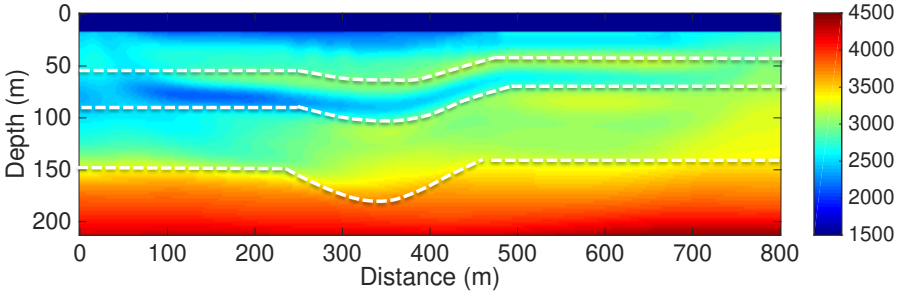

(a) 3 iterations over v_p with the hybrid strategy

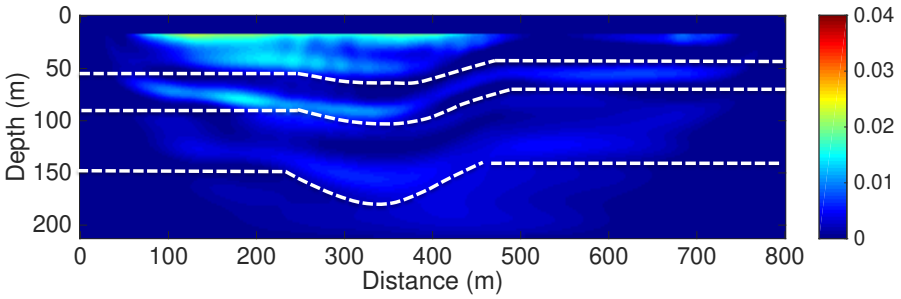

(b) 3 iterations over τ with the hybrid strategy

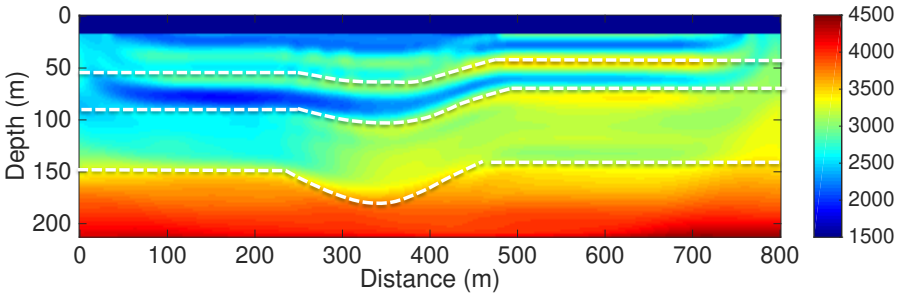

(c) 30 iterations over v_p with the hybrid strategy

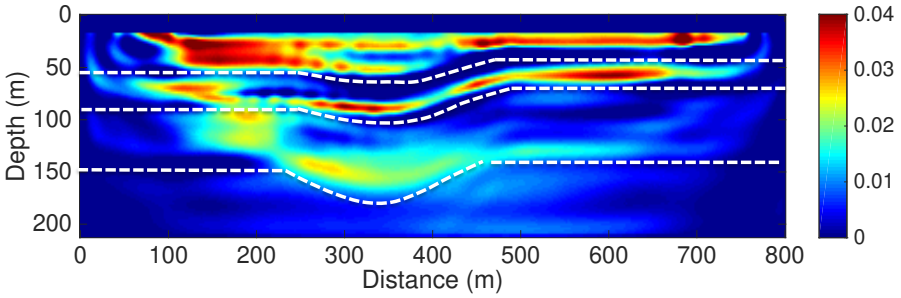

(d) 30 iterations over τ with the hybrid strategy

Figure 4.23: Inversion results of the hybrid strategy.

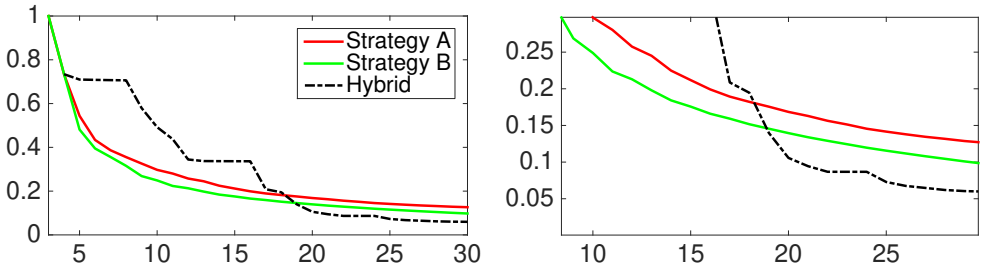

Figure 4.24: Misfit curves for Strategy A (solid red line), Strategy B (solid green line), the hybrid strategy (dashed black line).

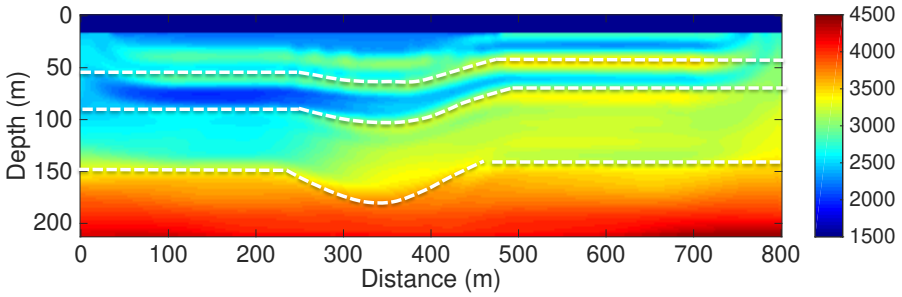

(a) 80 iterations over v_p with Strategy B

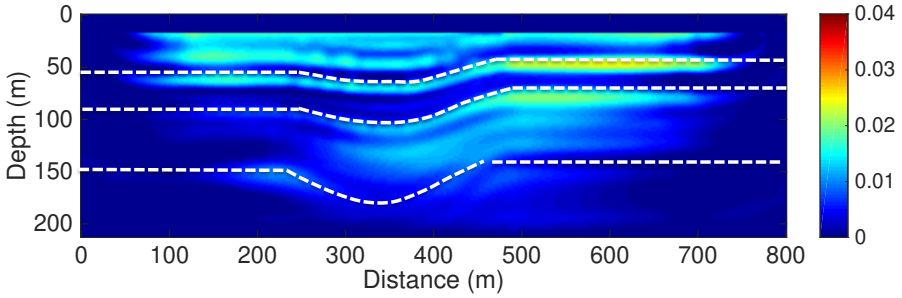

(b) 80 iterations over τ with Strategy B

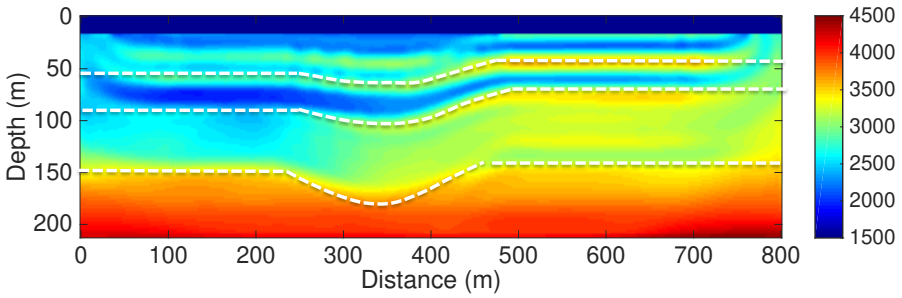

(c) 80 iterations over v_p with the hybrid strategy

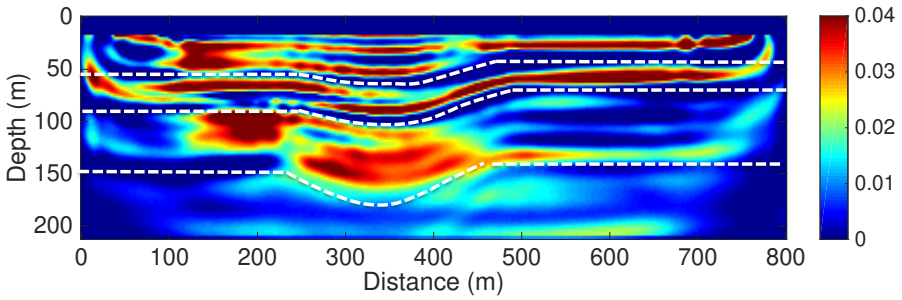

(d) 80 iterations over τ with the hybrid strategy

Figure 4.25: v_p and τ results after 80 iterations of Strategy B (a, b) and the hybrid strategy (c, d).

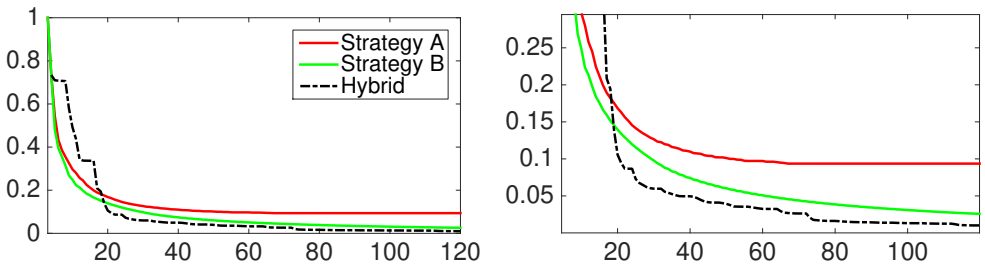

Figure 4.26: Misfit curves for Strategy A (solid red), Strategy B (solid green), and the hybrid strategy (dashed black) with 120 iterations.

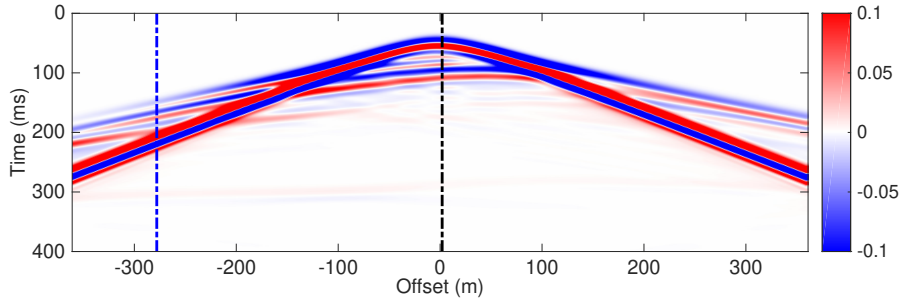

(a) Observed data

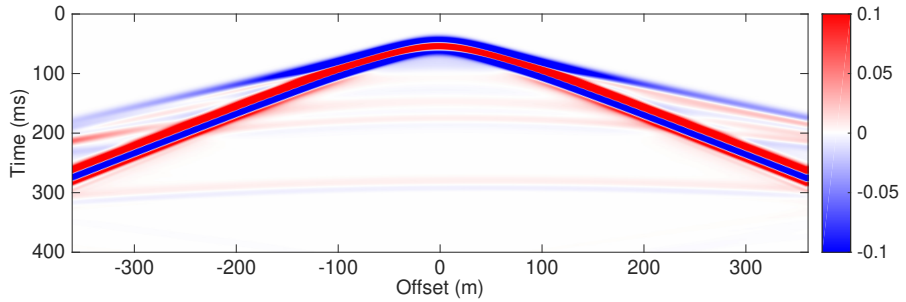

(b) Initial data

Figure 4.27: One observed shot gather (direct waves in water are removed) (a) and one shot gather of initial data (b) at position x = 400 m.

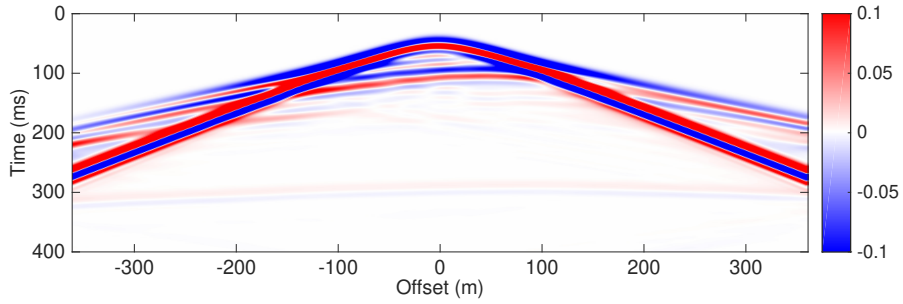

(a) Final data of Strategy A (80 iterations)

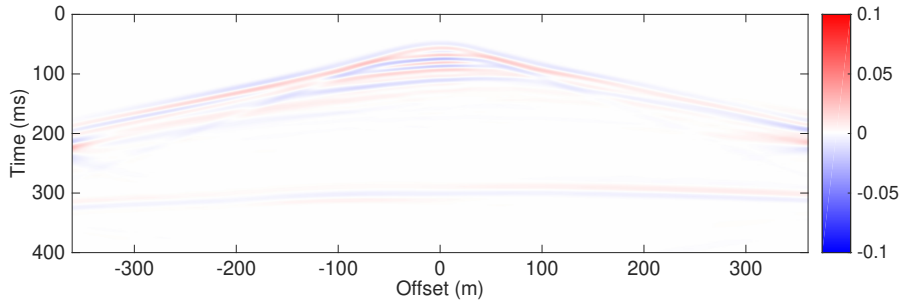

(b) Final data residual of Strategy A

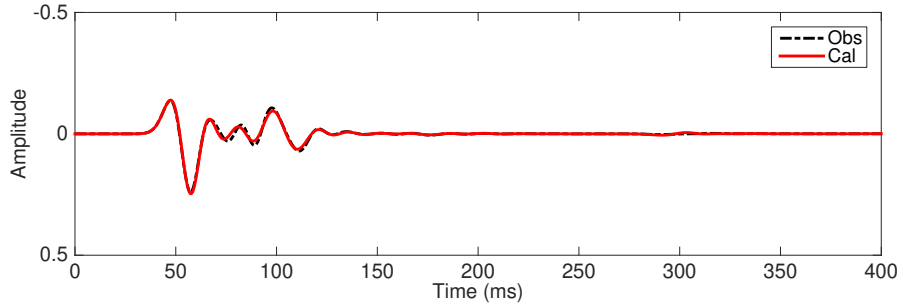

(c) Trace comparison at near offset of Strategy A

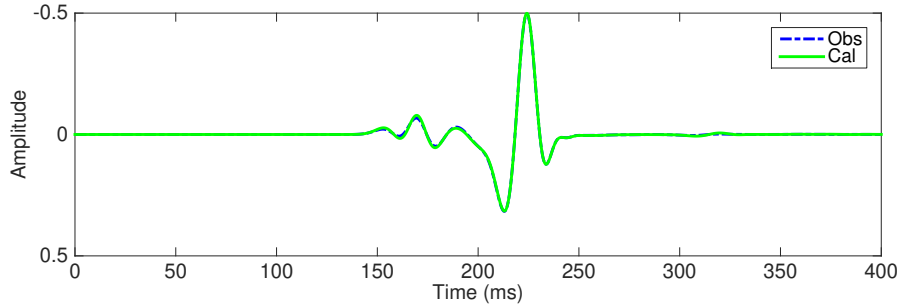

(d) Trace comparison at far offset of Strategy A

Figure 4.28: Data comparison for Strategy A at position $x = 400$ m, with final calculated data after 80 iterations (a) and final data difference (b), two traces of observed data (dashed blue and dark) and calculated data (solid green and red) are compared at near offset (c) and far offset (d).

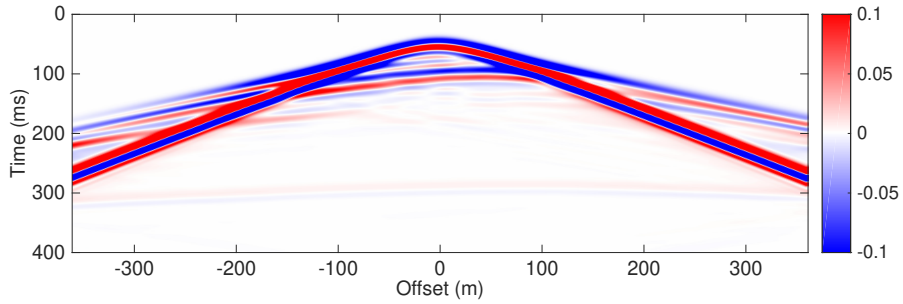

(a) Final data of Strategy B (80 iterations)

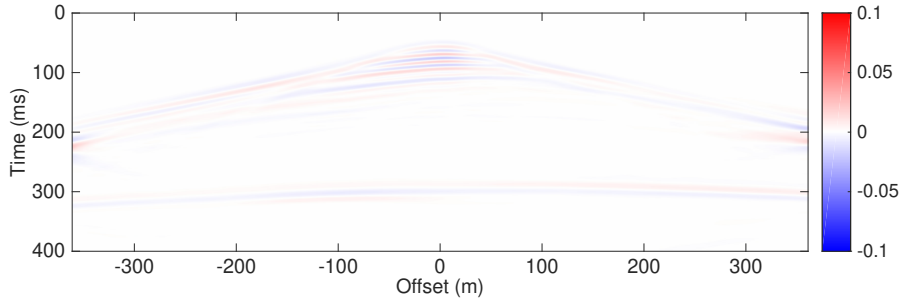

(b) Final data residual of Strategy B

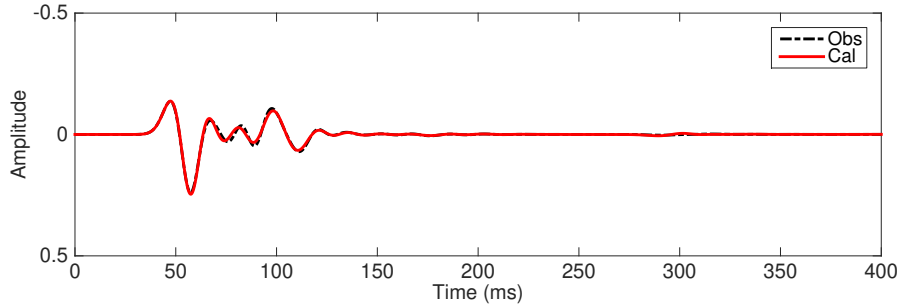

(c) Trace comparison at near offset of Strategy B

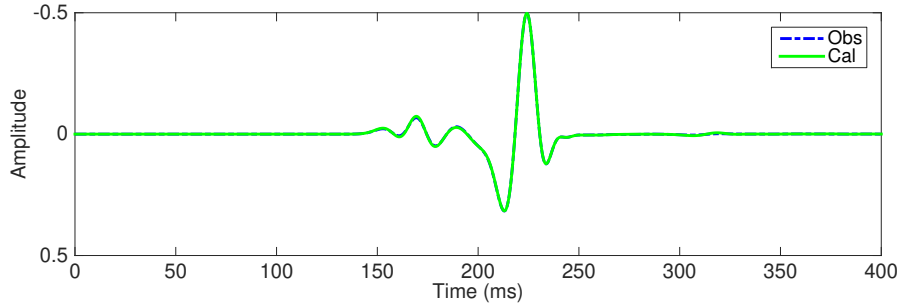

(d) Trace comparison at far offset of Strategy B

Figure 4.29: Same as Figure 4.28, but for data comparison for Strategy B.

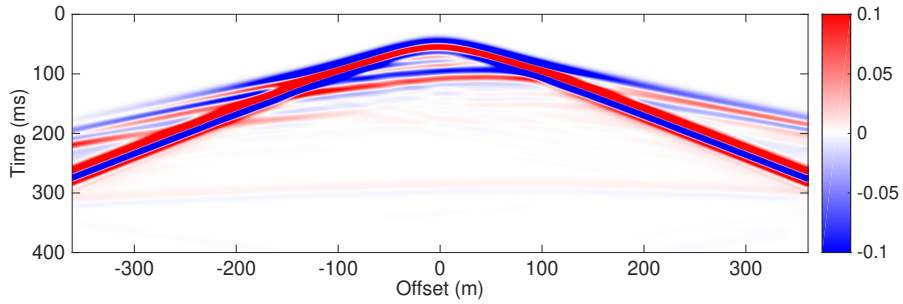

(a) Final data of the hybrid strategy (80 iterations)

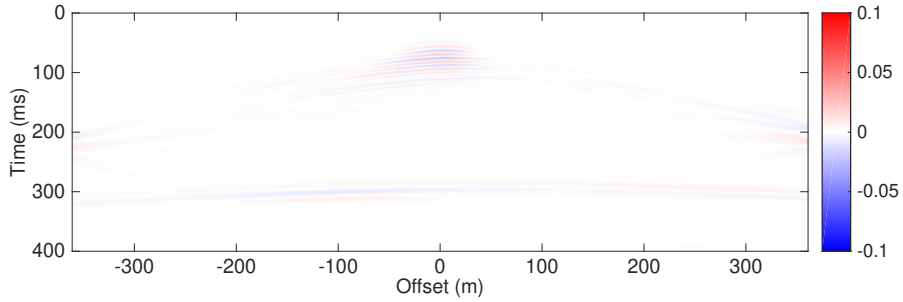

(b) Final data residual of the hybrid strategy

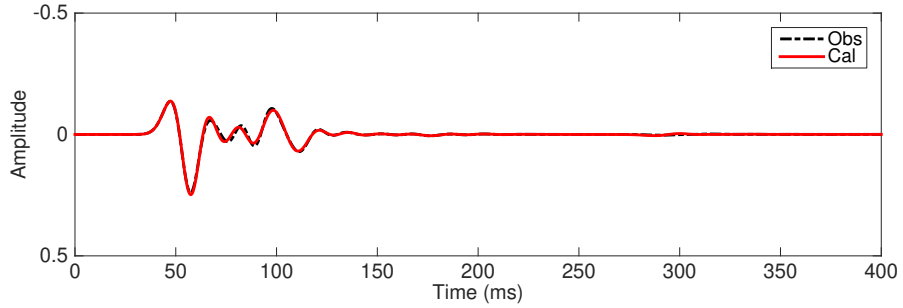

(c) Trace comparison at near offset of the hybrid strategy

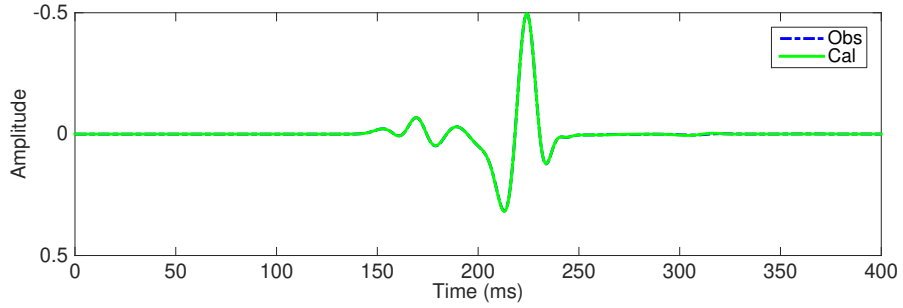

(d) Trace comparison at far offset of the hybrid strategy

Figure 4.30: Same as Figure 4.28, but for data comparison for the hybrid strategy.

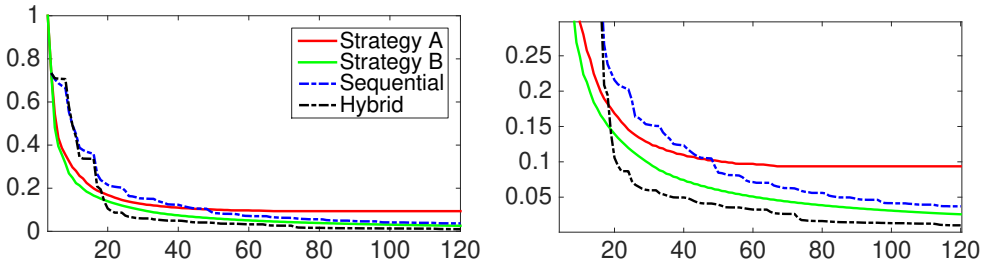

Figure 4.31: Misfit curves for Strategy A (solid red), Strategy B (solid green), the strategy of sequential inversion (dashed blue) and the hybrid strategy (dashed black) with 120 iterations.

4.4 Discussion

We incorporate the kinematic relationship to the visco-acoustic inversion. The results show that the hybrid strategy can guide the inversion and mitigate cross-talks. We need to discuss the following aspects: the model searching space, scaling factor between gradients, the Hessian matrix and the regularization terms.

First, the explicit kinematic relationship imposes strong constrains on the inversion, which reduces the searching space of model to guide the inversion. The simultaneous inversion has more flexibilities to explore the model space, but still suffers from cross-talks between parameters (e.g., Figure 4.15g, h). The accurate kinematic velocity is important for the hybrid inversion strategy to search in the less model space. The simple models test show that the retrieved parameters have higher resolution (e.g., Figure 4.11), fast convergence and lower misfit values (Figure 4.4, 4.13) based on the correct kinematic velocity models. For the 2D synthetic Middle-East model, the main difficulty is to update the kinematic velocity. The result shows that the modified inversion has lower misfit values (Figure 4.26). The retrieved v_p has comparable resolution as the one inverted by the simultaneous inversion (Figure 4.25a, c), the retrieved τ has higher average values (Figure 4.25b, d). However, the kinematic velocity for the hybrid strategy is determined for a single frequency, which is the same as the central frequency for a Ricker wavelet source. From the frequency spectrum of the source, the energy of central frequency is dominant. The inversion results of our examples with Ricker wavelet sources show that the central frequency is a proper choice to determine the kinematic velocity.

Second, the scaling factor of the gradients for simultaneous inversion based on conjugate gradient method are fixed before the inversion. The scaling factor $\alpha_{\boldsymbol{m}}$ (Equation 4.25) is used to determine the unitary searching step of each parameter (Plessix et al., 2016) with a conjugate gradient optimization scheme. For synthetic studies, $\alpha_{\boldsymbol{m}}$

can be obtained by the difference of lower and upper bounds of each model parameter divided by the iteration number (He et al., 2018). Therefore, the different choices of α_{v_p} and α_τ adjust the different sensitivities of parameters. However, the scaling factor is fixed during the inversion. As we discussed before for simple model cases, when the kinematic information is well retrieved, the v_p sensitivity is low. Increasing the α_{v_p}, the inversion accelerates the v_p updating, leading to a faster convergence speed. The factor of $\partial\tau(v_p)/\partial v_p|_{v_k}$ is a dynamic scaling factor to adjust the sensitivities between parameters.

Third, our comparison between different strategies is based on the conjugate gradient method. Newton method is more accurate in the case for quadratic behaviors, but is very expensive. Visco-acoustic FWI updates two parameters v_p and τ, the inverse of Hessian matrix can act as the scaling factor of the gradients of v_p and τ and mitigate cross-talks (Yang et al., 2018). Due to the ill-posed problem, the Hessian matrix has singular values and it is hard to obtain the inverse Hessian matrix. The Hessian matrix can be solved by second-order adjoint state method, but the difficulty lies in the negative eigenvalues (Métivier et al., 2014). Another way is to add a regularization term to objective function (Asnaashari et al., 2013). Then the inverse of Hessian matrix including a damping factor to scale the gradients. Prieux et al. (2013) show the different damping factors significantly impact the inversion results. The explicit kinematic relation provides a way to connect the two parameters during the inversion by the term $\partial\tau(v_p)/\partial v_p|_{v_k}$. It is a possible alternative to replace the empirical scaling factor.

To illustrate the impacts of the scaling factors, we select different scaling factors for Strategy B. We also apply the term $\partial\tau(v_p)/\partial v_p$ for Strategy B as a dynamic scaling factor during each iteration. The true v_p model is a homogeneous 2000 m/s with a blocky anomaly 2500 m/s (Figure 4.32a), and true τ model is homogeneous 0.023 (Q = 50) with a blocky anomaly 0.0923 (Q = 15) (Figure 4.32b). The initial v_p is 2000 m/s and initial τ is 0.023 (Figure 4.32c, d). Shots are on the top and receivers are on bottom.

The inversion only focuses on reconstructing the blocky v_p and τ anomalies. The lower and upper bounds of v_p are 2000 m/s and 2500 m/s, and the lower and upper bounds of τ are 0.023 and 0.0923. The $\alpha_{\boldsymbol{v_p}}$ and $\alpha_{\boldsymbol{\tau}}$ are given by the differences of lower and upper bounds dividing the a chosen a iteration number. For example, we select $\alpha_{\boldsymbol{v_p}}$ = 10 m/s and $\alpha_{\boldsymbol{\tau}}$ = 0.005, the ratio $\alpha_{\boldsymbol{\tau}}/\alpha_{\boldsymbol{v_p}}$ is 5×10^{-4}. The other different ratios can be obtained by choosing different $\alpha_{\boldsymbol{v_p}}$ and $\alpha_{\boldsymbol{\tau}}$. The different scaling factors have different convergence speeds (Figure 4.33). The scaling 1 represents the term $\partial\tau[v_p(\boldsymbol{x})]/\partial v_p(\boldsymbol{x})$ as a dynamic scaling factor, and the scaling 2 represents the spatial mean value of $\partial\tau[v_p(\boldsymbol{x})]/\partial v_p(\boldsymbol{x})$ ($\boldsymbol{x}$ is the spatial coordinates). Scaling 1 changes with spatial coordinates, but scaling 2 is a scalar value (Figure 4.34).

As we analyzed before, the first iteration mainly focuses on updating the velocity to fit the kinematic information. For the same step of updating v_p, a large scaling factor (e.g., 50×10^{-4} and 15×10^{-4}) increases the updating of τ, leading to a smaller misfit. However, a over-estimated large scaling factor constrains v_p updating. The scaling

factor 50×10^{-4} (Figure 4.33 dashed dark blue) has the largest misfit after 30 iterations. On the opposite, a over-estimated small scaling factor 0.5×10^{-4} also constrains τ updating (Figure 4.33 dashed blue). A proper scaling factor (e.g., 2.5×10^{-4} and 5×10^{-4}) is more consistent with the sensitivities between parameters, the inversion has lower misfit values. Among those proper scaling factors, a smaller one, e.g., 2.5×10^{-4} contributes more on velocity updating when the kinematic information is well matched, which has the lowest misfit value (Figure 4.33 dashed blown). A dynamic scaling factor (Figure 4.33 solid dark and dashed green) has comparable low misfit as fixed scaling factor, e.g., 5×10^{-4}.

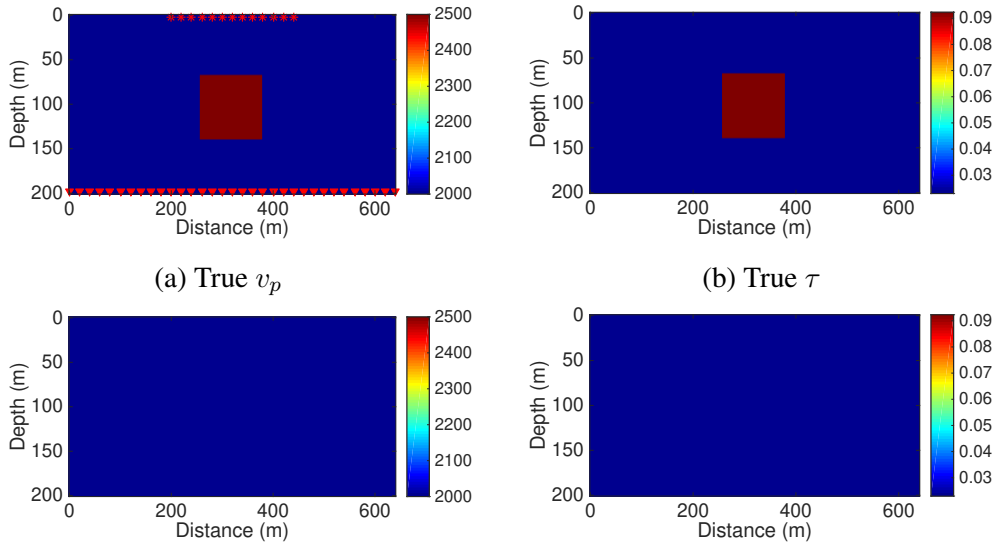

(a) True v_p

(b) True τ

(c) Initial v_p

(d) Initial τ

Figure 4.32: True velocity (a) and τ (b) models, initial velocity (c) and τ (d) models.

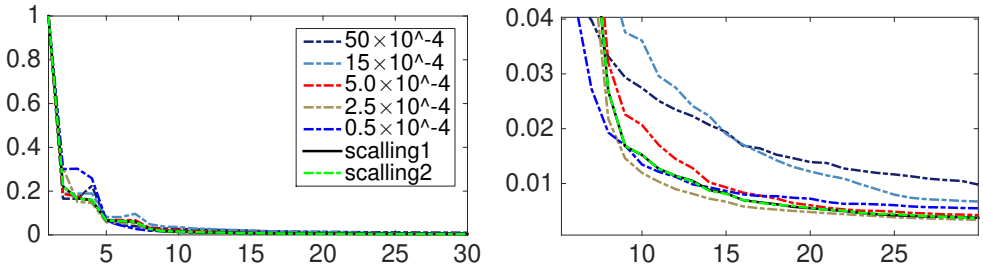

Figure 4.33: The misfit curves of different scaling factors, the scaling 1 uses the term $\partial\tau(v_p(\boldsymbol{x}))/\partial v_p(\boldsymbol{x})$ as a dynamic scaling factor, and the scaling 2 uses the spatial mean value of $\partial\tau(v_p(\boldsymbol{x}))/\partial v_p(\boldsymbol{x})$, where $\boldsymbol{x}$ is the spatial coordinates.

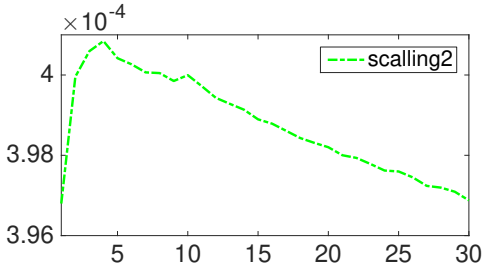

Figure 4.34: The scaling factor obtained by the spatial mean value of $\partial\tau(v_p(\boldsymbol{x}))/\partial v_p(\boldsymbol{x})$ for each iteration, where $\boldsymbol{x}$ is the spatial coordinates.

4.5 Conclusion

We have proposed a hybrid inversion strategy based on modification of the parameterization leading to a different gradient, by explicitly introducing the kinematic relationship. The total gradient is a combination between the partial derivatives of the objective function with v_p and τ. $\partial\tau(v_p)/\partial v_p$ is the linking term between v_p gradient and τ gradient. The term acts as a dynamic scaling factor. It is derived for a fixed v_k and modifies the v_p gradient to retrieve the parameters.

To apply the hybrid strategy, we first update the kinematic velocity, then decouple the parameters based on a fixed v_k. This strategy is a guided inversion with faster convergence speed. The four tested models are mainly dominated by transmitted waves. The kinematic velocity is relatively easy to be obtained from the transmitted waves, compared with the reflections. With a good approximated v_k, the hybrid strategy mitigates cross-talks and has a lower final misfit than conventional strategies, including the sequential and simultaneous inversions.

4.6 Appendix I: Introduction to FWI

The theory of full waveform inversion is based on Tarantola (1984a); Plessix (2006b); Virieux and Operto (2009). Based on Taylor expression, $\boldsymbol{m}$ practically can be decomposed into an initial model $\boldsymbol{m_0}$ with a perturbation of model $\Delta\boldsymbol{m}$ using a local optimization method based on gradient searching.

$$\boldsymbol{m} = \boldsymbol{m_0} + \Delta\boldsymbol{m} \tag{4.17}$$

The objective function can be written as a Taylor expansion in vicinity of $\boldsymbol{m_0}$

$$\mathcal{J}(\boldsymbol{m_0}+\Delta\boldsymbol{m}) = \mathcal{J}(\boldsymbol{m_0})+\nabla_m\mathcal{J}(\boldsymbol{m_0})\Delta\boldsymbol{m}+\frac{1}{2}\nabla_m^2\mathcal{J}(\boldsymbol{m_0})\Delta\boldsymbol{m}^2+\mathcal{O}(\Delta\boldsymbol{m}^3). \tag{4.18}$$

∇_m is the derivative with respect to $\boldsymbol{m}$. Taking the derivatives with respect to $\boldsymbol{m}$ on the both side of equation 4.18, with the minimum of the misfit function in vicinity of $\boldsymbol{m_0}$ reached, the left part vanishes and the right part neglect small perturbations, leading to

$$0 = \nabla_m\mathcal{J}(\boldsymbol{m_0}) + \nabla_m^2\mathcal{J}(\boldsymbol{m_0})\Delta\boldsymbol{m}. \tag{4.19}$$

From 4.19, the perturbed model can be obtain from

$$\Delta\boldsymbol{m} = -\left[\nabla_m^2\mathcal{J}(\boldsymbol{m_0})\right]^{-1}\nabla_m\mathcal{J}(\boldsymbol{m_0}), \tag{4.20}$$

where $\nabla_m\mathcal{J}(\boldsymbol{m_0})$ is the first-order derivative of objective function (gradient), and $\nabla_m^2\mathcal{J}(\boldsymbol{m_0})$ is second-order derivative of the objective function called Hessian matrix. In an explicit format, $\nabla_m\mathcal{J}(\boldsymbol{m_0})$ is written as

$$\begin{aligned}\nabla_m\mathcal{J}(\boldsymbol{m_0}) &= \frac{\partial}{\partial\boldsymbol{m}}\left(\frac{1}{2}\|d_{cal}-d_{obs}\|^2\right), \\ &= \left(\frac{\partial d_{cal}}{\partial\boldsymbol{m}}\right)^{\dagger}(d_{cal}-d_{obs}), \\ &= {J_0}^{\dagger}\delta d.\end{aligned} \tag{4.21}$$

δd is the data difference between the calculated and observed data. $\dagger$ is the transpose operator. J_0 is the data derivative with respect to model $\boldsymbol{m}$, which is also called sensitivity or Fréchet derivative matrix. With the explicit format of $\nabla_m\mathcal{J}(\boldsymbol{m_0})$, the Hessian matrix is written as

$$\nabla_m^2\mathcal{J}(\boldsymbol{m_0}) = {J_0}^{\dagger}J_0 + \frac{\partial J_0}{\partial\boldsymbol{m}}\delta d. \tag{4.22}$$

The Hessian matrix involves a second-order derivative with respect to $\boldsymbol{m}$, it is computationally expensive. The perturbed model with the explicit formats of $\nabla_m\mathcal{J}(\boldsymbol{m_0})$ and $\nabla_m^2\mathcal{J}(\boldsymbol{m_0})$ is express as

$$\Delta\boldsymbol{m} = -\left[{J_0}^{\dagger}J_0 + \frac{\partial J_0}{\partial\boldsymbol{m}}\delta d\right]^{-1}{J_0}^{\dagger}\delta d. \tag{4.23}$$

The best solution of $\boldsymbol{m}$ can be obtained by the iteratively updating the $\Delta\boldsymbol{m}$ until the objective function converges or satisfies with convergence criterion.

$$\boldsymbol{m_{k+1}} = \boldsymbol{m_k} - \left[{J_k}^\dagger J_k + \frac{\partial J_k}{\partial \boldsymbol{m}} \delta d^k \right]^{-1} {J_k}^\dagger \delta d^k \tag{4.24}$$

is the recursive optimization. $\boldsymbol{m_{k+1}}$ is updated by the previous model $\boldsymbol{m_k}$ plus the model perturbation. J_k denotes the d^k_{cal} derivative with respect to model and δd^k represents the data difference between d^k_{cal} and d_{obs}, where d^k_{cal} is generated by forward modeling based on model $\boldsymbol{m_k}$.

However, the Hessian matrix is hard to obtain due to computation limitation. The inverse of Hessian matrix contains many singularities because of the ill-posed problem. The different ways of incorporating of inverse of Hessian matrix divide the optimization methods into conjugate-gradient, Quasi-Newton, and Newton methods. Conjugate gradient approximates the inverse of Hessian as a positive scalar λ with a conjugate searching direction.

Based on conjugate gradient method, the model updating is obtain by

$$\boldsymbol{m_{k+1}} = \boldsymbol{m_k} - \lambda_k \frac{\alpha_{\boldsymbol{m}}}{\max\left(|\nabla_{\boldsymbol{m}} \mathcal{J}(\boldsymbol{m_0})|\right)} \boldsymbol{p}^k \Big|_{m=m_k}. \tag{4.25}$$

$\alpha_{\boldsymbol{m}}$ are scalars called unitary step length, which determine the basic unitary searching length for each parameters. $\alpha_{\boldsymbol{m}}$ are estimated by empirically. For different parameters, $\alpha_{\boldsymbol{m}}$ depend on the gradient scaling. $\max\left(|\nabla_{\boldsymbol{m}} \mathcal{J}(\boldsymbol{m_0})|\right)$ is maximum of absolute value of first gradient of each parameter to normalize the gradients during each iteration. The λ_k is the searching step length which is determined by a parabolic curve fitting method (Nocedal and Wright, 2006). $\boldsymbol{p}^k$ is the searching direction determined by conjugate gradient given as

$$\boldsymbol{p}^k = \nabla_{\boldsymbol{m}} \mathcal{J}(\boldsymbol{m_k}) + \beta^k \boldsymbol{p}^{k-1}, \tag{4.26}$$

β^k is used to determine the conjugate direction (Polak and Ribière, 1969; Nocedal and Wright, 2006) given as

$$\beta^k = \frac{\langle \nabla_{\boldsymbol{m}} \mathcal{J}(\boldsymbol{m_k}) - \nabla_{\boldsymbol{m}} \mathcal{J}(\boldsymbol{m_{k-1}}) | \nabla_{\boldsymbol{m}} \mathcal{J}(\boldsymbol{m_k}) \rangle}{\| \nabla_{\boldsymbol{m}} \mathcal{J}(\boldsymbol{m_k}) \|^2}. \tag{4.27}$$

4.7 Appendix II: Gradient of the objective function

We use L = 5 standard linear solid (SLS) to simulate constant Q with one τ and five τ_σ^l. As we presented before, 5 SLS produces a good approximation for constant Q from 1.5 Hz to 100 Hz. We rewrite the visco-acoustic wave equation in frequency domain.

$$\begin{cases} i\omega p + \kappa(L\tau+1)\left[\frac{\partial v_x}{\partial x} + \frac{\partial v_z}{\partial z}\right] + \sum_{l=1}^{L} r_p^l = f(x_s,\omega), \\ i\omega v_x + \frac{1}{\rho}\frac{\partial p}{\partial x} = 0, \\ i\omega v_z + \frac{1}{\rho}\frac{\partial p}{\partial z} = 0, \\ (i\omega + \frac{1}{\tau_\sigma^l})r_p^l + \frac{1}{\tau_\sigma^l}\tau\kappa\left(\frac{\partial v_x}{\partial x} + \frac{\partial v_z}{\partial z}\right) = 0, \qquad l =\in [1, L], \end{cases} \tag{4.28}$$

where κ is the relaxed modulus defined as the ρv_p^2. v_p is the P wave velocity and ρ is the density. p, v_x v_z and associated memory variables r_p^l are wave fields. The forward modeling is written as a operator format

$$\mathcal{S}(\boldsymbol{m})u(\boldsymbol{x},\omega) = \mathcal{F}, \tag{4.29}$$

where $\mathcal{S}(\boldsymbol{m})$ is the wave-equation operator in terms of the model parameters $\boldsymbol{m}$, $u(\boldsymbol{x},\omega)$ is the whole wave fields in whole spatial space $\boldsymbol{x}$, and $\mathcal{F}$ is the source term. The observed data $d_{cal}(\boldsymbol{s},\boldsymbol{r},\omega)$ is projected to source and receiver positions from the whole $u(\boldsymbol{x},\omega)$.

$$\mathcal{M}u = d_{cal}(\boldsymbol{s},\boldsymbol{r},\omega), \tag{4.30}$$

where $\mathcal{M}$ is projection operator defined as $\int d\boldsymbol{x}\delta(\boldsymbol{x}-\boldsymbol{s})\delta(\boldsymbol{x}-\boldsymbol{r})$.

The objective function can be extended as a Lagrangian formulation depending on $(\boldsymbol{m},\boldsymbol{u},\boldsymbol{\lambda})$. The model parameters include v_p and τ, the wave fields include p, v_x, v_z and r_p^l. λ are the adjoint state variables associated with p, v_x and v_z, denoted as λ_p, λ_{v_x}, λ_{v_z}, $\lambda_{r_p}^l$, which are all independent. The Lagrangian formulation is

$$\begin{aligned} \mathcal{L}(\boldsymbol{m},\boldsymbol{u},\boldsymbol{\lambda}) &= \frac{1}{2}\|\mathcal{M}u(\boldsymbol{x},\omega) - d_{obs}(\boldsymbol{s},\boldsymbol{r},\omega)\|^2 \\ &- < \lambda_p, i\omega p + \kappa(L\tau+1)(\frac{\partial v_x}{\partial x} + \frac{\partial v_z}{\partial z}) + \sum_{l=1}^{L} r_p^l - f(x_s,\omega) > \\ &- < \lambda_{v_x}, i\omega v_x + \frac{1}{\rho}\frac{\partial p}{\partial x} > - < \lambda_{v_z}, i\omega v_z + \frac{1}{\rho}\frac{\partial p}{\partial z} > \\ &- \sum_{l=1}^{L} < \lambda_{r_p}^l, (i\omega + \frac{1}{\tau_\sigma^l})r_p^l + \frac{1}{\tau_\sigma^l}\tau\kappa(\frac{\partial v_x}{\partial x} + \frac{\partial v_z}{\partial z}) > . \end{aligned} \tag{4.31}$$

The Lagrangian equation satisfies

$$\frac{\partial \mathcal{L}(\boldsymbol{m},\boldsymbol{u},\boldsymbol{\lambda})}{\partial \boldsymbol{\lambda}} = 0 \tag{4.32}$$

$$\frac{\partial \mathcal{L}(\boldsymbol{m},\boldsymbol{u},\boldsymbol{\lambda})}{\partial \boldsymbol{u}} = 0 \tag{4.33}$$

Equation 4.32 is called the state equation, which has to be satisfied by forward modeling of visco-acoustic wave equation. Equation 4.33 is called adjoint state equation, which gives as

$$\begin{array}{l}
\frac{\partial \mathcal{L}(\boldsymbol{m},\boldsymbol{u},\boldsymbol{\lambda})}{\partial p} = 0 = \mathcal{M}^{\dagger}(\mathcal{M}u(\boldsymbol{x},\omega) - d_{obs})(\boldsymbol{s},\boldsymbol{r},\omega) + i\omega\lambda_p + \frac{\partial}{\partial x}(\frac{\lambda_{v_x}}{\rho}) + \frac{\partial}{\partial z}(\frac{\lambda_{v_z}}{\rho}), \\
\frac{\partial \mathcal{L}(\boldsymbol{m},\boldsymbol{u},\boldsymbol{\lambda})}{\partial v_x} = 0 = \frac{\partial}{\partial x}\left[\kappa(L\tau+1)\lambda_p\right] + i\omega\lambda_{v_x} + \frac{\partial}{\partial x}\left(\sum_{l=1}^{L}\frac{1}{\tau_\sigma^l}\tau\kappa\lambda_{r_p}^l\right), \\
\frac{\partial \mathcal{L}(\boldsymbol{m},\boldsymbol{u},\boldsymbol{\lambda})}{\partial v_z} = 0 = \frac{\partial}{\partial z}\left[\kappa(L\tau+1)\lambda_p\right] + i\omega\lambda_{v_z} + \frac{\partial}{\partial z}\left(\sum_{l=1}^{L}\frac{1}{\tau_\sigma^l}\tau\kappa\lambda_{r_p}^l\right), \\
\frac{\partial \mathcal{L}(\boldsymbol{m},\boldsymbol{u},\boldsymbol{\lambda})}{\partial r_p^l} = 0 = (i\omega - \frac{1}{\tau_\sigma^l})\lambda_{r_p}^l - \lambda_p, \qquad l =\in [1,L].
\end{array} \tag{4.34}$$

The adjoint equation can be solved in time domain as

$$\begin{cases}
\frac{\partial \lambda_p}{\partial t} + \frac{1}{\rho}(\frac{\partial \lambda_{v_x}}{\partial x} + \frac{\partial \lambda_{v_z}}{\partial z}) = -\mathcal{M}^{\dagger}(\mathcal{M}u(\boldsymbol{x},\omega) - d_{obs}), \\
\frac{\partial \lambda_{v_x}}{\partial t} + \frac{\partial}{\partial x}\left[\kappa(L\tau+1)\lambda_p\right] + \frac{\partial}{\partial x}\left(\sum_{l=1}^{L}\frac{1}{\tau_\sigma^l}\tau\kappa\lambda_{r_p}^l\right) = 0, \\
\frac{\partial \lambda_{v_z}}{\partial t} + \frac{\partial}{\partial z}\left[\kappa(L\tau+1)\lambda_p\right] + \frac{\partial}{\partial z}\left(\sum_{l=1}^{L}\frac{1}{\tau_\sigma^l}\tau\kappa\lambda_{r_p}^l\right) = 0, \\
\frac{\partial \lambda_{r_p}^l}{\partial t} - \frac{\lambda_{r_p}^l}{\tau_\sigma^l} - \lambda_p = 0, \qquad l =\in [1,L].
\end{cases} \tag{4.35}$$

The adjoint state equation is solved for $\boldsymbol{\lambda}\big|_{t=T} = 0$. $-\mathcal{M}^{\dagger}(\mathcal{M}u(\boldsymbol{x},\omega) - d_{obs})$ is the adjoint source. To satisfy the initial condition, the adjoint state equation is solved with a back-propagation way, from the last time $t = T$ to the initial time $t = 0$. The last equation in equation 4.35 increases exponentially from time $t = 0$ to $t = T$. The back-propagation turns the equation as a exponentially decreasing function, which satisfies the physical meaning due to attenuation.

Finally, the gradient of the objective function becomes

$$\begin{array}{l}
\frac{\partial \mathcal{L}(\boldsymbol{m},\boldsymbol{u},\boldsymbol{\lambda})}{\partial v_p} = \frac{\partial \mathcal{J}(v_p,\tau)}{\partial v_p} + 2\rho v_p(L\tau+1)(\frac{\partial v_x}{\partial x} + \frac{\partial v_z}{\partial z})\lambda_p + 2\rho v_p\sum_{l=1}^{L}\frac{\tau}{\tau_\sigma^l}(\frac{\partial v_x}{\partial x} + \frac{\partial v_z}{\partial z})\lambda_{r_p}^l, \\
\frac{\partial \mathcal{L}(\boldsymbol{m},\boldsymbol{u},\boldsymbol{\lambda})}{\partial \tau} = \frac{\partial \mathcal{J}(v_p,\tau)}{\partial \tau} + (L\kappa+1)(\frac{\partial v_x}{\partial x} + \frac{\partial v_z}{\partial z})\lambda_p + \sum_{l=1}^{L}\frac{1}{\tau_\sigma^l}\kappa(\frac{\partial v_x}{\partial x} + \frac{\partial v_z}{\partial z})\lambda_{r_p}^l.
\end{array} \tag{4.36}$$

The gradient of objection function (Equations 4.11, 4.12) is obtained by cross-correlating the forward propagation wave fields with the back-propagation wave fields.

$$\begin{array}{l}
\frac{\partial \mathcal{J}(v_p,\tau)}{\partial v_p} = -\int_0^T 2\rho v_p(L\tau+1)(\frac{\partial v_x}{\partial x} + \frac{\partial v_z}{\partial z})\lambda_p + 2\rho v_p\sum_{l=1}^{L}\frac{\tau}{\tau_\sigma^l}(\frac{\partial v_x}{\partial x} + \frac{\partial v_z}{\partial z})\lambda_{r_p}^l, \\
\frac{\partial \mathcal{J}(v_p,\tau)}{\partial \tau} = -\int_0^T (L\kappa+1)(\frac{\partial v_x}{\partial x} + \frac{\partial v_z}{\partial z})\lambda_p + \sum_{l=1}^{L}\frac{1}{\tau_\sigma^l}\kappa(\frac{\partial v_x}{\partial x} + \frac{\partial v_z}{\partial z})\lambda_{r_p}^l.
\end{array} \tag{4.37}$$

To verify the accuracy of the gradient, we compare the gradient with a finite difference method, given by

$$\frac{\partial \mathcal{J}(v_p,\tau)}{\partial v_p} = \lim_{\Delta v_p \to 0}\frac{\mathcal{J}(v_p+\Delta v_p) - \mathcal{J}(v_p-\Delta v_p)}{2\Delta v_p} \tag{4.38}$$

$$= \lim_{\Delta v_p \to 0} \frac{\frac{1}{2}\|d_{obs} - d_{cal}(v_p + \Delta v_p)\|^2 - \frac{1}{2}\|d_{obs} - d_{cal}(v_p - \Delta v_p)\|^2}{2\Delta v_p}$$

Compared with adjoint state approach, the finite difference approach is very expensive. The initial model is a homogeneous model with v_p = 2000 m/s. The true model is a two-layer model, 2000 m/s and 2500 m/s, the interface is at the depth of 195 m. The Q model is homogeneous with Q = 50 (τ = 0.023). For the finite difference approach, the perturbation of velocity is 1 m/s. The comparison between the velocity gradients obtained from the adjoint state method and from the finite difference method (Figure 4.35) validates the accuracy of gradients computed from adjoint-state method.

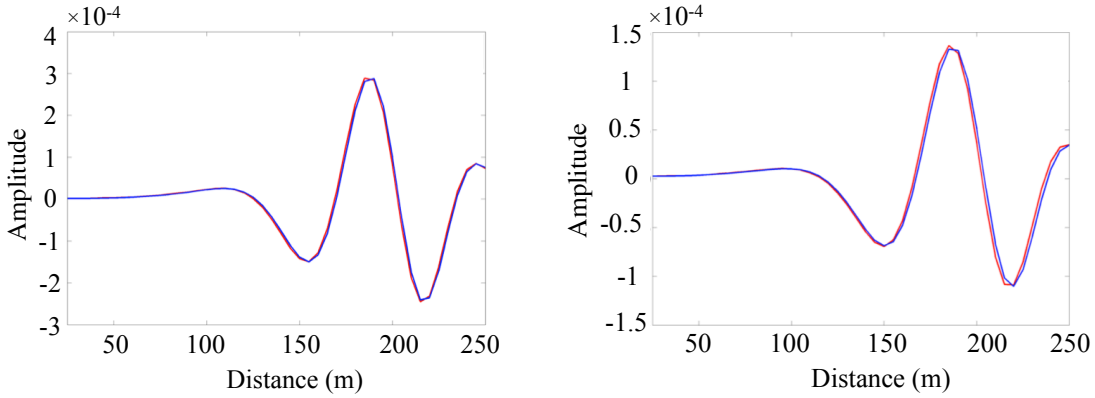

Figure 4.35: Velocity gradient comparison between velocity gradient $\partial\mathcal{J}(v_p, \tau)/\partial v_p$ obtained by finite difference (red) and the adjoint state (blue) methods, the left panel are the gradients without attenuation, the right panel are the gradients with Q = 50.

4.8 Appendix III: Implicit derivative $\partial\tau/\partial v_p$

Based on Equation 4.8, all the different combinations of v_p and τ have the same kinematic velocity. Taking perturbations of v_p and τ on the two sides, the equation becomes

$$0 = \frac{\partial f}{\partial v_p}\delta v_p + \frac{\partial f}{\partial \tau}\delta\tau. \tag{4.39}$$

Then the ratio between perturbations of v and τ is given as

$$\frac{\delta\tau}{\delta v_p} = -\frac{\partial f}{\partial v_p}\Big/\frac{\partial f}{\partial \tau}. \tag{4.40}$$

With the small perturbations, the derivative of τ with respect to v_p is expressed as

$$\frac{\partial\tau}{\partial v_p}\Big|_{v_k} = -\frac{\partial f}{\partial v_p}\Big/\frac{\partial f}{\partial \tau}. \tag{4.41}$$

For different kinematic velocity, we have different derivatives (Figure 4.36).

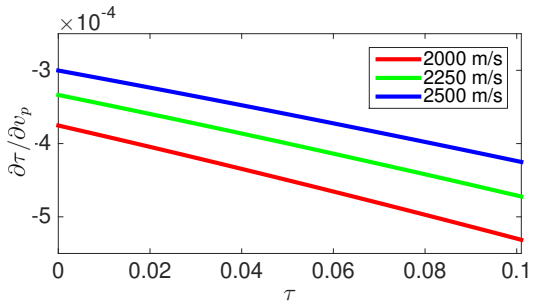

Figure 4.36: $\partial\tau/\partial v_p$ for fixed v_k of 2000 m/s (red), 2250 m/s (green) and 2500 m/s (blue).

4.9 Appendix IV: Equivalence between two ways for updating v_k

As we discussed in Section 4.2.2.4, there are two solutions for updating v_k. The first one is that v_k is updated by a modified gradient for fixed τ (Equations 4.15, 4.16). The other way first starts with mono-parameter v_p inversion for fixed τ (Strategy A), and a subsequent v_k is obtained based on Equation 4.8.

First, we derive the relation between v_k and v_p for fixed τ. We use the same approach as Appendix 4.8. v_p is the function of v_k for a fixed τ based on Equation 4.8. Taking perturbations of v_k and v_p on the two sides, the equation leads to

$$\delta v_k = \frac{\partial f}{\partial v_p}\delta v_p + 0 \tag{4.42}$$

The ratio between perturbations of v_k and v_p is given by

$$\frac{\delta v_k}{\delta v_p} = \frac{\partial f}{\partial v_p}. \tag{4.43}$$

The relation between v_k and v_p for fixed τ can be written by an explicit way

$$v_k(\boldsymbol{x}) = f[v_p(\boldsymbol{x}), \tau(\boldsymbol{x})] = v_p(\boldsymbol{x})\ \tilde{f}[\tau(\boldsymbol{x})], \tag{4.44}$$

where $\boldsymbol{x}$ is spatial locations. The linear relation between v_k and v_p for fixed τ leads to

$$\frac{v_k}{v_p} = \frac{\partial v_k}{\partial v_p}\Big|_\tau = \tilde{f}(\tau) = \frac{\delta v_k}{\delta v_p} = \frac{\partial f}{\partial v_p}\Big|_\tau, \tag{4.45}$$

where $|_\tau$ means that the τ is fixed.

The two ways for updating $v_k(\boldsymbol{x})$ need a initial $v_p^0(\boldsymbol{x})$, and initial $v_k^0(\boldsymbol{x}) = v_p^0(\boldsymbol{x})\,\tilde{f}[\tau(\boldsymbol{x})]$. The solution for updating v_k for fixed τ is

$$\begin{aligned} v_k &= v_k^0 - H_{v_k}^{-1}\frac{\partial J}{\partial v_k}\Big|_\tau, \\ &= v_p^0\,\tilde{f}[\tau(\boldsymbol{x})] - \tilde{f}[\tau(\boldsymbol{x})]H_{v_p}^{-1}\frac{\partial J}{\partial v_p}\Big|_\tau, \\ &= \tilde{f}[\tau(\boldsymbol{x})]\left(v_p^0 - H_{v_p}^{-1}\frac{\partial J}{\partial v_p}\Big|_\tau\right), \end{aligned} \tag{4.46}$$

where we have

$$\begin{aligned} \frac{\partial J}{\partial v_k}\Big|_\tau &= \frac{\partial v_p}{\partial v_k}\Big|_\tau\frac{\partial J}{\partial v_p}\Big|_\tau, \\ &= \frac{1}{\tilde{f}[\tau(\boldsymbol{x})]}\frac{\partial J}{\partial v_p}\Big|_\tau, \end{aligned} \tag{4.47}$$

and

$$\begin{aligned} H_{v_k}\Big|_\tau &= \frac{\partial}{\partial v_k}\left(\frac{\partial J}{\partial v_k}\right)\Big|_\tau, \\ &= \frac{1}{\tilde{f}[\tau(\boldsymbol{x})]}\frac{\partial}{\partial v_p}\left(\frac{1}{\tilde{f}[\tau(\boldsymbol{x})]}\frac{\partial J}{\partial v_p}\right)\Big|_\tau, \\ &= \frac{1}{\tilde{f}^2[\tau(\boldsymbol{x})]}H_{v_p}\Big|_\tau. \end{aligned} \tag{4.48}$$

The third formula of Equation 4.46 is composed of updating v_p for fixed τ

$$v_p = v_p^0 - H_{v_p}^{-1}\frac{\partial J}{\partial v_p}\Big|_\tau, \tag{4.49}$$

and the following step for updating v_k based on Equation 4.44

$$v_k = \tilde{f}[\tau(\boldsymbol{x})]v_p. \tag{4.50}$$

The two solutions are equivalent. In this thesis, we apply the conjugate gradient method without estimation of the Hessian matrix. The model updates are simplified as the searching step multiplying the gradient of objective function.

Chapter 5

Application on the Marmousi dataset

Contents

Résumé du chapitre 5

Dans ce chapitre, nous comparons trois stratégies : inversion mono-paramètre, inversion simultannée et inversion hybride sur l'exemple synthetique Marmousi. Du bruit gaussien est ajouté pour évaluer la robustesse de l'approche hybride. Enfin, une stratégie de continuation en fréquences, depuis les basses vers les hautes fréquences, est évaluée.

Abstract

In this chapter, we apply and compare three strategies, including mono-velocity inversion, simultaneous inversion and the hybrid inversion strategy described in Chapter 4, on the Marmousi model. During the discussion, Gaussian noise is added to the data to test the robustness of the hybrid strategy. We evaluate the mono-parameter τ inversion to discuss cross-talks between parameters and the reason of artifacts on τ. Finally, frequency continuation inversion is applied when higher frequencies are progressively included in the inversion scheme.

5.1 Introduction

FWI deals with all kinds of waves for inversion, including transmissions and reflections. Information contained in different waves combines the tomography mode and migration mode to build macro and fine structures (Mora, 1989). Transmissions / diving waves and post-critical reflections are applied to retrieve the long and intermediate wavelengths of the structures, regarded as an efficient scheme of FWI (Virieux and Operto, 2009; Zhou et al., 2015). This information is utilized to retrieve velocity and attenuation models using visco-acoustic / visco-elastic FWI (Prieux et al., 2013; Plessix et al., 2016). The 2D synthetic Middle-East model in Chapter 4 mainly focuses on the diving waves to build macro models. The traveltime of transmitted waves are connected with traveling distance and kinematic velocity straightforwardly. It is relatively easier to retrieve the kinematic velocity from transmitted waves, then further update v_p and τ. Compared with transmitted waves, the phases of reflections are more strongly affected by the kinematic velocity, depth of interfaces and interference overlaps of reflected waves on thin layers. The phase information explains the kinematic velocity as the combined effects of interface depth, and velocity and τ values inside each layer.

In this chapter, we focus on the reflections to retrieve the velocity and Q in the Marmousi model. The Marmousi model is composed by faults with strong horizontal and vertical velocity variations. Except for direct waves, reflections are the dominated wavefields on this model due to limited offset acquisition. We test the three strategies (Section 5.3) on the Marmousi model to validate the feasibility of the hybrid inversion strategy proposed in Chapter 4.

5.2 Marmousi model and acquisition system

The Marmousi model in this section is extracted from the entire Marmousi (Figure 5.1a). The model size is 6 km laterally and 2.2 km in depth with a 200 m water layer at the top. The space grid size is 20 m in both directions. 76 sources are located all over the surface.

The receivers are deployed at the interval of 20 m on the both sides of the source with the maximum offset of 3 km. The true τ model has two anomalies (Figure 5.1b). In terms of Q, the anomaly in light red has a Q value around 22 (τ = 0.052). The other anomaly in dark red has a Q value around 17 (τ = 0.0689). The initial velocity model is obtained by smoothing the true model (Figure 5.1c). The initial τ model is homogeneous (Q is 1000) (Figure 5.1d). The source is a Ricker wavelet with central frequency 4 Hz. The forward simulation time lasts 4 seconds.

5.3 Results

Three inversion strategies in this part include:

- Strategy A: mono-velocity inversion for fixed τ value.
- Strategy B: simultaneous inversion for v_p and τ.
- Hybrid Strategy (Strategy H): combination of Strategy A and Strategy C. Strategy A is applied to update the kinematic velocity v_k. Strategy C is the modified inversion to decouple v_p and τ based on the fixed v_k. The Strategy A and C are applied in an alternate sequence. Every 4 A-inversions are alternated with 4-C inversions (the workflow in Chapter 4).

After 5 iterations, the shallow part of v_p is the main updated areas for three inversion strategies (Figures 5.2a, 5.3a, 5.4a). τ is not updated for Strategy A, because it is fixed (Figure 5.2c). The shallow part τ is the main updated area for Strategy B (Figure 5.3b) and the hybrid strategy (Figure 5.4b). More iterations are needed to further analyze the inversions.

After 80 iterations with the three strategies, the shallow part of v_p is well-retrieved (Figures 5.2b, 5.3c, 5.4c). But v_p value of the bottom part is lower than the true value, due to weak energy of reflections from the deep layers. A proper pre-conditioner for enhancing gradients of the deep layers could improve the inversion.

We first analyze the retrieved v_p of Strategy A. Taking one vertical section from the results with Strategy A at the position x = 2500 m (Figure 5.6), the velocity profile matches well the true model only up to 1 km depth, but some obvious interface shifts occur at depth of 1.4 km and 1.8 km in the v_p profile. From the data comparison (Figure 5.10), the phase matches well, but the amplitude of the calculated data shows difference with the observed data without considering τ. This kind of shifts means that the kinematic velocity is translated into the combination of shallow depth and lower v_p (for the detailed analysis of retrieved v_p with Strategy B and the hybrid strategy, we discuss the results after 400 iterations in later paragraphs.).

τ result of Strategy B after 80 iterations shows that the inversion successfully detects the anomalies, except for large artifacts on the bottom (Figure 5.3d). The hybrid strategy after 80 iterations locates the τ anomalies with lower values compared to the true values (Figure 5.4d). Obvious artifacts are observed on the top of the retrieved τ model. More iterations are needed to improve the kinematic velocity v_k, and further update v_p and τ.

After 400 iterations, v_p and τ results (Figure 5.5a, c) are similar to the results after 80 iterations (Figure 5.3c, d) with Strategy B. Inverted v_p has a good resolution on the shallow part, but under-estimated values on the bottom. Inverted τ has strong artifacts on the bottom. The v_p result of the hybrid strategy after 400 iterations (Figure 5.5b) is similar to the previous result after 80 iterations. The τ result (Figure 5.5d) shows that the two anomalies are retrieved, but some artifacts are distributed on both the top and bottom parts. The τ anomalies on the top part is lightened.

We extract 3 sections from the results of Strategy B and the hybrid strategy at the position x = 2500 m, 3320 m and 4000 m, respectively (Figure 5.7). The three positions correspond to the areas, without τ anomaly, with the left τ anomaly and the right τ anomaly, respectively. We first analyze the v_p results. The v_p profiles of Strategy B (Figure 5.7a, b, c) and the hybrid strategy (Figure 5.7d, e, f) show the retrieved v_p matches well the true model on the shallow part. On the bottom part, the retrieved v_p is lower than the true value. The thin layers are not reconstructed due to lacking high frequencies. The τ result of Strategy B (Figure 5.7g, h, i) shows severe variations along the depth, although the structure of true τ is smooth except for two anomalies. The inverted two τ anomalies have larger values and a shift on the bottom interface of the anomalies. We observe that the lower under-estimated v_p value is consistent with the larger τ value on the bottom, e.g., the τ artifacts around 1.3–1.5 km at position x = 2500 m (Figure 5.7g), 1.6–1.8 km at position x = 3320 m (Figure 5.7h) and 1.7–1.9 km at position x = 4000 m (Figure 5.7i). The structure of inverted τ has relevance to v_p structure, which shows cross-talks between two parameters. The τ result of the hybrid strategy (Figure 5.7j, k, l) shows that the two anomalies are located around the correct position but with a vertical deeper shift. The anomaly value is close to the true model, especially for the anomaly at position x = 3320 m. The vertical shift is caused by the under-estimated low kinematic velocity v_k. The τ structure is related to the ratio of v_k and v_p based on kinematic relationship in Equation 4.8 (Figure 5.7m, n, o). For example, the anomaly at position x = 3320 m, the τ anomaly is located around 1.3–1.5 km (Figure 5.7k). The interfaces of v_p and v_k at depth of 1.3 km match well (Figure 5.7n), leading to the matches between observed and calculated waves reflected on this interface. To match the waves reflected on the bottom interface, the v_k has larger value than v_p, and a downshifted interface, leading to data fitting (the arrows in Figure 5.7n). We simulate one shot gather at position x = 3320 m by using $v_p = v_k$ and by setting τ as 0. The phase of calculated data matches well the observed data, except for the amplitude difference (Figure 5.13).

From the misfit curves for the 3 strategies after 400 iterations (Figure 5.8), the misfit

of Strategy A stops decreasing after 80 iterations due to the lack of τ updating. Strategy B has the smallest final misfit. The misfit of the hybrid strategy decreases slowly until a close misfit as Strategy B. The slow decreasing is due to the v_k updating. One shot data comparison at horizontal position x = 3320 m shows the large misfit of Strategy A (Figures 5.9 and 5.10). The final data misfit for Strategy B (Figure 5.11) and the hybrid strategy (Figure 5.12) is lower than 1%, and the data difference is mainly distributed between the later arrivals. The good data matches of both Strategy B and the hybrid strategy indicate that there are non-unique solutions, due to cross-talks between parameters, limited acquisition system, resolution of limited frequencies and so on.

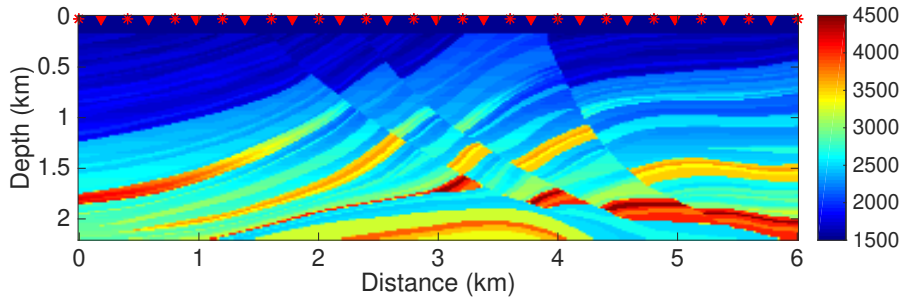

(a) True v_p model

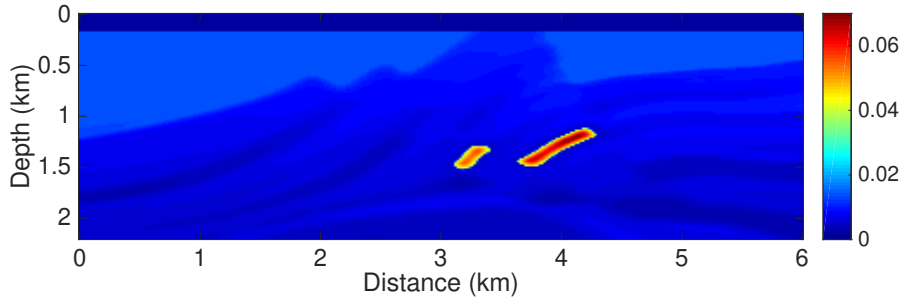

(b) True τ model

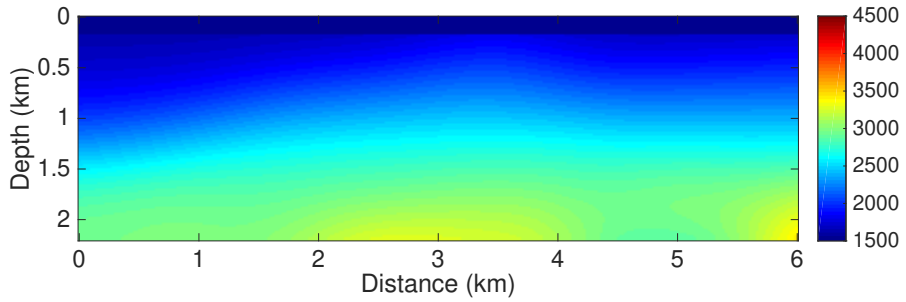

(c) Initial v_p model

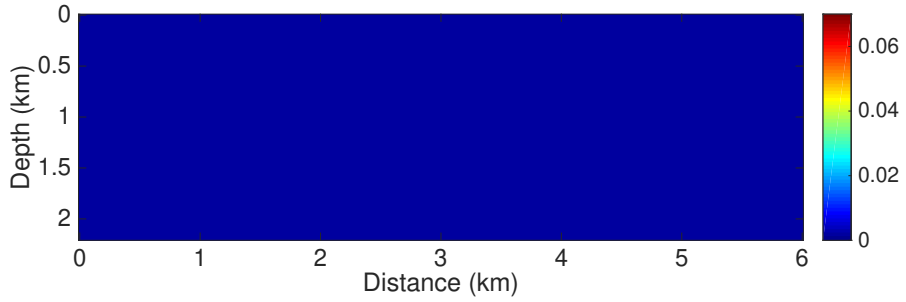

(d) Initial τ model

Figure 5.1: v_p and τ models: the true velocity values (a) go from 1500 m/s (water layer) to 4500 m/s (dark red on the bottom). The true τ model (b) is from 0.0011 (Q = 1000) to 0.0689 (Q = 17). τ in the water layer is set as 0.0011 (Q = 1000). The τ anomaly in light red is around 0.052 (Q = 22) and the right τ anomaly is around 0.0689 (Q = 17). The initial velocity model (c) is a smooth model. The initial τ model (d) is homogeneous with τ = 0.0011 (Q = 1000).

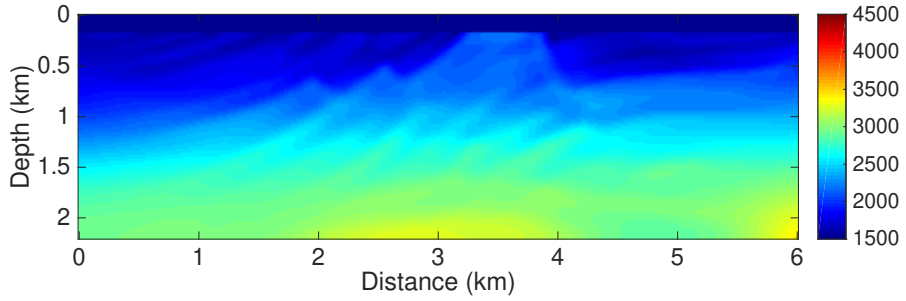

(a) 5 iterations over v_p with Strategy A

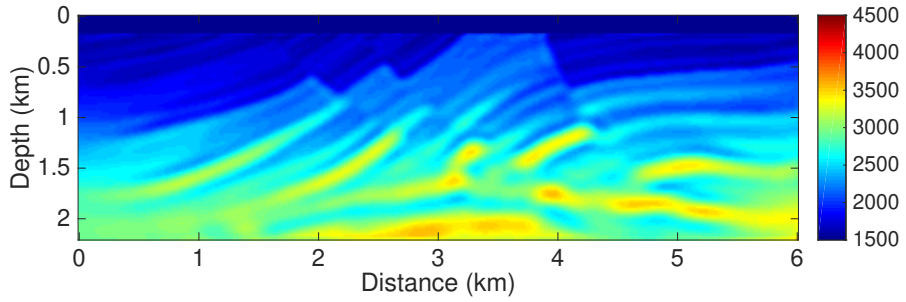

(b) 80 iterations over v_p with Strategy A

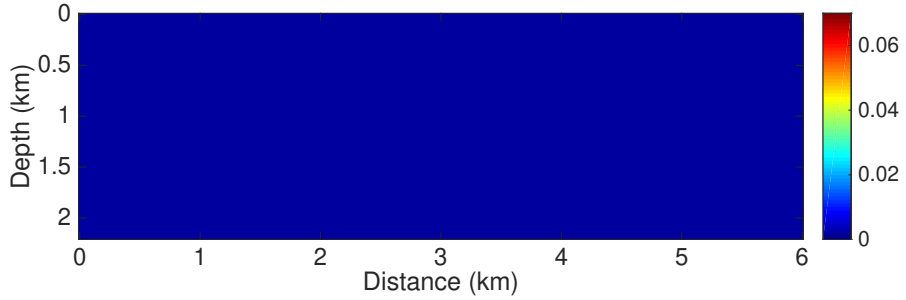

(c) Fixed τ with Strategy A

Figure 5.2: Inversion results of Strategy A after 5 iterations (a) and 80 iterations (b) over v_p, with τ always being fixed (c).

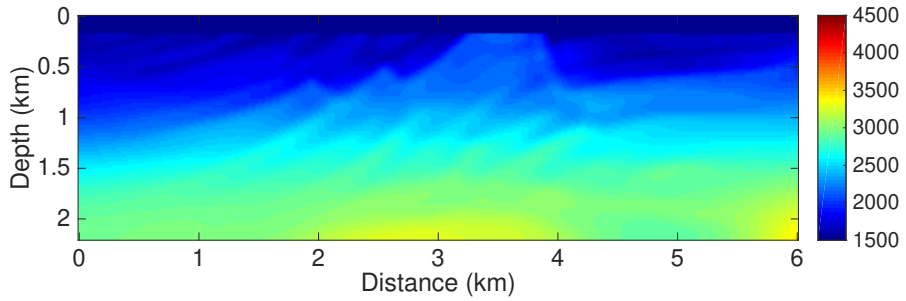

(a) 5 iterations over v_p with Strategy B

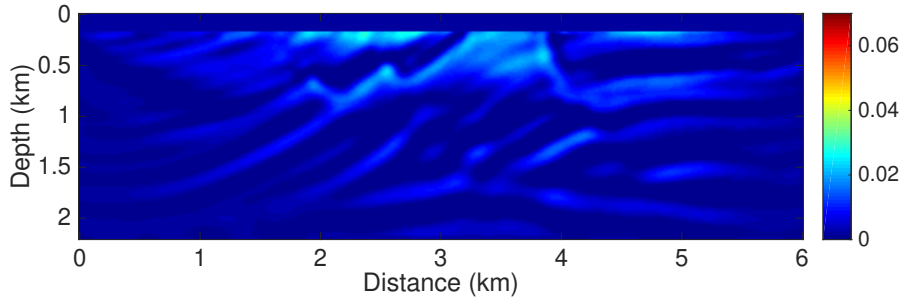

(b) 5 iterations over τ with Strategy B

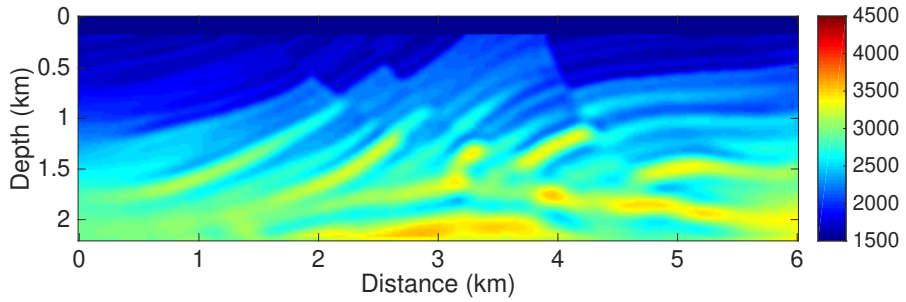

(c) 80 iterations over v_p with Strategy B

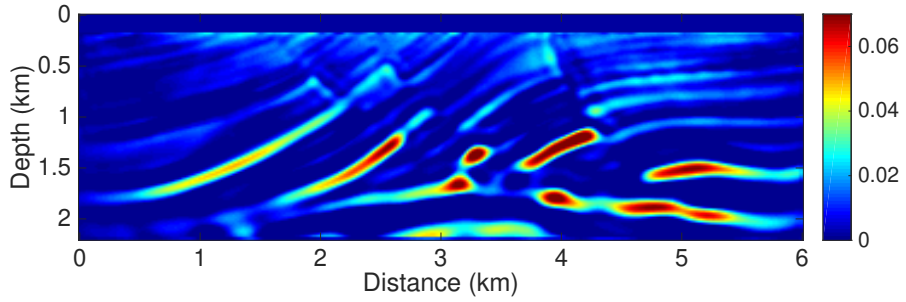

(d) 80 iterations over τ with Strategy B

Figure 5.3: Inversion results of Strategy B after 5 iterations (a) and 80 iterations (c) over v_p, and after 5 iterations (b) and 80 iterations (d) over τ.

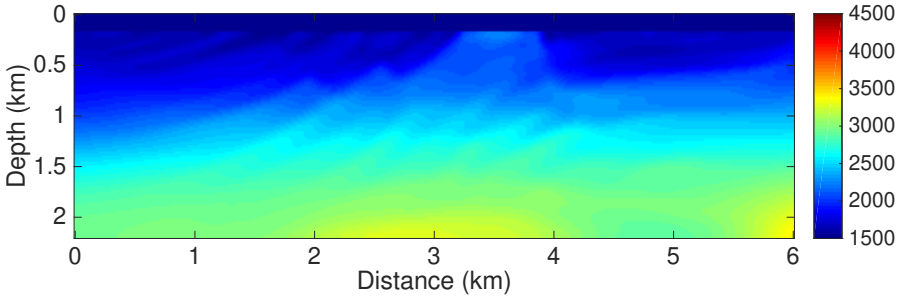

(a) 5 iterations over v_p with the hybrid strategy

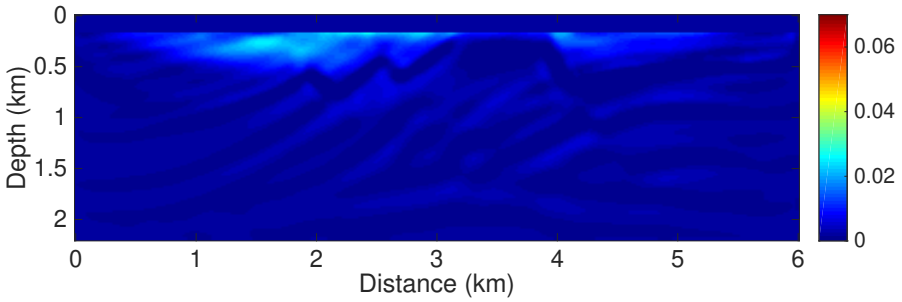

(b) 5 iterations over τ with the hybrid strategy

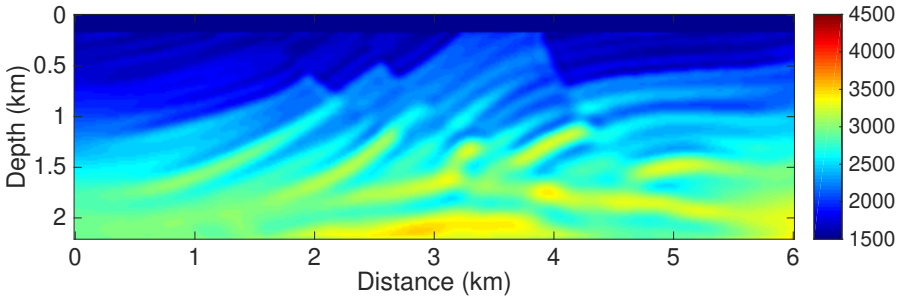

(c) 80 iterations over v_p with the hybrid strategy

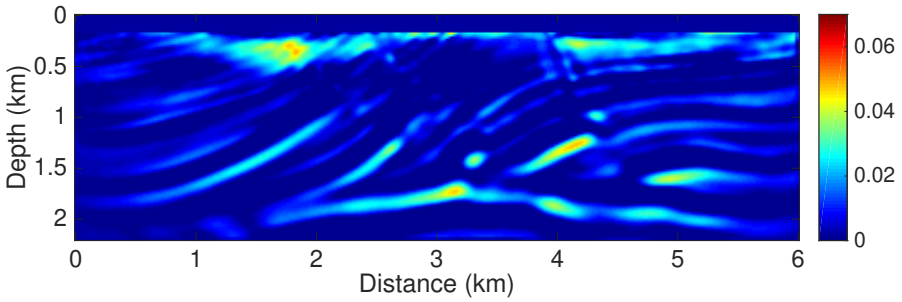

(d) 80 iterations over τ with the hybrid strategy

Figure 5.4: Same as Figure 5.3, except for the hybrid strategy.

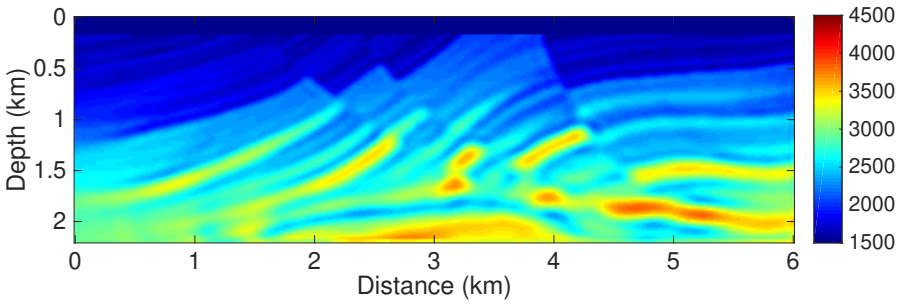

(a) 400 iterations over v_p with Strategy B

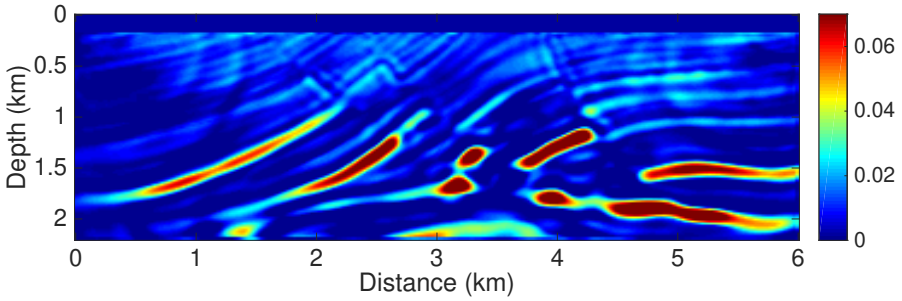

(b) 400 iterations over τ with Strategy B

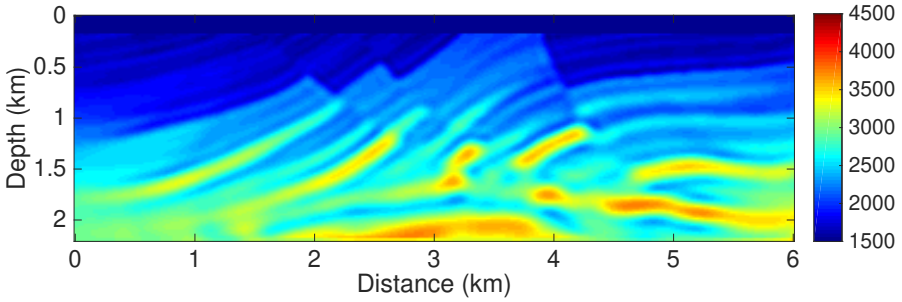

(c) 400 iterations over v_p with the hybrid strategy

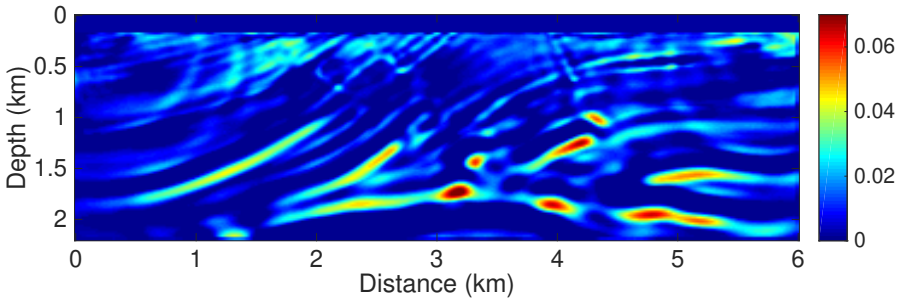

(d) 400 iterations over τ with the hybrid strategy

Figure 5.5: Final inversion results for (v_p,τ) with Strategy B (a, b) and with the hybrid strategy (c, d).

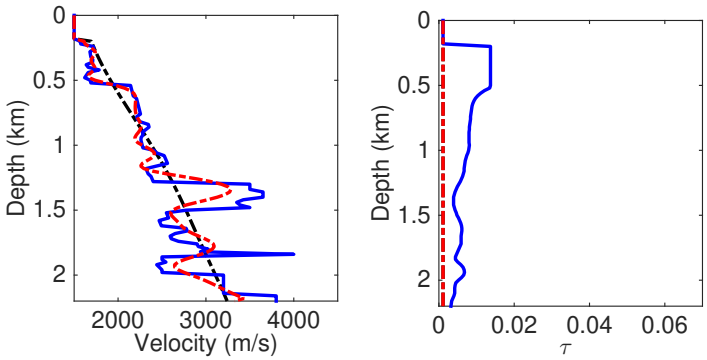

(a) v_p profile (b) τ profile

Figure 5.6: One vertical section extracted at position x = 2500 m from the v_p and τ models obtained with Strategy A (dashed red), compared with the initial model (dashed black) and the true model (solid blue).

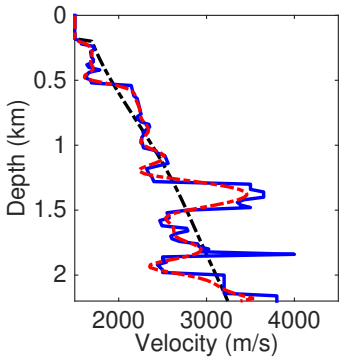

(a) B: v_p at 2500 m

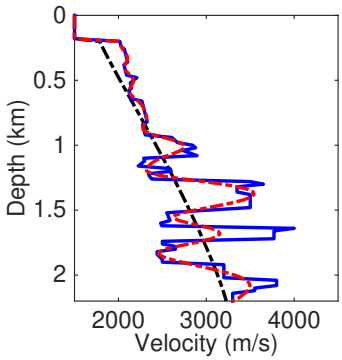

(b) B: v_p at 3320 m

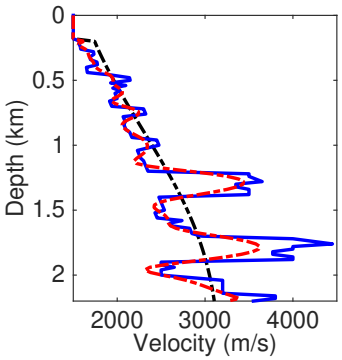

(c) B: v_p at 4000 m

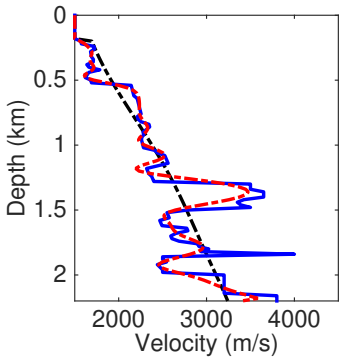

(d) H: v_p at 2500 m

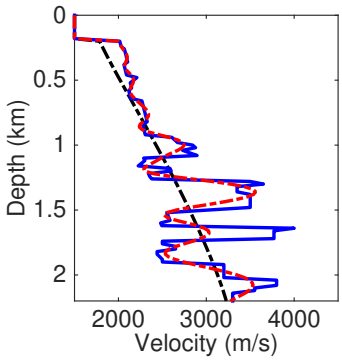

(e) H: v_p at 3320 m

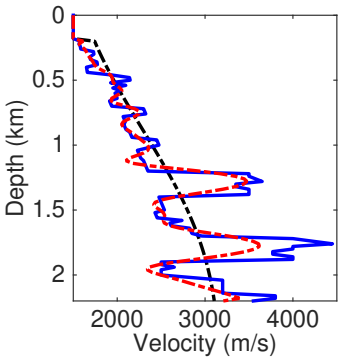

(f) H: v_p at 4000 m

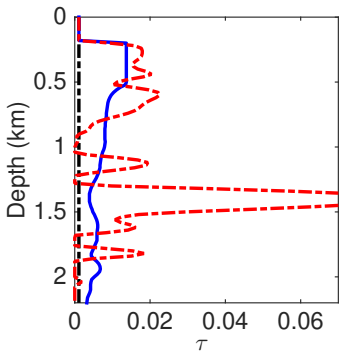

(g) B: τ at 2500 m

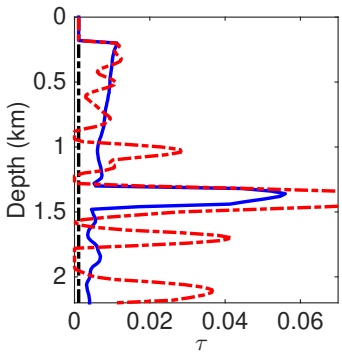

(h) B: τ at 3320 m

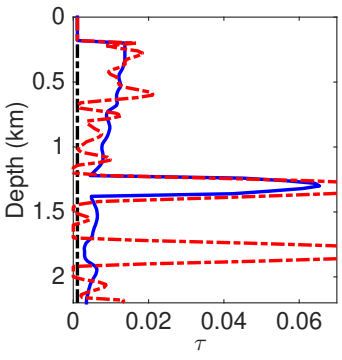

(i) B: τ at 4000 m

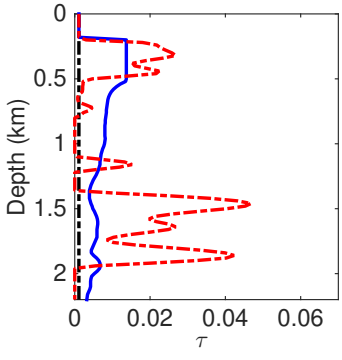

(j) H: τ at 2500 m

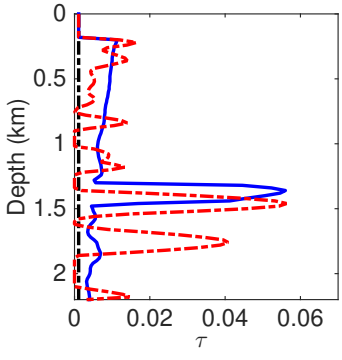

(k) H: τ at 3320 m

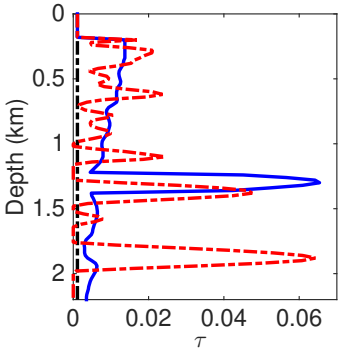

(l) H: τ at 4000 m

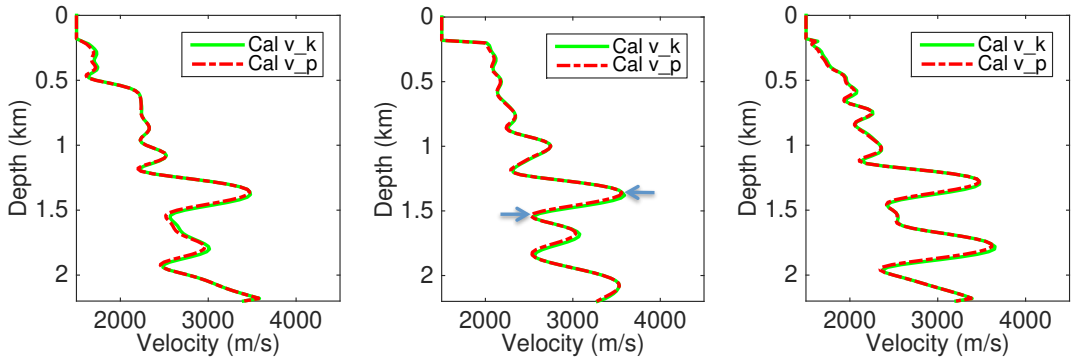

(m) H: v_k at 2500 m (n) H: v_k at 3320 m (o) H: v_k at 4000 m

Figure 5.7: Three vertical sections extracted at position x = 2500 m (left column: a, d, g, j), 3320 m (middle column: b, e, h, k) and 4000 m (right column: c, f, i, l) from inverted v_p and τ. B denotes Strategy B, and H denotes the hybrid strategy. Three profiles extracted from the inverted v_p and τ (dashed red) for Strategy B and for the hybrid strategy, compared with initial model (dashed black) and true model (solid blue). Inverted v_p (dashed red) and final v_k (dashed green) are compared at the three positions (m, n, o). The arrows in (n) denote the positions of the vertical shift between v_p and v_k profiles.

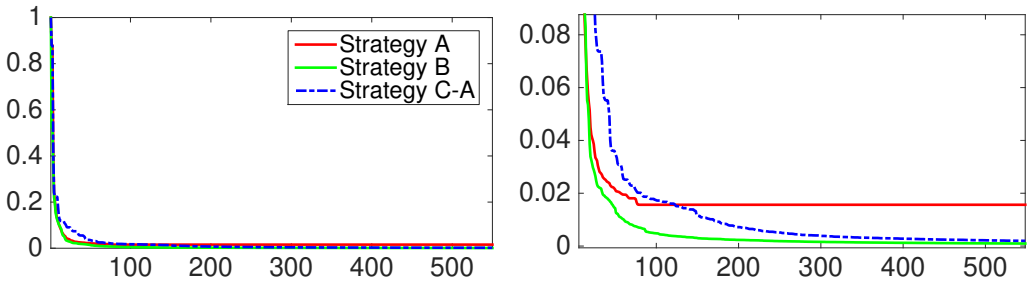

Figure 5.8: Misfit curves for Strategy A (solid red line), Strategy B (solid green line), and the hybrid strategy (dashed blue line) up to 550 iterations (left), and the enlarged misfit curves (right).

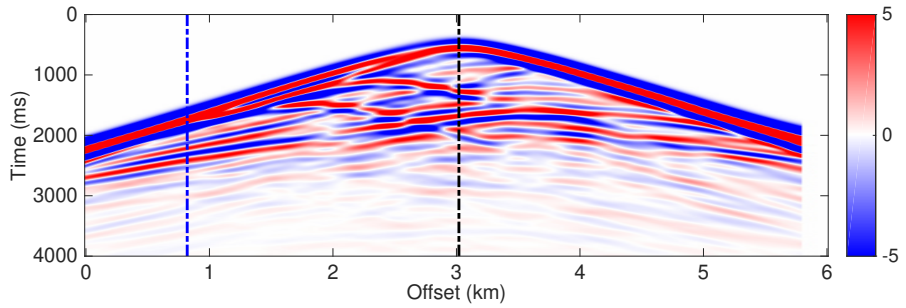

(a) Observed data

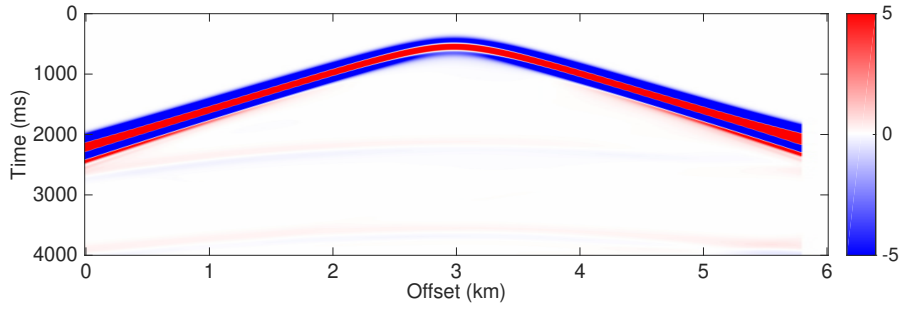

(b) Initial data

Figure 5.9: One observed shot gather (direct waves in water are removed) (a) and one shot gather of initial data (b) at position x = 3320 m.

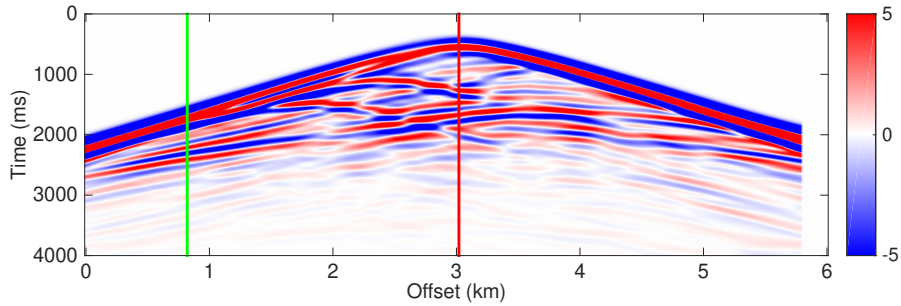

(a) Final data of Strategy A

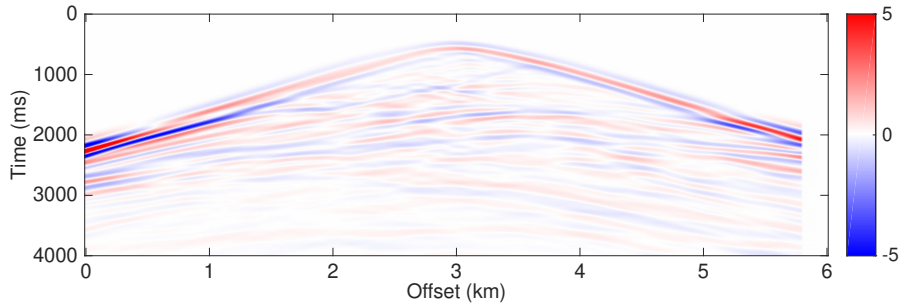

(b) Final data residual of Strategy A

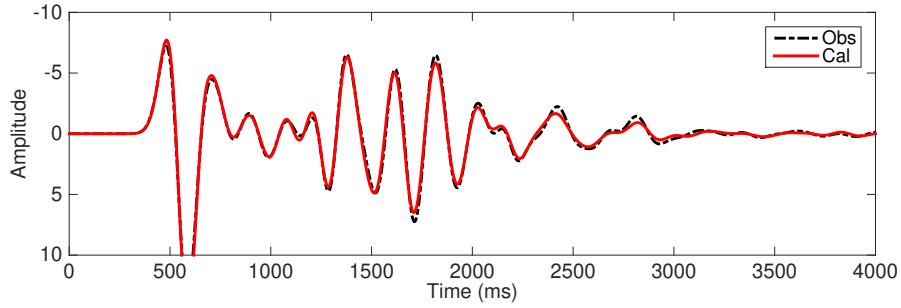

(c) Trace comparison at near offset of Strategy A

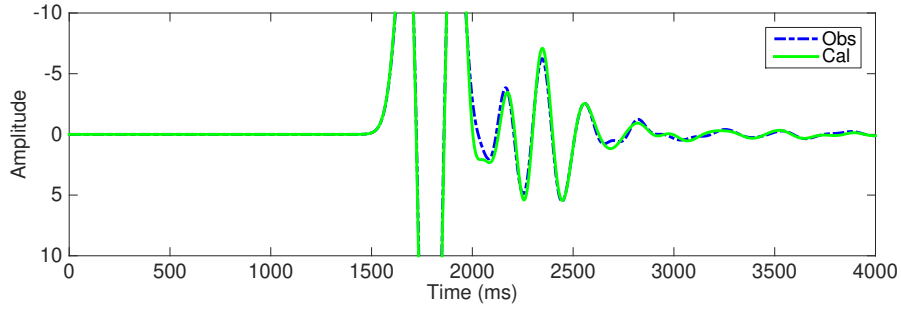

(d) Trace comparison at far offset of Strategy A

Figure 5.10: Data comparison for Strategy A at position x = 3320 m, with final calculated data after 400 iterations (a) and final data difference (b), two traces of observed data (dashed blue and dark) and calculated data (solid green and red) are compared at near offset (c) and far offset (d).

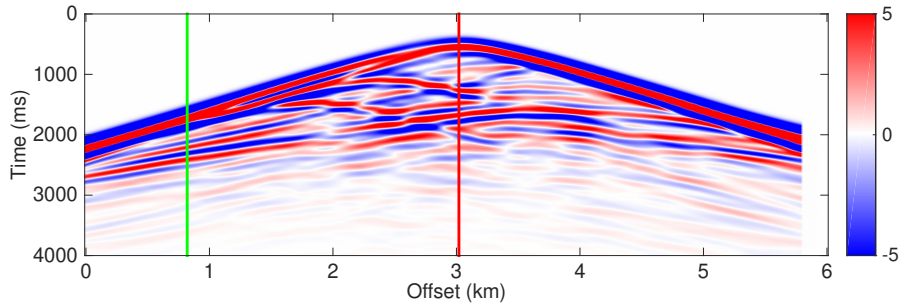

(a) Final data of Strategy B

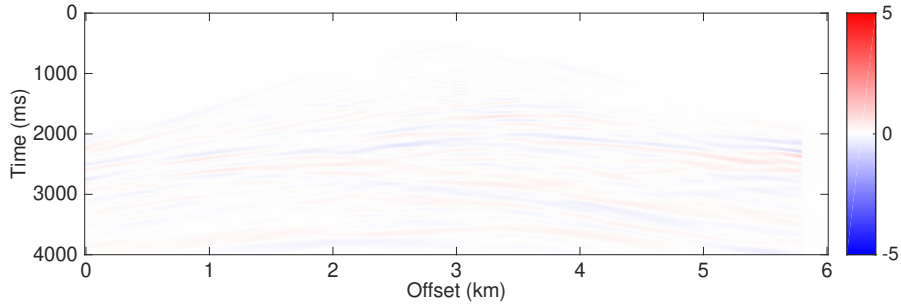

(b) Final data residual of Strategy B

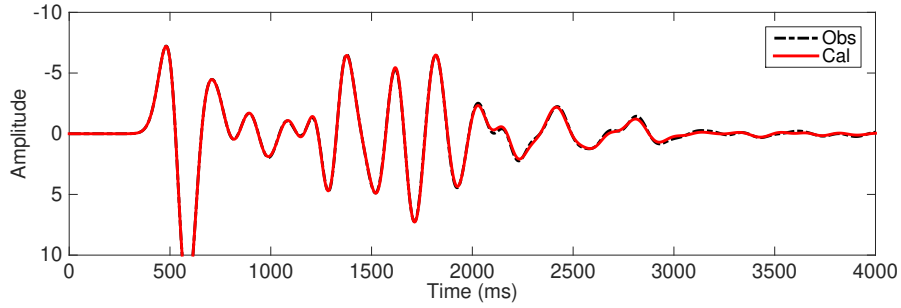

(c) Trace comparison at near offset of Strategy B

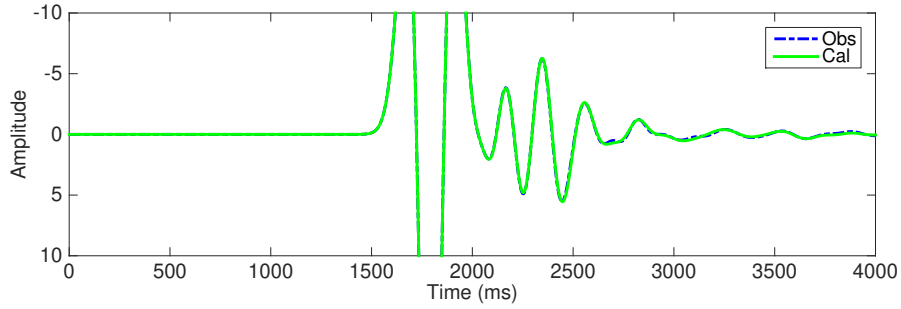

(d) Trace comparison at far offset of Strategy B

Figure 5.11: Same as Figure 5.10, but for data comparison for Strategy B.

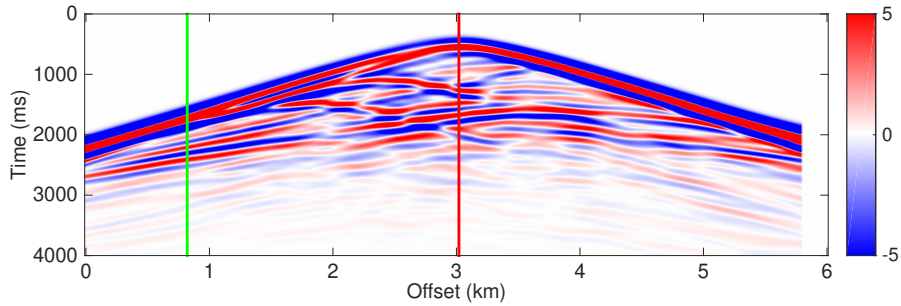

(a) Final data of the hybrid strategy

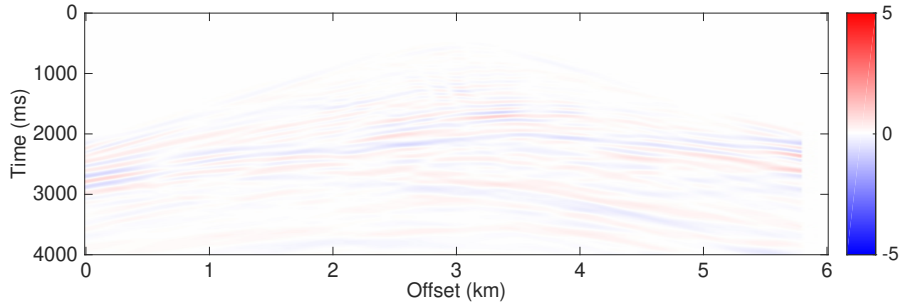

(b) Final data residual of the hybrid strategy

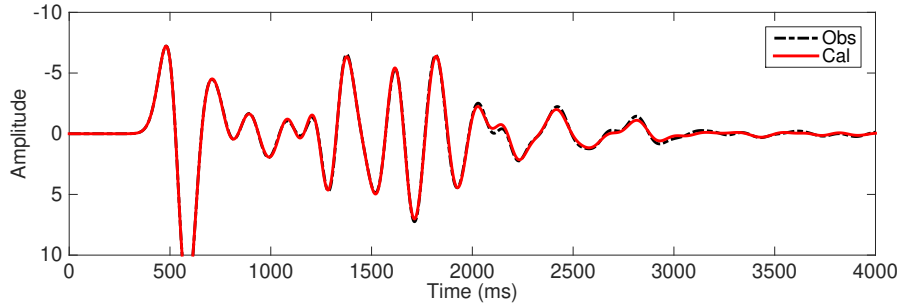

(c) Trace comparison at near offset of the hybrid strategy

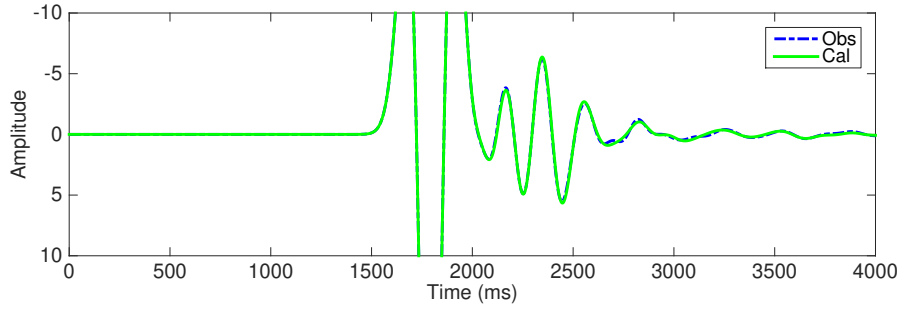

(d) Trace comparison at far offset of the hybrid strategy

Figure 5.12: Same as Figure 5.10, but for data comparison for the hybrid strategy.

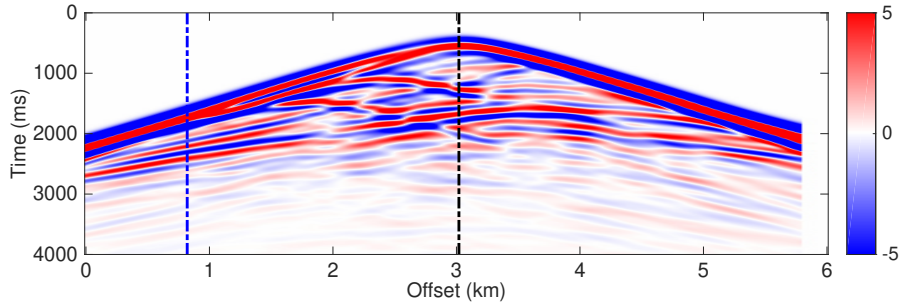

(a) Observed data

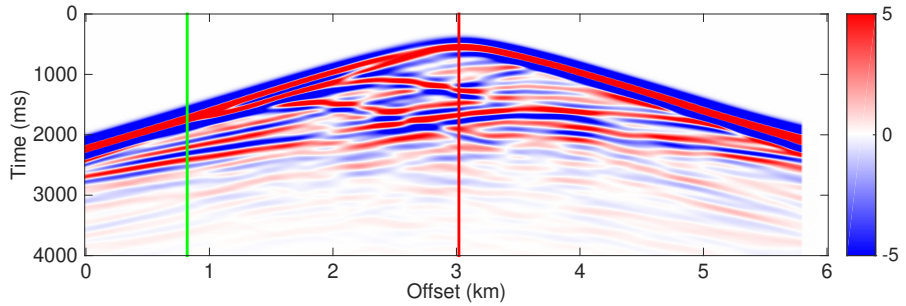

(b) Calculated data over v_k

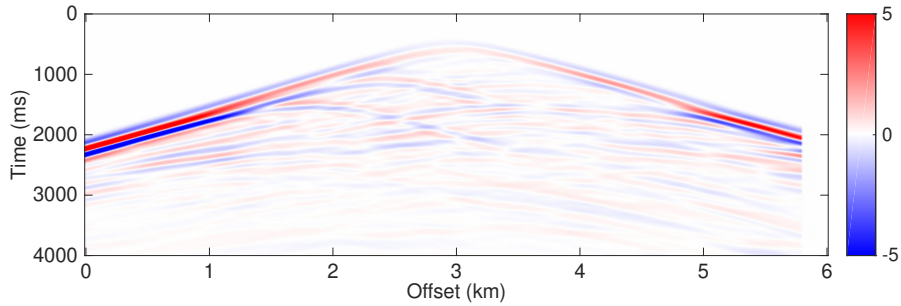

(c) Data difference

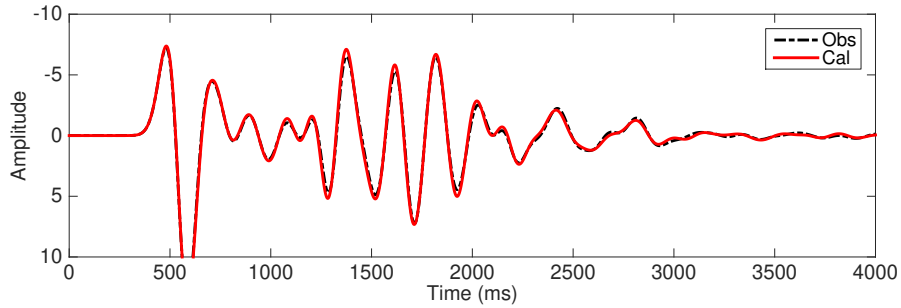

(d) Trace comparison at far offset

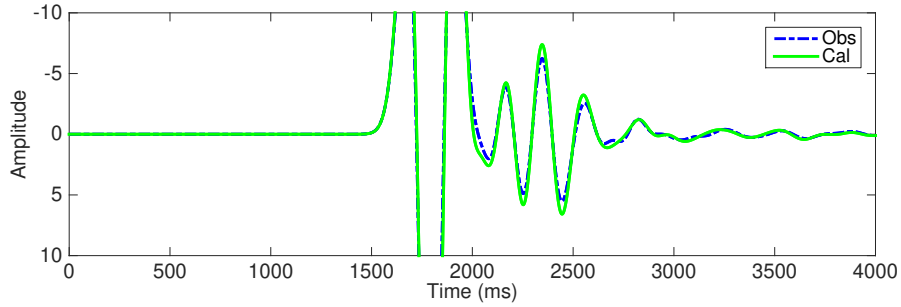

(e) Trace comparison at near offset

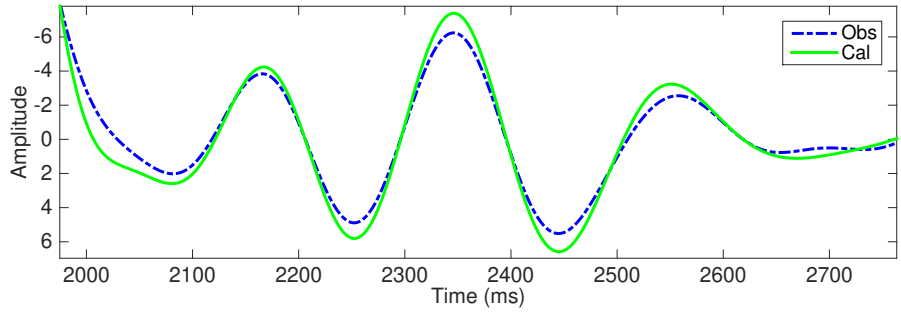

(f) Enlarged trace comparison at near offset

Figure 5.13: Same as Figure 5.10, except that the calculated data are simulated with $v_p = v_k$ and $\tau = 0$. Comparison between one observed shot gather (direct waves in water are removed) at position at x = 3320 m (a), calculated data over v_k ($v_p = v_k$) (b) and data difference (c). Comparison between observed data (dashed blue and dark) and calculated data over v_k (solid green and red) at near offset (d) and far offset (e) (enlarged panel f).

5.4 Discussion

5.4.1 Artifacts and checkerboard test

To better understand the τ anomaly impacts on the data, we remove one τ artifact from the τ result of Strategy B after 400 iterations (Figure 5.5b). The removed τ artifact is located around 2.7–3.4 km laterally and 1.56–1.82 km in depth (Figure 5.14). We simulate two shot gathers using the same v_p model (Figure 5.5a), but with two different τ models which are the τ model with the artifact removed (Figure 5.14) and τ result of Strategy B after 400 iterations (Figure 5.5b).

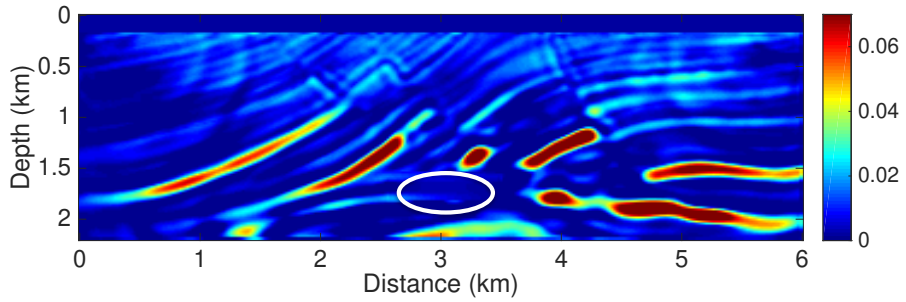

Figure 5.14: The τ model with the artifacts removed from 2.7–3.4 km laterally and 1.56–1.82 km in depth (area inside the white circle).

We compare the two simulated shot gathers (Figures 5.15 and 5.16). The data difference is very small. We need to investigate the τ resolution with small data difference.

To estimate the τ resolution (Malinowski et al., 2011), we add checkerboard perturbations on the retrieved τ model by Strategy B after 400 iterations (Figure 5.5b). The retrieved τ by simultaneous inversion contains strong artifacts on the bottom of the model, thus we add τ perturbations on that part, with the value being 0.01 (Q is around 100) (Figure 5.17), is lower than the τ anomalies (τ is around 0.06). We apply the mono-parameter τ inversion for fixed v_p. The retrieved τ model below the dashed line lacks resolution due to the limited acquisition coverage. Those less-resolution checkerboard artifacts can partly explain the artifacts of the reconstructed τ below the dashed line. Other reasons for strong artifacts in retrieved τ model (Figure 5.5b) are due to cross-talks between parameters, as we explained before.

In summary, the data difference is very small between the shot gathers simulated with / without the artifacts removed (Figures 5.15 and 5.16). But, the checkerboard test validates the high resolution of τ under the acquisition coverages by mono-parameter τ inversion (Figure 5.17) on small data difference. We conclude that the small data difference is difficult to reconstruct both v_p and τ correctly, due to cross-talks with the

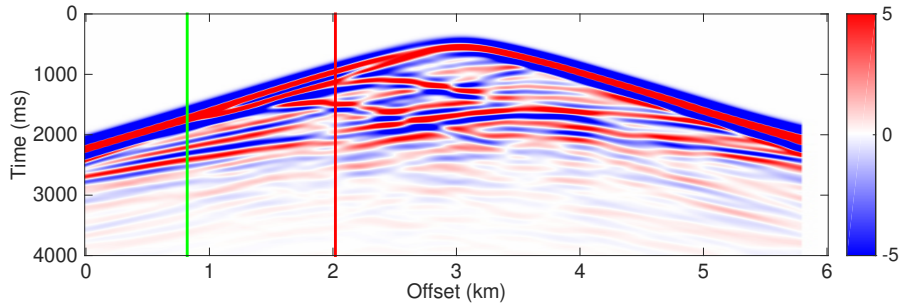

(a) Calculated shot gather in the model of retrieved τ with Strategy B (Figures 5.5b)

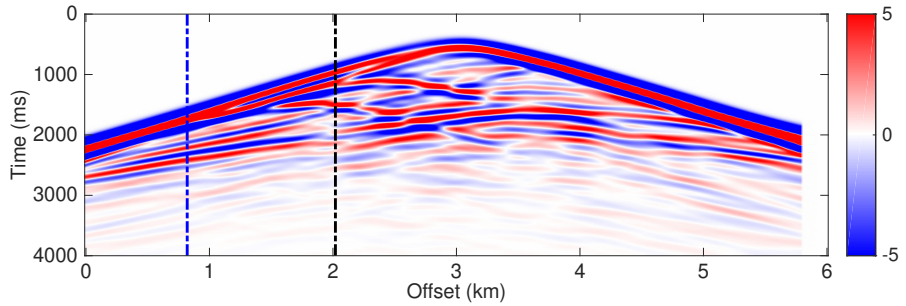

(b) Calculated shot gather in the τ model with one artifact replaced (Figures 5.14)

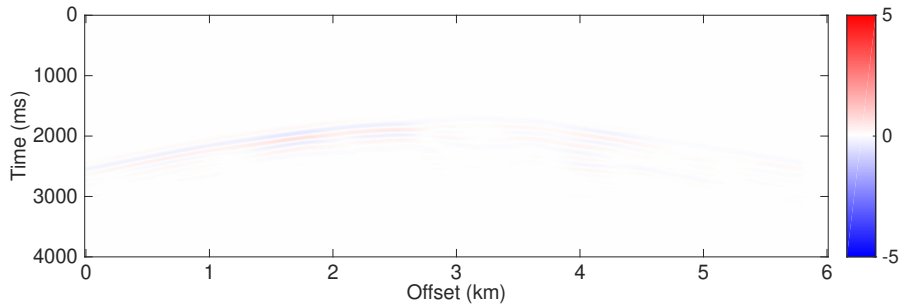

(c) Data difference

Figure 5.15: Comparison between the calculated shot gather for Strategy B (a), and the calculated shot gather in the τ model with one artifact removed (b), the data difference (c).

simultaneous inversion, but still can be correctly explained by mono-parameter τ inversion with correct input v_p model.

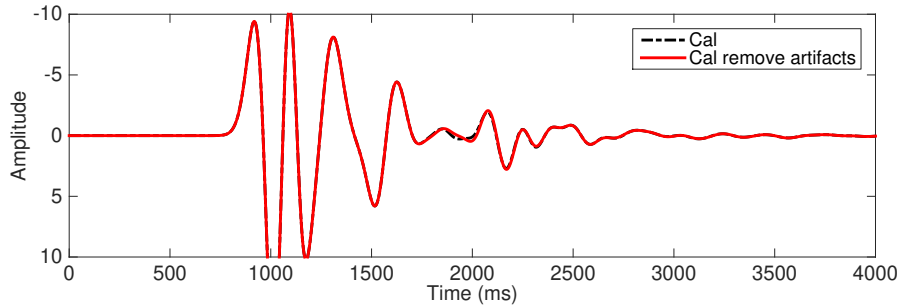

(a) Trace comparison at near offset

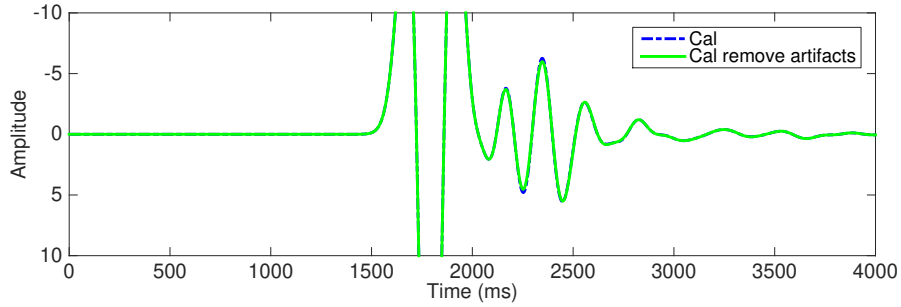

(b) Trace comparison at far offset

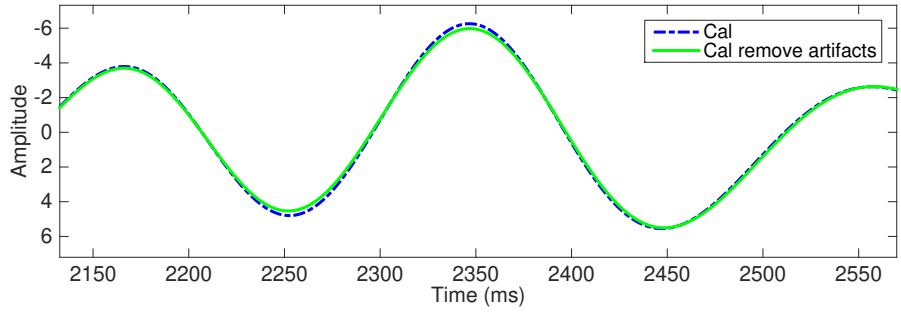

(c) Enlarged trace comparison at far offset

Figure 5.16: Following Figure 5.16, the trace comparison at near offset (d), and far offset (e), and enlarged comparison at far offset 800 m.

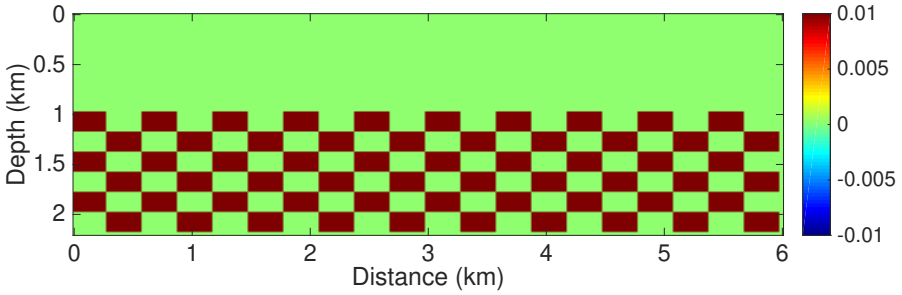

(a) True model of checkerboard

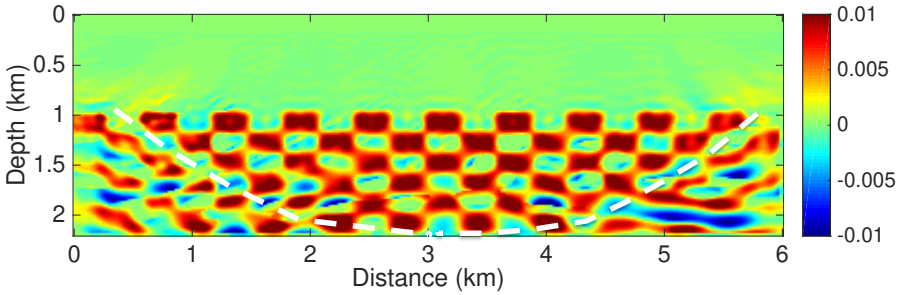

(b) Inverted model of checkerboard

Figure 5.17: The checkerboard consists of rectangular blocky zones, with fixed τ perturbations as 0.01 (Q around 100) from the depth of 1 km to the bottom part (a). τ is reconstructed for fixed v_p (b). The dashed line indicates the limit of the constrained inversion zone.

5.4.2 Impact of Gaussian noise

v_p and τ models are reconstructed until a small final data misfit, which is lower than 1%. We need to evaluate the impacts of noise on inversions. The hybrid strategy is the combination of Strategy A and Strategy C. Strategy C incorporates the kinematic velocity to update v_p and τ. An accurate kinematic velocity ensures a good phase match between observed and calculated data (Figure 5.13). Strategy C further fits the amplitude difference. To test the sensitivity to noise, we add strong Gaussian noise to real data (the signal-to-noise ratio is 8.4 dB) (Figure 5.20a). The results of Strategy B (Figure 5.18) using noisy data have similar results as the previous test without noise. The hybrid strategy using noisy data locates the two anomalies (Figure 5.19). The shallow part has some artifacts. The inversion results are similar to the previous test without noise. $\mathcal{L}_2$ norm is specific for Gaussian noise. The noise is insensitive to inversions with $\mathcal{L}_2$ norm (Tarantola, 1987). The phase of noisy observed data and calculated data matches well (Figures 5.21 and 5.22). The misfit curves of the two strategies converge (Figure 5.23), but the hybrid strategy still has larger final misfit than Strategy B, due to the underestimated kinematic velocity v_k. Therefore, for Gaussian distributed noise in observed data, both two strategies with $\mathcal{L}_2$ norm objective function is insensitive to noise up to 8.4 dB.

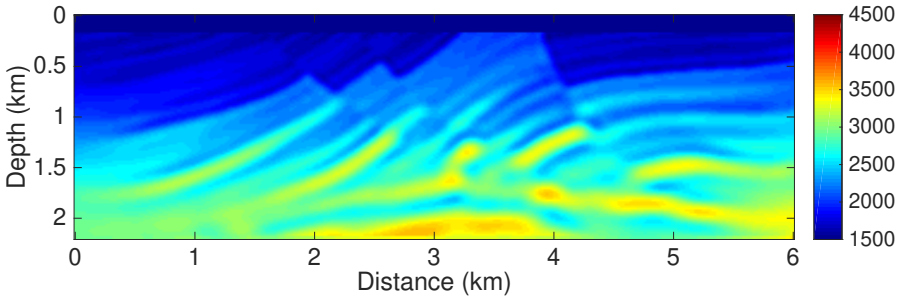

(a) 80 iterations over v_p with Strategy B

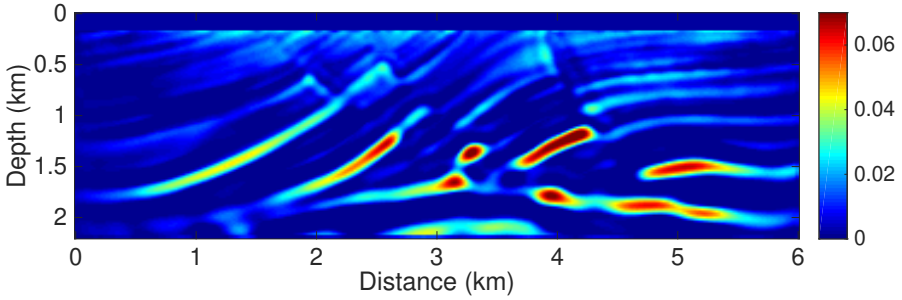

(b) 80 iterations over τ with Strategy B

Figure 5.18: Inversion results of Strategy B after 80 iterations over v_p (a) and τ (b).

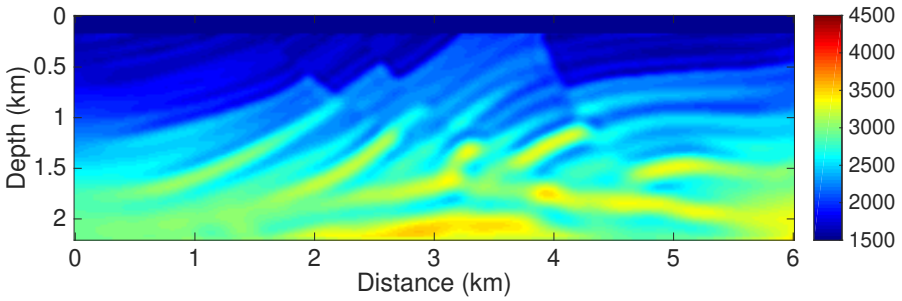

(a) 80 iterations over v_p with the hybrid strategy

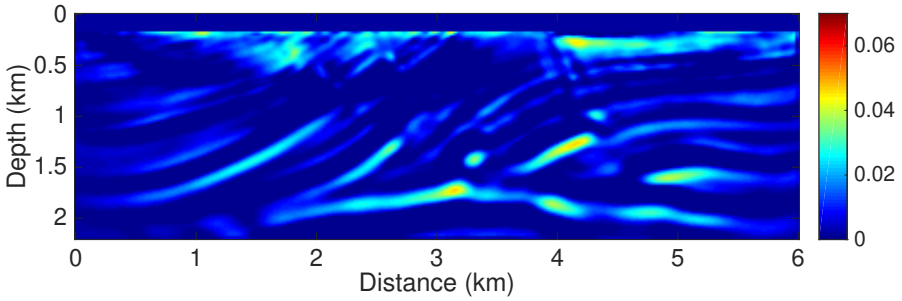

(b) 80 iterations over τ with the hybrid strategy

Figure 5.19: Same as Figure 5.18, but for inversion results of the hybrid strategy.

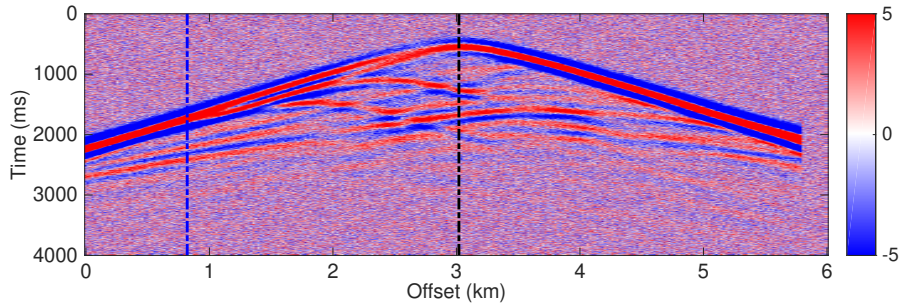

(a) Observed data

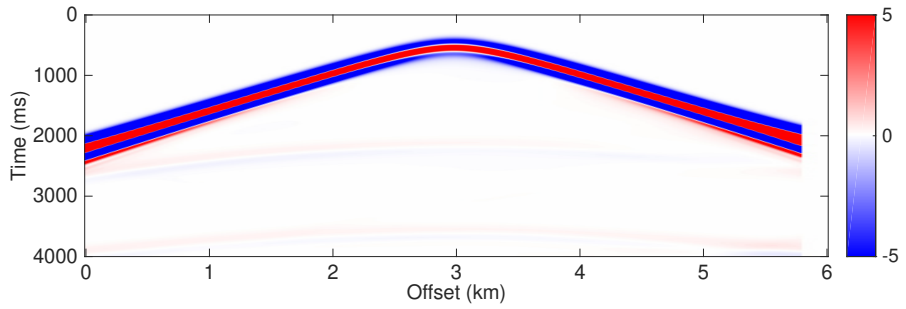

(b) Initial data

Figure 5.20: Same as Figure 5.9, except for the noisy observed data.

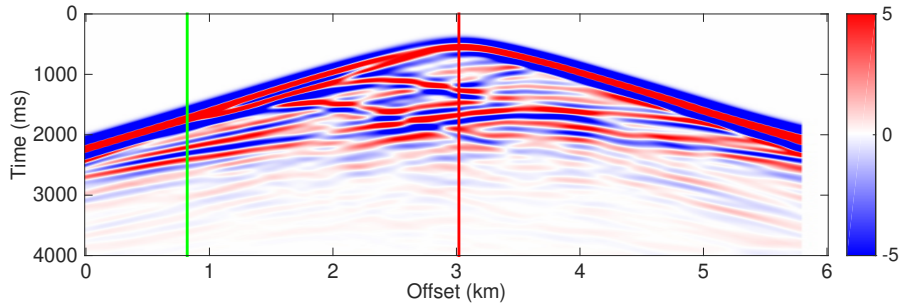

(a) Final data of Strategy B

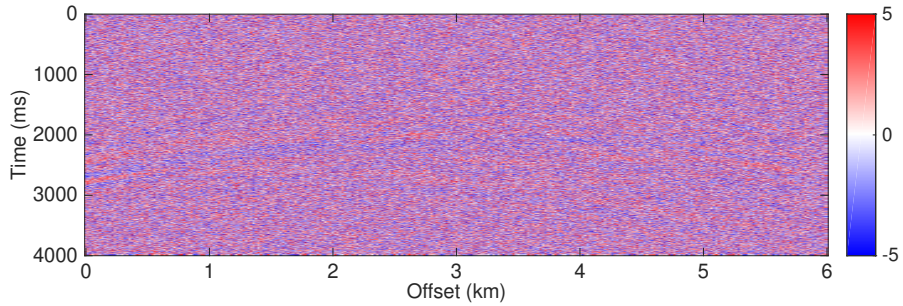

(b) Final data residual of Strategy B

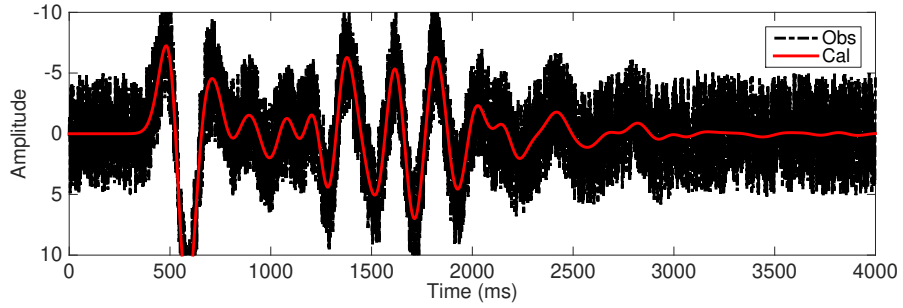

(c) Trace comparison of Strategy B at near offset

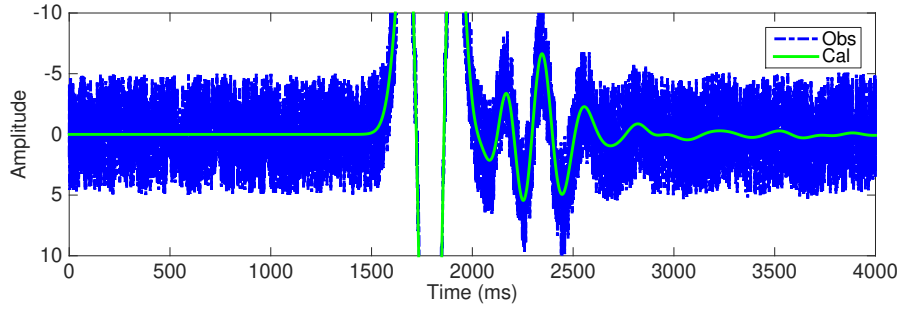

(d) Trace comparison of Strategy B at far offset

Figure 5.21: Same as Figure 5.11, except for the noisy observed data.

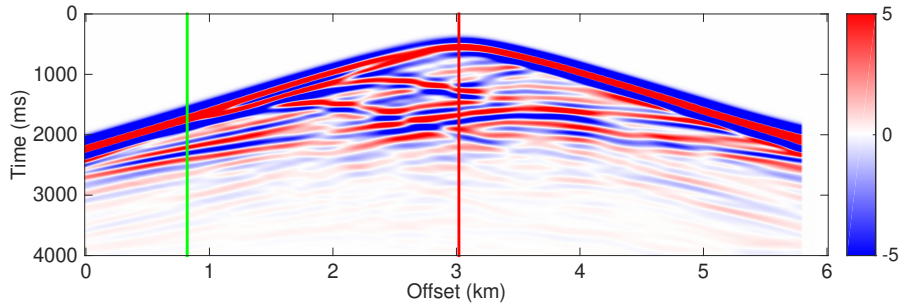

(a) Final data of the hybrid strategy

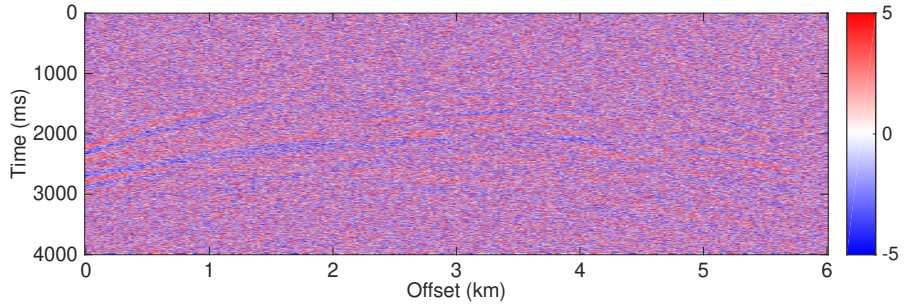

(b) Final data residual of the hybrid strategy

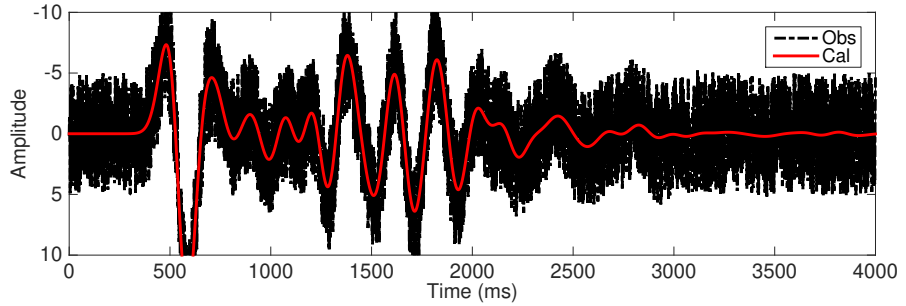

(c) Trace comparison of the hybrid strategy at near offset

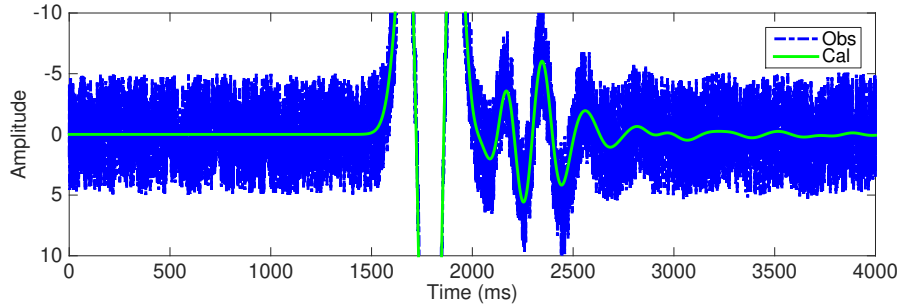

(d) Trace comparison of the hybrid strategy at far offset

Figure 5.22: Same as Figure 5.12, except for the noisy observed data.

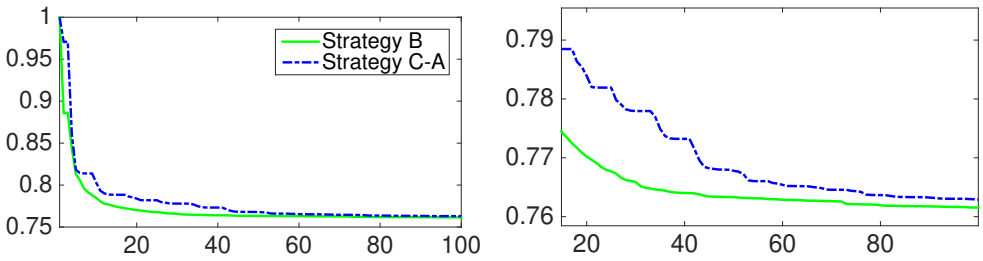

Figure 5.23: Same as Figure 5.8: misfit curves for Strategy B (solid green line), and the hybrid strategy (dashed blue line) up to 100 iterations (left), and the enlarged misfit curves (right).

5.4.3 Over-estimation and cross-talks

From the results of the three strategies in section 5.3, v_p and τ have cross-talks. The under-estimated lower v_p transfers the phase difference to τ, leading to a over-estimated τ (τ artifacts) in Strategy B and the hybrid strategy. Meanwhile, Strategy A over-estimates v_p without updating τ. We need to understand the inversion behaviors on over-estimation and cross-talks between parameters. We use different v_p models as input for mono-parameter τ inversion, and apply a simultaneous inversion over v_p and τ, including:

- Mono-τ 1: The initial v_p is the inverted result with Strategy A after 100 iterations.
- Mono-τ 2: The initial v_p is the true v_p model.
- Mono-τ 3: The initial v_p is the inverted result with Strategy B after 100 iterations.
- Simultaneous: The initial v_p is the inverted result with Strategy A after 100 iterations.

Mono-τ denotes the mono-parameter τ inversion for fixed v_p. Three v_p models are inverted v_p with Strategy A after 100 iterations, true v_p model and inverted v_p with Strategy B after 100 iterations. τ is almost not updated by mono-τ 1 (Figure 5.24), due to the incorrect over-estimated v_p model with a coupling of incorrect depth and velocity values (see the v_p profile in Figure 5.6). The kinematic information is mainly dominated by the velocity model v_p. There is not updating space for τ, because the inversion is stuck into the local minimum. With the same v_p model as input, the simultaneous inversion can not update v_p and τ (Figure 5.27) towards the true models. We observe that the retrieved v_p is larger than the true model at the locations of the two τ anomalies. The τ anomalies are not retrieved. To match the data, the under-estimated τ values transfer the kinematic information to over-estimated larger v_p. The over-estimated incorrect v_p makes the inversion be stuck into the local minimum, leading to no updating space for τ. The mono-τ 2 uses the true v_p model as input, the retrieved τ locates the anomalies and has identical structure as the true τ model (Figure 5.25). Meanwhile, the mono-τ 3 has the similar τ result (Figure 5.26) as Strategy B with many artifacts due to the under-estimated lower v_p.

From the three mono-τ inversions, τ updating is strongly affected by the v_p models. The incorrect v_p leads to the limited updating space for τ, even with a simultaneous inversion. The under-estimated v_p maps the phase difference into the over-estimations or artifacts on the τ result. The cross-talks between v_p and τ make the inversion get stuck into a local minimum.

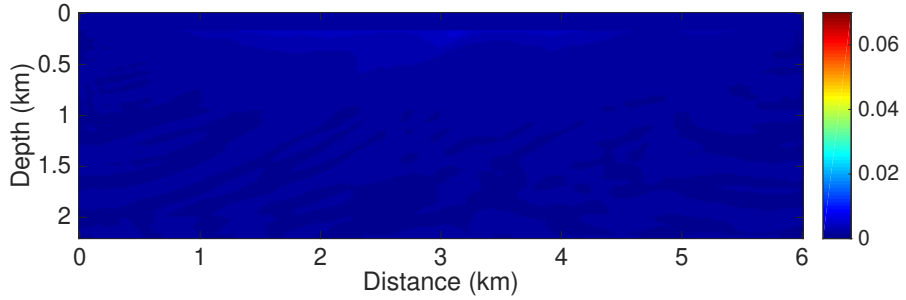

Figure 5.24: Mono-τ 1: the final τ inversion result; input v_p is from the Strategy A after 100 iterations.

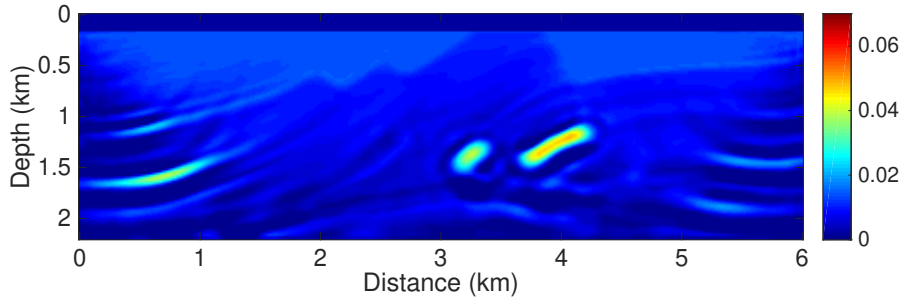

Figure 5.25: Same as Figure 5.24, but for mono-τ 2 inversion; input v_p is true v_p model.

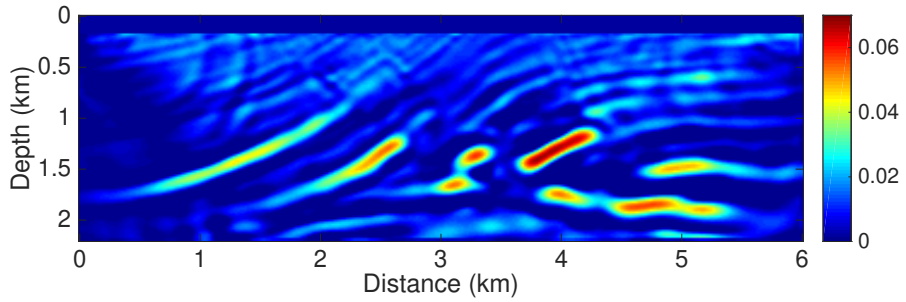

Figure 5.26: Same as Figure 5.24, but for mono-τ 3 inversion; input v_p is from Strategy B after 100 iterations.

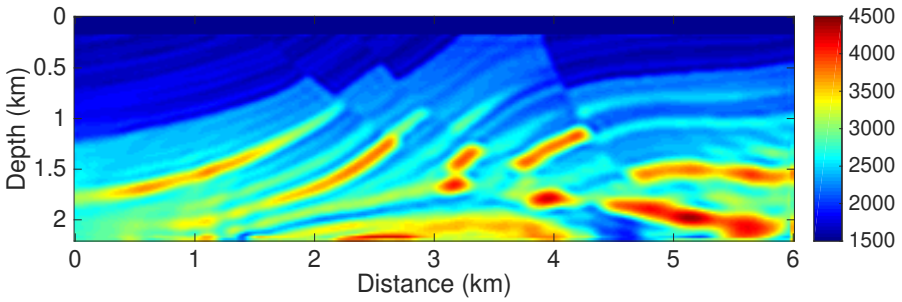

(a) Final v_p results

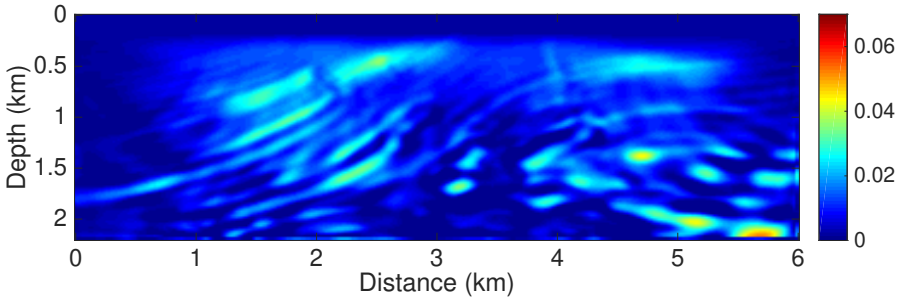

(b) Final τ results

Figure 5.27: Simultaneous inversion: the final v_p (a) and τ (b); input v_p is same as in Figure 5.24.

5.4.4 Frequency continuation inversion

The kinematic velocity v_k is the function of frequency, v_p and τ (Equation 4.8). The kinematic velocity v_k is determined at the central frequency of the source. The central frequency is defined as the peak frequency in all the previous examples. Concerning the broadband Ricker wavelet, we filter the Ricker wavelet into two narrow bandwidth sources. The Ricker wavelet in Section 5.3 is a 4 Hz central frequency wavelet. The maximum frequency is 10 Hz (Figure 5.28a). We apply the two band-pass filters to have a low and high frequency source term. The spectrum of the low frequency source is from 1.5–5 Hz (Figure 5.28b). The central frequency is 3.8 Hz. The spectrum of the high frequency source is from 4.5–6 Hz (Figure 5.28c). The central frequency is 4.8 Hz. We choose 3.8 Hz and 4.8 Hz for the determination of v_k. The low frequency and high frequency data both contain bandwidth of several frequencies. The high frequency data has 0.5 Hz bandwidth overlapping with low frequency data. This overlapping frequency continuation scheme is more stable than single frequency continuation scheme (Brossier et al., 2009).

We first apply the low frequency data with both Strategy B and the hybrid strategy for 40 iterations. Then the high frequency data is exploited to obtain the final results. Strategy B after first 40 iterations retrieves the main v_p structures (Figure 5.29a). With higher frequency data after another 40 iterations, more fine structures are retrieved, especially on the shallow part (Figure 5.29c). For the result of τ at low frequency, two anomalies are retrieved (Figure 5.29b). There are strong artifacts on the bottom for high frequency data (Figure 5.29d). For the hybrid inversion, v_p retrieved by high frequency data (Figure 5.30c) has more more detailed structure than v_p retrieved by low frequency data (Figure 5.30a). The two τ anomalies are retrieved by low frequency data (Figure 5.30b). There are some artifacts on the shallow part. After another 40 iterations with high frequency data, two anomalies are more clearly located (Figure 5.30d). τ artifacts on the shallow part is relieved with more iterations. Some of the artifacts are explained by the τ checkerboard result, showing the lack of resolution below the dashed line (Figure 5.17), due to the insufficient acquisition coverage. With the same iterations, τ anomalies are more obvious than τ result without data filtering (Figure 5.4). The misfits of Strategy B and the hybrid strategy both decease to be below 1% (Figure 5.31).

To obtain the results with 1% data misfit left (Figure 5.8), we need 170 iterations with the hybrid strategy without data filtering. The frequency continuation scheme needs 50 iterations to have the same data misfit. The frequency continuation scheme is around 3 time faster than previous one without data filtering to retrieve the τ anomalies with the same data misfit until 1%. The frequency continuation scheme has more accurate v_k, which is determined at the central frequency of each narrow frequency bandwidth, leading to a faster convergence.

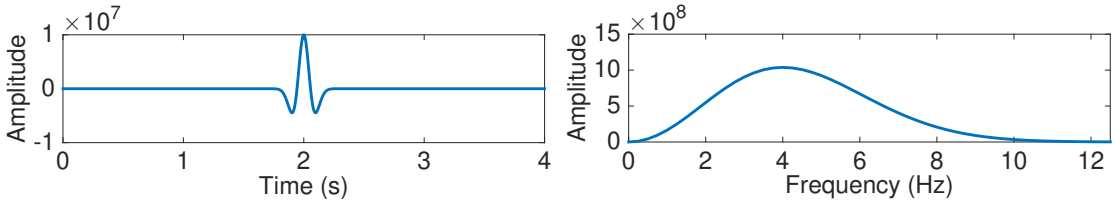

(a) 4 Hz Ricker wavelet

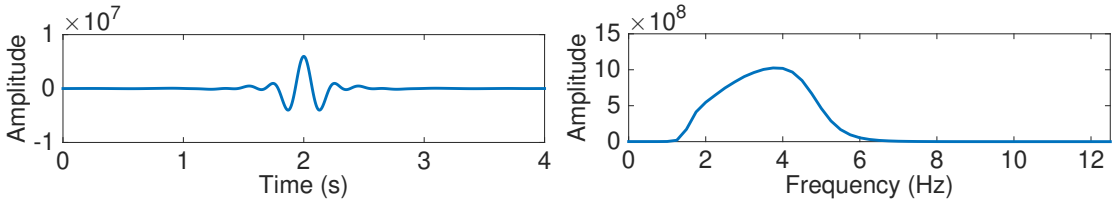

(b) Source after 1.5 Hz - 5 Hz filtering

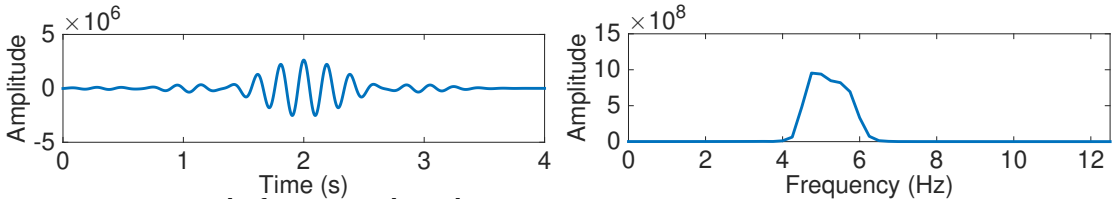

(c) Source after 4.5 Hz - 6 Hz filterng

Figure 5.28: Different frequency sources in the time (left) and frequency domains (right), 4 Hz central frequency Ricker wavelet (a), the source after 1.5–5 Hz band-pass filtering (b), and the source after 4.5–6 Hz band-pass filtering (c).

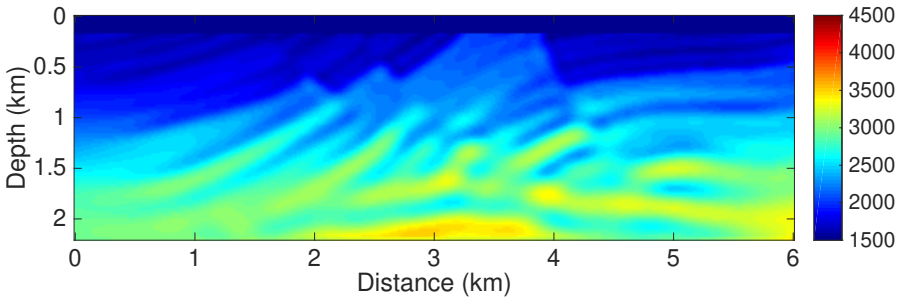

(a) 40 iterations over v_p with Strategy B

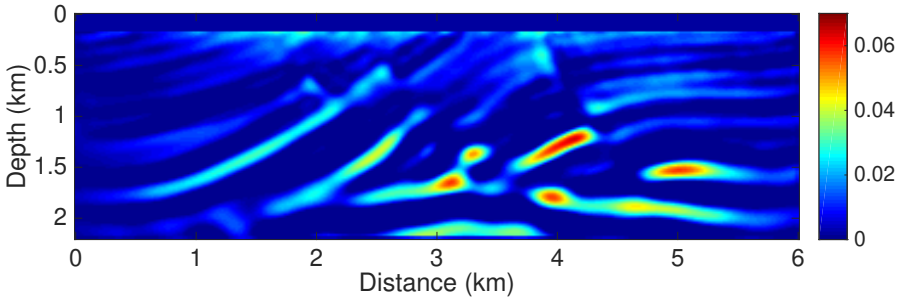

(b) 40 iterations over τ with Strategy B

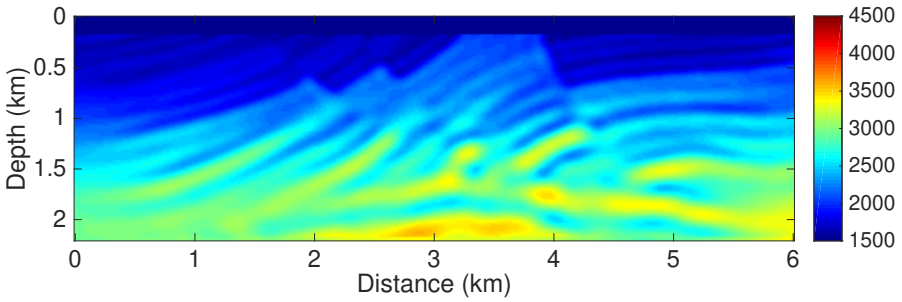

(c) 80 iterations over v_p with Strategy B

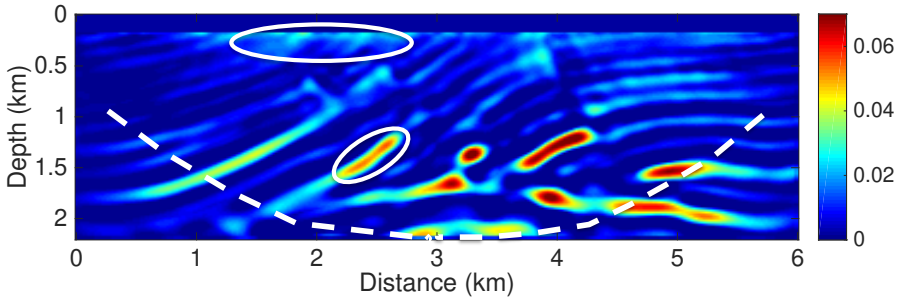

(d) 80 iterations over τ with Strategy B

Figure 5.29: Inversion results with Strategy B: 40 iterations (a) and 80 iterations (c) over v_p, and 40 iterations (b) and 80 iterations (d) over τ. The low frequency data are used in first 40 iterations, and the high frequency data are used in the subsequent 40 iterations.

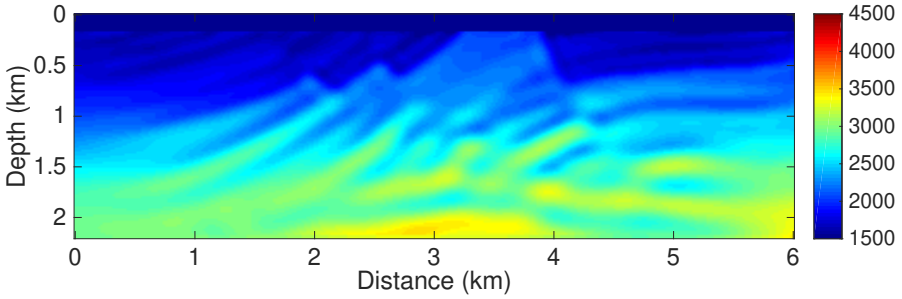

(a) 40 iterations over v_p with the hybrid strategy

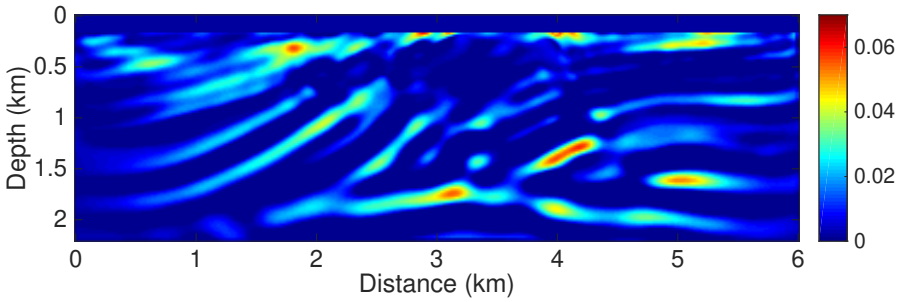

(b) 40 iterations over τ with the hybrid strategy

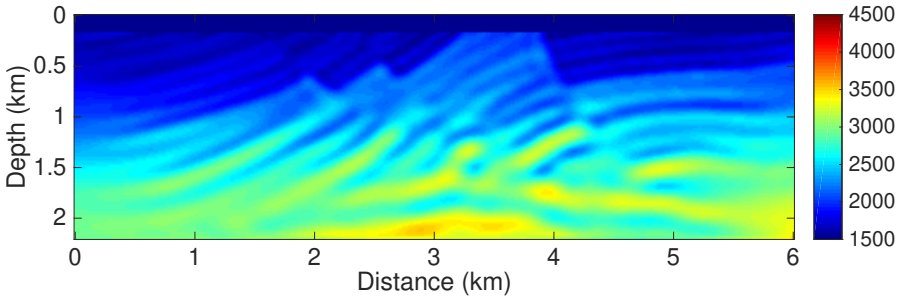

(c) 80 iterations over v_p with the hybrid strategy

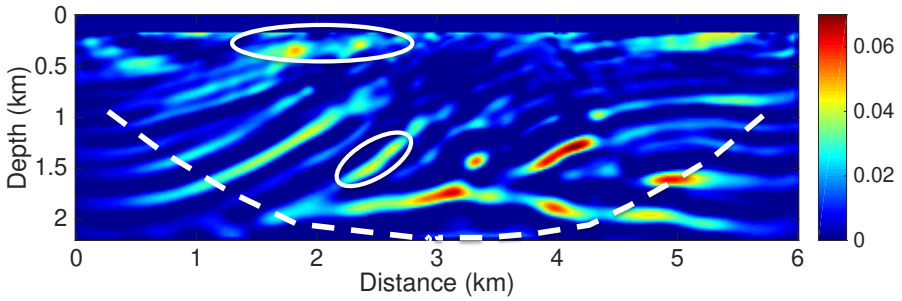

(d) 80 iterations over τ with the hybrid strategy

Figure 5.30: Same as Figure 5.29, but for the inversion results with the hybrid strategy.

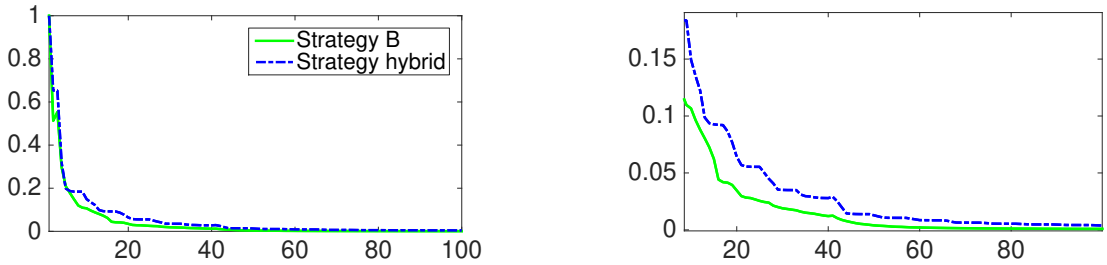

Figure 5.31: Misfit curves of Strategy B (solid green line), and the hybrid strategy (dashed blue line) up to 100 iterations (left), and the enlarged misfit curves (right).

5.5 Conclusions

We have applied the three strategies to the Marmousi model. The data is mainly composed of reflections, except for direct waves in the water layer.

The v_p is over-estimated with Strategy A without considering τ, ending with the combination of incorrect depth and velocity values. The incorrect over-estimated v_p makes the inversion get stuck into a local minimum. The mono-parameter v_p cannot perfectly match the data without updating τ.

Strategy B updates v_p and τ simultaneously. The two τ anomalies are retrieved, but the structure of inverted τ is affected by the structure of inverted v_p due to cross-talks. The shallow part of v_p is well-retrieved, meanwhile the bottom part of v_p is lower than true model. The under-estimated low v_p has cross-talks with τ, leading to strong artifacts on τ. This inversion behavior is validated by three mono-τ inversions. The deeper τ artifacts appear on the locations where v_p is insufficiently retrieved. Meanwhile, the mono τ inversion with the true v_p model as input has few artifacts. On the one side, the impacts of τ artifacts on the data are small, but this small data difference cannot correctly reconstruct v_p and τ at the same time. The simultaneous inversion ends with the final result of combination between strong τ artifacts and under-estimated low v_p values on the bottom part. On the other side, the checkerboard test indicates that the mono-parameter τ inversion has high resolutions on τ perturbations under the illustration zone controlled by acquisition coverage. The two aspects indicate that there are cross-talks between parameters. The inversion has to be guided to explain the small data difference.

Compared with results of Strategy B, τ artifacts with the hybrid strategy are lower, especially on the bottom part. The two anomalies are retrieved by the hybrid strategy, but with a vertical depth shift. The kinematic of final calculated is controlled by the v_k model, it matches well the kinematic of observed data. To match the waves reflected on the bottom interfaces of the τ anomalies, v_k has large values and deeper interfaces. τ is further updated based on the ratio of v_k and v_p to match the phase and amplitude,

leading to a vertical depth shift. This kinematic relationship assumes that v_k is a function of a single frequency, which is determined at the central frequency of source during the inversion. From the inversion results, this assumption proves to be proper and effective to retrieve v_p and τ. Frequency continuation scheme is also recommended to obtain more accurate v_k for the hybrid inversion strategy.

Finally, the hybrid inversion strategy incorporates the kinematic relationship to guide the inversion. Compared with simultaneous inversion, the hybrid strategy retrieves a good velocity model (mainly focus on the top) and locates the attenuation anomalies with less artifacts. This is an alternative way to retrieve v_p and τ models on complex models, e.g., Marmousi model that dominated by reflections, and insensitive to Gaussian noise with $\mathcal{L}_2$ norm objective fucntion.

Chapter 6

Conclusions and perspectives

Contents

Résumé du chapitre 6

Dans ce travail, j'ai développé et évalué différentes stratégies d'inversion pour l'inversion des formes d'onde visco-acoustique afin de retrouver la vitesse et l'atténuation. L'inversion hybride développée ici est basée sur la vitesse cinématique. Elle n'a pas besoin du Hessien et mitige les interférences. Les deux aspects importants sont : (1) la détermination de la vitesse cinématique et (2) le découplage entre vitesse et atténuation pour une relation cinématique donnée.

6.1 Conclusions

In this thesis, I have investigated different inversion strategies for visco-acoustic full waveform inversion to reconstruct velocity and attenuation models. Visco-acoustic FWI belonging to the multi-parameter inversion suffers from cross-talks between parameters. Conventional inversion strategies include sequential and simultaneous inversion strategies. Sequential inversion includes a first step of inverting the velocity model, and a subsequent step for updating the attenuation model. This approach may lead to parameter over-estimation. In this thesis, we apply the mono-parameter velocity inversion to investigate the inversion behaviors. The simultaneous inversion inverts velocity and attenuation at the same time. But it suffers from cross-talks between parameters without the introduction of the Hessian matrix.

In this thesis, I have proposed a hybrid inversion strategy to guide the inversion without relying on the information of the Hessian matrix and to mitigate cross-talks. This inversion strategy includes two key steps: (1) the determination of the kinematic velocity and (2) the decoupling between velocity and attenuation based on the kinematic relationship.

6.1.1 Hybrid strategy – A guided inversion

The hybrid inversion strategy incorporates the kinematic relationship to guide the inversion and mitigate cross-talks. To apply the hybrid strategy, we first update the kinematic velocity, then decouple the parameters based on a fixed v_k. For the fixed kinematic velocity, the total derivative of the objective function with respect to v_p is a combination between the partial derivatives of the objective function with respect to v_p and τ. $\partial\tau(v_p)/\partial v_p$ is the linking term between v_p and τ gradients. The term acts as a dynamic scaling factor to balance the gradient sensitivities without the information of the Hessian matrix. The hybrid strategy follows the kinematic curves to decouple the parameters.

I applied the hybrid strategy to transmitted-wave-dominated simple models and to the 2D Middle-East model (Chapter 4) and to reflected-wave-dominated Marmousi model (Chapter 5). I have compared the approach with conventional inversion strategies. The key factor of the hybrid strategy is to update the kinematic velocity. The kinematic velocity is relatively easy to invert in transmitted-wave-dominated models, leading to a faster converge speed and lower final data misfit, compared with conventional simultaneous inversion. The reflection-dominated Marmousi model needs more iterations to update the kinematic velocity. The hybrid inversion strategy successfully reconstructs the attenuation anomalies with lower artifacts, and has a comparable low final data misfit, compared with the conventional simultaneous inversion. For the 2D Middle-East model, 18 iterations with the hybrid strategy leads to a lower misfit than the misfit of the simultaneous inversion. But for the Marmousi model, more than 100 iterations with the hybrid strategy are needed to obtain a comparable low misfit as the one provided

by the simultaneous inversion. The frequency continuation scheme is more efficient to decouple the parameters, with the kinematic velocity being determined within narrow bandwidth.

In conclusion, the hybrid inversion strategy is an alternate inversion strategy to reconstruct velocity and attenuation models without the information of the Hessian matrix.

6.2 Perspectives

In this thesis, we focus on inverting velocity and attenuation models. The hybrid inversion strategy could extend to 3D and apply to real data. Furthermore, with the attenuation models, we also can incorporate Q model a passive parameter to build macro velocity through image-domain method and invert for velocity perturbation by reverse-time migration.

6.2.1 Extension to 3D

We implemented the time domain visco-acoustic FWI in 2D media. Considering the 3D media, the computation costs and memories consuming are significant large. First, the visco-acoustic wave equation involves with extra equations in a total number L for computing memory variable r_p^l, compared to pure acoustic wave equation. L is commonly chosen as 3 to have a constant Q (Plessix et al., 2016; Yang et al., 2018). Second, the 3D media has one extra dimension, leading to significant longer computation time. Third, the gradient is obtained by time integration of the cross-correlation between forward-propagation and back-propagation wavefields at each time step. The intuitive way is to store the forward-propagation wavefields, which leads to very large memories. Careful memory optimization is needed, e.g., checkpointing strategy (Griewank, 1992; Griewank and Walther, 2000; Symes, 2007; Anderson et al., 2012; Komatitsch et al., 2016). The checkpointing strategy allows the forward-propagation wavefields to be reconstructed within a time window with stored checkpointing snapshots. Yang et al. (2016) combined the checkpointing strategy with the reconstruction of forward-propagation wavefields by reverse propagation in time. The forward-propagation wavefields are recomputed from final snapshot with the stored boundary conditions. This method can efficiently stabilize the reverse propagation in the attenuating media to correctly reconstruct forward-propagation wavefields.

6.2.2 Application to real data

For the synthetic study, we assume that we know the source in advance. But for real data, we need to estimate the source. Due to the attenuation, high frequency parts are absorbed, leading to the difficulty for estimating accurate source. Besides, the more

accurate physical models are needed, e.g., the role of density and the anisotropy parameters. Limited acquisition system and noise should also be considered for the real data case.

6.2.3 Image domain macro velocity building with Q model

Image domain methods retrieves the macro velocity model by focusing the image panel (Chauris, 2000; Sava and Biondi, 2004; Symes, 2008; Shen, 2016; Cocher et al., 2017; Chauris and Cocher, 2017; Chauris et al., 2017; Li, 2018). Image domain can be implemented in common-shot or subsurface gathers (Symes, 2017). The image domain methods back-project the image residues to update the macro models (Sava and Biondi, 2004; Symes, 2008; Sava and Vasconcelos, 2011; Shen et al., 2012). Inaccurate velocity leads to a defocused energy of image panel (Figure 1.6). Based on this criteria, the macro velocity model can be updated for a known fixed Q model.

Migration velocity analysis (MVA) (Symes, 2008) and inversion velocity analysis (IVA) (Chauris and Cocher, 2017) optimize the common image gathers (CIG, image panels) to update the macro velocity model. Compared with MVA, IVA uses a direct pseudo inverse of the Born operator in shot-domain (Li and Chauris, 2018) or subsurface domain (Chauris and Cocher, 2017), instead of the adjoint Born operator. Only when the background velocity model is accurate, energy of CIGs will be focused. When the data is affected by attenuation, the attenuation and inaccurate macro velocity lead to dispersed CIGs. However, different combinations of velocity and Q values lead to the same kinematic velocity at the reference frequency. MVA or IVA only takes account of kinematic information. CIGs can be focused with the equivalent kinematic velocity when data is affected by attenuation, which means velocity and Q can not be updated simultaneously by MVA or IVA. To validate this, we apply IVA for macro velocity building with the visco-acosutic data to invert the kinematic velocity model. Then we incorporate the Q model as a passive parameter to invert the macro velocity model.

6.2.3.1 IVA for visco-acoustic data

We apply IVA for three datasets in subsurface domain (Chauris and Cocher, 2017). The criterion for evaluating focusing or dispersion of the CIG panel is

$$\mathcal{J}(v_0)\Big|_{\tau} = \frac{1}{2}\big|h\mathcal{I}(\mathbf{x},h)\big|^2, \tag{6.1}$$

where, v_0 is the background velocity model, h is the horizontal shift in subsurface offset, and $\mathbf{x}$ is the model space with horizontal distance x and depth z for 2D case. $\mathcal{I}(\mathbf{x},h)$ is the CIG. The accurate background macro velocity leads to focused CIG.

Three observed datasets are acoustic data, visco-acoustic data with $Q = 50$ and visco-acoustic data with $Q = 15$. The central frequency of source is 20 Hz. The true velocity

model is a two-layer model, the first layer velocity is 2000 m/s and the second layer velocity is 2100 m/s. The kinematic velocity of the first layer for the three datasets are 2000 m/s, 2060 m/s and 2234 m/s, respectively. We start IVA with the three datasets in a initial background velocity v_p = 2500 m/s.

We perform 6 iterations in pure acoustic media to update the background macro velocity. After 6 iterations, the energy of CIGs is focused (Figure 6.1). The background macro velocity models are updated with the 3 datasets (Figure 6.2). Without the information from the second layer, IVA only can retrieve the kinematic velocity of first layer. The inverted average kinematic velocity of the first layer is 2042 m/s, 2098 m/s and 2345 m/s, respectively. The results coincide with the predicted kinematic values for three models. It shows that MVA or IVA can not update the macro velocity and Q models independently. Thus, we need to incorporate the Q model as a passive parameter to update the macro velocity model.

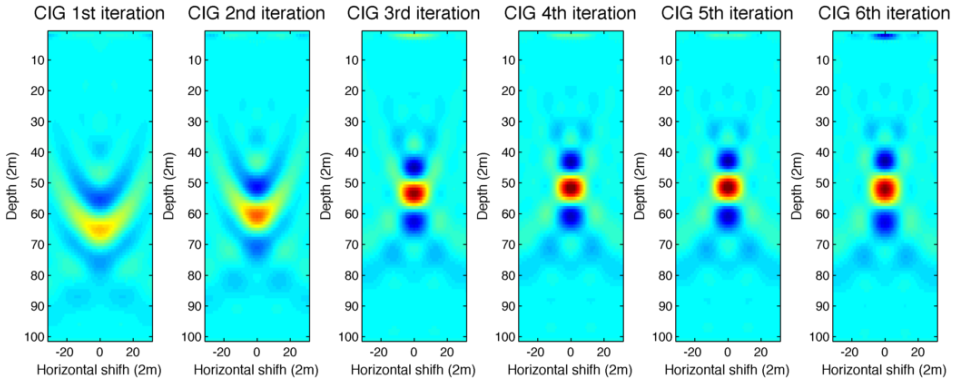

(a) CIGs for acoustic data

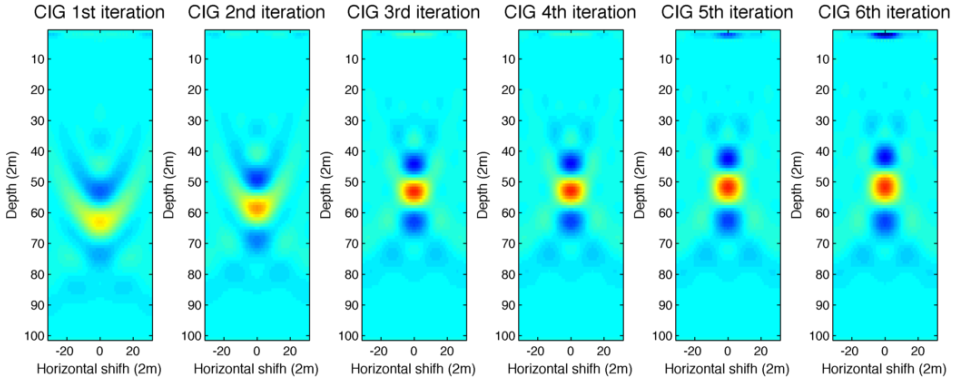

(b) CIGs for visco-acoustic data with $Q = 50$

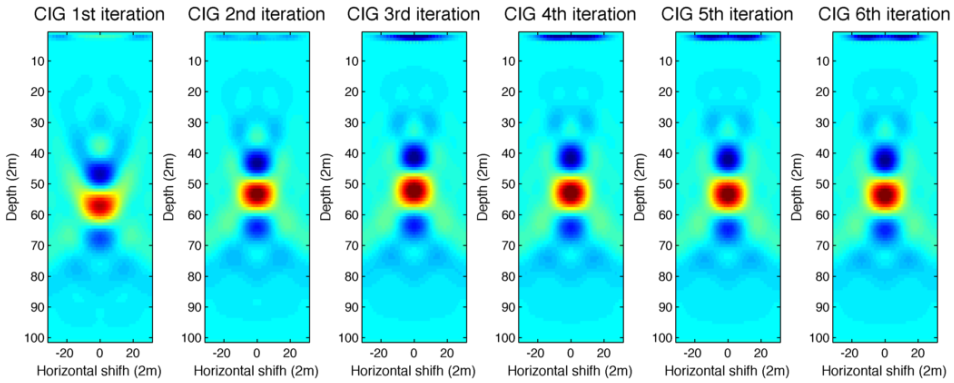

(c) CIGs for visco-acoustic data with $Q = 15$

Figure 6.1: CIGs of three datasets obtained from updated velocity with 6 iterations: acoustic data (top), visco-acoustic data with $Q = 50$ (middle), visco-acoustic data with $Q = 15$ (right).

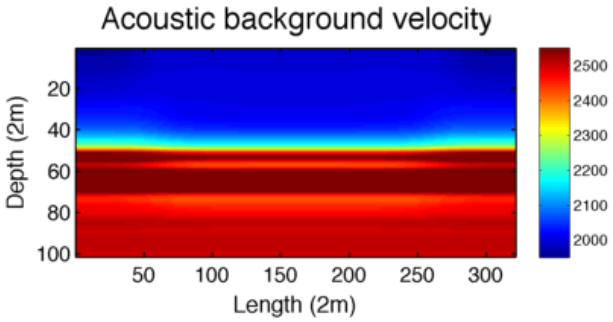

(a) IVA result for acoustic data

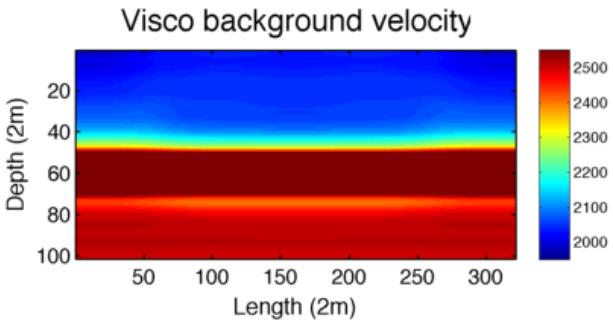

(b) IVA result for visco-acoustic data with $Q = 50$

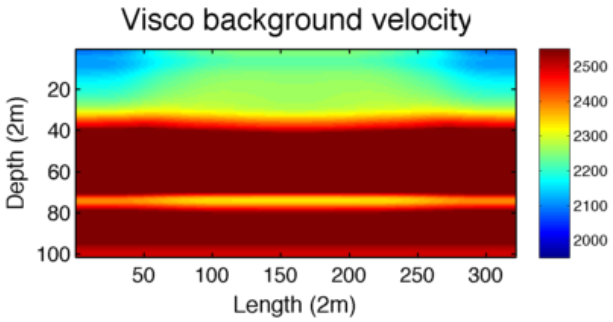

(c) IVA result for visco-acoustic data with $Q = 15$

Figure 6.2: IVA results of three datasets.

6.2.3.2 MVA with Q model

We incorporate Q model as a passive parameter to reconstruct the macro velocity model by MVA (Equation 6.1). But for the MVA in visco-acoustic media, we need to derive the equations for fixed Q.

First, the common image gather $\mathcal{I}(\mathbf{x}, h)$ in the subsurface offset is obtained from adjoint Born operator with a horizontal shift h, given by

$$\begin{aligned}\mathcal{I}(\mathbf{x}, h) &= -\frac{1}{2\rho v_0^2}\sum_{x_s}\sum_{x_r}\sum_{\omega}\Big[(L\tau+1)\nabla\cdot\boldsymbol{v}(x_s, x-h, \omega)q(x_r, x+h, \omega)\\ &\quad+\sum_{l=1}^{L}\frac{\tau}{\tau_\sigma^l}\nabla\cdot\boldsymbol{v}(x_s, x-h, \omega)s^l(x_r, x+h, \omega)\Big],\end{aligned} \tag{6.2}$$

where, p, v_x, v_z and r_p^l are forward-propagation wave fields, and q, u_x, u_z and s^l are back-propagation wavefields. Forward-propagation wave fields are obtained by visco-acosutic wave equation, in the frequency, given as

$$\begin{cases} i\omega p+\kappa(L\tau+1)(\frac{\partial v_x}{\partial x}+\frac{\partial v_z}{\partial z})+\sum_{l=1}^{L} r_p^l = f(x_s,\omega)\\ i\omega v_x+\frac{1}{\rho}\frac{\partial p}{\partial x}=0\\ i\omega v_z+\frac{1}{\rho}\frac{\partial p}{\partial z}=0\\ (i\omega+\frac{1}{\tau_\sigma^l})r_p^l+\frac{1}{\tau_\sigma^l}\tau\kappa(\frac{\partial v_x}{\partial x}+\frac{\partial v_z}{\partial z})=0, \qquad l=\in[1,L].\end{cases} \tag{6.3}$$

The back-propagation wave fields are the adjoint state variables of the forward-propagation wavefields, obtained by the adjoint state equation

$$\begin{cases} i\omega q+\frac{1}{\rho}(\frac{\partial u_x}{\partial x}+\frac{\partial u_z}{\partial z})=-\delta d(x_g,\omega;x_s)\\ i\omega u_x+\kappa(L\tau+1)\frac{\partial q}{\partial x}+\sum_{l=1}^{L}\frac{\tau}{\tau_\sigma^l}\kappa\frac{\partial s^l}{\partial x}=0\\ i\omega u_z+\kappa(L\tau+1)\frac{\partial q}{\partial z}+\sum_{l=1}^{L}\frac{\tau}{\tau_\sigma^l}\kappa\frac{\partial s^l}{\partial z}=0\\ (i\omega-\frac{1}{\tau_\sigma^l})s^l-q=0, \qquad l=\in[1,L].\end{cases} \tag{6.4}$$

The gradient of $\partial\mathcal{J}/\partial v_0|_\tau$ is obtained by the adjoint state method (Plessix, 2006b). The objective function is extended as a Lagrangian formulation depending on $(\boldsymbol{m}, \boldsymbol{U}, \boldsymbol{\lambda})$. The model parameter $\boldsymbol{m}$ is v_0, $\boldsymbol{U}$ is the wavefield, which include forward-propagation wave fields p, v_x, v_z and r_p^l, back-propagation wave fields q, u_x, u_z and s^l and CIG $\mathcal{I}$. λ are the adjoint state variables associated with p, v_x, v_z, r_p^l, q, u_x, u_z, s^l and $\mathcal{I}$, which are all independent. The Lagrangian formulation is

$$\begin{aligned}\mathcal{L}(\boldsymbol{m}, \boldsymbol{U}, \boldsymbol{\lambda}) &= \sum_{\omega}\sum_{h}\frac{1}{2}\big|h\mathcal{I}(\mathbf{x}, h)\big|^2\\ &- <\lambda_1, i\omega p+\kappa(L\tau+1)(\frac{\partial v_x}{\partial x}+\frac{\partial v_z}{\partial z})+\sum_{l=1}^{L} r_p^l - f(x_s,\omega)>\end{aligned} \tag{6.5}$$

$$
\begin{aligned}
- & < \lambda_2, i\omega v_x + \frac{1}{\rho}\frac{\partial p}{\partial x} > \\
- & < \lambda_3, i\omega v_z + \frac{1}{\rho}\frac{\partial p}{\partial z} > \\
- & < \lambda_4^l, (i\omega + \frac{1}{\tau_\sigma^l}) r_p^l + \frac{1}{\tau_\sigma^l}\tau\kappa(\frac{\partial v_x}{\partial x} + \frac{\partial v_z}{\partial z}) > \\
- & < \lambda_5, i\omega q + \frac{1}{\rho}(\frac{\partial u_x}{\partial x} + \frac{\partial u_z}{\partial z}) + \delta d(x_g, \omega; x_s) > \\
- & < \lambda_6, i\omega u_x + \kappa(L\tau + 1)\frac{\partial q}{\partial x} + \sum_{l=1}^{L}\frac{\tau}{\tau_\sigma^l}\kappa\frac{\partial s^l}{\partial x} > \\
- & < \lambda_7, i\omega u_z + \kappa(L\tau + 1)\frac{\partial q}{\partial z} + \sum_{l=1}^{L}\frac{\tau}{\tau_\sigma^l}\kappa\frac{\partial s^l}{\partial z} > \\
- & < \lambda_8^l, (i\omega - \frac{1}{\tau_\sigma^l}) s^l - q > \\
- & < \lambda_9, \mathcal{I}(\mathbf{x}, h) + \frac{1}{2\rho v_0^2}\sum_{x_s}\sum_{x_r}\sum_{\omega}\Big[(L\tau + 1)\nabla\cdot\boldsymbol{v}(x_s, x-h, \omega) q(x_r, x+h, \omega) \\
& + \sum_{l=1}^{L}\frac{\tau}{\tau_\sigma^l}\nabla\cdot\boldsymbol{v}(x_s, x-h, \omega) s^l(x_r, x+h, \omega)\Big] >
\end{aligned}
$$

The Lagrangian equation satisfies

$$
\frac{\partial\mathcal{L}(\boldsymbol{m}, \boldsymbol{U}, \boldsymbol{\lambda})}{\partial\boldsymbol{\lambda}} = 0 \tag{6.6}
$$

$$
\frac{\partial\mathcal{L}(\boldsymbol{m}, \boldsymbol{U}, \boldsymbol{\lambda})}{\partial\boldsymbol{U}} = 0 \tag{6.7}
$$

Equation 6.6 is called the state equation, which has to be satisfied by Equations 6.2, 6.3, 6.4. Equation 6.7 is called adjoint state equation, which gives as

$$
\frac{\partial\mathcal{L}(\boldsymbol{m}, \boldsymbol{U}, \boldsymbol{\lambda})}{\partial p} = i\omega\lambda_1 + \frac{1}{\rho}(\frac{\partial\lambda_2}{\partial x} + \frac{\partial\lambda_3}{\partial z}) \tag{6.8}
$$

$$
\begin{aligned}
\frac{\partial\mathcal{L}(\boldsymbol{m}, \boldsymbol{U}, \boldsymbol{\lambda})}{\partial v_x} = & \frac{\partial}{\partial x}(\kappa(L\tau + 1)\lambda_1) + i\omega\lambda_2 + \frac{\partial}{\partial x}(\sum_{l=1}^{L}\frac{\tau}{\tau_\sigma^l}\kappa\lambda_4^l) \\
& + \sum_h \frac{1}{2\rho v_0^2}(L\tau + 1)\frac{\partial}{\partial x} q(x + 2h)\lambda_9(x + h) \\
& + \sum_h \frac{1}{2\rho v_0^2}\sum_{l=1}^{L}\frac{\tau}{\tau_\sigma^l}\frac{\partial}{\partial x} s^l(x + 2h)\lambda_9(x + h)
\end{aligned} \tag{6.9}
$$

$$\begin{aligned}
\frac{\partial \mathcal{L}(\boldsymbol{m},\boldsymbol{U},\boldsymbol{\lambda})}{\partial v_z} &= \frac{\partial}{\partial x}(\kappa(L\tau+1)\lambda_1) + i\omega\lambda_2 + \frac{\partial}{\partial z}(\sum_{l=1}^{L}\frac{\tau}{\tau_\sigma^l}\kappa\lambda_4^l) \qquad (6.10)\\
&+ \sum_h \frac{1}{2\rho v_0^2}(L\tau+1)\frac{\partial}{\partial z}q(x+2h)\lambda_9(x+h)\\
&+ \sum_h \frac{1}{2\rho v_0^2}\sum_{l=1}^{L}\frac{\tau}{\tau_\sigma^l}\frac{\partial}{\partial z}s^l(x+2h)\lambda_9(x+h)\\
\frac{\partial \mathcal{L}(\boldsymbol{m},\boldsymbol{U},\boldsymbol{\lambda})}{\partial r_p^l} &= -\lambda_1 + (i\omega - \frac{1}{\tau_\sigma^l})\lambda_4^l \qquad (6.11)\\
\frac{\partial \mathcal{L}(\boldsymbol{m},\boldsymbol{U},\boldsymbol{\lambda})}{\partial q} &= i\omega\lambda_5 + \frac{\partial}{\partial x}[\kappa(L\tau+1)\lambda_6] + \frac{\partial}{\partial z}[\kappa(L\tau+1)\lambda_7] \qquad (6.12)\\
&+ \sum_{l=1}^{L}\lambda_8^l + \sum_h \frac{1}{2\rho v_0^2}(L\tau+1)\nabla\cdot\boldsymbol{v}(x-2h)\lambda_9(x-h)\\
\frac{\partial \mathcal{L}(\boldsymbol{m},\boldsymbol{U},\boldsymbol{\lambda})}{\partial u_x} &= \frac{\partial}{\partial x}(\frac{1}{\rho}\lambda_5) + i\omega\lambda_6 \qquad (6.13)\\
\frac{\partial \mathcal{L}(\boldsymbol{m},\boldsymbol{U},\boldsymbol{\lambda})}{\partial u_z} &= \frac{\partial}{\partial z}(\frac{1}{\rho}\lambda_5) + i\omega\lambda_7 \qquad (6.14)\\
\frac{\partial \mathcal{L}(\boldsymbol{m},\boldsymbol{U},\boldsymbol{\lambda})}{\partial s^l} &= (i\omega + \frac{1}{\tau_\sigma^l})\lambda_8 + \frac{\tau}{\tau_\sigma^l}\kappa(\frac{\partial\lambda_6}{\partial x} + \frac{\partial\lambda_7}{\partial z}) \qquad (6.15)\\
&+ \sum_h \frac{1}{2\rho v_0^2}\frac{\tau}{\tau_\sigma^l}\nabla\cdot\boldsymbol{v}(x-2h)\lambda_9(x-h)\\
\frac{\partial \mathcal{L}(\boldsymbol{m},\boldsymbol{U},\boldsymbol{\lambda})}{\partial \mathcal{I}} &= h^2\mathcal{I} - \lambda_9(\mathbf{x},h) \qquad (6.16)
\end{aligned}$$

We reorganize the equations

$$\lambda_9(\mathbf{x},h) = h^2\mathcal{I}(\mathbf{x},h) \qquad (6.17)$$

$$\begin{cases}
i\omega p + \kappa(L\tau+1)(\frac{\partial v_x}{\partial x} + \frac{\partial v_z}{\partial z}) + \sum_{l=1}^{L} r_p^l = -\sum_h \frac{1}{2\rho v_0^2}(L\tau+1)\nabla\cdot\boldsymbol{v}(x-2h)\lambda_9(x-h)\\
i\omega v_x + \frac{1}{\rho}\frac{\partial p}{\partial x} = 0\\
i\omega v_z + \frac{1}{\rho}\frac{\partial p}{\partial z} = 0\\
(i\omega + \frac{1}{\tau_\sigma^l})r_p^l + \frac{1}{\tau_\sigma^l}\tau\kappa(\frac{\partial v_x}{\partial x} + \frac{\partial v_z}{\partial z}) = -\sum_h \frac{1}{2\rho v_0^2}\frac{\tau}{\tau_\sigma^l}\nabla\cdot\boldsymbol{v}(x-2h)\lambda_9(x-h), l =\in [1,L],
\end{cases} \qquad (6.18)$$

where, λ_5, λ_6, λ_7 and λ_8^l are written as p, v_x,v_z, r_p^l respectively.

$$\begin{cases} i\omega q + \frac{1}{\rho}(\frac{\partial u_x}{\partial x} + \frac{\partial u_z}{\partial z}) = 0 \\ i\omega u_x + \kappa(L\tau+1)\frac{\partial q}{\partial x} + \sum_{l=1}^{L}\frac{\tau}{\tau_\sigma^l}\kappa\frac{\partial s^l}{\partial x} &= -\sum_h \frac{1}{2\rho v_0^2}(L\tau+1)\frac{\partial q(x+2h)}{\partial x}\lambda_9(x+h) \\ & \quad -\sum_h \frac{1}{2\rho v_0^2}\sum_{l=1}^{L}\frac{\tau}{\tau_\sigma^l}\frac{\partial s^l(x+2h)}{\partial x}\lambda_9(x+h) \\ i\omega u_z + \kappa(L\tau+1)\frac{\partial q}{\partial z} + \sum_{l=1}^{L}\frac{\tau}{\tau_\sigma^l}\kappa\frac{\partial s^l}{\partial z} &= -\sum_h \frac{1}{2\rho v_0^2}(L\tau+1)\frac{\partial q(x+2h)}{\partial z}\lambda_9(x+h) \\ & \quad -\sum_h \frac{1}{2\rho v_0^2}\sum_{l=1}^{L}\frac{\tau}{\tau_\sigma^l}\frac{\partial s^l(x+2h)}{\partial z}\lambda_9(x+h) \\ (i\omega - \frac{1}{\tau_\sigma^l})s^l - q = 0, l =\in [1, L] \end{cases} \tag{6.19}$$

where λ_1, λ_2, λ_3 and λ_4^l are written as q, u_x, u_z and s^l respectively. Therefore, $\boldsymbol{\lambda}$ are obtained by solving the adjoint state equations (Equations 6.17, 6.18 and 6.19). Finally, the gradient of objective function becomes

$$\frac{\partial \mathcal{L}(\boldsymbol{m}, \boldsymbol{U}, \boldsymbol{\lambda})}{\partial \boldsymbol{m}} = \frac{\partial \mathcal{J}}{\partial \boldsymbol{m}} - \sum_{i=1}^{N} < \lambda_i, \frac{\mathcal{F}(\boldsymbol{U}(\boldsymbol{m}), \boldsymbol{m})}{\partial \boldsymbol{m}} >, \tag{6.20}$$

where $\mathcal{F}(\boldsymbol{U}(\boldsymbol{m}), \boldsymbol{m})$ is forward functions, defined as the group of Equations 6.2, 6.3, 6.4. As $\boldsymbol{m}$ is defined as v_0, the macro velocity is updated by

$$\begin{aligned} \frac{\partial \mathcal{J}(v_0)}{\partial v_0}\Big|_\tau = & - 2\rho v_0 \Bigg\{ (L\tau+1)\nabla\cdot\boldsymbol{v}\lambda_1 + \sum_{l=1}^{L}\frac{\tau}{\tau_\sigma^l}\nabla\cdot\boldsymbol{v}\lambda_4^l \\ & + (L\tau+1)\frac{\partial q}{\partial x}\lambda_6 + \sum_{l=1}^{L}\frac{\tau}{\tau_\sigma^l}\frac{\partial s^l}{\partial x}\lambda_6 \\ & + (L\tau+1)\frac{\partial q}{\partial z}\lambda_7 + \sum_{l=1}^{L}\frac{\tau}{\tau_\sigma^l}\frac{\partial s^l}{\partial z}\lambda_7 \\ & - \frac{2}{v_0^4}\Big[\sum_h (L\tau+1)\nabla\cdot\boldsymbol{v}(x-h)q(x+h)\lambda_9(x,h)\Big] \\ & - \frac{2}{v_0^4}\Big[\sum_h \Big(\sum_{l=1}^{L}\frac{\tau}{\tau_\sigma^l}\nabla\cdot\boldsymbol{v}(x-h)s^l(x+h)\lambda_9(x,h)\Big)\Big] \Bigg\}. \end{aligned} \tag{6.21}$$

For example, we have a two-layer model with velocity being 2100 m/s and 2200 m/s. The interface is at the depth of 51. Q model is homogeneous with the value being 1000. Initial velocity is 2500 m/s and input Q is 1000. We obtain the gradient with respect to the macro velocity (Figure 6.3). The blue area indicates the negative gradient to decrease the velocity values.

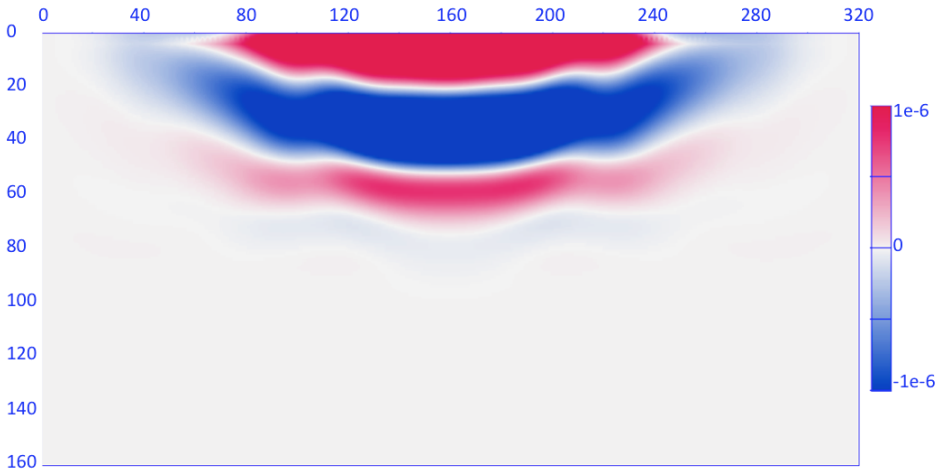

Figure 6.3: The gradient of the objective function with respect to the macro velocity.

6.2.4 Inverting velocity perturbation with Q model

The velocity model can be divided into a background macro model and a velocity perturbation under the Born approximation. The velocity perturbation is also called seismic image in reflection seismology. Seismic image characterizes the structures of the geological bodies, which is useful for interpretation. Based on Born approximation, the velocity perturbation leads to perturbed data. The velocity perturbation is inverted with the adjoint Born operator applied to the perturbed data (Claerbout, 1992). It can be implemented by wave-equation reverse-time migration (RTM) (McMechan, 1983; Baysal et al., 1983). To compensate for insufficient illumination and geometrical spreading effects, true-amplitude migration is applied to retrieved the velocity perturbation (Zhang et al., 2003, 2005; Zhang and Sun, 2009; Zhang et al., 2014b). Seismic attenuation absorbs wave energy, leading to imaging blurring under the attenuation area. There are two ways to improve the seismic images. The first way is Q compensated RTM, which is implemented on the pre-stacked data by enhancing the wave energy (Zhang et al., 2010). The other way is to apply the least-squares RTM (LS-RTM) to iteratively update the velocity perturbations with Q being a passive parameter (Zhang et al., 2014a; Dutta and Schuster, 2014; Zeng et al., 2017).

6.2.4.1 Q least-squares RTM

The least-squares RTM is an iterative scheme to update the seismic images (Zhang et al., 2014a; Dutta and Schuster, 2014; Zeng et al., 2017). Q is incorporated as a passive parameter. LS-RTM is similar to the mono-parameter velocity inversion for visco-acoustic FWI with fixed true Q model, except for a linearized inversion (Lailly, 1983; Lines and

Treitel, 1984; Tarantola, 1984b). This aspect is not discussed in detail.

6.2.4.2 Q compensated RTM

Conventional methods of compensating attenuation are implemented in the data domain by an inverse Q-filter (Wang, 2008). This Q-filter is based on a 1D Q model, which is hard to handle complicated geological models. As the visco-elastic / visco-acoustic simulation becomes achievable, the Q compensated RTM was first proposed by Zhang et al. (2010). The basic idea is to compensate for the energy absorptions during the wave extrapolation (Figure 6.4). The seismic images are obtained by the zero-lag cross-correlation between source side forward-propagation with receiver side back-propagation wave fields (Claerbout, 1971). Zhu and Harris (2014) and Zhu et al. (2014) extended the fractional derivative visco-acoustic wave equation into a dispersion-absorption-split wave equation. Through changing the absorption term, the Q compensated extrapolation is achieved. However, the simulation needs to solve the fractional derivative with space Fourier transform, which is computational expensive. Based on our previous analysis of kinematic velocity (Section 2.6.3), we modifies the visco-acoustic wave equation (Equation 2.42) to fix the kinematic velocity and to compensate the absorption.

We rewrite the visco-acoustic wave equation into the second-order form with constant density, given as

$$(i\omega)^2 p - \frac{1}{\rho}\left\{\left[\kappa(L\tau+1) - \sum_{l=1}^{L}\frac{\kappa\tau}{1+\omega^2\tau_{\sigma l}^2}\right] + i\cdot\phi\left[\sum_{l=1}^{L}\frac{\kappa\tau\omega\tau_{\sigma l}}{1+\omega^2\tau_{\sigma l}^2}\right]\right\}\nabla^2 p = F(x_s,\omega), \tag{6.22}$$

where ϕ is equal to 1 for the visco-acoustic wave equation. As we analyzed before, the real term of the complex velocity is related to the kinematic effects. The imaginary term of the complex velocity corresponds to the energy absorption with a positive ϕ. Therefore, a negative ϕ corresponds to energy compensation. To obtain the compensated image condition, ϕ turns into -1 to amplify the energy. The first-order velocity-pressure equations for forward modeling is

$$\begin{cases} \frac{\partial p}{\partial t} + \kappa(L\tau+1)(\nabla\cdot\boldsymbol{v}) + \sum_{l=1}^{L} r_p^l = f(x_s,t) \\ \frac{\partial \boldsymbol{v}}{\partial t} + \frac{1}{\rho}\nabla p = 0 \\ -\frac{\partial r_p^l}{\partial t} + \frac{1}{\tau_\sigma^l}(r_p^l + \tau\kappa(\nabla\cdot\boldsymbol{v})) = 0, l\in[1,L], \end{cases} \tag{6.23}$$

where p, v_x, v_z and r_p^l are forward-propagation wave fields. And the back-propagation wave fields are obtained by

$$\begin{cases} \frac{\partial q}{\partial t} + \nabla\cdot(\frac{1}{\rho}\boldsymbol{u}) = -\delta d(x_g,t;x_s) \\ \frac{\partial \boldsymbol{u}}{\partial t} + \nabla\kappa(L\tau+1)q + \nabla(\sum_{l=1}^{L}\frac{\tau}{\tau_\sigma^l}\kappa s^l) = 0 \\ \frac{\partial s^l}{\partial t} + \frac{s^l}{\tau_\sigma^l} + q = 0, l\in[1,L], \end{cases} \tag{6.24}$$

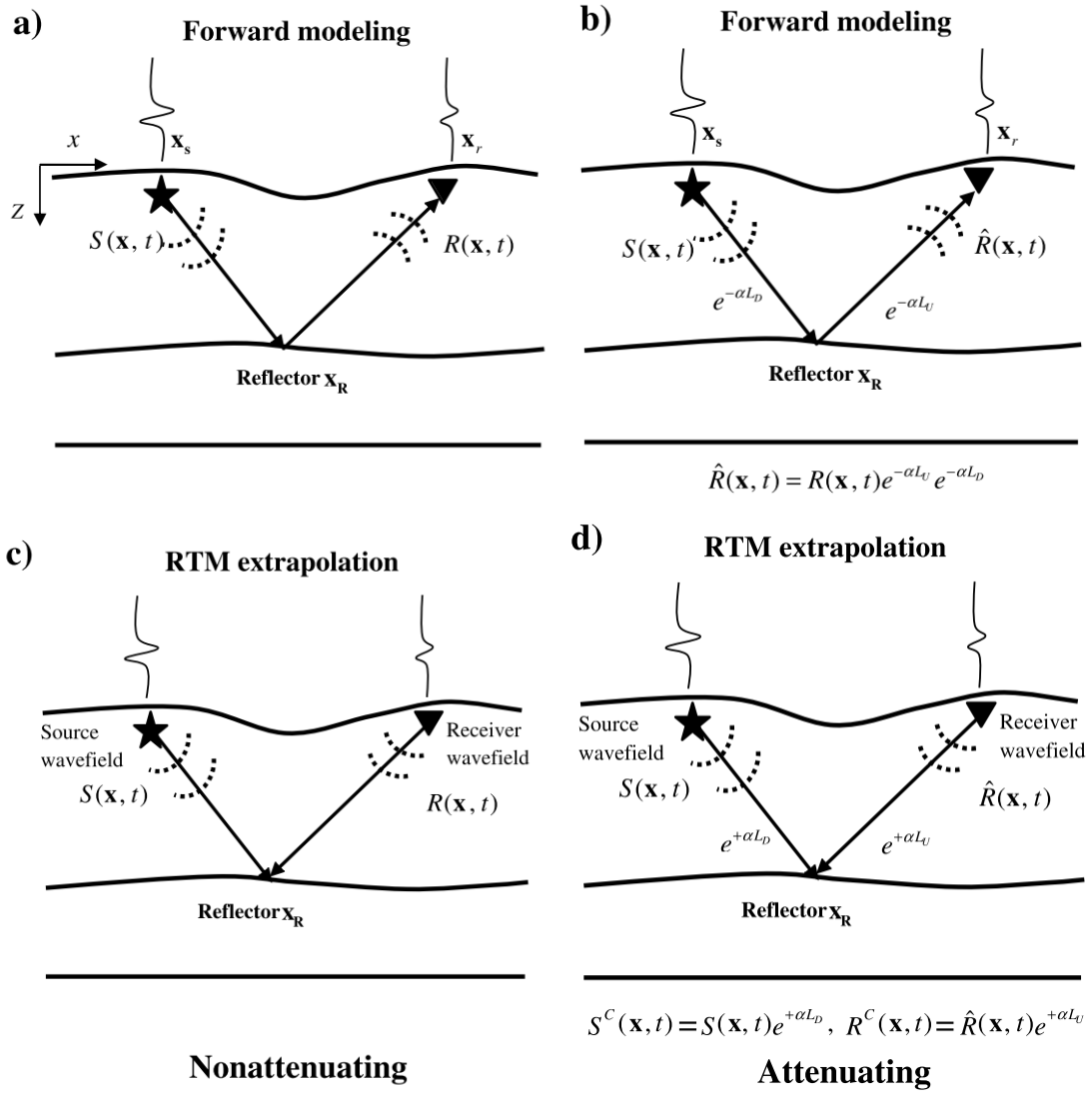

Figure 6.4: The image condition for non-attenuating (a, c) and attenuating media (b, d) by cross-correlating the source side forward-propagation with receiver side back-propagation wave fields (c, d) at zero-lag. For attenuating media, the forward data are attenuated by $e^{-\alpha L_D}e^{-\alpha L_U}$ (b). To obtain the same quality of seismic images, the source side and receiver side wave fields should be compensate the energy by $e^{\alpha L_D}$ and $e^{\alpha L_U}$, respectively (d) (Adapted from Zhu et al. (2014)).

where q, u_x, u_z and s^l are back-propagation wave fields. The r_p^l in the third line of Equation 6.23 is exponentially increasing with time, and s^l in the third line of Equation 6.24 is exponentially increasing with reverse-time. The increases of r_p^l and s^l stand

for the Q compensation. The amplifying leads to unstable computations, especially for higher frequency noise during extrapolation. A low-pass filter is needed to stabilize the computations (Zhang et al., 2010; Zhu et al., 2014). Finally, we implement the Q compensated RTM with the visco-acoustic wave equation based on nearly constant Q model (the results are not presented here).

Bibliography

Aki, K. [1980a] Attenuation of shear-waves in the lithosphere for frequencies from 0.05 to 25 Hz. *Phys. Earth Planet. Inter.*, **21**, 50–60. (cit. on p. 5.)

Aki, K. [1980b] Scattering and attenuation of shear waves in the lithosphere. *J. Geophys. Res.*, **85**, 6496–6504. (cit. on p. 5.)

Aki, K. [1982] Scattering and attenuation. *Bulletin of the Seismological Society of America*, **72**(6B), S319–S330. (cit. on p. 5.)

Aki, K. and Richards, P.G. [1980] *Quantitative seismology*. W. H. Freeman and Co. (cit. on pp. 3, 5, 7, 9, 15, 32, 41, 49, 66, and 68.)

Alford, R., Kelly, K. and Boore, D.M. [1974] Accuracy of finite-difference modeling of the acoustic wave equation. *Geophysics*, **39**(6), 834–842. (cit. on p. 38.)

Alterman, Z. and Karal-Jr., F.C. [1968] Propagation of elastic waves in layered media by finite difference methods. *Bulletin of the Seismological Society of America*, **58**(1), 367–398. (cit. on p. 35.)

Anderson, D.L. [1967] The anelasticity of the mantle. *Geophys. J. R. Astr. Soc.*, **14**, 135–164. (cit. on p. 4.)

Anderson, J.E., Tan, L. and Wang, D. [2012] Time-reversal checkpointing methods for RTM and FWI. *Geophysics*, **77**(4), S93–S103. (cit. on p. 160.)

Asnaashari, A., Brossier, R., Garambois, S., Audebert, F., Thore, P. and Virieux, J. [2013] Regularized seismic full waveform inversion with prior model information. *Geophysics*, **78**(2), R25–R36. (cit. on p. 107.)

Bagley, L. [1989] Power law and fractional calculus model of viscoelasticity. *AIAA Journel*, **27**(10), 1412–1417. (cit. on pp. 56 and 57.)

Bai, J., Yingst, D., Bloor, R. and Leveille, J. [2012] Waveform inversion with attenuation. In: *SEG Technical Program Expanded Abstracts 2012*. (cit. on pp. 11 and 66.)

Bai, J., Yingst, D., Bloor, R. and Leveille, J. [2014] Viscoacoustic waveform inversion of velocity structures in the time domain. *Geophysics*, **79**(3), R103–R119. (cit. on pp. 11 and 66.)

Bao, X., Dalton, C.A., Jin, G., Gaherty, J.B. and Shen, Y. [2016] Imaging Rayleigh wave attenuation with USArray. *Geophysical Journal International*, **206**(1), 241–259. (cit. on p. 4.)

Barnes, C. and Charara, M. [2009] Viscoelastic full waveform inversion of North Sea

offset VSP data. In: *SEG Technical Program Expanded Abstracts 2009*. 1822–1825. (cit. on pp. 11 and 66.)

Barnes, C. and Charara, M. [2010] Anisotropic anelastic full waveform inversion: Application to North Sea offset VSP data. In: *SEG Technical Program Expanded Abstracts 2010*. 972–976. (cit. on pp. 11 and 66.)

Barnes, C., Charara, M. and Tsuchiya, T. [2004] Borehole seismic data inversion for attenuating media. In: *66th EAGE Conference and Exhibition, Extended Abstracts*. (cit. on pp. 11 and 66.)

Barnes, C., Charara, M. and Williamson, P. [2014] P and S Wave Attenuation Effects on Full-Waveform Inversion for Marine Seismic Data. In: *SEG Technical Program Expanded Abstracts 2014*. 949–953. (cit. on pp. 11, 66, and 67.)

Barton, N. [2007] *Rock quality, seismic velocity, attenuation and anisotropy*. Taylor & Francis, United Kingdom. (cit. on p. 7.)

Baysal, E., Kosloff, D.D. and Sherwood, J.W. [1983] Reverse time migration. *Geophysics*, **48**(11), 1514–1524. (cit. on p. 169.)

Belahi, T., Fuji, N. and Singh, S.C. [2015] Elastic versus viscoelastic full waveform inversion of near-offset and wide-angle data in the presence of attenuation. In: *77th EAGE Conference and Exhibition, Extended Abstracts*. (cit. on pp. 11 and 66.)

Ben-Menahem, A. and Singh, S.J. [1981] *Seismic waves and sources*. Springer, New York. (cit. on pp. 26 and 58.)

Bérenger, J.P. [1994] A perfectly matched layer for the absorption of electromagnetic waves. *Journal of computational physics*, **114**(2), 185–200. (cit. on p. 39.)

Best, A.I., MaCann, C. and Sothcott, J. [1994] The relationships between the velocities, attenuations and petrophysical properties of reservoir sedimentary rocks. *Geophysical Prospecting*, **42**, 151–178. (cit. on p. 65.)

Blair, G.S., Veinoglou, B.C. and Caffyn, J.E. [1947] Limitation of the Newtonian time scale in relation to non- equilibrium rheological states and a theory of quasi-properties. *Proc. Roy. Soc. A*, **189**, 69–87. (cit. on p. 55.)

Blanch, J.O., Robertsson, J.O.A. and Symes, W.W. [1995] Modelling of a constant Q: Methodology and algorithm for an efficient and optimally inexpensive viscoelastic technique. *Geophysics*, **60**(1), 176–184. (cit. on pp. 8, 23, 26, 28, 29, 30, 32, 33, 36, 59, 68, and 69.)

Bland, D.R. [1960] *The Theory of Linear Viscoelasticity*. McGraw-Hill Book Co. (cit. on p. 57.)

Boit, M.A. [1954] Theory of stress-strain relations in anisotropic visco-elasticity and relaxation phenomena. *J. Appl. Phys.*, **25**, 1358–1391. (cit. on pp. 26 and 58.)

Boltzmann, L. [1876] Theorie der elastiche Nachwirkung. *Ann. Phys. Chem. Erqanzung*, **7**, 624–654. (cit. on pp. 23 and 24.)

Bongajum, E.L. [2011] *Investigating seismic wave scattering in heterogeneous environments and implications for seismic imaging*. Ph.D. thesis, University of Toronto. (cit. on p. 5.)

Boore, D.M., Larner, K.L. and Aki, K. [1971] Comparison of two independent methods for the solution of wave-scattering problems: Response of a sedimentary basin to vertically incident SH wave. *J. Geophys. Res.*, **78**, 558–569. (cit. on p. 7.)

Bregman, N.D., Bailey, R.C. and Chapman, C.H. [1989] Traveltime and amplitude inversion in crosshole seismology. *J. Geophys. Res.*, 7577–7587. (cit. on pp. 10 and 66.)

Brossier, R., Etienne, V., Operto, S. and Virieux, J. [2010] Frequency-domain numerical modelling of visco-acoustic waves based on finite-difference and finite-element discontinuous Galerkin methods. *Acoustic Waves, SCIYO*, 125–158. (cit. on pp. 32 and 35.)

Brossier, R., Operto, S. and Virieux, J. [2009] Seismic imaging of complex onshore structures by 2D elastic frequency-domain full-waveform inversion. *Geophysics*, **74**(6), WCC105–WCC118. (cit. on pp. 33, 35, 39, and 150.)

Brzostowski, M. and McMechan, G. [1992] 3D tomographic imaging of near-surface seismic velocity and attenuation. *Geophysics*, **57**, 396–403. (cit. on pp. 9, 12, and 66.)

Cadoret, T., Mavko, G. and Zinszner, B. [1998] Fluid distribution effect on sonic attenuation in partially saturated limestones. *Geophysics*, **63**(1), 154–160. (cit. on p. 3.)

Carcione, J.M. [2010] A generalization of the Fourier pseudospectral method. *Geophysics*, **75**, A53–56. (cit. on p. 8.)

Carcione, J.M. [2011] *Wave Fields in Real Media: Wave Propagation in Anisotropic, Anelastic, Porous and Electromagnetic Media*. Elsevier, Amsterdam, Netherlands. (cit. on pp. xi, xii, 8, 26, 28, 56, and 57.)

Carcione, J.M., Cavallini, F., Mainardi, F. and Hanyga, A. [2002] Time-domain modelling of constant-Q seismic waves using fractional derivatives. *Pure Appl. Geophys.*, **159**, 1719–1736. (cit. on pp. xi, 8, 36, and 61.)

Carcione, J.M., Kosloff, D. and Kosloff, R. [1988a] Wave propagation simulation in a linear viscoacoustic medium. *Geophysical Journal International*, **93**, 393–407. (cit. on pp. 8, 23, 26, 28, 33, 52, 53, 57, 58, 61, and 68.)

Carcione, J.M., Kosloff, D. and Kosloff, R. [1988b] Wave propagation simulation in a linear viscoelastic medium. *Geophysical Journal International*, **95**, 597–611. (cit. on pp. 8, 23, 26, 28, 33, 58, and 68.)

Causse, E. and Mittet, R. [1996] Finite-difference inversion in viscoacoustic media. In: *58th EAGE Conference and Exhibition, Extended Abstracts*. (cit. on pp. 11 and 66.)

Causse, E., Mittet, R. and Ursin, B. [1999] Preconditioning of full-waveform inversion in viscoacoustic media. *Geophysics*, **64**, 130–145. (cit. on pp. 11 and 66.)

Cavalca, M. and Fletcher, R. [2009] Estimation of the near-surface Q distribution from pre-stack surface seismic data. In: *EAGE/SEG Research Workshop*. (cit. on pp. 9 and 66.)

Cavalca, M., Moore, I., Zhang, L., Ng, S.L., Fletcher, R.P. and Bayly, M.P. [2011] Ray-based Tomography for Q Estimation and Q Compensation in Complex Media. In: *73rd EAGE Conference and Exhibition, Extended Abstracts*. (cit. on pp. 9 and 66.)

Chaljub, E., Komatitsch, D., Vilotte, J.P., Capdeville, Y., Valette, B. and Festa, G. [2007]

Spectral element analysis in seismology. In: Advances in Wave Propagation in Heterogeneous Media. Academic Press. (cit. on p. 35.)

Charara, M., Barnes, C. and Tarantola, A. [1996] The state of affairs in inversion of seismic data: an OVSP example. In: *SEG Technical Program Expanded Abstracts 1996*. 1999–20002. (cit. on pp. 10 and 66.)

Charara, M., Barnes, C. and Tarantola, A. [2000] *Full waveform inversion of seismic data for a viscoelastic medium*. Springer Berlin Heidelberg, Berlin, Heidelberg, 68–81. (cit. on pp. 11 and 66.)

Charara, M., Barnes, C. and Tsuchiya, T. [2004] Crosswell seismic data tomography for heterogeneous viscoelastic media. In: *SEG Technical Program Expanded Abstracts 2004*. 1822–1825. (cit. on pp. 11 and 66.)

Chauris, H. [2000] *Analyse de vitesse par migration pour l'imagerie des structures complexes en sismique réflexion*. Ph.D. thesis, Thèese de doctorat, Ecole des Mines de Paris. (cit. on pp. 12 and 161.)

Chauris, H. and Cocher, E. [2017] From migration to inversion velocity analysis. *Geophysics*, **82**(3), S207–S223. (cit. on pp. 12 and 161.)

Chauris, H., Li, Y. and Cocher, E. [2017] Image-domain versus data-domain velocity analysis based on true-amplitude subsurface extended migration. In: *79th EAGE Conference and Exhibition 2017-Workshops*. (cit. on pp. 12 and 161.)

Cheng, X., Jiao, K., Sun, D. and Vigh, D. [2015] A new approach of viscoacoustic waveform inversion in the time domain. In: *SEG Technical Program Expanded Abstracts 2015*. (cit. on pp. 11 and 66.)

Chew, W.C. and Liu, Q. [1996] Perfectly Matched Layers for elastodynamics: a new absorbing boundary condition. *Journal of Computational Acoustics*, **4**, 341–359. (cit. on p. 39.)

Christensen, R.M. [1982] *Theory of Viscoelasticity*. Academic press, New York, USA. (cit. on pp. 23 and 25.)

Claerbout, J.F. [1971] Toward a unified theory of reflector mapping. *Geophysics*, **36**(3), 467–481. (cit. on p. 170.)

Claerbout, J.F. [1992] *Earth soundings analysis: Processing versus inversion*. Blackwell Scientific Publications. (cit. on p. 169.)

Cocher, E., Chauris, H. and Plessix, R.É. [2017] Seismic iterative migration velocity analysis: two strategies to update the velocity model. *Computational Geosciences*, **21**, 1–22. (cit. on pp. 12 and 161.)

Collino, F. and Tsogka, C. [2001] Applications of the PML absorbing layer model to the linear elastodynamic problem in anisotropic heterogeneous media. *Geophysics*, **66**, 294–305. (cit. on p. 39.)

Courtant, R., Friedrichs, K.O. and Lewy, H. [1928] Uber die partiellen differenzengleichungen der mathematischen physik. *Mathematische Annalen*, **100**, 32–74. (cit. on p. 38.)

Dalton, C.A. and Ekstrom, G. [2006] Global models of surface wave attenuation. *Jour-*

nal of Geophysical Research: Solid Earth, **111**(B5). (cit. on p. 4.)

Day, S.M. and Minister, J.B. [1984] Numerical simulation of wave fields using a Pade approximation method. *Geophysical Journal of the Royal Astronomical Society*, **78**, 105–118. (cit. on pp. 7 and 8.)

Deng, F. and McMechan, G.A. [2007] True-amplitude prestack depth migration. *Geophysics*, **72**, S155–166. (cit. on p. 7.)

Dutta, G. and Schuster, G.T. [2014] Attenuation compensation for least-squares reverse time migration using the viscoacoustic-wave equation. *Geophysics*, **79**(6), S251–S262. (cit. on pp. 5 and 169.)

Emmerich, H. [1992] PSV-wave propagation in a medium with local heterogeneities: A hybrid formulation and its application. *Geophysics*, **109**, 54–64. (cit. on pp. 8 and 33.)

Emmerich, H. and Korn, M. [1987] Incorporation of attenuation into time-domain computations of seismic wave fields. *Geophysics*, **52**, 1252–1264. (cit. on pp. xii, 8, 23, 24, 26, 28, 32, 36, 52, 53, 57, 58, 61, and 68.)

Fabien-Quellet, G., Gloaguen, E. and Giroux, B. [2017] Time domain viscoelastic full waveform inversion. *Geophysical Journal International*, **209**, 1718–1734. (cit. on pp. 11, 15, 66, 67, 68, and 71.)

Fah, D. [1992] *A hybrid technique for the estimation of strong ground motion in sedimentary basins*. Ph.D. thesis, Swiss Fed. Inst. of Technol., Zurich, Switzerland. (cit. on pp. 8 and 33.)

Faul, U.H., Gerald, J.D.F. and Jackson, I. [2004] Shear wave attenuation and dispersion in melt-bearing olivine polycrystals: 2. Microstructral interpretation and seismological implications. *J. Geophys. Res.*, **109**(B06202). (cit. on p. 4.)

Fielitz, D. and Wegler, U. [2015] Intrinsic and scattering attenuation as derived from fluid induced microseismicity at the German Continental Deep Drilling site. *Geophysical Journal International*, **201**(3), 1346–1361. (cit. on p. 5.)

Fletcher, R.P., Nichols, D. and Cavalca, M. [2012] Wavepath-consistent effective Q estimation for Q-compensated reverse time migration. In: *82nd EAGE Conference and Exhibition, Extended Abstracts*. (cit. on p. 5.)

Fung, Y.C. [1965] *Foundations of solid mechanics*. Prentice-Hall, Upper Saddle River, New Jersey, USA. (cit. on pp. 23, 26, 53, and 58.)

Futterman, W.I. [1962] Dispersive body wave. *J. Geophys. Res.*, **67**, 5279–5291. (cit. on pp. 7, 9, 15, 66, and 68.)

Gamar, F., Carotti, D., Guillaume, P., Gacha, A. and Lopes, L. [2015] Success of high-resolution volumetric Q-tomography in the automatic detection of gas anomalies on offshore Brunei data. In: *SEG Technical Program Expanded Abstracts 2015*. 5184–5188. (cit. on p. 5.)

Gamar, F., Janot, L., Carotti, D., Gout, J.M., Mascomere, J.P. and Mikkelsen, G. [2016] Image Quality Enhancement Using Volumetric Q- tomography and Q-PSDM - Martin Linge Case Study. In: *78th EAGE Conference and Exhibition, Extended Abstracts*. (cit. on p. 5.)

Gao, F. and Wang, Y. [2016] Simultaneous inversion for velocity and attenuation by waveform tomography. *Journal of applied geophysics*, **131**, 103–108. (cit. on pp. 11 and 66.)

Gardner, G.H.F., Wyllie, M.R.J. and Droschak, D.M. [1964] Effects of pressure and fluid saturation on the attenuation of elastic waves in sands. *J. Petro Tech.*, **16**, 189–198. (cit. on p. 3.)

Gemant, A. [1938] On fractional differentials. *Phil. Mag. (Ser. 7)*, **25**, 540–549. (cit. on p. 55.)

Goes, S., Govers, R. and Vacher, P. [2000] Shallow mantle temperature under Europe from P and S wave tomography. *J. Geophys. Res.*, **105**(11), 153–169. (cit. on p. 4.)

Gosselin-Cliche, B. and Giroux, B. [2014] 3D frequency-domain finite-difference viscoelastic-wave modeling using weighted average 27-point operators with optimal coefficients. *Geophysics*, **79**(3), T169–T188. (cit. on p. 32.)

Graves, R. [1996] Simulating seismic wave propagation in 3D elastic media using staggered-grid finite differences. *Bulletin of the seismological society of America*, **86**, 1091–1106. (cit. on p. 35.)

Griewank, A. [1992] Achieving logarithmic growth of temporal and spatial complexity in reverse automatic differentiation. *Optimization Methods and Software*, **1**, 35–54. (cit. on p. 160.)

Griewank, A. and Walther, A. [2000] Algorithm 799: Revolve: An implementation of checkpointing for the reverse or adjoint mode of computational differentiation. *ACM Transactions on Mathematical Software*, **26**, 19–45. (cit. on p. 160.)

Hamilton, E.L. [1972] Compressional-wave attenuation in marine sediments. *Geophysics*, **37**, 620–646. (cit. on p. 7.)

Hammond, W.C. and Humphreys, E.D. [2000a] Upper mantle seismic wave velocity: effects of realistic partial melt distribution. *J. Geophys. Res.*, **105**(10), 987–999. (cit. on p. 4.)

Hammond, W.C. and Humphreys, E.D. [2000b] Upper mantle seismic wave velocity: effects of realistic partial melt geometries. *J. Geophys. Res.*, **105**(10), 975–986. (cit. on p. 4.)

Hanyga, A. and Seredynska, M. [2003] Power-law attenuation in acoustic and isotropic anelastic media. *Geophysical Journal International*, **155**, 830–838. (cit. on p. 56.)

He, W., Plessix, R. and Singh, S. [2018] Parametrization study of the land multiparameter VTI elastic waveform inversion. *Geophysical Journal International*, **213**(3), 1660–1672. (cit. on p. 107.)

Hestholm, S. [2002] Composite memory variable velocity-stress viscoelastic modelling. *Geophys. J. Int.*, **148**, 153–162. (cit. on pp. 8 and 33.)

Hicks, G.J. and Pratt, R.G. [2001] Reflection waveform inversion using local descent methods: estimating attenuation and velocity over a gas-sand deposit. *Geophysics*, **66**, 598–612. (cit. on pp. 11, 32, and 66.)

Hong, T. [2004] Scattering attenuation ratios of P and S waves in elastic media. *Geo-*

physical Journal International, **158**(1), 211–224. (cit. on p. 5.)
Igel, H., Mora, P. and Riollet, B. [1995] Anisotropic wave propagation through finite-difference grids. *Geophysics*, **60**, 1203–1216. (cit. on p. 38.)
Jackson, D.D. and Anderson, D.L. [1970] Physical mechanisms of seismic?wave attenuation. *Review of Geophysics*, **8**(1), 1–63. (cit. on p. 5.)
Jackson, I., Gerald, J.D.F., Faul, U.H. and Tan, B.H. [2002] Grain-size sensitive seismic wave attenuation in polycrystalline olivine. *J. Geophys. Res.*, **107**(B12), 2360. (cit. on p. 4.)
Jiang, H. and Chauris, H. [2018] A modified 2D visco-acoustic waveform inversion scheme. In: *80th EAGE Conference and Exhibition, Extended Abstracts*. (cit. on pp. 11 and 66.)
Jo, C.H., Shin, C. and Suh, J.H. [1996] An optimal 9 point, finite difference, frequency space, 2-D scalar wave extrapolator. *Geophysics*, **61**(2), 529–537. (cit. on p. 35.)
Kamei, R. and Pratt, R.G. [2008] Waveform tomography strategies for imaging attenuation structure for cross-hole data. In: *70th EAGE Conference and Exhibition, Extended Abstracts*. (cit. on pp. 11 and 66.)
Kamei, R. and Pratt, R.G. [2013] Inversion strategies for visco-acoustic waveform inversion. *Geophysical Journal International*, **194**(2), 859–884. (cit. on pp. 11, 50, 66, 67, 68, and 71.)
Karato, S. [1993] Importance of anelasticity in the interpretation of seismic tomography. *Geophys. Res. Lett.*, **20**, 1623–1626. (cit. on p. 4.)
Kay, I. and Krebes, E.S. [1999] Applying finite element analysis to the memory variable formulation of wave propagation in anelastic media. *Geophysics*, **64**, 300–307. (cit. on pp. 8 and 33.)
Kelly, K.R., Ward, R.W., Treitel, S. and Alford, R.M. [1976] Synthetic seismograms: A finite-difference approach. *Geophysics*, **41**(1), 2–27. (cit. on p. 35.)
Kjartansson, E. [1979] Constant Q-wave propagation and attenuation. *J. Geophys. Res.*, **84**, 4737–4748. (cit. on pp. 7, 8, 26, 27, 32, 52, 53, 56, 57, 58, and 60.)
Klimentos, T. [1995] Attenuation of P- and S-waves as a method of distinguishing gas and condensate from oil and water. *Geophysics*, **60**(2), 447–458. (cit. on pp. 3 and 4.)
Klimentos, T. and MaCann, C. [1990] Relationships among compressional wave attenuation, porosity, clay content, and permeability in sandstones. *Geophysics*, **55**, 998–1014. (cit. on p. 66.)
Knopoff, L. [1956] The seismic pulse in materials possessing solid friction. *Bulletin of the Seismological Society of America*, **46**, 175–184. (cit. on pp. 26, 58, and 66.)
Knopoff, L. [1964] Q. *Reviews of Geophysics*, **2**(4), 625–660. (cit. on p. 7.)
Kolsky, H. [1956] The propagation of stress pulses in viscoelastic solid. *Phys. Mag.*, **1**, 693–710. (cit. on pp. 5 and 7.)
Komatitsch, D. [1997] *Méthodes spectrales et elements spectraux pour l'équation de l'élastodynamics 2D et 3D en milieu hétérogène*. Ph.D. thesis, Institut de Physique du Globe de Paris, Paris, France. (cit. on p. 35.)

Komatitsch, D. and Martin, R. [2007] An unspoilt convolutional perfectly matched layer improved at grazing incident for the seismic wave equation. *Geophysics*, **72**, SM155–SM167. (cit. on pp. 16, 18, and 39.)

Komatitsch, D. and Tromp, J. [1999] Introduction to the spectral element method for three-dimensional seismic wave propagation. *Geophysical Journal International*, **139**, 806–822. (cit. on p. 35.)

Komatitsch, D. and Tromp, J. [2002] Spectral-element simulations of global seismic wave propagation, II. 3D models, oceans, rotation, and self-gravitation. *Geophysical Journal International*, **150**, 303–318. (cit. on p. 35.)

Komatitsch, D. and Tromp, J. [2003] A perfectly matched layer absorbing boundary condition for the second-order seismic wave equation. *Geophysical Journal International*, **154**(1), 146–153. (cit. on p. 39.)

Komatitsch, D. and Vilotte, J.P. [1998] The spectral element method: an efficient tool to simulate the seismic response of 2D and 3D geological structures. *Bulletin of the seismological society of America*, **88**(2), 368–392. (cit. on p. 35.)

Komatitsch, D., Xie, Z., Bozdag, E., de Andrade, E.S., Peter, D., Liu, Q. and Tromp, J. [2016] Anelastic sensitivity kernels with parsimonious storage for adjoint tomography and full waveform inversion. *Geophysical Journal International*, **206**(3), 1467–1478. (cit. on p. 160.)

Kurzmann, A., Przebindowska, A., Kohn, D. and Bohlen, T. [2013] Acoustic full waveform tomography in the presence of attenuation: A sensitivity analysis. *Geophysical Journal International*, **195**, 985–1000. (cit. on pp. 11, 66, and 67.)

Kurzmann, A., Shigapov, R. and Bohlen, T. [2015] Viscoacoustic full waveform inversion for spatially correlated and uncorrelated problems in refection seismics. In: *77th EAGE Conference and Exhibition, Extended Abstracts*. (cit. on pp. 11, 66, and 67.)

Lailly, P. [1983] The seismic inverse problem as a sequence of before stack migrations: Conference on Inverse Scattering, Theory and Application. In: *Society for Industrial and Applied Mathematics, Expanded Abstracts*. 206–220. (cit. on pp. 10, 66, and 169.)

Lameloise, C.A., Chauris, H. and Noble, M. [2015] Improving the gradient of the image-domain objective function using quantitative migration for a more robust migration velocity analysis. *Geophysical Prospecting*, **63**(2), 391–404. (cit. on pp. xi and 12.)

Leggett, M., Goulty, N.R. and Kragh, J.E. [1992] Study of traveltime and amplitude time-lapse tomography using physical model data. In: *Abstracts of 54th EAEG Meeting*. 248–249. (cit. on pp. 9 and 66.)

Levander, A.R. [1988] Fourth-order finite-difference P-SV seismograms. *Geophysics*, **53**, 1425–1436. (cit. on pp. 35 and 38.)

Li, H., Yang, W., Wang, E. and Yong, X. [2015] 2D time-domain visco-acoustic full waveform inversion method. In: *SEG Technical Program Expanded Abstracts 2015*. 1215–1219. (cit. on pp. 11 and 66.)

Li, Y. [2018] *Subsurface seismic imaging based on inversion velocity analysis in both*

image and data domains. Ph.D. thesis, Thèese de doctorat, PSL Research University - MINES ParisTech. (cit. on pp. 12 and 161.)

Li, Y. and Chauris, H. [2018] Coupling direct inversion to common-shot image-domain velocity analysis. *Geophysics*, **83**(5), R497–R514. (cit. on p. 161.)

Liao, Q. and McMechan, G.A. [1995] 2.5D full-wavefield viscoacoustic inversion. *Geophysical Prospecting*, **43**(8), 1043–1059. (cit. on pp. 10 and 66.)

Liao, Q. and McMechan, G.A. [1996] Multifrequency viscoacoustic modeling and inversion. *Geophysics*, **61**(5), 1371–1378. (cit. on pp. 11, 32, and 66.)

Lines, L. and Treitel, S. [1984] Tutorial: A review of least-squares inversion and its application to geophysical problems. *Geophysical prospecting*, **32**(2), 159–186. (cit. on p. 169.)

Liu, H.P., Anderson, D.L. and Kanamori, H. [1976] Velocity dispersion due to anelasticity; Implications for seismology and mantle composition. *Geophysical Journal of the Royal Astronomical Society*, **47**, 41–58. (cit. on pp. 7, 8, 23, 26, 28, 36, 58, and 68.)

Mainardi, F. [2010] *Fractional Calculus and Waves in Linear Viscoelasticity*. Imperial College Press, London, United Kingdom. (cit. on pp. 52, 53, 55, 56, 57, and 60.)

Mainardi, F. and Spada, S. [2011] Creep, relaxation and viscosity properties for basic fractional models in rheology. *The European Physical Journal Special Topics*, **193**(1), 133–160. (cit. on p. 55.)

Malinowski, M., Operto, S. and Ribodetti, A. [2011] High-resolution seismic attenuation imaging from wide-aperture onshore data by visco-acoustic frequency-domain full waveform inversion. *Geophysical Journal International*, **186**, 1179–1204. (cit. on pp. 11, 13, 49, 66, 67, and 137.)

Marfurt, K.J. [1984] Accuracy of finite-difference and finite-element modelling of the scalar and elastic wave equations. *Geophysics*, **49**, 533–549. (cit. on pp. 35 and 38.)

Marion, D.P. and Coudin, P. [1992] From ray to effective medium theories in stratified media: an experimental study. In: *SEG Technical Program Expanded Abstracts 1992*. 1341–1243. (cit. on p. 66.)

Martin, R. and Komatitsch, D. [2009] An unspoilt convolutional perfectly matched layer technique improved at grazing incident for the viscoelastic wave equation. *Geophys. J. Int.*, **179**, 333–344. (cit. on pp. 16, 18, and 39.)

Martin, R., Komatitsch, D. and Ezziani, A. [2008] An unsplit convolutional perfectly matched layer improved at grazing incidence for seismic wave propagation in poroelastic media. *Geophysics*, **73**(4), T51–T61. (cit. on p. 38.)

McDonal, F.J., Angona, F.A., Milss, R.L., van Nostrand, R.G. and White, J.E. [1958] Attenuation of shear and compressional waves in Pierre shale. *Geophysics*, **23**, 421–439. (cit. on pp. xi, 7, 8, and 58.)

McMechan, G. [1983] Migration by extrapolation of time-dependent boundary values. *Geophysical Prospecting*, **31**(3), 413–420. (cit. on p. 169.)

Métivier, L., Bretaudeau, L., Brossier, R., Operto, S. and Virieux, J. [2014] Full waveform inversion and truncated Newton method: quantitative imaging of complex sub-

surface structures. *Geophysical Prospecting*, **62**(6), 1203–1483. (cit. on pp. 11, 13, and 107.)

Métivier, L., Brossier, R., Virieux, J. and Operto, S. [2013] Full waveform inversion and the truncated Newton method. *SIAM Journal on Scientific Computing*, **35**(2), B401–B437. (cit. on pp. 11 and 13.)

Moczo, P., Bystricky, E., Kristek, J., Carcione, J.M. and Bouchon, M. [1997] Hybrid modeling of P-SV seismic motion at inhomogeneous viscoelastic topographic structures. *Bulletin of the Seismological Society of America*, **87**, 1305–1323. (cit. on pp. 8 and 33.)

Moczo, P. and Kristek, J. [2005] On the rheological models used for time-domain methods of seismic wave propagation. *Geophys. Res. Lett.*, **83**, L01306. (cit. on pp. xii, 8, 23, 24, 28, 29, 52, 53, 57, and 58.)

Mora, P. [1989] Inversion = migration + tomography. *Geophysics*, **54**(12), 78–101. (cit. on p. 119.)

Mukhopadhyay, S. and Tyagi, C. [2008] Variation of intrinsic and scattering attenuation with depth in NW Himalayas. *Geophysical Journal International*, **172**(3), 1055–1065. (cit. on p. 5.)

Muller, T.M., Gurevich, B. and Lebedev, M. [2010] Seismic wave attenuation and dispersion resulting from wave-induced flow in porous rocks - A review. *Geophysics*, **75**(5), A147–A164. (cit. on p. 3.)

Munasinghe, M. and Farnell, G.W. [1973] Finite difference analysis of Rayleigh wave scattering at vertical discontinuities. *J. Geophys. Res.*, **78**, 2454–2466. (cit. on p. 7.)

Murphy, W.F. [1982] Effects of partial water saturation on attenuation in Massilon Sandstone and Vycor Porous Glass. *J. Acoust. Soc. Am.*, **71**(6), 1458–1468. (cit. on p. 4.)

Nocedal, J. and Wright, S. [2006] *Numerical Optimization*. Springer. (cit. on p. 111.)

Nutting, P. [1921] A new general law of deformation. *Journal of the Franklin Institute*, **191**(5), 679–685. (cit. on p. 55.)

O'Connell, R.J. and Budiansky, B. [1978] Measures of dissipation in viscoelastic media. *J. Geophys. Res.*, **5**, 5–8. (cit. on pp. 26 and 58.)

Operto, S., Brossier, R., Combe, L., Métivier, L., Ribodetti, A. and Virieux, J. [2014] Computationally-efficient three-dimensional visco-acoustic finite-difference frequency-domain seismic modeling in vertical transversely isotropic media with sparse direct solver. *Geophysics*, **79**(5), T257–T275. (cit. on pp. 11, 15, 32, 35, and 66.)

Operto, S. and Miniussi, A. [2018] On the role of density and attenuation in three-dimensional multiparameter viscoacoustic VTI frequency-domain FWI: an OBC case study from the North Sea. *Geophysical Journal International*, **213**, 2037–2059. (cit. on pp. 11 and 66.)

Operto, S., Miniussi, A., Brossier, R., Combe, L., Métivier, L., Monteiller, V., Ribodetti, A. and Virieux, J. [2015] Efficient 3-D frequency-domain mono-parameter full-waveform inversion of ocean-bottom cable data: application to Valhall in the

visco-acoustic vertical transverse isotropic approximation. *Geophysical Journal International*, **202**, 1362–1391. (cit. on pp. 11, 15, 32, and 66.)

Operto, S., Ribodetti, A., Grini, M. and Virieux, J. [2007a] Mixed-grid finite difference frequency-domain visco-acoustic wave modeling in 2D TTI anisotropic media. In: *SEG Technical Program Expanded Abstracts 2007*. 2099–2103. (cit. on p. 35.)

Operto, S., Virieux, J., Amestoy, P., L'Excellent, J., Giraud, L. and Ali, H.B.H. [2007b] 3D finite-difference frequency-domain modeling of visco-acoustic wave propagation using a massively parallel direct solver: A feasibility study. *Geophysics*, **72**, SM195–SM211. (cit. on pp. 32, 33, and 35.)

Park, S.W. [2001] Analytical modelling of viscoelastic dampers for structural and vibration control. *International Journal of Solids and Structures*, **38**(44–45), 8065–8092. (cit. on pp. 55 and 56.)

Peselnick, L. and Outerbridge, W.F. [1961] Internal friction in shear and shear modulus of Solenholfen limestone over a frequency range of 10^7 cycles per second. *Journal of Geophysical Research*, **66**, 581–588. (cit. on p. 7.)

Peselnick, L. and Zietz, I. [1959] Internal friction of fine grained limestones at ultrasonic frequencies. *Geophysics*, **24**, 285–296. (cit. on p. 7.)

Pipkin, A.C. [1986] *Lectures on viscoelasticity theory*. Springer, Verlag, Germany. (cit. on p. 28.)

Plessix, R.E. [2006a] Estimation of velocity and attenuation coefficient maps from crosswell seismic data. *Geophysics*, **71**(6), S235–S240. (cit. on pp. 10 and 66.)

Plessix, R.E. [2006b] A review of the adjoint-state method for computing the gradient of a functional with geophysical applications. *Geophysical Journal Inernational*, **167**(2), 495–503. (cit. on pp. 18, 110, and 165.)

Plessix, R.E., Stopin, A., Kuehl, H., Goh, V. and Overgaag, K. [2016] Visco-acoustic full waveform inverision. In: *78th EAGE Conference and Exhibition, Extended Abstracts*. (cit. on pp. xi, 4, 11, 13, 15, 66, 67, 71, 106, 119, and 160.)

Polak, E. and Ribière, G. [1969] Note sur la convergence de méthodes de directions conjuguées. *Revue Française d'Informatique et de Recherche Opérationnelle*, **16**, 35–43. (cit. on p. 111.)

Pratt, R., Hou, F., Bauer, K. and Weber, M. [2005] Waveform tomography images of velocity and inelastic attenuation from the Mallik 2002 crosshole seismic surveys. *Bulletin-Geological Survey of Canada*, **585**, 122. (cit. on pp. 11, 32, 66, and 67.)

Pratt, R.G. [1990] Frequency domain elastic wave modeling by finite differences: A tool for crosshole seismic imaging. *Geophysics*, **55**(5), 626–632. (cit. on p. 35.)

Pratt, R.G. [1999] Seismic waveform inversion in the frequency domain, Part I: Theory and verification in a physical scale model:. *Geophysics*, **64**, 888–901. (cit. on pp. 10 and 35.)

Prieux, V., Brossier, R., Operto, S. and Virieux, J. [2013] Multiparameter full waveform inversion of multicomponent OBC data from Valhall. Part 1: imaging compressional wavespeed, density and attenuation. *Geophysical Journal International*,

194(3), 1640–1664. (cit. on pp. 11, 15, 32, 49, 66, 67, 68, 71, 107, and 119.)

Qi, Q., Muller, T.M. and Pervukhina, M. [2017] Sonic Qp/Qs ratio as diagnostic tool for shale gas saturation. *Geophysics*, **82**(3), MR97–MR103. (cit. on p. 4.)

Quan, Y. and Harris, J. [1997] Seismic attenuation tomography using the frequency shift method. *Geophysics*, **62**(3), 895–905. (cit. on pp. 10, 12, and 66.)

Ribodetti, A. and Hanyga, A. [2004] Some effects of the memory kernel singularity on wave propagation and inversion in viscoelastic media - II. Inversion. *Geophysical Journal International*, **158**, 426–442. (cit. on p. 56.)

Ribodetti, A., Operto, S., Virieux, J., Lambaré, G., Valéro, H.P. and Gibert, D. [2000] Asymptotic viscoacoustic diffraction tomography of ultrasonic laboratory data: a tool for rock properties analysis. *Geophysical Journal International*, **140**, 324–340. (cit. on p. 10.)

Ribodetti, A. and Virieux, J. [2000] Asymptotic theory for imaging the attenuation factor Q. *Geophysics*, **63**(5), 1767–1778. (cit. on p. 10.)

Ricker, N. [1953] The form and laws of propagation of seismic wavelets. *Geophysics*, **18**, 10–40. (cit. on pp. 5, 7, and 32.)

Robertsson, J.O.A. [1996] A numerical free-surface condition for elastic/ viscoelastic finite-difference modelling in the presence of topography. *Geophysics*, **61**, 1921–1934. (cit. on pp. 8 and 33.)

Robertsson, J.O.A., Blanch, J.O. and Symes, W.W. [1994] Viscoelastic finite-difference modeling. *Geophysics*, **59**, 1444–1456. (cit. on pp. 8, 23, 26, 28, 33, 36, 38, and 68.)

Saenger, E.H. and Bohlen, T. [2002] Parallel 3-D viscoelastic finite difference seismic modelling. *Computers & Geosciences*, **28**, 887–899. (cit. on p. 36.)

Saenger, E.H. and Bohlen, T. [2004] Finite-difference modeling of viscoelastic and anisotropic wave propagation using the rotated staggered grid. *Geophysics*, **69**(2), 583–591. (cit. on pp. 36 and 38.)

Sambridge, M. and Mosegaard, K. [2002] MONTE CARLO METHODS IN GEOPHYSICAL INVERSE PROBLEMS. *Reviews of Geophysics*, **40**(3), 1–29. (cit. on p. 71.)

Sasso, M., Palmieri, G. and Amodio, D. [2011] Application of fractional derivative models in linear viscoelastic problems. *Mech Time-Depend Mater*, **15**, 367–387. (cit. on p. 25.)

Sato, H., Fehler, M.C. and T, M. [2012] *Seismic wave propagation and scattering in the heterogeneous earth*. Springer. (cit. on pp. xi, 5, and 6.)

Sato, H., Sacks, I.S. and Murase, T. [1989] The use of laboratory velocity data for estimating temperature and partial melt fraction in the low velocity zone: comparison with heat flow and electrical conductivity studies. *J. Geophys. Res.*, **94**, 5689–5704. (cit. on p. 4.)

Sava, P. and Biondi, B. [2004] Wave-equation migration velocity analysis. I. Theory. *Geophysical Prospectings*, **52**, 593–606. (cit. on pp. 12 and 161.)

Sava, P. and Vasconcelos, I. [2011] Extended imaging conditions for wave-equation

migration. *Geophysical Prospectings*, **59**, 35–55. (cit. on pp. 12 and 161.)
Sei, A. and Symes, W. [1995] Dispersion analysis of numerical wave propagation and its computational consequences. *Journal of Scientific Computing*, **10**(1), 1–27. (cit. on p. 38.)
Shapiro, S.A. and Hubra, P. [1999] *Elastic waves in random media*. Springer. (cit. on p. 5.)
Shapiro, S.A. and Kneib, G. [1993] Seismic Attenuation By Scattering: Theory and Numerical Results. *Geophysical Journal International*, **114**(2), 373–391. (cit. on p. 5.)
Shen, Y. [2016] *Wave-equation migration Q analysis*. Ph.D. thesis, Stanford University. (cit. on pp. 5, 12, and 161.)
Shen, Y., Biondi, B. and Nichols, D. [2012] Wave-equation migration Q analysis. In: *74th EAGE Conference and Exhibition, Extended Abstracts*. (cit. on pp. 12 and 161.)
Shen, Y. and Zhu, T. [2015] Image-based Q tomography using reverse time Q migration. In: *SEG Technical Program Expanded Abstracts 2015*. 3694–3698. (cit. on p. 12.)
Sheriff, R.E. and Geldart, L.P. [1995] *Exploration seismology*. Cambridge University press, 2 edn., 59–60. (cit. on pp. 3 and 7.)
Smith, W.D. [1975] The application of finite element analysis to body wave propagation problems. *Geophysical Journal of the Royal Astronomical Society*, **42**, 747–768. (cit. on p. 35.)
Song, Z., Williamson, P.R. and Pratt, R.G. [1995] Frequency-domain acoustic-wave modeling and inversion of crosshole data: Part II–Inversion method, synthetic experiments and real-data results. *Geophysics*, **60**, 796–809. (cit. on pp. 11, 32, 50, and 66.)
Stekl, I. and Pratt, R.G. [1998] Accurate viscoelastic modeling by frequency-domain finite difference using rotated operators. *Geophysics*, **63**, 1779–1794. (cit. on pp. 32 and 35.)
Strick, E. [1967] The determination of Q, dynamic viscosity and creep curves from wave propagation measurements. *Geophysical Journal of the Royal Astronomical Society*, **13**, 197–218. (cit. on p. 7.)
Symes, B. [2017] Extended Waveform Inversion. In: *79th EAGE Conference and Exhibition 2017-Workshops*. (cit. on pp. 12 and 161.)
Symes, W.W. [2007] Reverse time migration with optimal checkpointing. *Geophysics*, **72**(5), SM213–SM221. (cit. on p. 160.)
Symes, W.W. [2008] Migration velocity analysis and waveform inversion. *Geophysical Prospecting*, **56**, 765–790. (cit. on pp. 12 and 161.)
Tarantola, A. [1984a] Inversion of seismic reflection data in the acoustic approximation. *Geophysics*, **49**(8), 1259–1266. (cit. on pp. 10, 66, 70, and 110.)
Tarantola, A. [1984b] Linearized inversion of seismic reflection data. *Geophysical prospecting*, **32**(6), 998–1015. (cit. on p. 170.)
Tarantola, A. [1987] *Inverse Problem Theory - Methods for Data Fitting and Model*

Parameter Estimation. Elsevier Science. (cit. on p. 141.)

Tarantola, A. [1988] Theoretical background for the inversion of seismic waveforms, including elasticity and attenuation. *Pure and Applied Geophysics*, **128**, 365–399. (cit. on pp. 10, 12, 49, and 66.)

Thomsen, L.A., Barkved, O., Haggard, B., Kommedal, J.H. and Rosland, B. [1997] Converted wave imaging of Valhall reservoir. In: *59th EAGE Conference and Exhibition, Extended Abstracts*. (cit. on p. 66.)

Thorbecke, J. [2015] *2D Finite-Difference wavefield modelling*. (cit. on pp. xii and 39.)

Thorne, L. and Wallace, T.C. [1995] *Modern Global Seismology*. Academic Press, Cambridge, Massachusetts, United States. (cit. on pp. xix and 7.)

Toksoz, M.N. and Johnston, D.H. [1981] *Seismic Wave Attenuation*. Geophysics Reprint Series, No. 2, Society of Exploration Geophysicists, Tulsa, OK. (cit. on pp. 7, 49, and 65.)

Toksoz, M.N., Johnston, D.H. and Timur, A. [1979] Attenuation of seismic waves in dry and saturated rocks: I. Laboratory measurements. *Geophysics*, **44**(4), 681–690. (cit. on p. 7.)

Tonn, R. [1991] The determination of the seismic quality factor Q from VSP data: A comparison of different computational methods. *Geophysical Prospecting*, **39**, 1–27. (cit. on pp. 10 and 66.)

Tullos, F.N. and Reid, A.C. [1969] Seismic attenuation of Gulf coast sediments. *Geophysics*, **34**, 516–528. (cit. on p. 7.)

Virieux, J. [1986] P-SV wave propagation in heterogeneous media: velocity-stress finite-difference method. *Geophysics*, **51**(4), 889–901. (cit. on pp. 18, 35, 36, and 38.)

Virieux, J., Calandra, H. and Plessix, R. [2011] A review of the spectral, pseudo-spectral, finite-difference and finite-element modelling techniques for geophysical imaging. *Geophysical Prospecting*, **59**, 794–813. (cit. on p. 35.)

Virieux, J. and Operto, S. [2009] An overview of full-waveform inversion in exploration geophysics. *Geophysics*, **74**(6), WCC1–WCC26. (cit. on pp. 66, 70, 110, and 119.)

Voigt, W. [1892] Ueber innere Reibung fester Korper, insbesondere der Metalle. *Ann. Phys. Chem. Neue Folge*, **47**, 671–693. (cit. on pp. 5 and 7.)

Walls, J., Taner, M.T., Mavko, G. and Dvorkin, J. [2002] Seismic attenuation for reservoir characterization. Report of U.S. Department of Energy, Office of Scientific and Technical Information. (cit. on p. 4.)

Wang, M., Xie, Y., Xiao, B., Ratcliffe, A. and Latter, T. [2018] Visco-acoustic full-waveform inversion in the presence of complex gas clouds. In: *SEG Technical Program Expanded Abstracts 2018*. (cit. on pp. 11, 66, and 67.)

Wang, Y. [2008] *Seismic Inverse Q Filtering*. Wiley-Blackwell, Hoboken, New Jersey. (cit. on pp. 3, 7, 65, and 170.)

Wang, Y. [2016] Generalized viscoelastic wave equation. *Geophysical Journal International*, **204**, 1216–1221. (cit. on p. 56.)

White, J. [1965] *Seismic waves: Radiation, transmission and attenuation*. Pergamon,

New York. (cit. on p. 57.)
Winkler, K.W. and Nur, A. [1979] Pore fluids and seismic attenuation in rocks. *Geophys. Res. Lett.*, **61**, 1–4. (cit. on p. 3.)
Winkler, K.W. and Nur, A. [1982] Seismic attenuation: Effects of pore fluids and frictional?sliding. *Geophysics*, **47**(1), 1–15. (cit. on p. 3.)
Xu, T. and McMechan, G.A. [1995] Composite memory variables for viscoelastic synthetic seismograms. *Geophys. J. Int.*, **121**, 634–639. (cit. on pp. 8 and 33.)
Xue, Z., Sun, J., Fomel, S. and Zhu, T. [2017] Accelerating full-waveform inversion with attenuation compensation. *Geophysics*, **83**(1), A13–A20. (cit. on p. 5.)
Yang, P., Brossier, R., Metivier, L. and Virieux, J. [2018] A time-domain preconditioned truncated Newton approach to visco-acoustic multiparameter full waveform inversion. *SIAM Journal on Scientific Computing*, **40**(4), B1101–B1130. (cit. on pp. 11, 13, 66, 67, 107, and 160.)
Yang, P., Brossier, R., Mtivier, L. and Virieux, J. [2016] Wavefield reconstruction in attenuating media: A checkpointing-assisted reverse-forward simulation method. *Geophysics*, **81**(6), R349–R362. (cit. on p. 160.)
Zener, C. [1948] *Elasticity and anelasticity of metals*. University of Chicago Press, Chicago, Illinois. (cit. on p. 25.)
Zeng, C., Dong, S. and Wang, B. [2017] A guide to least-squares reverse time migration for subsalt imaging: Challenges and solutions. *Interpretation*, **5**(3), SN1–SN11. (cit. on p. 169.)
Zhang, C. and Ulrych, T.J. [2002] Estimation of quality factors from CMP records. *Geophysics*, **67**, 1542–1547. (cit. on p. 10.)
Zhang, Y., Duan, L. and Xie, Y. [2014a] A stable and practical implementation of least-squares reverse time migration. *Geophysics*, **80**(1), V23–V31. (cit. on p. 169.)
Zhang, Y., Ratcliffe, A., Roberts, G. and Duan, L. [2014b] Amplitude-preserving reverse time migration: From reflectivity to velocity and impedance inversion. *Geophysics*, **79**(6), S271–S283. (cit. on p. 169.)
Zhang, Y. and Sun, J. [2009] Practical issues in reverse time migration: true amplitude gathers, noise removal and harmonic source encoding. *First Break*, **27**(1295), 204–204. (cit. on p. 169.)
Zhang, Y., Zhang, G. and Bleistein, N. [2003] True amplitude wave equation migration arising from true amplitude one-way wave equations. *Inverse Problems*, **19**(5), 1113–1138. (cit. on p. 169.)
Zhang, Y., Zhang, G. and Bleistein, N. [2005] Theory of true-amplitude one-way wave equations and true-amplitude common-shot migration. *Geophysics*, **70**(4), E1–E10. (cit. on p. 169.)
Zhang, Y., Zhang, P. and Zhang, H. [2010] Compensating for visco-acoustic effects in reverse-time migration. In: *SEG Technical Program Expanded Abstracts 2010*. 3160–3164. (cit. on pp. 5, 8, 169, 170, and 172.)
Zhou, J., Birdus, S., Huang, B., Teng, K.H., Xie, Y., Chagalov, D., Cheang, A.,

Wellen, D. and J, G. [2011] Compensating attenuation due to shallow gas through Q-tomography and Q-PSDM, a case study from Brazil. In: *SEG Technical Program Expanded Abstracts 2011*. 3332–3336. (cit. on pp. xi, 5, and 65.)

Zhou, W., Brossier, R., Operto, S. and Virieux, J. [2015] Full waveform inversion of diving & reflected waves for velocity model building with impedance inversion based on scale separation. *Geophysical Journal International*, **22**, 1535–1554. (cit. on p. 119.)

Zhu, T. and Harris, M. [2014] Modeling acoustic wave propagation in heterogeneous attenuating media using decoupled fractional Laplacians. *Geophysics*, **69**(3), T105–T116. (cit. on pp. 8 and 170.)

Zhu, T., Harris, M. and Biondi, B. [2014] Q-compensated reverse-time migration. *Geophysics*, **79**(3), S77–S87. (cit. on pp. xviii, 5, 170, 171, and 172.)

Zucca, J.J., Hutchings, L.J. and W, K.P. [1994] Seismic velocity and attenuation structure of the Geysers geothermal field, California. *Geothermics*, **23**, 111–126. (cit. on p. 66.)

RÉSUMÉ

L'atténuation sismique est un paramètre physique très utile pour décrire et imager les propriétés du sous-sol, et tout particulièrement les roches saturées et les nuages de gaz. Les approches classiques analysent l'amplitude du spectre des données ou bien la distorsion de ce spectre, avec des méthodes asymptotiques. L'inversion des formes d'onde (Full Waveform Inversion en anglais, FWI) est une approche alternative qui prend en compte les aspects de fréquences finies. En pratique, à la fois les vitesses et l'atténuation doivent être déterminées. Il est connu que l'inversion multi-paramètre ne conduit pas à un résultat unique.

Ce travail se focalise sur la détermination des vitesses et de l'atténuation. La dispersion liée à l'atténuation produit des modèles de vitesse équivalents en termes de cinématique. Je propose une inversion hybride : la « relation cinématique » est un moyen de guider l'inversion des formes d'onde non-linéaire. Elle se décompose en deux étapes. Dans un premier temps, l'information cinématique est remise à jour, et ensuite les vitesses et l'atténuation sont modifiées, pour une cinématique donnée. Différentes approches sont proposées et discutées au travers d'applications sur des données synthétiques 2D, en particulier sur les modèles Midlle-East et Marmousi.

MOTS CLÉS

imagerie sismique, atténuation, inversion des formes d'onde, dispersion

ABSTRACT

Seismic attenuation is a useful physical parameter to describe and to image the properties of specific geological bodies, e.g., saturated rocks and gas clouds. Classical approaches consist of analyzing seismic spectrum amplitudes or spectrum distortions based on ray methods. Full waveform inversion is an alternative approach that takes into account the finite frequency aspect of seismic waves. In practice, both seismic velocities and attenuation have to be determined. It is known that the multi-parameter inversion suffers from cross-talks.

This thesis focuses on retrieving velocity and attenuation. Attenuation dispersion leads to equivalent kinematic velocity models, as different combinations of velocity and attenuation have the same kinematic effects. I propose a hybrid inversion strategy: the kinematic relationship is a way to guide the non-linear full waveform inversion. The hybrid inversion strategy includes two steps. It first updates the kinematic velocity, and then retrieves the velocity and attenuation models for a fixed kinematic velocity. The different approaches are discussed through applications on 2D synthetic data sets, including the Midlle-East and Marmousi models.

KEYWORDS

seismic imaging, attenuation, full waveform inversion, dispersion